UNIVERSITY OF SOUTHAMPTON

Space debris cloud evolution in Low Earth Orbit

by

Francesca Letizia

A thesis submitted in partial fulfilment for the degree of Doctor of Philosophy

in the
Faculty of Engineering and the Environment
Aeronautics, Astronautics and Computational Engineering

February 2016

UNIVERSITY OF SOUTHAMPTON

ABSTRACT

FACULTY OF ENGINEERING AND THE ENVIRONMENT
Aeronautics, Astronautics and Computational Engineering

Doctor of Philosophy

Space debris cloud evolution in Low Earth Orbit

by Francesca Letizia

The Earth is surrounded by inoperative objects generated from past and current space missions. Because of the high orbital speed, even the impact with small fragments is a hazard to operational spacecraft as it could lead to the partial or complete loss of the mission. Therefore, it is important to assess the collision risk due to space debris considering small fragments, which are usually not included in space debris modelling because their large number would make simulations extremely complex. In this work, an analytical approach is developed to describe the evolution of debris clouds created by fragmentations in Low Earth Orbit. In contrast to traditional approaches, which follow the trajectory of individual fragments, with the proposed method the cloud behaviour is studied globally, so that the presence of small fragments can be modelled. This give a deeper insight into the dynamics of debris clouds and reduces the computational effort needed to estimate the consequences of a collision. A standard breakup model is used to describe the dispersion of the fragments in terms of characteristic length, area-to-mass ratio and velocity. From the velocity distribution, the fragment spatial dispersion is derived. The cloud density is expressed by a continuous function that depends on the altitude and that is set as initial condition for the orbit propagation. Based on an analytical approach proposed in the literature for interplanetary dust and spacecraft swarms, the fragment cloud evolution in time is derived through the continuity equation, which is used to describe the variation of debris density considering the effect of atmospheric drag. The approach has been extended to express the cloud density as a function of multiple orbital parameters and to model additional perturbations such as the Earth's oblateness. The method has been validated through the comparison with the traditional numerical propagation and then applied to study many breakup scenarios. The proposed approach proves to be flexible and able to study the collision risk coming from several breakup events and to evaluate the vulnerability of different targets. It is also applied to derive an index of the environmental criticality of spacecraft.

Contents

List of Figures

List of Tables

List of Symbols

Greek symbols

β	Latitude [rad or deg]
Δv	Relative velocity [$\mathrm{km\,s^{-1}}$]
Φ	Flux of fragments
μ	Mean value
μ_E	Earth's planetary gravitational constant [$\mathrm{km^3\,s^{-2}}$]
ν	True anomaly [rad or deg]
Ω	Longitude of the ascending node [rad or deg]
ω	Argument of the periapsis [rad or deg]
φ	Longitude or azimuthal angle [rad or deg]
ρ	Atmosphere density [$\mathrm{kg\,m^{-3}}$]
σ	Standard deviation
σ_c	Collisional cross-sectional area [$\mathrm{m^2}$]
θ	Polar angle [rad or deg]

Roman symbols

A	Cross-sectional area [$\mathrm{m^2}$]
a	Semi-major axis [km]
a_d	Drag acceleration [$\mathrm{m\,s^{-2}}$]
c_d	Drag coefficient
$\mathcal{E}$	Energy
$\mathrm{E}[x]$	Complete elliptic integral of the second kind

e Eccentricity

err_{peak} Relative error on the peak height of the density profile

err_{prof} Mean absolute error on the density profile

err_{tot} Relative error on the integral of the density profile

$\mathbf{f}$ Vector field

f Spatial density as function of the latitude only

F Cumulative distribution function (cdf)

$\hat{F}_n$ Empirical cumulative distribution function

H Scale height for the atmospheric model [km]

h Altitude [km]

i Inclination [rad or deg]

I_k Modified Bessel function of the first kind and order k

j Imaginary unit

J_2 Second zonal harmonic coefficient for the Earth

L_c Fragment characteristic length [m]

M Mass [kg]

M_e Reference mass for collision [kg]

M_p Projectile mass [kg]

$\bar{n}$ Mean motion

$\mathcal{N}$ Normal distribution

N Number of collisions

N_b Number of bins

N_f Number of fragments

n Fragment density

$\bar{n}$ Mean motion

P Probability

p Semi-latus rectum [km]

p_c	Cumulative probability
r	Radial distance [km]
R_E	Earth's equatorial radius [km]
R_h	Reference altitude for the atmospheric model [km]
S	Non-dimensional empirical factor for fragment generation for explosions
s	Spatial density as function of the distance only
T	Orbital period [s]
T_B	Time for band formation [s]
u	Argument of latitude at epoch [rad or deg]
V	Volume [km^3]
v	Velocity [$\mathrm{km\,s^{-1}}$]
v_c	Collision velocity [$\mathrm{km\,s^{-1}}$]
w	Width of bins in altitude [km]
$\mathbb{Z}$	Set of integer numbers

Subscripts and Superscripts

$\dot{\bullet}$	Derivation with respect to time
$\bullet_a$	Apocentre
$\bullet'$	Derivation with respect to radial distance r
$\bullet_{\mathrm{F}}$	Relative to fragments
$\bullet_p$	Pericentre
$\bullet_{\mathrm{ref}}$	Values at the reference altitude for the atmospheric model
$\bullet_{\mathrm{T}}$	Relative to target spacecraft

List of Acronyms

ADR	Active Debris Removal
ASI	Agenzia Spaziale Italiana
CiELO	debris Cloud Evolution in Low (Earth) Orbit
CONCEPT	CONsequences of Cloud Evolution Prediction Tool
CNR	Consiglio Nazionale delle Ricerche
CNSA	China National Space Administration
CPU	Control Processing Unit
CDF	Cumulative Distribution Function
DAMAGE	Debris Analysis and Monitoring Architecture for the Geosynchronous Environment
DCP	Debris Cloud Propagator
DELTA	Debris Environment Long-Term Analysis
DISCOS	Database and Information System Characterising Objects in Space
DLR	Deutsches Zentrum für Luft- und Raumfahrt
DMSP	Defense Meteorological Satellite Program
EC	Environmental Criticality
ECOB	Environmental Consequences of Orbital Breakups
ESA	European Space Agency
FADE	FAst Debris Evolution
FEM	Finite Element Methods
FOM	Figure Of Merit

FOP	Fast Orbit Propagator
GEI	Geocentric Equatorial Intertial
GEO	Geosynchronous Earth Orbit
GPS	Global Positioning System
IADC	Inter-Agency Space Debris Coordination Committee
IFAC	Istituto di Fisica Applicata *N. Carrara*
ISTI	Istituto di Scienza e Tecnologie dellInformazione *A. Faedo*
ISS	International Space Station
LEGEND	LEO-to-GEO Environment Debris model
LEO	Low Earth Orbit
LUCA	Long-Term Utility for Collision Analysis
MASTER	Meteoroid and Space Debris Terrestrial Environment Reference
MEDEE	Modelling the Evolution of space Debris on the Earth's Environment
MOID	Minimum Orbital Intersection Distance
NASA	National Aeronautics and Space Administration
ODE	Ordinary Differential Equation
ORDEM	ORbital Debris Engineering Model
PDE	Partial Differential Equation
PL	Payload
PlanODyn	Planetary Orbital Dynamics
RAM	Random Access Memory
RB	Rocket Body
SANE	Simple ANalytical Evolution
SC	Spacecraft
SDM	Space Debris Mitigation
SPDA	Space Debris Prediction and Analysis
STAT	STochastic Analog Tool

Declaration of Authorship

I, Francesca Letizia declare that this thesis and the work presented in it are my own and has been generated by me as the result of my own original research.

Space debris cloud evolution in Low Earth Orbit

I confirm that:

1. This work was done wholly or mainly while in candidature for a research degree at this University;
2. Where any part of this thesis has previously been submitted for a degree or any other qualification at this University or any other institution, this has been clearly stated;
3. Where I have consulted the published work of others, this is always clearly attributed;
4. Where I have quoted from the work of others, the source is always given. With the exception of such quotations, this thesis is entirely my own work;
5. I have acknowledged all main sources of help;
6. Where the thesis is based on work done by myself jointly with others, I have made clear exactly what was done by others and what I have contributed myself;
7. Either none of this work has been published before submission, or parts of this work have been published as:
   - Journal papers
     - F. Letizia, C. Colombo, and H. G. Lewis. Analytical model for the propagation of small debris objects clouds after fragmentations. *Journal of Guidance, Control, and Dynamics*, 38(8):1478–1491, 2015c
     - F. Letizia, C. Colombo, and H. G. Lewis. Collision probability due to space debris clouds through a continuum approach. *Journal of Guidance, Control, and Dynamics*, 2015i. doi: 10.2514/1.G001382. Accessed 10 September 2015
     - F. Letizia, C. Colombo, and H. G. Lewis. Multidimensional extension of the continuity equation method for debris clouds evolution. *Advances in Space Research*, 2015a. doi:10.1016/j.asr.2015.11.035. Accessed 8 December 2015
   - Conference proceedings
     - F. Letizia, C. Colombo, H. G. Lewis, and C. R. McInnes. Debris cloud evolution in Low Earth Orbit. In *64th International Astronautical Congress*, Paris, France, September 2013. International Astronautical Federation. IAC-13.A6.P.12
     - F. Letizia, C. Colombo, and H. G. Lewis. Analytical model for the propagation of small debris objects after a fragmentation event. In *24th AAS/AIAA Space Flight Mechanics Meeting*. AAS/AIAA, January 2014a. AAS 14-324

– F. Letizia, C. Colombo, and H. G. Lewis. Continuity equation approach for the analysis of the collision risk due to space debris clouds generated by a fragmentation event. In *65th International Astronautical Congress*, Paris, France, September 2014b. International Astronautical Federation. IAC-14.A6.P.31
– F. Letizia, C. Colombo, and H. G. Lewis. Small debris fragments contribution to collision probability for spacecraft in Low Earth Orbit. In *Space Safety is No Accident, 7th IAASS Conference*, pages 379 – 387. Springer International Publishing, May 2015d. ISBN 978-3-319-15981-2
– F. Letizia, C. Colombo, and H. G. Lewis. 2D continuity equation method for space debris cloud collision analysis. In *25th AAS/AIAA Space Flight Mechanics Meeting*. AAS/AIAA, January 2015g. AAS 15-293
– F. Letizia, C. Colombo, and H. G. Lewis. Density based approach for collision risk computation. In *25th International Symposium on Space Flight Dynamics*, October 2015h

Signed: _____

Date: _____

Solo il caso ci ha portato
dall'altra parte del mare.

Acknowledgements

I would like to thank Camilla Colombo and Hugh Lewis for the extremely valuable guidance they have given me in these three years. I am aware that I have been very privileged in having not only one, but even two attentive supervisors. Our conversations have been sources of inspiration for the research and of advice for professional development. A special thanks to Camilla for having believed in me at a time when others did not.

I would like to thank the University of Southampton for providing access to IRIDIS High Performance Computing Facility, and associated support services, which have been essential in the completion of this work. I also would like to acknowledge that part of this work was funded by EPSRC through the grant EP/K503150/1.

In these three years I have received precious support by different organisations. First and foremost, I would like to thank Zonta International for having awarded me with an Amelia Earth Fellowship in 2012. The fellowship allowed me to enrich my PhD with different experiences and gave me the opportunity to meet some very inspirational women. Beside Zonta International, I would like to acknowledge the financial support to attend different conferences that I received from the Institution of Engineering and Technology (IET), the Space Generation Advisory Council (SGAC), ESA Education Office, Women in Science and Engineering (WISE), DLR, the Institut de mécanique céleste et de calcul des éphémérides (IMCCE) and the University of Lille. I acknowledge the support received again from the IET to organise a visiting period at the ESA Debris Office.

The visiting period in Darmstadt has been a concrete added value to my PhD as it made me see the topic of my research from a different perspective, more oriented to potential applications. It has also been an occasion to experience, even if only for a short period, the positive environment of the Debris Office and of ESOC in general. For these reasons, I sincerely thank Holger Krag for having made the visiting period possible. I also would like to thank Jan Siminski for having helped me in the validation of the environmental index, Stijn Lemmans for the support with DISCOS, and Sergio Ventura, from ESA Independent Safety Office, for his feedback on the formulation and the applications of the environmental index.

Finally, I would like to thank the people that supported me the most in all these years. First, I thank my family for their continuous and immense support. It is almost ten years since I left home, but we are as close as always. You gave me a solid basis on which I could start again and build something new here in Southampton. I think we can be proud of what we have reached so far. In the end, a very big thank you to Jeroen. You helped me during these three years enduring rehearsals of presentations, reading papers, midnight talks about codes. You also supported me in all the difficult moments, teaching me how to see the value in what I do and in what I am. Thank you.

Introduction

The term *space debris* indicates the collection of all non-operative objects in orbit around the Earth. *Space debris* includes spent rocket bodies and inactive satellites, but also fragments generated by destructive events (such as collisions and explosions) and objects released during operations. More than $16\,000$ objects (including active satellites) are catalogued and tracked by radar from the Earth (IADC, 2013). For objects in Low Earth Orbit (LEO), it is usually considered that they can be tracked if their size is larger than 5-$10\,\mathrm{cm}$ (Xu et al., 2009). In addition to this, there is a much larger population of small objects that cannot be tracked, but that can still be a serious hazard in case of collision with operational spacecraft, due to the high orbital speed. As a reference, at the altitude of the International Space Station (ISS), space debris moves with a speed of around $7\,\mathrm{km\,s^{-1}}$. At this speed, a collision with a $1\,\mathrm{cm}$ object releases the same amount of energy of an hand grenade or the same energy associated with the crashing of a small car travelling at $40\,\mathrm{km/h}$. This simple example shows how a collision with a piece of space debris, even a very small one, may affect the correct functioning of a spacecraft or cause the failure of a mission and thus a relevant loss for its owner. Moreover, any collision generates new fragments that may collide with other objects: if the debris density is too high, this mechanism may produce more objects than the ones than decay from their orbits. This uncontrolled growth of space debris, often called the *Kessler syndrome* (Kessler and Cour-Palais, 1978), may interfere with the future exploitation of the space around the Earth and with the sustainability of space activities. This is problematic since space infrastructures have become essential for our society, as in the case of the Global Positioning System (GPS) and telecommunication systems.

Obtaining a reliable picture of the space debris environment and understanding its evolution are two key elements to evaluate the collision risk for operative spacecraft, to analyse possible mitigation strategies and to suggest future policies to increase the sustainability of the space sector. Current studies of space debris evolution (Liou et al., 2013b) have focussed mostly on objects larger than $10\,\mathrm{cm}$, which are considered the most dangerous ones in case of collision as they are able to create new large fragment clouds. The reason for the choice of this specific cutoff size is twofold. On one hand, only trackable objects are included, so that the models' forecast can be verified with observable data. On the other hand, the threshold limits the number of objects to be

included in the simulation, so that they are still manageable with current computing capabilities. However, as anticipated, also objects smaller than $10\,\mathrm{cm}$ can represent a threat to operational spacecraft. It is usually considered that any object larger than $1\,\mathrm{cm}$ can destroy a satellite in case of collision and that any object larger than $1\,\mathrm{mm}$ can cause anomalies (Krisko, 2007). Differently from large objects, small pieces of debris cannot be tracked and, therefore, cannot be avoided by manoeuvres. For this reason, McKnight et al. (2014) classify the fragments in this size range as *lethal non-trackable* objects and identify them as the leading detrimental factor to the safety of operational spacecraft.

The inclusion of small fragments in debris modelling could be useful to obtain a more complete picture of the debris environment, but the large number of objects included in the simulation and the uncertainty on their characteristics should be carefully considered. It is estimated that the number of objects between $1\,\mathrm{cm}$ and $10\,\mathrm{cm}$ is around several hundred thousand, whereas the number of objects between $1\,\mathrm{mm}$ and $1\,\mathrm{cm}$ is larger than 100 million (IADC, 2013). These numbers suggest that the modelling techniques adopted for large objects may not be suitable also for small ones. For large objects, a deterministic approach is usually adopted: each object is studied individually, evaluating the evolution of its trajectory under the effect of relevant perturbations and its probability of collision with other objects. If this approach were extended to small objects, the computational time would be proportional to the total number of objects and it would grow exponentially as the size threshold is reduced. Some existing debris models deal with this issue by grouping a certain amount of small fragments in *representative* objects (Rossi et al., 1995b). These synthetic objects are propagated similarly to the large ones (i.e. individually) and the distribution of small objects is reconstructed *a posteriori*. With this approach, the dependence of the required computational resources on the number of objects is weaker, but not removed because the debris objects (real and synthetic) are still propagated individually.

The current work investigates an alternative approach to the propagation evaluating the feasibility of formulations that do not focus on single debris objects, but rather on fragments' distributions. These kinds of methods already exist, for example, for Geosynchronous Earth Orbit (GEO), whereas this work focusses on LEO as this is the region of space where the debris density is maximum and where most fragmentations have occurred. The research questions that arise are then:

- which modelling techniques are able to describe the long term evolution of space debris in LEO without requiring the propagation of single objects?
- which level of accuracy and which computational resources are associated with this technique?
- how can this technique be used to assess the collision risk to operational satellites?
- which new analyses on the collision risk are enabled by the novel modelling technique?

The starting point to answer to the first question is the work by McInnes (1993), who proposed to study the debris population in terms of its spatial density, applying the continuity equation to model the effect of atmospheric drag and the creation of new objects due to collisions. This approach has two main advantages. First, it is able to arrive at an analytical expression for the debris density as a function of altitude and time, meaning that with a very limited computational effort it is possible to model the evolution of space debris including objects of any size. Second, the formulation in spatial density allows for a natural connection to the computation of the collision probability, as it will be shown later. For these two reasons, the approach by McInnes (1993) is set as the cornerstone of the propagation method proposed in this work. Some important variations and extension to the work by McInnes (1993) have been developed in this work. First, whereas McInnes (1993) studies the global debris population, the focus of this work is on modelling single fragmentation events. The idea behind this shift in scope is that the current work aims to develop an approach that could be used by satellite operators to assess the increase in the collision risk for their spacecraft as a result of a fragmentation or to identify under which conditions a fragmentation is more likely to affect their satellite. For these applications, single fragmentation events need to be modelled. In addition, adopting this point of view, the proposed propagation method does not want to compete with established debris models (Sdunnus et al., 2004), but rather to extend their capabilities by improving the representation of small debris objects. The second important difference with respect to McInnes (1993) is that in this work the propagation with the continuity equation has been extended to multiple dimensions. In this way, the debris spatial density is not expressed as a function of the altitude only, but also the dependence on other variables, such as the fragments' area-to-mass ratio and orbital parameters, can be considered. This increases remarkably the applicability of the method, extending the orbital regions where it can be used, the length of the time span that can be simulated, the number of perturbations that can be modelled.

The second research question was addressed by setting up a comparison with traditional numerical propagation methods and simulating different breakup scenarios. Validation cases with different classes of fragmentations, different levels of energy, and different breakup locations were studied. It will be shown how the proposed approach is suitable to study the region of LEO with the highest density of space debris and the highest number of operational spacecraft. As already mentioned, the two core concepts in the work by McInnes (1993), namely the representation in spatial density and the availability of an analytical solution, contribute to the reduction of the request of computational resources, both in terms of time and RAM. This means that many breakup scenarios can be simulated without the use of supercomputers. This point is particularly relevant if one aims to develop a method that can be adopted by general users where the availability of supercomputer facilities cannot be assumed. Moreover, as it will be discussed in the following, reducing the request of computational resources does not mean only running

a simulation faster, but making new analyses possible and suggesting new points of view for the study of the consequences of fragmentations.

The third point focusses on the transition from describing only the evolution of a fragment cloud to studying how it interacts with other objects. The formulation in spatial density allows the common analogy with the kinetic theory of gases (Su and Kessler, 1985b) to be adopted to estimate the collision probability for a spacecraft crossing the fragment cloud. The kinetic theory of gases requires not only information on the cloud density, but also on the relative velocity between the objects in the cloud and the spacecraft crossing it. Also for this point, an analytical formulation should be sought to keep the computational resources low. An expression based on the orbital configuration of the fragment cloud and the one of the spacecraft will be discussed and validated.

Finally, several possible applications of the proposed method will be discussed. These range from the estimation of the effect of fragmentations on a specific spacecraft to the extended analysis of which fragmentation conditions lead to the largest increase in the collision probability for a set of targets. It will be also shown how the proposed method can be used to build a tool to quickly asses the effect of a fragmentation on the space environment and on operational spacecraft. Thanks to its limited computational time, the analytical method discussed in this work can also be the basis of an environmental index that ranks spacecraft depending on the severity of the consequences of their breakup on other satellites.

Contributions

The contents of this thesis have been presented in different journal articles and conference papers. The following list provides a brief overview of the topics discussed in each work.

- F. Letizia, C. Colombo, H. G. Lewis, and C. R. McInnes. Debris cloud evolution in Low Earth Orbit. In *64th International Astronautical Congress*, Paris, France, September 2013. International Astronautical Federation. IAC-13.A6.P.12
  Poster presentation: best poster in the Space Debris symposium and short-listed for the award of best poster. The paper presents the preliminary formulation of the method to describe the effect of atmospheric drag on debris clouds.
- F. Letizia, C. Colombo, and H. G. Lewis. Analytical model for the propagation of small debris objects after a fragmentation event. In *24th AAS/AIAA Space Flight Mechanics Meeting*. AAS/AIAA, January 2014a. AAS 14-324
  Oral presentation. The paper presents an improvement in the definition of the initial condition for the analytical propagator, which enhances the method's robustness.

- F. Letizia, C. Colombo, and H. G. Lewis. Analytical model for the propagation of small debris objects clouds after fragmentations. *Journal of Guidance, Control, and Dynamics*, 38(8):1478–1491, 2015c
  The article discusses in detail the formulation of the model for the evolution of space debris clouds under the effect of atmospheric drag. The validation through the comparison with numerical propagation is presented and an example of application is reported.
- F. Letizia, C. Colombo, and H. G. Lewis. Continuity equation approach for the analysis of the collision risk due to space debris clouds generated by a fragmentation event. In *65th International Astronautical Congress*, Paris, France, September 2014b. International Astronautical Federation. IAC-14.A6.P.31
  Poster presentation: short-listed for the award of best poster. The paper introduces the formalisation of how the analytical approach can be applied to compute the collision probability for a spacecraft crossing a debris cloud.
- F. Letizia, C. Colombo, and H. G. Lewis. Small debris fragments contribution to collision probability for spacecraft in Low Earth Orbit. In *Space Safety is No Accident, 7th IAASS Conference*, pages 379 – 387. Springer International Publishing, May 2015d. ISBN 978-3-319-15981-2
  Oral presentation: winning paper of the competition organised by the Space Generation Advisory Council. The paper discusses possible applications of the analytical approach to study different collision scenarios.
- F. Letizia, C. Colombo, and H. G. Lewis. Collision probability due to space debris clouds through a continuum approach. *Journal of Guidance, Control, and Dynamics*, 2015i. doi: 10.2514/1.G001382. Accessed 10 September 2015
  The article presents in detail the method to compute the collision probability for a spacecraft crossing a fragment cloud, showing also the validation performed with the comparison with a traditional numerical approach. It also introduces the modelling of the distribution in latitude.
- C. Colombo, A. Wittig, F. Letizia, and R. Armellin. Density of debris fragments through differential algebra and averaged dynamics. In *25th AAS/AIAA Space Flight Mechanics Meeting*. AAS/AIAA, January 2015. AAS 15-391
  Oral presentation. The paper discusses the problem of debris cloud propagation in regions different from Low Earth Orbit by adopting the formulation in terms of spatial density, but using differential algebra instead of the continuity equation to model the cloud evolution.
- F. Letizia, C. Colombo, and H. G. Lewis. Continuity equation method for debris cloud evolution. In *Key Topics in Orbit Propagation Applied to SSA*, April 2014c
  Oral presentation. The talk introduces the extension of the continuity equation method to multiple dimensions to improve the method accuracy and increase its applicability.

- F. Letizia, C. Colombo, and H. G. Lewis. Multidimensional extension of the continuity equation method for debris clouds evolution. *Advances in Space Research*, 2015a. doi:10.1016/j.asr.2015.11.035. Accessed 8 December 2015
  The article discusses in detail the extension of the approach to multiple dimensions, presenting the applications to the modelling of the effect of the Earth's oblateness, the description of the distribution of the fragments in area-to-mass ratio and in eccentricity.
- F. Letizia, C. Colombo, and H. G. Lewis. 2D continuity equation method for space debris cloud collision analysis. In *25th AAS/AIAA Space Flight Mechanics Meeting*. AAS/AIAA, January 2015g. AAS 15-293
  Oral presentation. The paper extends the computation of the collision probability to the case where the continuity equation is formulated in multiple dimensions.
- F. Letizia, C. Colombo, and H. G. Lewis. Density based approach for collision risk computation. In *25th International Symposium on Space Flight Dynamics*, October 2015h
  Poster presentation. The paper introduces a formulation where, differently from the previous cases, the representation in terms of spatial density is applied right after the breakup. This allows the simulation of large fragmentation events. The application to a real explosion is discussed.
- F. Letizia, C. Colombo, and H. G. Lewis. Density approach to debris propagation. In *Key Topics in Orbit Propagation Applied to SSA*, October 2015f
  Oral presentation. The talk gives a general overview of the method and its application to real fragmentation events and to the definition on an environmental index.

In addition, the following papers are in preparation:

- F. Letizia, C. Colombo, and H. G. Lewis. Improved continuity equation method for space debris cloud collision analysis, 2015e. Manuscript in preparation
  The paper discusses the computation of the collision probability when the formulation with multiple variables is adopted. Some applications of the method are presented.
- F. Letizia, C. Colombo, H. G. Lewis, and H. Krag. Assessment of breakup severity on operational satellites, 2015j. Manuscript submitted for publication
  The paper proposes an environmental index to rank different breakups depending on their effect on active satellites.

Structure of the thesis

The outline of the current work is as follows. Chapter 1 provides a brief introduction to debris modelling. Chapter 2 introduces the analytical model, and describes the results

obtained with the model on the propagation of debris clouds produced by breakups with different energies and in different location. The comparison with traditional propagation methods is presented. Chapter 3 discusses how the method can be used to study the collision probability for a target crossing the fragment cloud produced by a breakup. The method is applied to study some real breakups and to analyse how the collision probability of a spacecraft is affected by the fragmentation conditions. Chapter 4 explains the extension of the continuity equation method to multiple dimensions and shows some cases when the new formulation is beneficial. Chapter 5 presents the computation of the collision probability for the case with the propagation with multiple variables and some applications to computation of the collision probability of different satellites are shown. Finally, Chapter 6 explores the feasibility of a formulation where the propagation of single objects is completely removed and how this can be applied to develop an environmental index for spacecraft. Further details on validations, implementation and mathematical proofs are given in Appendix A and B.

1

Space debris modelling

Since the launch of Sputnik in 1957, around 6600 satellites have been placed in orbit around the Earth and around 3600 are still in orbit now.[1] However, less than one third of these satellites are still operational; the others are currently orbiting, out of control, occupying useful slots and representing a threat of collision with operational spacecraft. A public catalogue[2] is maintained to keep track of objects in orbit and avoid collisions. In addition to intact spent satellites, also objects released in different phases of missions are in orbit. The catalogue contains any object larger than 5-10 cm in LEO and larger than $1\ \mathrm{m}$ in GEO. As of 2011, active satellites represent the 5.6% of the catalogued objects, inactive spacecraft are the 16.3% and 10.5% of the catalogue is formed by the spent rocket bodies used to insert the satellites in their orbits (IADC, 2013). The remaining population is made by objects released during launch and operation (11.3%) and a large part (56.3%) by *fragmentation* debris, which is all the objects produced by collisions and explosions (e.g. caused by remaining fuel in rocket bodies or by failed batteries).

This classification of objects makes it evident that, quoting Chobotov (2002), space debris is a "self-perpetuating" issue as any space mission generates new objects. For this reason, all the major space agencies are involved in the definition of guidelines to limit the debris proliferation, for example by requesting the removal of fuel from rocket bodies after the injection in orbit (*rocket passivation*) or by defining some protected regions that should be left clear at the end of the mission (e.g., the *25-year rule* that prescribes spacecraft in LEO to decay or to reach a graveyard orbit within 25 years of the end of the mission).

[1] ESA, About Space Debris, [Online] last access 22 September 2015

[2] Space Track catalogue available at `https://www.space-track.org`, last access 22 Septeber 2015

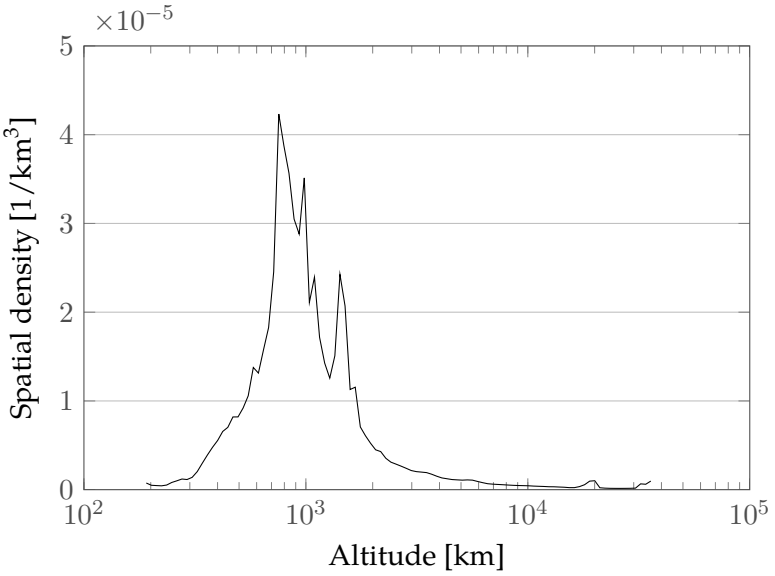

Figure 1.1: Estimated spatial density of objects larger than $1\,\mathrm{mm}$ as a function of altitude according to the MASTER 2009 population.

While it is not clear if these measures are sufficient to stabilise the debris population, two important events raised the attention even more on the space debris issue. The first one is the infamous Chinese anti-satellite test in 2007: a satellite, Fengyun-1C, with a mass of $880\,\mathrm{kg}$, was intentionally destroyed generating almost 2000 new catalogued objects, increasing the spatial density of objects at the fragmentation altitude by more than 60% (Pardini and Anselmo, 2007). The orbit of the destroyed satellite made the event even more serious: at $863\,\mathrm{km}$, where the fragmentation occurred, atmospheric drag, the only available natural sink mechanism for space debris, is not very effective and the fragments will stay in orbit for a long time (Pardini and Anselmo, 2011). Moreover, the specific orbit, sun-synchronous[3], was already the region of space with the highest debris density because of its particular interest for Earth observation missions, and because it has been affected by other fragmentation events in the past (Figure 1.1).

The second important event took place in 2009 and it was the collision between two satellites, Cosmos 2251 and Iridium 33, that generated more than 2000 new catalogued objects (Pardini and Anselmo, 2014). The collision occurred at an altitude ($789\,\mathrm{km}$) close to the one of the Chinese test, resulting in similar problems in terms of the fragment orbital life. While the Cosmos satellite was already non operational before the collision, Iridium 33 was still functioning. In theory, it could have manoeuvred to avoid the impact, but it was moved, for operational purposes, in the direction of the abandoned spacecraft because the operators did not have accurate information on the position of Cosmos 2251 (Pardini and Anselmo, 2011). Even if many close approaches between the two satellites

[3]The plane defined by a *sun-synchronous* orbit keeps a constant angle with respect to the Sun, so that a spacecraft on this orbit passes above a specific place on the Earth surface always at the same time of the day; this is particularly useful for Earth observation missions as it allows multiple observations with similar lighting conditions.

were predicted, they were not considered at high risk. This shows how uncertainty plays a very important role in debris studies and models should consider this aspect in their predictions (Finkleman, 2014).

Besides the event in 2009, three other collisions were documented between satellites and catalogued fragments (Pardini and Anselmo, 2014). In addition, since 2012, in at least six occasions, a collision between an uncatalogued piece of debris and a satellite was proposed as an explanation of satellite anomalies (NASA Orbital Debris Program Office, 2012a, 2015, 2012b, 2013). One example is the breakup of Iridium 47 on 7$^{\text{th}}$ June 2014, when ten new pieces of debris were observed: the difference in the orbital period among the fragments suggests that an event with considerable energy took place. More recently, in February 2015, the satellite DMSP-F13 supposedly exploded in orbit due to a malfunctioning of a battery, producing 160 new objects that were added to the debris population (Berger and Gruss, 2015); this forced all satellite operators to assess the resulting collision risk to their own missions (Berger, 2015).

Historically, since 1961, 142 fragmentations occurred in LEO: this data is derived from the detailed list in (Orbital Debris Program Office, 2014) valid until 2003 and the analysis of the updates published on the Orbital Debris Quarterly News[4]. Figure 1.2 shows the distribution of the number of events and of the produced fragments with semi-major axis and inclination. As anticipated, it appears clearly how the region between 700 and $900\,\mathrm{km}$ is the most affected by breakups, especially in the subset of sun-synchronous orbits (inclination between 90 and 100 degrees).

The effect of fragmentations is not limited to the orbits where they happened, but rather they affect the global debris environment. For example, in March 2012, the six astronauts of the ISS sheltered in the Soyuz spacecraft as a precaution during a close passage of a fragment generated by the 2009 Cosmos-Iridium collision. More recently, on 27$^{\text{th}}$ October 2014, the ISS performed another manoeuvre to avoid a $8\,\mathrm{cm}$ fragment generated as well by the Cosmos-Iridium collision. This shows how crucial it is to predict the motion of objects generated by a fragmentation event and evaluate their effect on the collision risk in the long term. The models used for this purpose usually discriminate the objects considering their size, both for implementation reasons and for practical considerations. In LEO, radar can track objects larger than 5-$10\,\mathrm{cm}$, whereas the population of centimetre-sized objects can be statistically derived from radar data and the number of even smaller objects is inferred from impact records (Xu et al., 2009). The reference population for most debris analyses usually includes objects larger than $10\,\mathrm{cm}$, even though some studies that consider objects down to $5\,\mathrm{cm}$ (White and Lewis, 2014) and $1\,\mathrm{cm}$ (Martin et al., 2004; Walker et al., 2000, 2002) are available. The choice of defining a threshold value for the fragments' size is motivated by the fact that they are usually

[4]For the fragmentations described in the Orbital Debris Quarterly News the number of produced fragments was updated by checking `https://www.space-track.org`. Data retrieved between June and July 2015.

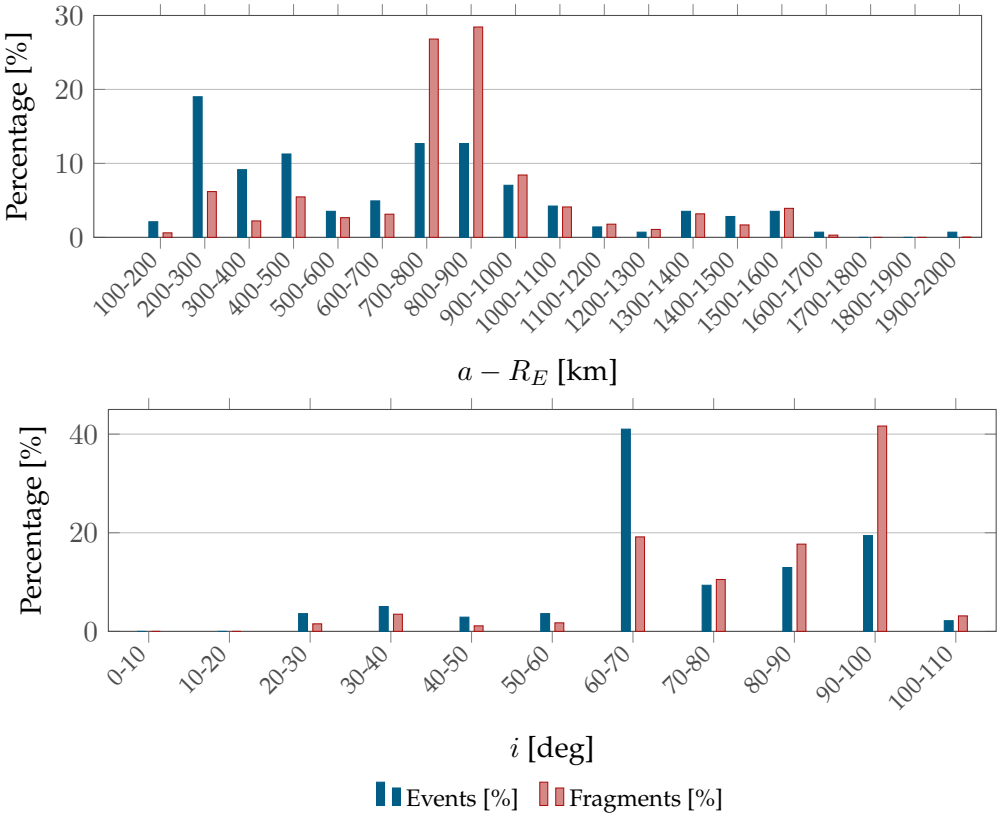

Figure 1.2: Distribution of events (blue) and number of generated fragments (red) for the breakups in LEO in semi-major axis a and inclination i between year 1961 and year 2015. The values are expressed as percentage of the total number of events (142) and fragments (16115).

considered the most dangerous impactors, i.e. the ones able to generate large debris clouds and to influence the long term evolution of the debris population (Rossi et al., 2015a). This limitation is also introduced because the number of small objects is so large (Figure 1.3) that considering all of them would make simulations extremely expensive in terms of computational time. For this reason, even if the radar technology is evolving, so that it will be possible to track smaller and smaller objects, Crowther (2013) highlighted that in the future the problem of space debris may also involve how to manage a large database of objects both in terms of computational time and avoiding false alarms[5].

Besides the capabilities of radar, a cutoff on the dimension of the modelled space debris objects is usually introduced for computational reasons. This partial representation of space debris environment may result in an underestimation of the collision risk for operational satellites. Even though very small fragments ($< 1\,\mathrm{cm}$) can in theory be neutralised using shields[6] (Crowther, 2013), there is a large population of objects between 1 and $10\,\mathrm{cm}$ that is considered extremely dangerous. They are too large for shields but too small to be tracked, and thus they pose a risk to operational spacecraft (Wiedemann

[5]This is partially happening already now as in the case of the Cosmos/Iridium collision. In that case, the operators were receiving a large amount of alerts for close encounters that they got used to ignore.

[6]In practice, this is currently done only on the ISS.

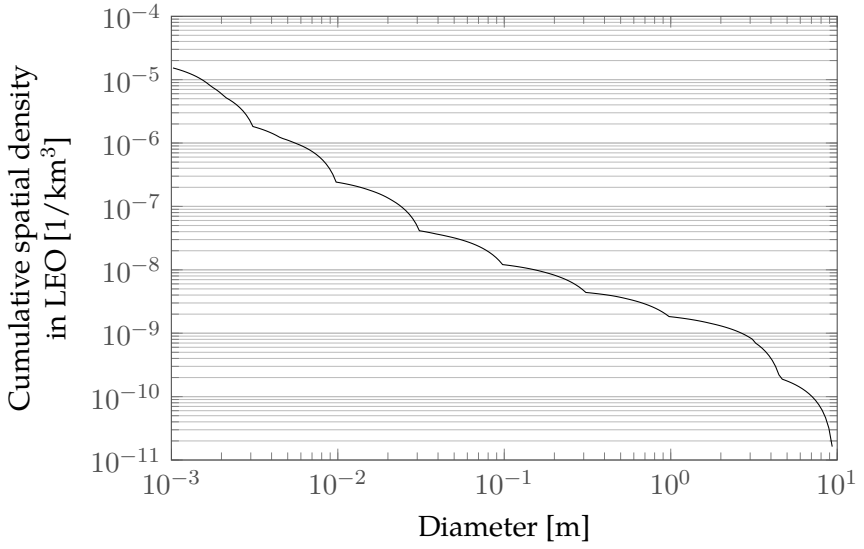

Figure 1.3: Estimated cumulative spatial density of objects in LEO as a function of their size according to the MASTER 2009 population.

et al., 2013) as it may cause spacecraft anomalies (McKnight and Di Pentino, 2013) or even more serious damage to satellites (Krisko, 2007). For example, Giacomuzzo et al. (2010) has shown that, for satellites similar to COSMO-SkyMed,[7] the largest damage would be generated by objects in the size range between $1\,\mathrm{mm}$ and $1\,\mathrm{cm}$. Recently, McKnight et al. (2014) highlighted how the so-called *lethal non-trackable* objects may become the leading factor in the decrease of flight safety.

White and Lewis (2014) showed that the effect of remediation measures is not the same on the population of objects larger than $10\,\mathrm{cm}$ and on objects between 5 and $10\,\mathrm{cm}$ as the latter may still increase even when the former is supposed to decrease. For this reason and because of the potential threat represented by small objects, an increasing effort is currently underway to obtain a better understanding of their contribution to the debris population. For example, Krisko et al. (2015) has compared the modelling of fragments with size between $1\,\mathrm{mm}$ and $1\,\mathrm{cm}$ in the space debris models used by NASA and ESA (respectively, ORDEM and MASTER), finding substantial differences in the values of the predicted flux both at the ISS orbit and for a typical sun-synchronous orbit. This suggests the importance of further analysis on how small objects are generated and handled in the models. It also demonstrates the evolution towards including them in space debris environment prediction.

The inclusion of small fragments and the request for quick estimations of the space debris evolution result in the formulation of simplified models of debris dynamics, which is, instead, quite complex. The objects produced by explosions and collisions have larger area-to-mass ratio than common satellites, so fragments are highly affected by the perturbative forces whose intensity depends on the cross-sectional area (e.g. atmospheric

[7] An Earth observation constellation formed by four identical medium-sized satellites in sun-synchronous orbits (97.9°) at a nominal altitude of $619\,\mathrm{km}$.

drag and solar radiation pressure) (Colombo and McInnes, 2011a). Perturbing accelerations are sometimes neglected when dealing with satellite motion, which can be studied using the analytical expression provided by the Keplerian laws of planetary motion. On the other hand, the study of effect of perturbations is essential to predict space debris motion. The next Section describes in detail how perturbations affect the evolution of a fragment cloud generated by a collision or an explosion.

1.1 Perturbations and debris cloud evolution

Space debris is present in all regions of space where missions operate, ranging from LEO to GEO, and the perturbations to which space debris is exposed vary largely across the different regions. In GEO, debris motion is affected by the Earth's oblateness, by the effect of the Moon and the Sun, and by the solar radiation pressure. For this reason, the consequences of a fragmentation in GEO are highly affected by the longitude of the event and can result in localised increases in the debris density (Anderson and Schaub, 2014). In LEO the drivers of the debris evolution are the Earth's oblateness and the atmospheric drag, which is the only natural way debris objects are removed from their orbits, to re-enter and burn in the atmosphere.

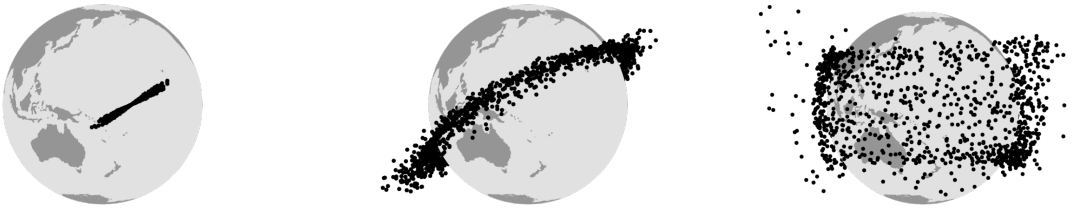

(a) Ellipsoid **(b)** Toroid **(c)** Band

Figure 1.4: Phases of debris cloud evolution as classified by Jehn (1991). The simulation refers to a collision on a parent orbit with inclination equal to 30°.

Besides the effect of perturbations on the global debris population, it is important to study the effect of perturbations on a cloud of debris fragments, generated by a fragmentation event (collision or explosion) in LEO. The evolution of a debris cloud can be split into three main phases (Figure 1.4), each one with different geometry and different driving forces (Ashenberg, 1994; McKnight, 1990). A fragmentation event generates a number of objects that initially forms a dense ellipsoidal cloud (Figure 1.4a). At the moment of the event, all the fragments have the same position, equal to the fragmentation location; their velocity is, instead, different depending on how the fragmentation energy is distributed among the fragments. This process is described by breakup models, which will be discussed in detail in Section 2.1. As the fragments have different initial velocity, their energy, and therefore their orbits, are different. This causes the cloud to be stretched along the parent orbit, forming a ring around the Earth. Considering the cloud globally, the mean anomaly, M, is quickly randomised. In this phase, which lasts

only few orbits, the orbital perturbations are negligible and the dynamics of the system can be studied by applying the two-body problem equations. In particular, the orbital parameters of the fragments are often assumed to be constant in this phase.

In the following phases, perturbations become more relevant. Without perturbations the fragments would maintain a ring shape, which is characterised by a point, named the *pinch point*, where all the fragments pass and which corresponds to the breakup location (Chobotov, 1990). This geometry is changed by the effect of the Earth's oblateness, which causes the nodal precession of the orbits: the argument of periapsis ω and of the longitude of the ascending node Ω are modified with time, with a rate that depends on the fragment's orbital parameters. As in the previous phase, each fragment has different orbital parameters and so each orbit is modified (i.e. rotated) at a different rate. For this reason, the pinch point disperses; the spreading of ω transforms the ring into a flat torus (Figure 1.4b), which covers the area between the smallest perigee and the largest apogee; the diffusion of Ω creates a band around the Earth, limited in latitude by the value of inclination of the parent orbit (Figure 1.4c). This transition can last between some months to some years depending on the altitude and the inclination of the orbit.

Once the band has formed, ω and Ω can be considered random: this means that the forces acting on ω, Ω, as the Earth's oblateness, are not relevant over the long term (Rossi et al., 1998a). Atmospheric drag becomes the most important perturbation in this phase as it causes the fragment decay, but its effect is highly dependent on the altitude. At high altitude ($> 800\,\mathrm{km}$), also the luni-solar perturbation and the solar radiation pressure may affect the fragment evolution, especially for objects with a large area-to-mass ratio A/M.

1.2 Space debris models overview

Different models are used to study the risk due to space debris in different time scales. When short-term analyses are performed, the purpose of these models is to provide a quick estimation of the evolution of the resulting debris cloud and of the collision risk due to a recent breakup. This can be done by exploiting the fact that the perturbations can be neglected in the first phase of the cloud evolution, so it is possible to write purely analytical models to describe how the cloud volume changes with time (Ashenberg, 1992; Chobotov, 1990; Heard, 1976; Jehn, 1991). These methods are based on the linearisation of the equations of relative motion of the fragments with respect to the parent orbit: they are very fast in computing the collision risk, but they can only be used for a few revolutions after the fragmentation event. In fact, even if some formulations take into account the short-term effect of perturbations (Ashenberg, 1992), they are not able to describe the cloud evolution once the fragments are spread around the Earth.

Numerical methods are required to follow the evolution of space debris on the long term and account for the effect of perturbations. Long term studies (100-200 years) usually aim to model not only a single event but the global debris population. This is done to evaluate the efficacy of present and proposed policies to reduce the risk to operating satellites. These kinds of studies require models and methods able to deal with a variety of phenomena, such as the description of the fragmentation of an object, the study of the dynamics of fragments, the computation of collision risk among fragments and with other spacecraft, and the representation of the surrounding environment. The models in this category are called *debris environment models* or *debris evolutionary models*. Some extensive lists of the available models were compiled by Chobotov (2002) and Sdunnus et al. (2004), where the rationale of each model is described.

As an example, the Space Debris Mitigation (SDM) model by Rossi et al. (1995b) propagates the objects included in the provided initial debris population considering the effect of gravitational and non-gravitational forces. In detail, the so-called Fast Orbit Propagator (FOP), included in SDM, integrates the evolution of the object orbital parameters considering the geo-potential, third body perturbations, the effect of solar radiation pressure (including shadows), and the effect of drag. The result of the propagation is used to compute the collision probability among the objects. Two different algorithms for the collision probability computation are included in SDM: one, fully analytical, can be applied only to orbit with low eccentricity, and a second one, CUBE developed by NASA, that can be applied to any orbital regime. In addition to the propagators and algorithms for the computation of the collision probability, SDM includes a breakup model to simulate the production of objects due to explosions and collisions; a traffic model that describes launch routines; mitigation model that describe end-of-life strategies (e.g. graveyard orbits) and Active Debris Removal (ADR) scenarios (e.g. the removal of a fixed number of objects among the largest uncontrolled ones).

A similar approach is used also in the debris model by the University of Southampton, Debris Analysis and Monitoring Architecture for the Geosynchronous Environment (DAMAGE) (Lewis et al., 2012), that uses a semi-analytical propagator to model the effect of atmospheric drag, solar radiation pressure, Earth gravity harmonics (J_2, J_3 and $J_{2,2}$) and luni-solar gravitational effect.

As seen from the two examples of SDM and DAMAGE, evolutionary debris models make some assumptions on natural phenomena (e.g. atmosphere model, solar flux), future activities (e.g. number of launches, compliance with mitigation guidelines, active removal) and debris evolution (e.g. criteria for collision, number of fragmentation events per year). All these elements and the lack of an extensive amount of experimental data introduce a degree of uncertainty (Dolado-Perez et al., 2015), whereas space debris models are required to provide sufficiently accurate and reliable information for decision making. This is true both in the short term, for example in case of a collision avoidance manoeuvre, and over the long term, to define policies and guidelines to use space in

a safe and sustainable way. For this reason, the Monte Carlo method is used in debris modelling: each scenario of debris evolution is run between 10 and 1000 times to obtain reliable statistical data (Anselmo et al., 1999; Jenkin and Gick, 2005; Krisko, 2007; Rossi et al., 1995b). This dramatically increases the computational time and limits the variety of the possible analyses.

As a reference, the computational time with DAMAGE is around 90 minutes for a single run of a scenario of 200 years. The largest contribution to the simulation time comes from the computation of the collision probability and the propagation of the fragments' trajectory, in particular to consider the effect of atmospheric drag and luni-solar perturbations. Extending this approach to small fragments results in a prohibitive computational time: for example, if in DAMAGE all the fragments down to $2\,\mathrm{mm}$ are followed, the computational time required to simulate one day of evolution is equal to one *real* day.[8]

1.3 Statistical and simplified methods

The necessity of reducing the computational time has promoted the development of different techniques for debris propagation. For example, SDM by Rossi et al. (1995b) provides an alternative propagator, called Debris Cloud Propagator (DCP), where the propagation of fragments in LEO is simplified in three ways:

- only the most relevant perturbations, i.e. drag, are considered to study the fragment motion,
- the dynamics are modelled by analytical expressions, such as the ones obtained by King-Hele (1987) to describe the secular effect of atmospheric drag,
- only some representative objects are propagated.

This propagator is included not only in SDM, but also in an alternative statistical model STochastic Analog Tool (STAT), which proposes a simple mathematical model for the debris evolution (Rossi et al., 1998a). The debris population is divided into bins of semi-major axis, eccentricity and object size, and only a single representative object per bin is propagated. The result of the propagation is used to estimate how fragments move among the bins. The launch/retrieval frequency and explosion and collision rates for each bin are computed, so that the evolution of the object number per bin N_i is obtained from

$$\begin{aligned}\frac{dN_i}{dt} =&(\text{launches})_i - (\text{retrievals})_i + \\ &+ \sum_j \{(\text{explosions})_{j\to i} + (\text{propagation})_{j\to i}\} + \sum_{jk} (\text{collisions})_{jk\to i}.\end{aligned} \tag{1.1}$$

[8] Hugh G. Lewis, Senior lecturer at the University of Southampton, personal communication.

The computation of the collision risk is computed starting from the density in each bin, considering not average values, but extracting numbers from a Poisson distribution to reflect the fact these events are rare and using a constant average value would alter the final result. Different launch routines can be implemented to simulate different traffic models and, similarly, the retrieval frequency models the compliance with regulations and active removal missions.

A similar point of view is adopted in the model Space Debris Prediction and Analysis (SPDA) (Nazarenko, 2002). Nazarenko (1997) and Smirnov et al. (2001) divide the objects into so-called *classes* of size, perigee altitude, eccentricity, inclination, ballistic coefficient. The number of objects in each class N_j is obtained from

$$\frac{\partial N_j}{\partial t} = -W_j \frac{\partial N_j}{\partial r} - N_j \frac{\partial W_j}{\partial r} + \dot{N}_j, \tag{1.2}$$

where W_j is the radial velocity of the objects and $\dot{N}_j$ the rate of variation in the number of objects due to external causes. As in Rossi et al. (1998b), the single objects are not propagated and only the evolution of the number of objects per class is studied. Smirnov et al. (2001) explain how this approach enables the study of the debris population without any constraint on the fragment size as the method performance is independent from the number of objects. In addition, in SPDA single breakups are not modelled, but rather an annual increase in the fragment number is computed. In SPDA, the computation of the collision probability is obtained applying the analogy with the kinetic theory of gas. According to this analogy, the number of collisions is function of the object density and the distribution of velocity among the objects. Both the density and the distribution of velocity are derived from the values of N_j and the definition of the classes, so that the study of individual objects is not required.

Another option to reduce the computational load of the simulation is to build simplified models based on the full numerical ones. The two examples in the previous section, SDM and DAMAGE, can be considered *high-fidelity* models, able to predict in a quasi-deterministic way the position of the propagated objects. However, the desired output is often only the knowledge on the general trend of debris evolution in response to the variation of some parameters, such as the traffic routines or the compliance with regulations. This can be done by starting from a variational approach such as the ones in Equation 1.1 and Equation 1.2. For example, Kebschull et al. (2013); Radtke et al. (2013) have shown how the parameters in the evolution Equation 1.1 can be obtained through a fitting process of a full numerical model (LUCA in their case). This means that the output of the simplified model is coherent with the full numerical one, but the simulation time is strongly reduced, so that the simulation of a whole scenario of the evolution of the global debris population is performed in the order of seconds. Similarly, SPDA can be used to precompute the terms of an engineering model (SPDA-E) that allows for a fast evaluation and visualisation of the debris evolution (Nazarenko and Menshikov, 2001).

In the same way, the simplified model FADE uses the results of DAMAGE full model to estimate the terms in Equation 1.1 (Lewis et al., 2009).

More recently, the output of DAMAGE was used to build the simplified model CONCEPT (CONsequences of Cloud Evolution Prediction Tool) (Rossi et al., 2013), which is able to study the consequences of a single collision event. Although the current implementation considers only objects larger than $10\,\mathrm{cm}$, this approach can be extended to smaller fragments. The simulation of the fragmentation event is divided into two phases. In the first one, which is valid for all the tested scenarios, the background debris population is built from multiple runs of DAMAGE, whose output is stored in bins of altitude, right ascension and declination: for each bin the distribution of relevant quantities (e.g. spatial density, collision probability, object type, mass, area, orbital parameters) is stored. Secondly, CONCEPT is used to simulate a specific event. It is able to estimate the most likely parameters (i.e. mass and energy) for a fragmentation event. At this point, DAMAGE is used again to generate the debris cloud and to numerically propagate only the new fragments; at each time step the distributions stored in the bins are updated with the contribution from the new cloud, so that it is possible to assess the impact of the simulated event on the global population. As the background population is not actually propagated, but derived from DAMAGE, CONCEPT requires only five minutes to propagate a typical scenario for 200 years.

These last examples rely on several runs of a full model, whose output is then stored and used by the simplified model. This implies that, if part of the full model changes (for example, the breakup model), it should be run again to obtain updated parameters.

1.4 Analytical methods

Another way of reducing the computational time is to use analytical models, able to express directly the debris evolution without requiring long numerical integration. As explained in Section 1.1, in the first phase of the cloud evolution the perturbations play a minor role, so that the analytical keplerian motion is a good approximation of the cloud evolution. This was exploited by Chobotov (1990) who proposed a method based on the linearised equations for relative motion to describe the short-term evolution of the volume of a debris cloud, given the initial dispersion due to the breakup model. The volume of the cloud was then used to compute the fragment spatial density and the resulting collision probability for a spacecraft crossing the cloud. Chobotov (1990) also described the evolution of the cloud volume under the effect of the Earth's oblateness, so that it can be applied in the first days after the collision, when the resulting fragment cloud is quite dense and it can largely increase the local collision risk. A similar approach was also proposed by Hoots and Hansen (2014), who described the evolution of the cloud bounds in the two-body problem to define the most dangerous areas for operational

satellites. It is important to stress that, as perturbations are not considered, this approach is valid only in the first days of cloud evolution and it is applied only in GEO.

A more radical analytical approach was proposed by Valk et al. (2009b), who wrote a Hamiltonian formulation for the dynamics of space debris under the effect of gravity potential (considering J_2 and J_{22}), luni-solar perturbation, and solar radiation pressure (Valk et al., 2009a). Drag is not considered, as it is not a conservative force, so this model is not applicable for LEO, but it allows a fast evaluation of the debris population in GEO over several hundreds of years. Similarly, Izzo (2006) proposed a method that describes the debris population globally through the definition of some density functions. In the examples shown in (Izzo, 2006; Izzo and Valente, 2004) the propagation of the population was performed by studying how the density functions in ω and Ω change under the effect of the Earth's oblateness. Since also in this case drag is not considered, the method is suitable to describe the GEO region, but not LEO.

However, LEO can be considered as the most crucial area for space debris studies. First of all, the density of fragments is much higher in LEO than in GEO (Figure 1.1). In some regions, e.g. synchronous orbits, it is likely to be very close to the critical value, where the density is so high that the collisions among fragments create more new objects than the ones that are removed by drag (Kessler and Cour-Palais, 1978; Liou, 2011). Secondly, the ISS is in LEO and its protection from space debris is essential both for the presence of astronauts and for the delicate experiments, which need to be interrupted in case of collision avoidance manoeuvres (Foster, 2001). Finally, the relative velocity is much higher in LEO than in GEO and so collisions tend to be more dangerous (Chobotov, 2002).

A simple analytical model for the LEO debris population was proposed by Talent (1992), who developed a so called *particle-in-a-box* approach. According to the model, the rate of change of the number of objects in LEO (N) can be described by the differential equation

$$\dot{N} = A + BN + CN^2 \tag{1.3}$$

where A, B, C are, respectively, the coefficients of *deposition*, *removal*, and *collision*, which are derived from the physical properties of LEO. The approach has a very low computational effort, but it cannot be easily extended to study single fragmentation events. An alternative analytical approach is described in the following section.

1.5 Continuity equation method

Another fully analytical model applicable in LEO is the one proposed by McInnes (1993). The central idea of this approach is considering the debris population as a fluid with continuous properties. In this way, the analysis of the single objects is abandoned and the fragment density becomes the only parameter of the study. This concept was present

already in Heard (1976), who was among the first to transfer the idea of a *continuum approach* from stellar dynamics to space debris modelling. Whereas Heard (1976) focussed on the description of the spreading of a cloud right after the breakup, McInnes (1993) studied the long term evolution of the debris density under the effect of perturbations.

This is obtained through the continuity equation, a traditional approach of fluid dynamics, where it is used to link the fluid density with its velocity. Similarly, when applied in astrodynamics, it provides a description of the change in the density of a dispersed set starting from the knowledge of the velocities of the particles. In particular, if n represents the fragment density, the continuity equation can be written as

$$\frac{\partial n}{\partial t} + \nabla \bullet \mathbf{f} = \dot{n}^{+} - \dot{n}^{-} \tag{1.4}$$

where ∇ indicates the divergence. $\nabla \bullet \mathbf{f}$ accounts for the *slow*/continuous phenomena (e.g. drag effect) and $\dot{n}^{+} - \dot{n}^{-}$ the *fast*/discontinuous event (e.g. the injection of new fragments due to the release of operational debris objects during launches). Once the initial distribution of n is known, the continuity equation is used to obtain its evolution with time, with very low computational effort.

The method is quite general and it has also been applied to describe the evolution of interplanetary dust (Gor'kavyi, 1997; Gor'kavyi et al., 1997), nano-satellites constellations (McInnes, 2000) and high area-to-mass spacecraft (Colombo and McInnes, 2011b) as, in all these cases, continuous and/or discontinuous phenomena have to be described (Table 1.1).

Table 1.1: Summary of the application for the continuity equation method. a and e are the orbit semi-major axis and eccentricity; r is the distance from the central body; Φ the angle between the Sun-Earth line and the direction of the orbit pericentre.

Application	Solution space	Slow phenomena	Fast events	Ref.
Interplanetary dust	(a, e)	Poynting-Robertson drag Planetary resonances	Gravitational scattering Mutual collisions	(Gor'kavyi, 1997) (Gor'kavyi et al., 1997)
Space debris	(r, t)	Atmospheric drag	Mutual collisions Launches	(McInnes, 1993)
Nanosatellites	(r, t)	Atmospheric drag	Launches and failures	(McInnes, 2000)
High A/M objects	(e, Φ)	Earth's oblateness Solar radiation pressure	-	(Colombo and McInnes, 2011b)

What it is interesting to observe from Table 1.1 is that the continuity equation can be used to find the evolution of the system both in the physical space (such as for space debris and nanosatellites) and in the phase space (such as for interplanetary dust and high A/M objects). This makes the method very flexible as it is possible to describe the evolution of the system in the space with the most convenient formulation.

Focussing on the application to the space debris population (McInnes, 1993), the method is written to model the evolution of the global population in the long term. Drag effect and mutual collisions are modelled and studied separately. In particular, mutual collisions are assumed to be the driving factor in the evolution and so most of the analysis

on future scenarios is carried out neglecting drag and considering only the objects at altitudes higher than $750\,\mathrm{km}$. However, the possibility of treating atmospheric drag in the model is what makes the method unique as it can be applied in LEO.

Note how the terms in Equation 1.4 have the same meaning as the ones in Equation 1.2, observing that the second and the third term in Equation 1.2 can be obtained from Equation 1.4 considering the dependence on the radial distance only and writing the divergence in Cartesian coordinates. This suggests that a model based on the continuity equation is intrinsically a statistical model, so it presents the same advantages of this kind of models. These include a reduction in the computational time, the possibility of including objects of any size and a more natural connection to the statistical nature of the problem (i.e. fragment distribution with uncertain initial conditions) (Nazarenko, 2002).

Starting from the important results of McInnes (1993), the present work aims to move the scope from the global debris population to a single fragmentation event. This is required to develop a method that can be used by operators to study the effect of a specific breakup and to rank spacecraft depending on how their fragmentation would affect other satellites. On the other hand, an analytical method of the global debris population could be useful to estimate general trends in the evolution of the debris density, for example, identifying which orbital regions are the closest to the critical density. For that application, the analytical model would face additional challenges as the modelling of discrete events (e.g. launch routines, active debris removal missions), through the terms $\dot{n}^+, \dot{n}^-$ in Equation 1.4. In this work, instead, those terms are considered equal to zero and the focus is on the modelling of perturbations and on the study of how the debris cloud interacts with other spacecraft. As these two aspects are relevant also for a model of the global population, the current work could also be regarded as an essential initial step in the development of a more general model. In addition, the analytical model proposed in this work can already be exploited by the evolutionary models to include small fragments in their analysis. In fact, the evolutionary models are able to predict, in a stochastic sense, when, where and how a new fragmentation will occur. These elements are used by the model to generate the new large fragments, but they can also be passed as inputs to the analytical model to produce the small fragments and follow their evolution. By accounting also for the contribution of small fragments, the evaluation of the consequences of a single event can be improved and the estimation of the collision risk can be more accurate. On the other hand, the computational resources required by the simulations are less dependent on the number of studied fragments since the state variable of the problem is the density.

Changing the application from the evolution of the total population to a single event requires some important changes to the method proposed by McInnes (1993). First of all, the method should be able to simulate the production of fragments due to a collision; then, the arbitrary initial distribution used by McInnes (1993) should be substituted

with the actual distribution of fragments; only at this point the propagation based on the continuity equation can be applied to obtain an analytical expression for the cloud evaluation and a fast evolution of the collision risk for operative spacecraft.

Summary

The study of space debris aims to clarify the sustainability of space activity both in the short term (e.g. the rise in the collision risk due to a recent breakup) and over very long term. Recent events such as the Chinese anti-satellite test in 2007 and the collision between Cosmos 2251 and Iridium 33 in 2009 have highlighted the danger coming from fragmentation events able to *contaminate* large regions of space.

Different models have been developed for the mentioned purposes. For the short term analysis, the collision probability resulting from a breakup is estimated assuming that the fragments are in keplerian orbits or considering only the effect of the Earth's oblateness. This formulation allows a quick estimation of the collision risk, but it is applicable only for a limited amount of orbits. To the other extreme, evolutionary models are used to study space debris evolution across hundreds of years. In this case, the scope is not the single fragmentation event, but the whole debris population. For this reason, elements such as launch routines, compliance with debris mitigation rules needs to be modelled. The effect of perturbations is taken into account by using numerical methods to propagate the trajectory of each debris object.

This makes the simulations expensive in terms of computational resources and limits the number (and, therefore, the size) of the studied objects. Only objects larger than $10\,\mathrm{cm}$ are usually followed by evolutionary models, even if smaller fragments can interfere with or destroy a spacecraft. To include small fragments in the simulation, it is necessary to abandon the numerical propagation of single objects and to alternative formulations based on global quantities (e.g. spatial density), representative objects or analytical methods. However, most of the analytical methods available in literature are only applicable to the GEO region as the effect of drag is not considered. Only methods that model drag effects can be applied to study the LEO region, where the debris density and the relative velocities among spacecraft are the highest.

One method applicable in LEO is the one by McInnes (1993). It is based on representing the fragments in terms of their spatial density, whose evolution under the effect of drag can be obtained analytically by applying the continuity equation. The method was originally formulated to model the evolution of the whole debris population, whereas here it is studied how it can be adapted to follow single breakup events. In this way, the method proposed in this thesis does not want to substitute the existing evolutionary models, but rather to expand their capabilities. Evolutionary models are able to model many phenomena that would be difficult to include in an analytical model. Enabling

them to consider also the presence of small fragments would also allow them to refine their analyses and improve the reliability of their forecast.

Part of the content of this Chapter was published in F. Letizia, C. Colombo, and H. G. Lewis. Analytical model for the propagation of small debris objects clouds after fragmentations. Journal of Guidance, Control, and Dynamics, *38 (8):1478–1491, 2015c.*

2

Analytical approach

The aim of this work is to develop an efficient method to describe the evolution of the fragment cloud produced by a collision or an explosion in space. The algorithm to achieve this goal is composed of the following building blocks (Figure 2.1):

- a break up model that generates the fragment properties (i.e. number, mass, area, speed), given the energy of the fragmentation event;
- a numerical propagator to describe the evolution with time of the fragment orbital parameters until the analytical propagation becomes applicable;
- a method to translate the information about the orbital parameters of each single fragment into a continuous density function, useful to compute the collision risk associated to the cloud;
- a fully analytical propagator to express the evolution with time of the cloud spatial density in the long term.

In this Chapter, all the blocks of the proposed model, named debris Cloud Evolution in Low (Earth) Orbit (CiELO), are described in detail. Some applications of the model are explained and its results are compared to a standard piece-wise numerical propagation.

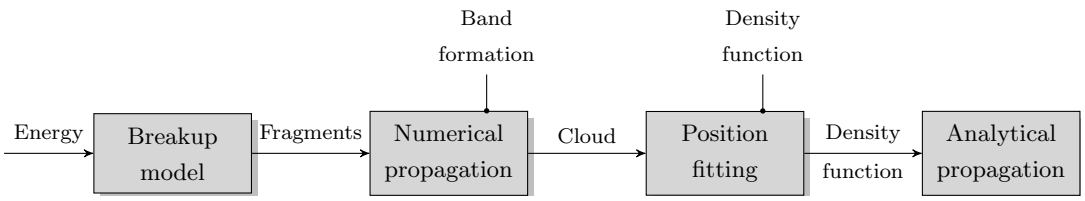

Figure 2.1: CiELO building blocks.

2.1 Breakup modelling

A breakup model translates the initial conditions of an explosion or a collision into the characterisation of the produced fragments, in terms of number, size, mass, ballistic coefficient and velocity variation (Johnson and Krisko, 2001; McKnight, 1991). These parameters, which depend on the energy involved in the fragmentation event and the nature of the event (i.e., collision or explosion), are required to simulate the evolution of a fragment cloud.

Breakup models can be classified as (Barrows, 1996; Barrows et al., 1996):

- *complex*, if the model is based on physical laws and the fragmentation is simulated through a hydrodynamic code
- *semi-analytical*, if the model is developed starting from theoretical expressions and calibrated through experiments
- *empirical*, if the model is derived from the curve fitting of experimental data.

The first two classes of breakup models provide expressions valid for a large range of conditions, whereas the empirical models extrapolate from experimental data, which are limited due to the complexity of tests and the difficulty of varying the testing conditions (Chobotov, 2002; Johnson and Krisko, 2001). As a result, empirical models are not always consistent: it has been shown that models with similar expressions but different values of the parameters provide quite different results that may have a great impact on the long-term cloud evolution (Martin et al., 2004). In spite of the limited applicability, empirical models are widely used as they are easy to implement and require limited computational time. On the other hand, they introduce a level of uncertainty that should be considered when dealing with the long-term evolution of debris clouds (Dolado-Perez et al., 2014).

2.1.1 NASA breakup model

The first space debris breakup model was developed by NASA in 1975, by studying the mass distribution resulting from hypervelocity impacts (Bess, 1975). Since then, different models have been developed (McKnight, 1990, 1991; Rossi et al., 1995a; Su and Kessler, 1985b), using on-orbit observations and orbital tracking of fragments to improve the results.

The breakup model adopted in most debris evolutionary models, such as ORDEM, MASTER, DAMAGE (Sdunnus et al., 2004), is the empirical NASA breakup model, proposed by Johnson and Krisko (2001). The model uses the characteristic length L_c of the fragment as the independent variable to define the features of the cloud: the fragment properties (i.e. mass, area, velocity) are not constant for all objects with the same L_c, but their values

are extracted from distribution functions. This means that the breakup model, at each run, provides different results for the same initial condition; in particular, a normal distribution is used to express the dependence of A/M on the characteristic length L_c and the dependence of the velocity change on the area-to-mass ratio A/M; the parameters of the distributions change depending on the characteristic length.

Different expressions are used for explosions and collisions: as the underlying physical processes are different, the number of fragments and the ejection velocities are not the same in the two cases. Explosions tend to produce larger fragments with lower speed, whereas collisions usually generate a large number of very small fragments with high relative velocities (Barrows, 1996). The model also distinguishes between catastrophic and non-catastrophic collisions, whether or not the target of the collision is completely destroyed. Experiments show that this occurs when the impactor kinetic energy per target mass exceeds $40\,\mathrm{J\,g^{-1}}$, so this value is set as a threshold in the model (Krisko, 2007). More recent observations have shown that non-catastrophic collisions were observed also in cases where the impact energy per target mass exceeded the threshold value because the NASA breakup model does not consider the effect of the location of impact (Pardini and Anselmo, 2014). In other words, a collision will have a different effect if the projectile hits the satellite in the centre of its body or in one of its appendages. As non-catastrophic collisions are more common, most of the results in the following will refer to this kind of fragmentation.

The equations of the NASA model, reported in Appendix A.1, fully characterise the cloud, but some additional steps are needed to simulate a fragmentation event. Firstly, the fragment characteristics are expressed by continuous distribution functions: a discretisation is required in the implementation to pass from a continuous distribution to a finite set of fragments. This aspect is discussed in detail in Appendix A.1. The method also does not take into consideration the conservation of the mass during the fragmentation, so Krisko (2011) suggests that the distributions need to be modified, but a univocal method is not prescribed. Moreover, the distribution of velocity obtained by the model expresses only the velocity magnitude, not its direction. A model of the ejection directions is then required to study the evolution of the fragment trajectories. Random directions (Pardini and Anselmo, 2005; Rossi et al., 1995b) or the choice of ejecta directions to conserve the angular momentum (Chobotov et al., 1988) can be used. Finally, some authors introduce a limit on the maximum ejection velocity (Rossi et al., 2006), or modify the A/M distribution for low speed collision (Hanada et al., 2009).

2.1.2 Implementation in CiELO

In this work, the NASA breakup model is implemented setting $1\,\mathrm{mm}$ as lower size limit, following the recommendations on the correct use of the model (Krisko, 2011). The upper size limit is set to $10\,\mathrm{cm}$, as the analytical method is applied to study the propagation of

small fragments. It is assumed that the number of large fragments is always limited, so that their piece-by-piece propagation is feasible and it is the approach to be followed. As a consequence, no mass conservation correction is applied in the current implementation because it affects mainly the distribution of large fragments (Krisko, 2011). Moreover, all the results refer to the density and the collision probability resulting only from fragments between $1\,\mathrm{mm}$ and $10\,\mathrm{cm}$. It is assumed that the contribution from larger fragments is assessed through alternative traditional approaches. Random direction for the velocity variation is used and the maximum ejection velocity is set equal to $1.3\,v_c$, where v_c is the collision relative velocity: this is done because without any limit the method generates a small number of fragments with a very high ejection velocity (in the order $60\,\mathrm{km\,s^{-1}}$). This practice is commonly adopted in different implementations of the NASA breakup model (Rossi et al., 2006).

2.1.3 Comments to NASA breakup model

As introduced, the NASA breakup model does not have a unique implementation. Rossi et al. (2006) showed the effect of the different implementations of the model among the different space agencies: for example, in 2006, the number of objects larger than $1\,\mathrm{mm}$ was almost double in an ESA implementation compared to a NASA one.[1] This partly explains the scepticism of the detractors of the method. For example, the Russian model SPDA does not rely on this fragmentation approach. It considers a statistical growth of the fragment number due to explosions and collisions. Basically, the model avoids the examination *piece-by-piece*, where the fragments are individually generated and then their trajectories are individually integrated with high precision. In fact the breakup model is not considered to be reliable and accurate enough, therefore the accurate propagation of a highly uncertain initial condition appears questionable (Nazarenko, 2002).

This is particularly relevant in the range of small objects as the NASA breakup model, especially in the sub-centimetre range, is based on a limited database, so it is not clear how representative the model is (Schäfer et al., 2013b). Some authors, such as Jehn (1996) and Martin et al. (2004), reported large discrepancies in the number of fragments produced between the NASA breakup model and the Battelle model, which was the fragmentation model used in older versions of the ESA MASTER model (Klinkrad et al., 1995). The Battelle model was formulated in 1993 performing some ground tests and collecting the fragments to obtain the distributions of the different relevant quantities (e.g. mass, velocity) (Fucke and Sdunnus, 1993). Later, it was noted that the distributions of velocity variation and area-to-mass ratio are more easily obtained from on-orbit observations[2]. The distributions obtained in this way differ noticeably from the ones predicted by the Battelle model that was therefore abandoned. The Battelle model contains in any case

[1] ESA implementation of the NASA breakup model was later corrected.

[2] Holger Krag, Head of Space Debris Office, ESA, personal communication, May 2015.

some interesting elements such as an intrinsic check on the conservation of the mass and a distribution of the area-to-mass ratio that depends on the object size, assuming a shell shape for large objects and a compact shape for the small ones. On this point, Hanada et al. (2009) observed how the distribution of small fragments predicted by the NASA breakup model is compatible with experimental results only for what concerns the size distribution, but not the mass. A modification of the breakup model was suggested to change the area-to-mass distribution into a binormal one to consider the presence of low and high density material. Still now, some studies are ongoing to improve the model, adding more data points (Liou et al., 2013a) or introducing some physical equations (e.g., the momentum conservation) to switch from an empirical to a semi-analytical model (Schäfer et al., 2013a,b).

However, at the moment no better breakup model is available and the NASA model can be considered as a standard as it is the most used in space debris models (Dolado-Perez et al., 2014; Sdunnus et al., 2004) (LEGEND, MASTER, DAMAGE, DELTA, MEDEE). For this reason, the NASA breakup model is used in this work. Moreover, the analytical method proposed here does not rely on a specific breakup model: any other model, such as for example IMPACT (Sorge, 2008), could also be used. In the future, when an updated breakup model becomes available, only the first block shown in Figure 2.1 will need to be changed, whereas the other blocks will not require any modification. The flexibility of the propagation method was validated by applying it to different class of fragmentation events (i.e. collisions and explosions) and for different levels of energies. The results for these cases are shown later in this Chapter, but it can be anticipated that the proposed method works with different initial distribution and appears flexible to how the initial condition is generated. This is one of the advantages of the proposed analytical approach.

2.2 Numerical propagation and band formation

Once the fragments are generated and their characteristics are defined, the orbital parameters for each fragment orbit are obtained starting from the information on their position and velocity. Then, the orbital parameters are numerically propagated using Gauss' variational equations to compute the effect of atmospheric drag and the Earth's oblateness (Vallado, 2013). The effect of drag is estimated using an exponential density model

$$\rho = \rho_{\text{ref}} \exp\left(- \frac{h - h_{\text{ref}}}{H} \right) \tag{2.1}$$

where ρ is the atmosphere density, h is the altitude, and H is the scale height. The reference values ρ_{ref} and H depend on the reference altitude h_{ref}; the values used are from Vallado (2013). In the present work, h_{ref} is set to the closest tabulated value to the altitude where the collision occurs and its value is kept constant for the whole simulation; no

atmospheric rotation is considered and the maximum altitude below which drag is considered is $1000\,\mathrm{km}$. This simple exponential model represents a rough approximation of the reality, but this choice is unavoidable as the proposed analytical method requires an analytical formulation for the atmosphere density. To compare the traditional numerical approach and the proposed analytical method rather than different density models, Equation 2.1 is used for both the propagation methods for the validation. It will be shown in Section 5.4.3 how the proposed method works also when updating the values of ρ_{ref} and H for different values of h_{ref}. This enables to include different (and more realistic) models of the atmosphere with the only condition that they can be locally approximated with an exponential fitting, as already suggested by Jehn (1996). Whereas the modification in Section 5.4.3 is important for the correct application of the method, the expression in Equation 2.1 is still good for the derivation and the validation of the analytical method. In particular, using Equation 2.1 both for the numerical propagation used as a benchmark and as a basis of the derivation of the analytical approach one can isolate the effect of the analytical formulation on the error.

The variation of orbital parameters due to drag is computed with the expressions derived by King-Hele (1987) describing the secular variation of the orbital elements. Three different sets of the equations from King-Hele (1987) are implemented, covering different range of eccentricity (0.2-0.01,0.01-0.001, and circular orbits). In detail, the expressions of the average rate of variation in one orbit of the semi-major axis a and of the eccentricity e are

- $0.01 \leq e \leq 0.2$

$$\begin{aligned}\frac{da}{dt} &= -\frac{c_d A}{M}\sqrt{\mu_E a}\rho_{\text{ref}}\exp\Big(-\frac{a-R_h}{H}\Big)\Big[I_0 + 2eI_1 + \frac{3}{4}e^2(I_0+I_2) + \frac{e^3}{4}(3I_1+I_3)\Big]\\ \frac{de}{dt} &= -\frac{c_d A}{M}\sqrt{\frac{\mu_E}{a}}\rho_{\text{ref}}\exp\Big(-\frac{a-R_h}{H}\Big)\end{aligned}$$

- $0.001 \leq e < 0.01$

$$\begin{aligned}\frac{da}{dt} &= -\frac{c_d A}{M}\sqrt{\mu_E a}\rho_{\text{ref}}\exp\Big(-\frac{a-R_h}{H}\Big)\Big[I_0 + 2eI_1\Big]\\ \frac{de}{dt} &= -\frac{c_d A}{M}\sqrt{\frac{\mu_E}{a}}\rho_{\text{ref}}\exp\Big(-\frac{a-R_h}{H}\Big)\Big[I_1 + \frac{e}{2}(I_0+I_2)\Big]\end{aligned} \tag{2.2}$$

- $e < 0.001$

$$\begin{aligned}\frac{da}{dt} &= -\frac{c_d A}{M}\sqrt{\mu_E a}\rho_{\text{ref}}\exp\Big(-\frac{a-R_h}{H}\Big)\\ \frac{de}{dt} &= 0\end{aligned}$$

where c_d is the drag coefficient, A is the cross-sectional area; M is the mass. Indicating the Earth's radius with R_E, $R_h = R_E + h_{\text{ref}}$. I_k, with

$$I_k(z) = \frac{1}{\pi}\int_0^{\pi} \mathrm{e}^{z\cos\theta}\cos(k\theta)\,d\theta \quad k \in \mathbb{Z}, \tag{2.3}$$

is the modified Bessel function of the first kind and order n with argument $z = \frac{ae}{H}$. The propagation is stopped when the perigee altitude h_p falls below $50\,\mathrm{km}$ as, in this case, the fragment is considered to be re-entering through the atmosphere. More details on the implementation can be found in Section A.2.

The Earth's oblateness is included in terms of the long term effect of the zonal harmonic J_2 on the orbital parameters. This choice can be explained with two reasons. Firstly, over the long term, perturbations such as the Earth's oblateness, that affect only ω, Ω, are not relevant, so it is not worth implementing them up to very high precision. Secondly, as introduced in Section 1.1 and detailed in Section 2.2.1, the effect of the Earth's oblateness on the cloud transforms it from a ring into a flat torus around the Earth. The theoretical descriptions of this transition, which are used to estimate the duration of this process, consider the effect of J_2 only. The secular effect of J_2 on the orbital parameters is expressed by

$$\frac{d\omega}{dt} = \dot{\omega} = \frac{3}{2} J_2 \frac{R_E^2}{p^2} \bar{n} (2 - \frac{5}{2} \sin^2 i) \tag{2.4}$$

$$\frac{d\Omega}{dt} = \dot{\Omega} = -\frac{3}{2} J_2 \frac{R_E^2}{p^2} \bar{n} \cos i. \tag{2.5}$$

where $p = a(1 - e^2)$ is the semi-latus rectum of the orbit, $\bar{n} = \sqrt{\mu_E / a^3}$ is the mean motion, and i is the orbit inclination.

The fragment orbital parameters are numerically propagated until the last phase of cloud evolution (the *band* described in Section 1.1, Figure 1.4c) is reached. In fact, the analytical method proposed in this Chapter, and based on the equations derived by McInnes (2000), can be used only to study the long term evolution of the cloud under the effect of atmospheric drag. This means that it can be applied only once the band is formed, which is when the mean anomaly M and the angles ω, Ω are randomised. This can be verified numerically comparing the distribution of the angles (M, ω, Ω) with a uniform distribution between $-\pi$ and π. The mean anomaly M is not considered as its dispersion (transition from the dense ellipsoid, Figure 1.4a, to the ring, Figure 1.4b) is much faster. The distributions of ω, Ω are evaluated through the Kolmogorov-Smirnov test, which compares the *empirical* cumulative distribution function (in this case the fragment angles coming from the simulation) and a reference cumulative distribution function (CDF) $F(x)$ (in this case the uniform distribution) (Gentle, 2002). The *empirical* cumulative distribution function $\hat{F}_n(x)$ counts the number of observations x_j with $x_j \leq x$ and it is defined as

$$\hat{F}_n(x) = \frac{1}{n} \sum_{j=1}^{n} \mathbf{1}_{x_j \leq x}, \tag{2.6}$$

where n is number of observations and $\mathbf{1}_A$ is the indicator function

$$\mathbf{1}_A = \begin{cases} 1 & \text{if } x \in A \\ 0 & \text{if } x \notin A. \end{cases} \tag{2.7}$$

The Kolmogorov-Smirnov distance is the maximum distance between $\hat{F}_n(x)$ and $F(x)$

$$D_n = \sup_x |\hat{F}_n(x) - F(x)|. \tag{2.8}$$

The *null hypothesis* of the test is that the samples x_j are extracted from the distribution with cumulative function $F(x)$; it is rejected at level α if

$$\sqrt{n} D_n > K_\alpha \tag{2.9}$$

where K_α is found from

$$\Pr(K \leq K_\alpha) = 1 - \alpha, \tag{2.10}$$

with Pr cumulative distribution function of the Kolmogorov distribution. This procedure to evaluate the band formation is similar to the one proposed by Jehn (1991), who uses a chi-squared goodness-of-fit test.

When the hypothesis of uniform distribution is valid for both the angles, so the null hypothesis is not rejected in both cases, the band is considered formed. However, this would require all the fragments to be propagated instant by instant, whereas here the propagation is done fragment by fragment, exploiting the possibility of parallelising the code and reducing the computational time. For this reason, the proposed approach requires an *a priori* criterion to stop the numerical propagation, based only on the knowledge of the initial orbit. Some estimations (Ashenberg, 1994; Chobotov, 1990; McKnight, 1990) are available in literature for this purpose and they rely on the hypothesis that apsidal and nodal dispersion is complete when the faster fragment, in terms of apsidal/nodal rate, reaches the slowest one.

2.2.1 Period estimation for band formation

Chobotov (1990) states that the last phase (i.e. the *band*, Figure 1.4c) is reached when the apsidal and nodal dispersion is complete, so when the faster fragment, in terms of apsidal/nodal rate, encounters the slowest one. The expressions for secular effect of J_2 on the orbital parameters were reported in Equation 2.5. Assuming the fragmentation event causes mainly a variation in the semi-major axis (Δa) with respect to the initial semi-major axis a_0, the fragment with the minimum initial semi-major axis ($a_0 - \Delta a$) will have the maximum apsidal and nodal rate ($\dot{\omega}_+, \dot{\Omega}_+$); on the other hand, the fragment with the maximum initial semi-major axis ($a_0 + \Delta a$) will have the minimum drift rate

$(\dot{\omega}_-, \dot{\Omega}_-)$. The band formation period is then

$$T_\omega^{\text{Ch}} = \frac{\pi}{|\dot{\omega}_+ - \dot{\omega}_-|} \qquad T_\Omega^{\text{Ch}} = \frac{\pi}{|\dot{\Omega}_+ - \dot{\Omega}_-|}. \tag{2.11}$$

McKnight (1990) uses a similar approach, but the fastest fragment is compared with the cloud centre of mass, which is assumed to have the same parameters as the orbit where the fragmentation event occurred; only Ω is considered to define the band formation:

$$T_\Omega^{\text{MK}} = \frac{2\pi}{|\dot{\Omega}_+ - \dot{\Omega}_0|}. \tag{2.12}$$

Ashenberg (1994) starts from similar observations, but his method relies only on the knowledge of the initial orbit (before the fragmentation event). A weak isotropic explosion is considered, so, as for Chobotov (1990), it is assumed that the velocity variation (Δv) is much lower than the orbital speed (v_0); this allows the expansion of the orbital elements in $\Delta v / v_0$. Δv is then decomposed into the in-plane and out-of-plane components and Gauss's equations are used to relate the velocity variation to the variation of the orbital parameters. Indicating with β the out-of-plane angle of Δv, the estimated apsidal rate $\delta\dot{\bar{\omega}}$ can be written as

$$\delta\dot{\bar{\omega}} \approx -\frac{3}{2} J_2 \frac{R_E^2}{a^3} \left[7\left(2 - \frac{5}{2}\sin i^2\right)\cos\beta + \frac{5}{2}\sin 2i \cos u \sin\beta \right] \Delta v \tag{2.13}$$

where R_E is the Earth radius and $u = \omega + \nu$ argument of latitude, with ν true anomaly. The fastest relative apsidal rate $\delta\dot{\bar{\omega}}_{\text{max}}$ is obtained when

$$\tan\beta = \frac{5 \sin 2i \cos u}{14(2 - 5/2 \sin^2 i)}; \tag{2.14}$$

similarly, the fastest relative nodal rate $\delta\dot{\bar{\Omega}}$ can be expressed as

$$\delta\dot{\bar{\Omega}} \approx -\frac{3}{2} J_2 \frac{R_E^2}{a^3} \left(7\cos i \cos\beta + \sin i \cos u \sin\beta \right) \Delta v, \tag{2.15}$$

and the maximum $\delta\dot{\bar{\Omega}}_{\text{max}}$ is found for

$$\tan\beta = 1/7 \tan i \cos u. \tag{2.16}$$

Similarly to Chobotov, the times for the parameter dispersion are then defined as

$$T_x = \frac{\pi}{\dot{x}_+ - \dot{x}_-} = \frac{\pi}{\dot{x}_0 + |\delta\dot{\bar{x}}_{\text{max}}| - (\dot{x}_0 - |\delta\dot{\bar{x}}_{\text{max}}|)} = \frac{\pi}{2|\delta\dot{\bar{x}}_{\text{max}}|} \tag{2.17}$$

where x indicates ω or Ω, so

$$T_\omega^{\text{As}} = \frac{\pi}{2|\delta\dot{\bar{\omega}}_{\text{max}}|} \qquad T_\Omega^{\text{As}} = \frac{\pi}{2|\delta\dot{\bar{\Omega}}_{\text{max}}|} \tag{2.18}$$

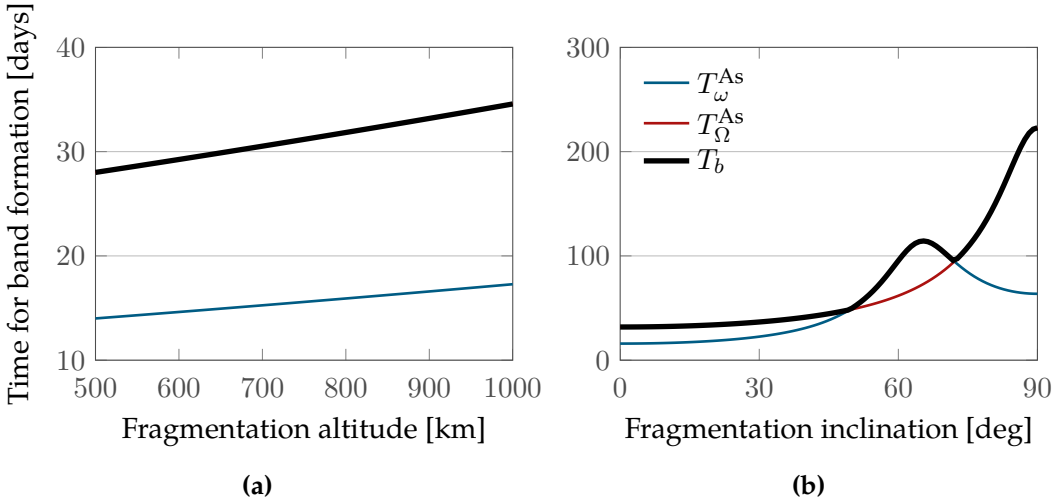

Figure 2.2: Days required to form the band, according to Ashenberg (1994), as a function (a) of the fragmentation altitude with null inclination and (b) of the inclination of the parent orbit with a fixed altitude of $800\,\text{km}$.

and the time for band formation T_b as the maximum between the two

$$T_b = \max(T_\Omega^{\text{As}}, T_\omega^{\text{As}}). \tag{2.19}$$

The expressions by Ashenberg (1994) are very useful as they allow the evaluation of the dependence of the band formation period on the orbital parameters of the initial orbit; the dependence of T_b on the altitude and on the inclination of the initial orbit is shown in Figure 2.2. It is interesting to observe that Ashenberg's formulation also assigns a finite time for the band formation for the cases

$$i = \arcsin\left(\frac{2\sqrt{5}}{5}\right) \qquad \text{and} \qquad i = \frac{\pi}{2}$$

that corresponds to the cases for which, respectively,

$$\dot{\omega} = 0 \qquad \text{and} \qquad \dot{\Omega} = 0.$$

This occurs because, even if a weak explosion is considered, the fragment velocity variation will have an out-of-plane component that results in a change in inclination. The case of a fragmentation cloud produced by a non-catastrophic collision, with energy equal to $100\,\text{J}$, and parent orbit with inclination equal to $\pi/2$ was simulated, numerically propagating the trajectories of all the fragments to understand the dynamic of their dispersion. Figure 2.3 shows the distribution of the fragment inclination at the breakup. The fragments with the highest difference in the inclination from the critical value $i+\pi/2$ *drive* the formation of the band as shown in Figure 2.4, which represents the fragment distribution in semi-major axis and longitude of the ascending node in three different time instants, computed with the numerical method.

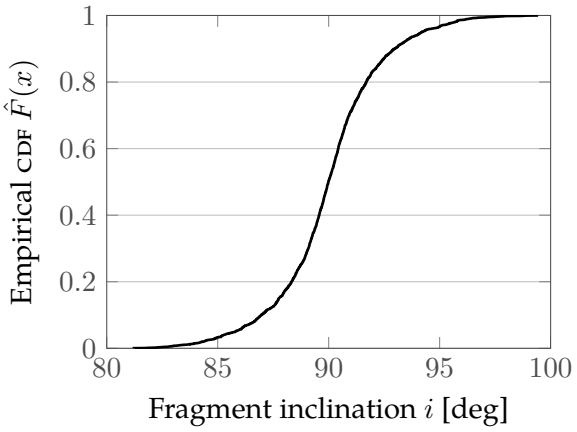

Figure 2.3: Empirical cumulative distribution function for the inclination of the fragments generated by a non-catastrophic collision with energy equal to $50\,\mathrm{kJ}$ and parent orbit with inclination equal to $\pi/2$.

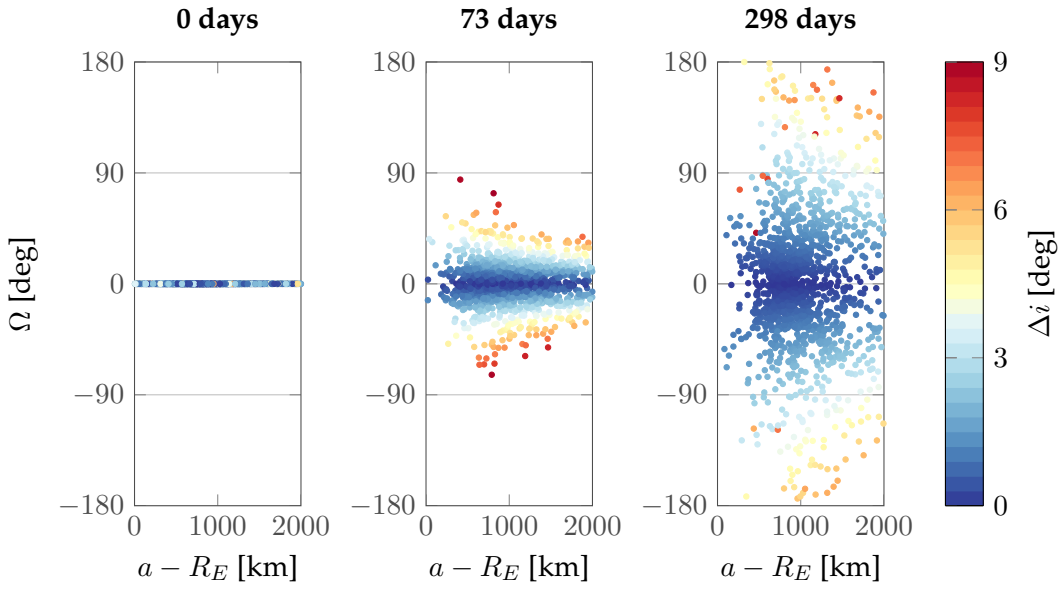

Figure 2.4: Fragment distribution in semi-major axis and longitude of the ascending node in three different time instants for a non-catastrophic collision with energy equal to $50\,\mathrm{kJ}$. The colour of the marker refer to the inclination difference Δi with respect to the inclination of the parent orbit, equal to $\pi/2$.

2.2.2 Analytical and numerical estimation of band formation

Some simulations were carried out to compare the different estimations for the band formation introduced in Section 2.2.1. The analysis starts from the premise that the expressions for the band formation are useful if they allow the estimation of the required time for the band formation *a priori*, without actually simulating the evolution of all the fragments in the cloud. For this reason, in Equations 2.11 and 2.12 the actual *fastest/slowest* fragments are not used, but the reference value of the apsidal and nodal dispersion are obtained starting from the average velocity variation $Deltav_{\mathrm{avg}}$ resulting from the breakup. The maximum value of the semi-major axis is obtained when the

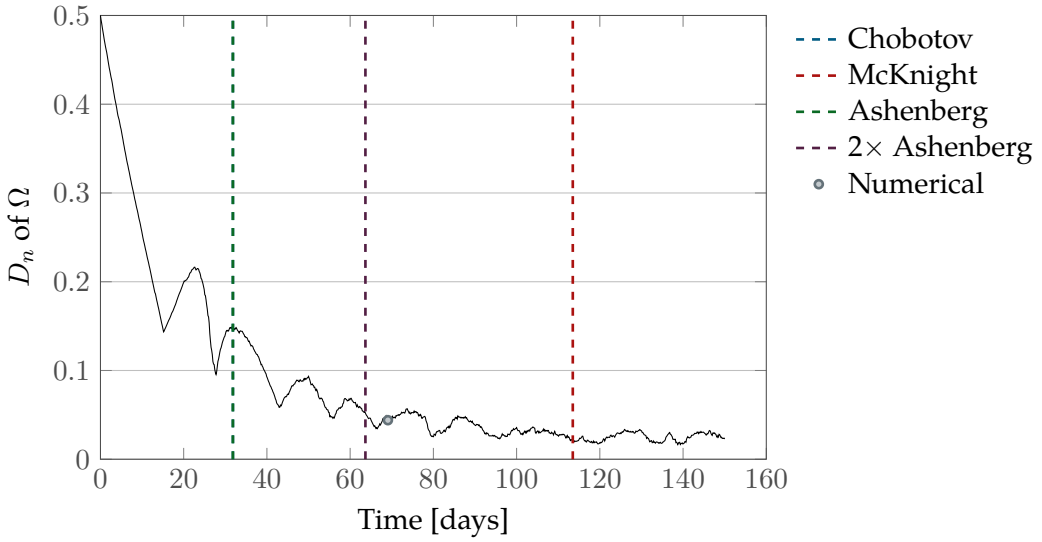

Figure 2.5: Kolmogorov-Smirnov distance D_n for the ascending node Ω as a function of time for a fragmentation event at $h = 800\,\mathrm{km}$, $i = 0°$.

Δv_{avg} is in the direction opposite to the orbital one; the opposite is true to define the slowest fragment. Computing the energy $\mathcal{E}$ for these two cases, it is possible to obtain the corresponding value of the semi-major axis

$$\mathcal{E}_+ = -\frac{\mu_E}{2a_+} = \frac{(v_0 - \Delta v_{\text{avg}})^2}{2} - \frac{\mu_E}{r_0} \rightarrow a_+ \tag{2.20}$$

$$\mathcal{E}_- = -\frac{\mu_E}{2a_-} = \frac{(v_0 + \Delta v_{\text{avg}})^2}{2} - \frac{\mu_E}{r_0} \rightarrow a_-, \tag{2.21}$$

where r_0 is the fragmentation radial distance.

The accuracy of all these analytical expressions can be evaluated by comparing them with the numerical estimation T_{KS} obtained with the Kolmogorov-Smirnov test; in particular, the band is considered formed at the time from which the Kolmogorov-Smirnov test is true for at least 90% of the following instants. [3] The result of the comparison among different estimations of time for band formation, for a fragmentation event at $h = 800\,\mathrm{km}$, $i = 0°$, is shown in Figure 2.5, which presents the value of the Kolmogorov-Smirnov distance[4] for the Ω distribution during cloud evolution. The expression by McKnight (1990) appears to overestimate the time of band formation. Observe that, besides for the cases with $i = k\pi/2$ with $k \in \mathbb{Z}$, the centre of mass represent neither the fastest nor the slowest point in the cloud. As a result, the estimation of the band formation time with

[3] In Figure 2.5 it is evident that the Kolmogorov-Smirnov test presents numerous oscillations that required the definition stated in the test to set the moment when the band is considered formed. The oscillations are due to the fact that the result of the test (i.e. the maximum distance between the two cumulative distributions) is affected by the *shape* of the empirical cumulative distribution function in such a way that the same distribution shifted along the domain can obtain different output of the test. The use of a chi-squared goodness-of-fit test as Jehn (1991) would limit this issue.

[4] the Kolmogorov-Smirnov distance is used for the visualisation for the sake of simplicity, but the actual test in MATLAB is performed as in Equation 2.9 with the significance level set to 0.05

this approach will always give a larger value than the other two options. As previously observed, Chobotov (1990) and Ashenberg (1994) provide the same estimation of the time of band formation, but their value is much lower than the one obtained with the numerical test. This can be explained by observing that in the formulations by Chobotov (1990) and Ashenberg (1994), the band formation period is defined as the time required by the difference in the nodal/apsidal rate to cover π instead of 2π. It was verified that in this way only an incomplete band is obtained. Correcting Equation 2.19 considering the time for the dispersion over 2π, the purple curve in Figure 2.5 is obtained ($2\times$ Ashenberg), which is much closer to the numerical value. Another reason why the two methods (also with the correction of 2π instead of π) underestimate the time of band formation is because, as explained by Jehn (1991), the band cannot be considered formed when the fastest particle meets the slowest: at this moment the fragments are not yet uniformly distributed in ω and Ω, and so their state cannot be described only as a function of the distance r.

This emerges clearly in Figures 2.6 and 2.7, which refer to a fragmentation event at $h = 800\,\mathrm{km}$, $i = 20°$. In Figure 2.6 the distribution of Ω in different times from the fragmentation is shown: the analytical expressions by Chobotov (1990) and Ashenberg (1994) state that the band is formed after 33 days, but actually at that time it is still possible to identify two peaks in the Ω distribution and even at 101 days the distribution is still not uniform. Figure 2.7 shows an alternative visualisation of the band formation in the same instants as in Figure 2.6: at 33 days the *trace* of the parent orbit is still clearly visible.

To define a stopping criterion for the numerical propagation of the cloud, up to the band formation, that does not involve a continuous check of the results, several scenarios were run for different altitudes and inclinations to estimate a safety factor n_{SF} to apply to the prediction by Ashenberg (1994). $n_{SF} = 3$ was chosen as a reasonable value, so the band formation time for the CiELO model is set to

$$T_B = 3T_b. \tag{2.22}$$

It is interesting to verify what happens if the initial condition is built using different values of the safety factor n_{SF}. The cloud density profile was compared at four time intervals with different values of n_{SF}. Figure 2.8 shows the relative error compared to the results with $n_{SF} = 4$: the relative error is computed measuring the difference in the number of fragments in each altitude bin (with a width of $25\,\mathrm{km}$) between the case $n_{SF} = j$ with $j = 1, 2, 3$ and the reference profile with $n_{SF} = 4$. Note that, since the relative error is computed bin-wise, the peaks in the relative error are due to errors in the location of the peak in the density profile and not to large differences between the curves. This was easily verified by comparing the overall shape of the density profiles, evaluating their integral. The relative error on the integral between the cases with $n_{SF} < 4$ and the reference case with $n_{SF} = 4$ is always lower than 3%, so the method appears quite

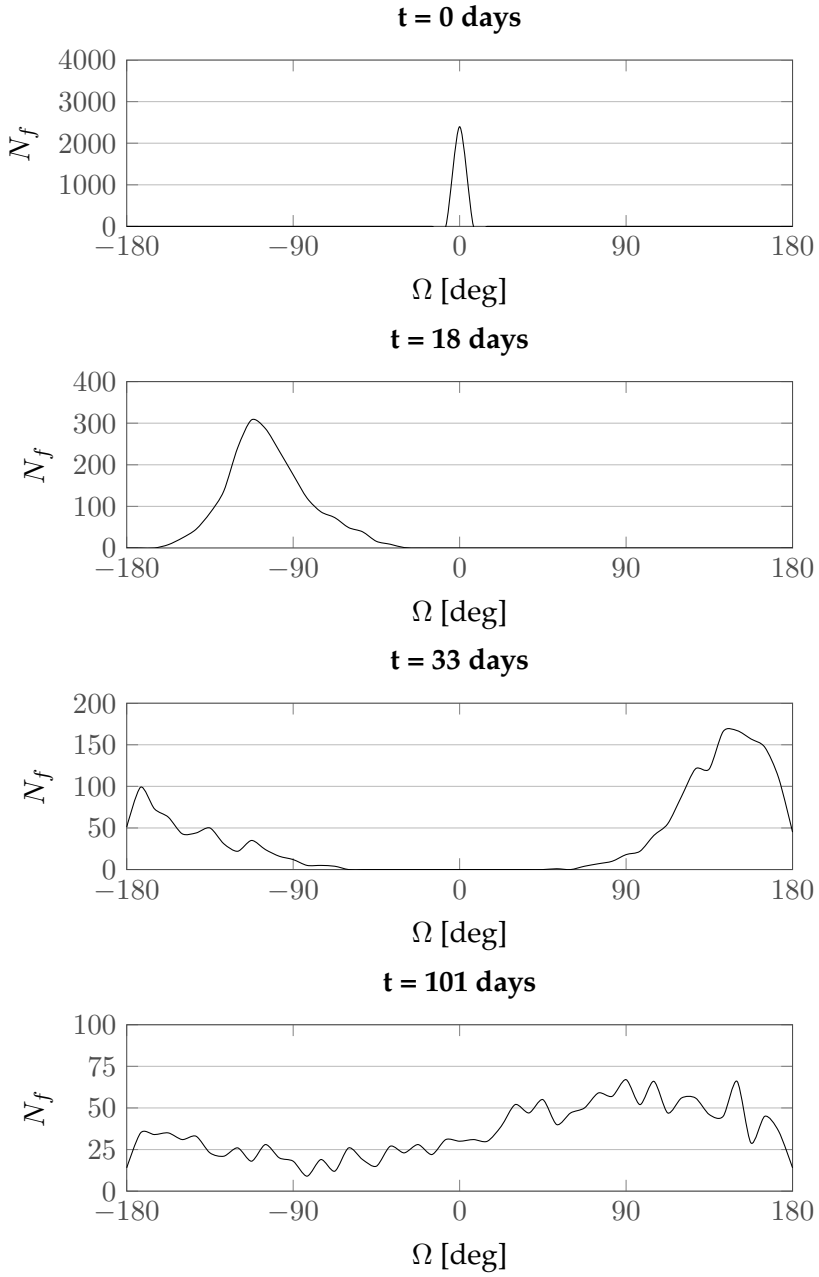

Figure 2.6: Distribution of the ascending node Ω at different time instants for a fragmentation event that took place at $h = 800\,\mathrm{km}$, $i = 20°$. N_f indicates the number of fragments.

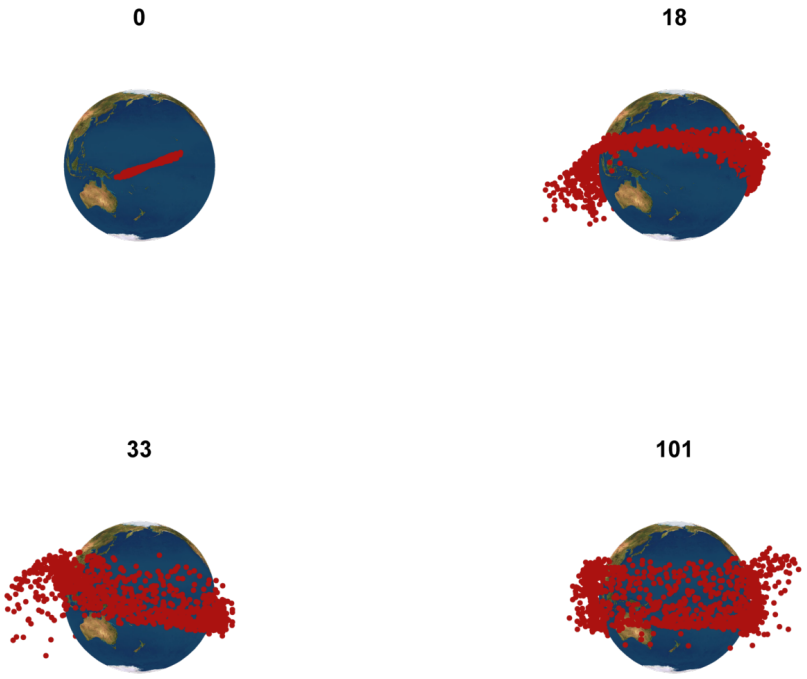

Figure 2.7: Debris cloud evolution at different time instants for a fragmentation event at $h = 800\,\mathrm{km}$, $i = 20°$. The number above each plot indicates the number of days after the fragmentation.

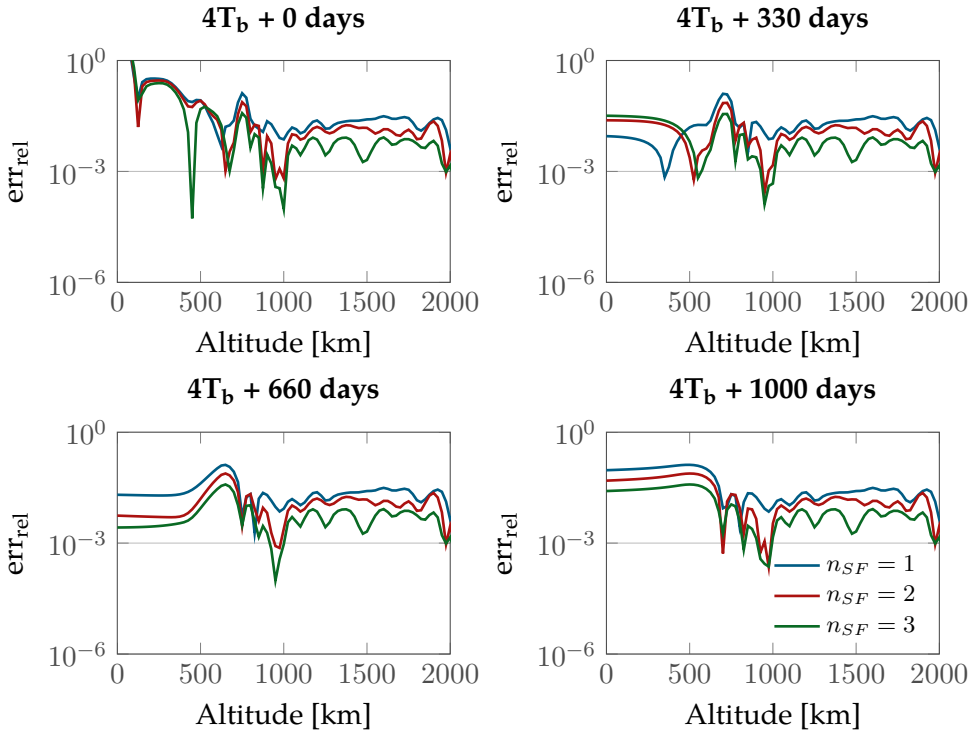

Figure 2.8: Relative error on the cloud density profile at four time intervals with four different values of n_{SF} for a fragmentation at $800\,\mathrm{km}$ on an equatorial orbit. The reference profile is obtained with $n_{SF} = 4$. $T_b = 31.8$ days.

robust to the choice of the initial condition. The importance of switching to the analytical formulation as early as possible during the cloud propagation is motivated by the fact, as it will be shown later, the computational time of the whole simulation is proportional to the length of the phase where the numerical simulation of the single fragments is adopted. For this reason, analyses such as the one in Figure 2.8 may be used to better understand which is the effect, in terms of the error in the long term propagation, of anticipating the adoption of the analytical propagation before the band is formed. This is left for future work.

2.3 Position fitting

Once the band is formed, the information on the fragment positions is translated into a continuous density function that will be the initial condition for the analytical propagation method. Several approaches are possible: the first decision to make is whether to use a distribution function or interpolation to represent the initial density; the second decision is on which variable is the most significant to be represented.

2.3.1 Distribution function versus interpolation

The initial condition for the fragment density can be built by fitting the distribution of the fragment altitude with some standard distribution functions. This process can be performed through the parametric approach, where it is assumed that the functional form of the fitting function is known and only some parameters need to be calculated (Gentle, 2002). In this Section, the function to fit is the distribution of fragments in altitude at the time T_B. Some standard distribution functions were tested and their fitness was evaluated through the quantile-quantile plot[5] (Figure 2.9a) and the Kolmogorov-Smirnov statistic, which, as already mentioned in Section 2.2, measures the maximum distance between the empirical cumulative distribution function of the (simulation) data and the cumulative distribution function used to fit the data (Figure 2.9b). In particular, the latter approach allows the quantification of the fitness of different tested distribution functions and so it provides a criterion to rank them; as a result, the algorithm is able to choose the best function for each application.

[5] A quantile-quantile plot compares the quantiles of the tested distribution and the ones of the empirical CDF. Quantiles are values taken at regular intervals for the inverse function of the CDF of a random variable: if x_α is the α-quantile means that $F(x_\alpha) = \alpha$. In the quantile-quantile plot the two CDF are divided in the same number q of quantiles. A point (x, y) on the plot represents the quantiles of the second distribution (y-axis) against the same quantiles of the first distribution (x-axis). If the two distribution are similar, the points will lie along the line $y = x$.

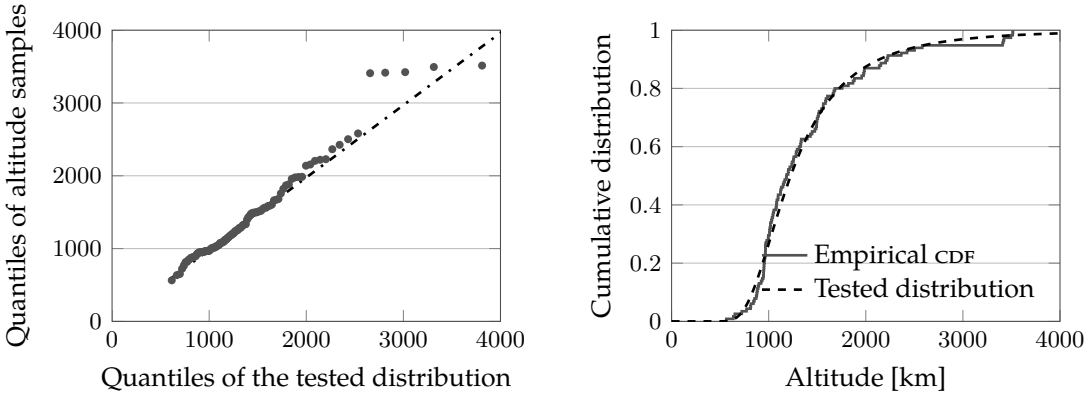

(a) Quantile-quantile plot **(b)** Cumulative distribution

Figure 2.9: (a) Quantile-quantile plot of the generalised extreme value and (b) its cumulative distribution function plotted against the empirical cumulative distribution function for a fragmentation at 800 km.

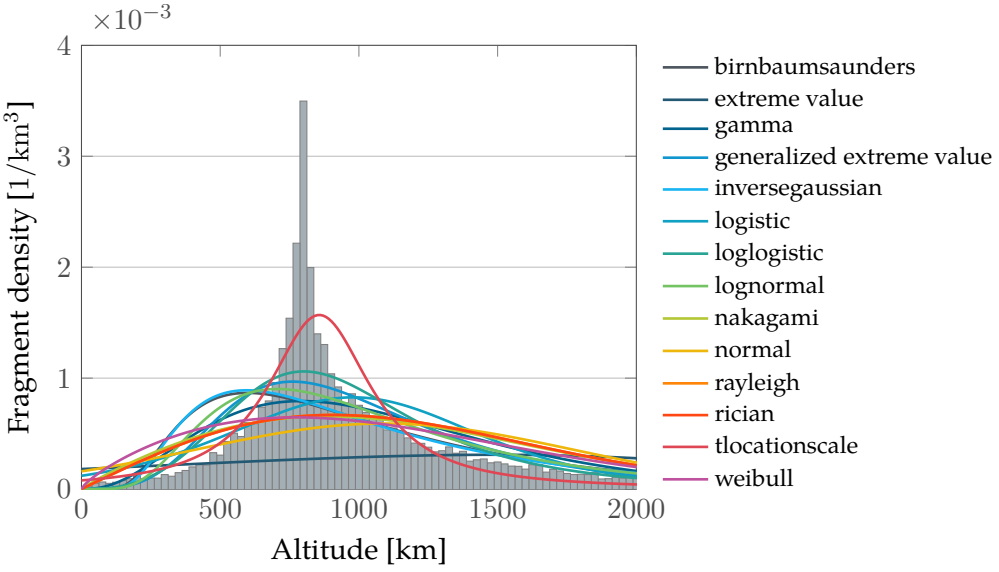

Figure 2.10: Histogram representation of the fragment altitude distribution after the band formation for a fragmentation at 800 km.

The first advantages of the approach with distributions is that it provides a full analytical expression for the initial condition[6]. In addition, the distributions are defined by a very small number of parameters (maximum 3 in the tested cases) that may be related to the features of the fragmentation event. However, this approach also present two major drawbacks. The level of precision of the fit attainable is not very high even for the distribution functions with the best statistics. Figure 2.10 shows the test performed with all distributions present in MATLAB and it can be observed how the *tlocationscale* is the distribution that gives the *best* results, but even in this case the density peak height and its location are not well captured. Moreover, the value of the distribution parameters

[6]This can be particularly relevant if the propagation of the cloud is then performed not with the continuity equation as in this case, but with the differential algebra as in (Colombo et al., 2015; Wittig et al., 2014)

and the choice of which distribution is the best to fit the data are highly affected by the time when the initial condition is built. These two aspects have a large impact on the reliability of the solution and, therefore, the approach with the distribution functions was discarded in favour of an interpolation procedure. In particular, a piecewise cubic interpolation is adopted. This approach does not offer the possibility of relating the shape of the initial condition to the fragmentation parameters, but ensures that the density profile is well represented.

2.3.2 Variable for the fitting

The simplest approach to define the initial condition for the analytical propagation would be to set it equal to the actual distribution of fragments with altitude at the time of the band formation (T_B). This was done in a preliminary version of the model (Letizia et al., 2013), where the density function was built from the distribution of fragments in distance from the Earth r or semi-major axis a. However, in this way, the initial condition depended on the moment when the band is considered formed and on the specific run of the breakup model used to simulate the fragmentation. This is due to the fact that the NASA breakup model contains some randomly chosen parameters (e.g. to describe the dependence of the velocity variation on the fragment area-to-mass ratio). A Monte Carlo approach can be adopted to give statistical meaning to the results.

Another approach was preferred. The fragment position is not directly used as initial condition, but the fragments' orbital parameters (namely, the semi-major axis a, the eccentricity e, the inclination i) are used to describe the fragment distribution in space, considering that the other parameters (i.e. the longitude of the ascending node Ω, the argument of the periaspis ω and the mean anomaly M) are randomised within the cloud. In particular, the initial distribution of the orbital parameters is used to build the *probability* of finding fragments at a certain altitude. In this way, the dependence on the band formation time and on the run of the breakup model is reduced. Figure 2.11 presents the comparison among three possible initial conditions; three different runs of the break-up model are presented, each one plotted with a different colour. One can see that, in contrast to the simple distribution in h (Figure 2.11c), the probability density (Figure 2.11a) has only a limited variation with the specific analysed run; moreover, the distribution in h tends to the probability density if many cases are run and averaged.

Besides the reduced variability, this approach presents another advantage when compared to the distribution in semi-major axis (Figure 2.11b). The probability density presents a much stronger connection with the computation of the collision probability for spacecraft or debris objects crossing the fragment cloud as it will be shown in Chapter 3.

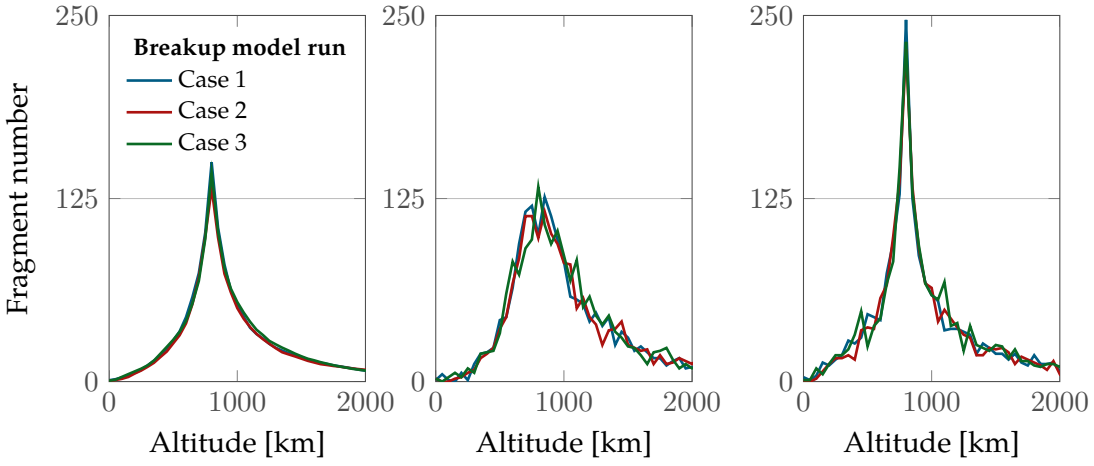

(a) Probability **(b)** Semi-major axis **(c)** Distance

Figure 2.11: Comparison among three different distributions that may be used to describe the initial condition: (a) refers to the probability density, (b) to the semi-major axis distribution, (c) to distance distribution. Each colour refers to a different run of the break-up model.

2.3.3 Expressions for the spatial density

Different authors have studied how to express the spatial density of a fragment cloud given the distribution of the fragments' orbital parameters (Jehn, 1996; Kessler, 1981; McInnes and Colombo, 2013; Sykes, 1990). In Section B.1 and B.2 the equivalence between some of these formulations is shown. All approaches express the probability of finding a particle, at a certain distance from the central body r and a certain latitude β, knowing its orbital parameters a, e, i and assuming that the distribution of the other parameters ω, Ω, ν can be considered random. These expressions depend only on the geometry, so they have been applied to different problems related to space debris (Kessler, 1990; Su and Kessler, 1985a), the design of disposal trajectories (Jenkin and Gick, 2005), but also asteroids (Sykes, 1990) and Jupiter's outer moons (Kessler, 1981). Moreover, the dependence on the distance and on the latitude can be studied separately, which is particularly useful in the current application as the evolution of the two parameters occurs with different time scales and drivers, as it will be discussed in Section 3.2. For this reason, in this part only the expression related to the distance r is analysed, whereas the role of latitude will be discussed in Section 3.2.

Using the same notation as Kessler (1981), the spatial density in a particle band can be expressed as

$$S(r, \beta) = s(r) f(\beta) \tag{2.23}$$

where

$$s(r) = \frac{1}{4\pi^2 r a^2} \frac{1}{\sqrt{e^2 - \left(\frac{r}{a} - 1\right)^2}} \tag{2.24}$$

$$f(\beta) = \frac{2}{\pi} \frac{1}{\sqrt{\cos^2\beta - \cos^2 i}}, \tag{2.25}$$

where $s(r)$ is the spatial density averaged over all latitudes, and $f(\beta)$ is the ratio of the spatial density at latitude β to the spatial density averaged over all latitudes. If only the dependence on the distance is considered, Equation 2.24 can be used to build the initial condition $n_0(r) = s(r)$.

When modelling a fragment cloud generated by a breakup, the dispersion of the orbital parameters a, e among the fragments should be considered. This means that Equation 2.24 cannot be applied directly to describe the density of the cloud using from the initial value of a, e of the orbit where the fragmentation occurred. Instead, it should be applied to each fragment to take into account how the energy is distributed among them; the total density is then obtained by simply summing the contribution of each fragment

$$n(r) = \sum_{j=1}^{N_F} n_j(r). \tag{2.26}$$

2.3.4 Validation of the density expression

The expression of the spatial density can be initially tested considering its accuracy in modelling the initial density profile, which is the distribution of the fragments at the band formation. This was done both on single runs of the NASA breakup model and on an average distribution obtained with ten runs of the NASA breakup model.

Figure 2.12 shows the test performed on ten different runs of the NASA breakup model for a non-catastrophic collision with energy equal to $50\,\mathrm{kJ}$, occurring on a circular equatorial orbit at $800\,\mathrm{km}$. The grey bars represent the average distribution of fragments from the numerical propagation; the black lines the profiles obtained applying Equation 2.26 to each run of the breakup model.

The comparison is expressed in terms of the number of fragments in an altitude shell of width equal to $25\,\mathrm{km}$ and so the result of Equation 2.24, which provides a spatial density, is multiplied by the volume of the spherical shell

$$V_{\text{shell}} = \frac{4}{3}\pi(r_+^3 - r_-^3) \tag{2.27}$$

where $r_\pm = r \pm \Delta r/2$ with r centre of the altitude bin and Δr bin width. From Figure 2.12 it is possible to observe how the analytical expression captures the general shape of the

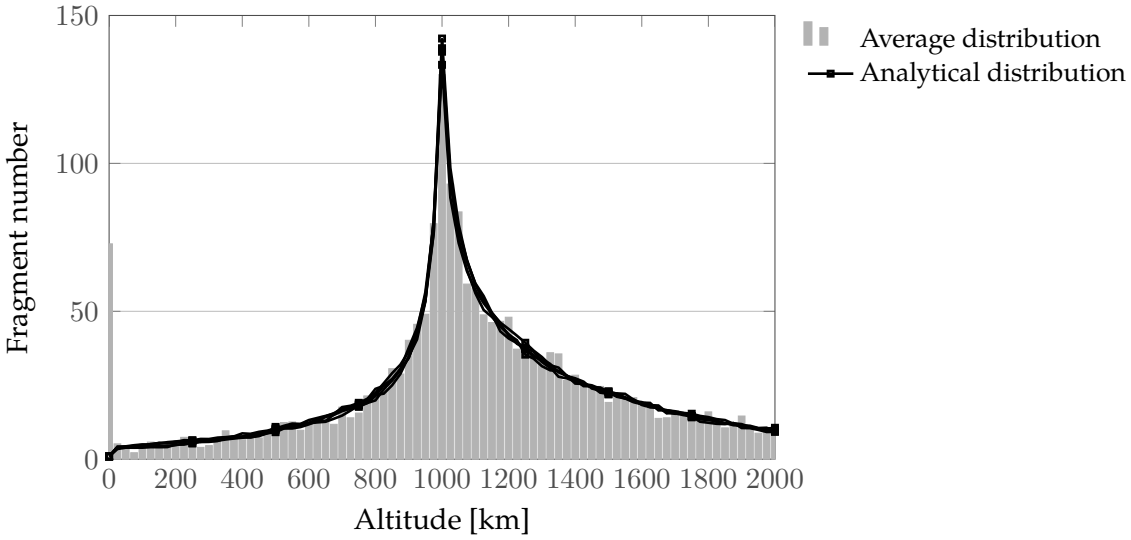

Figure 2.12: Comparison between the density expressions to represent the average fragment spatial distribution at the band formation obtained with ten runs of the breakup model.

distribution and, importantly, shows low variability among the different runs. This observation is important because it confirms that the results obtained with the proposed analytical method have a limited dependence on the specific run of the breakup model used to model a fragmentation.

2.4 Analytical propagation

Once the initial fragment density of the band is defined, the continuity equation is used to analytically derive the fragment density evolution with time. As described in Section 1.5, the continuity equation can be written as

$$\frac{\partial n}{\partial t} + \nabla \bullet \mathbf{f} = \dot{n}^{+} - \dot{n}^{-}, \tag{2.28}$$

where n is the fragment density. In this work, no discontinuous events are considered, so $\dot{n}^{+} - \dot{n}^{-} = 0$; the term $\nabla \bullet \mathbf{f}$ models continuous phenomena, in this case drag, following the approach developed by McInnes (2000).

The radial distance r is the only considered coordinate, so a spherical symmetry is assumed. This assumption and modelling only the drag effect imply that the analytical propagation becomes applicable after the cloud has formed a continuous band around the Earth (Figure 1.4c). The vector field has then only one component in the radial direction

$$f_r = v_r n(r, t). \tag{2.29}$$

The drift velocity in the radial direction v_r is obtained from the expression of drag acceleration

$$a_d = \frac{1}{2}\frac{c_d A}{M}\rho(r)v^2 \tag{2.30}$$

where c_d is the drag coefficient of the fragment, which is assumed to be constant and equal to 2.2 (Vallado, 2013); A is the fragment cross-sectional area; M is the fragment mass; v is the fragment velocity and $\rho(r)$ is the atmosphere density, which depends on the radial distance from the Earth as in Equation 2.1. The effect of drag is to reduce the orbit energy $\mathcal{E}$ with a rate equal to

$$\frac{d\mathcal{E}}{dt} = -v_\theta a_d \tag{2.31}$$

where v_θ is the transversal velocity that, with the hypothesis of quasi-circular orbits, can be considered

$$v_\theta = \sqrt{\frac{\mu_E}{r}}. \tag{2.32}$$

Applying again the hypothesis of quasi-circular orbits, the energy variation can also be written as

$$\frac{d\mathcal{E}}{dt} = \frac{d}{dt}\Big(-\frac{\mu_E}{2r}\Big) = \frac{\mu_E}{2r^2}v_r. \tag{2.33}$$

Observe that the hypothesis of quasi-circular orbit is essential to the derivation of a closed-form solution, but it also has an impact on the accuracy of the method as it will be discussed in Section 2.8. Combining Equations 2.31 and 2.33, the radial velocity can be written as

$$v_r = -2r^2\frac{v_\theta a_d}{\mu_E}; \tag{2.34}$$

substituting a_d and v_θ with their expressions in Equations 2.30 and 2.32, and putting $v^2 = v_\theta^2 + v_r^2 \approx v_\theta^2$, the following expression for the radial velocity is obtained

$$v_r = -\sqrt{\mu_E r}\frac{c_d A}{M}\rho(r). \tag{2.35}$$

Similarly to McInnes (2000), the parameter ε is introduced,

$$\varepsilon = \sqrt{\mu_E}\frac{c_d A}{M}\rho_{\text{ref}}, \tag{2.36}$$

which collects all the terms that do not depend on r. Observe that here the definition of ε is slightly different from the original one in McInnes (2000) because, to increase the numerical accuracy, it is convenient to compute the exponential term always as $\exp\left(-\frac{h-h_{\text{ref}}}{H}\right)$ and not as two separate terms $\exp\left(-\frac{h}{H}\right), \exp\left(\frac{h_{\text{ref}}}{H}\right)$. Putting $R_h = R_E + h_{\text{ref}}$, the final expression for v_r is obtained

$$v_r = -\varepsilon\sqrt{r}\exp\Big(-\frac{r-R_h}{H}\Big). \tag{2.37}$$

This expression of v_r allows the term $\nabla \bullet \mathbf{f}$ in the continuity equation (Equation 2.28) to be rewritten. Using spherical coordinates, the expression for $\nabla \bullet \mathbf{f}$ is

$$\nabla \bullet \mathbf{f} = \frac{1}{r^2}\frac{\partial(r^2 f_r)}{\partial r} + \frac{1}{r\sin\theta}\frac{\partial}{\partial\theta}(f_\theta \sin\theta) + \frac{1}{r\sin\theta}\frac{\partial f_\phi}{\partial\phi}, \tag{2.38}$$

with θ polar angle and ϕ azimuthal angle. As only $f_r \neq 0$, Equation 2.28 becomes

$$\frac{\partial n(r,t)}{\partial t} + \frac{1}{r^2}\frac{\partial}{\partial r}\left[r^2 v_r n(r,t)\right] = 0. \tag{2.39}$$

Performing the derivation and collecting the terms with respect to n, Equation 2.39 can be rewritten as (McInnes, 2000)

$$\frac{\partial n(r,t)}{\partial t} + v_r\frac{\partial n(r,t)}{\partial r} + \left[\frac{2}{r}v_r + v_r'\right]n(r,t) = 0, \tag{2.40}$$

where $()'$ indicates the derivation with respect to r. Equation 2.40 is a first order linear partial differential equation that can be solved with the method of characteristics[7], whose solution in this case is

$$G(r,t) = \exp\left(\frac{r-R_h}{H}\right) + \varepsilon\frac{\sqrt{R_h}}{H}t, \tag{2.41}$$

obtained with the approximation

$$\sqrt{r} \approx \sqrt{R_h}. \tag{2.42}$$

Also the effect of this approximation is analysed in detail in Section 2.8. Applying this procedure, McInnes (2000) found an explicit expression for the density evolution,

$$n(r,t) = \frac{\Psi[G(r,t)]}{r^2 v_r} = \frac{\Psi\{\exp[-\frac{r-R_h}{H}] + (\varepsilon\sqrt{R_h}/H)t\}}{-\varepsilon r^{5/2}\exp[-\frac{r-R_h}{H}]}. \tag{2.43}$$

The function Ψ is obtained from the initial condition $n(r, t=0)$

$$\Psi[G(r,0)] = n(r,0)r^2 v_r, \tag{2.44}$$

and from the characteristics at $t = 0$

$$z = G(r,0) = \exp\left(\frac{r-R_h}{H}\right), \tag{2.45}$$

which can be inverted finding

$$\tilde{r} = R_h + H\log(z) \tag{2.46}$$

[7] All the mathematical details on the method of characteristics and its application to Equation 2.28 are shown in Appendix B.3.

so that

$$\Psi(z) = n(\tilde{r}(z), 0)\tilde{r}^2(z)v_r(\tilde{r}(z)). \tag{2.47}$$

Equation 2.43 provides a fully analytical expression to compute the effect of drag on the cloud and the analytical propagation always acts on the cloud globally, not on the single fragments. Therefore, in this case, the model is *analytical* in the sense that, once the initial density is known, the cloud density at any time is immediately known, without any long term numerical integration of the fragment trajectories, differently from previous models (Kebschull et al., 2013; Rossi et al., 1995b, 2013).

Moreover, Equation 2.47 shows that no particular operation is needed on the function $n(r, 0)$, providing large flexibility on the functions that can be used to describe the initial condition. This means that the initial condition can be easily built, starting from different kind of fragmentation phenomena. It is important to observe that the shape of the initial condition is used only as a starting point for the analytical method, which is able to modify the function shape to follow the cloud evolution as demonstrated in Appendix B.4.

It is also important to notice that the parameter ε, defined in Equation 2.36, is not constant for the whole cloud as the fragments have different area-to-mass ratios, A/M. To improve the accuracy of the model, N bins in area-to-mass ratio are here defined. For each bin, an average ε_i is assumed and the corresponding density n_i is obtained according to Equation 2.43; all the partial densities n_i are summed to obtain the global cloud density n.

$$n(r,t) = \sum_i n_i = \sum_i \frac{\Psi\{\exp\left[-\frac{r-R_H}{H}\right] + (\varepsilon_i\sqrt{R_H}/H)t\}}{-\varepsilon_i r^{5/2}\exp\left[-\frac{r-R_H}{H}\right]} \tag{2.48}$$

Different definitions of the bins are possible: in particular, two options were tested and compared:

- *same fragment number*: the bins in A/M are defined so that each one contains the same number of fragments at the band formation,
- *logarithmically spaced*: the edges of the bins are defined as logarithmically spaced in A/M intervals having as bounds the maximum/minimum of the fragment population at the band formation.

Figure 2.13 shows the method accuracy and the computational time as a function of the number of bins in A/M, defined with the two described approaches. The accuracy is measured by two parameters. The first is the mean absolute error between the density profile obtained with the analytical method and the profile obtained with the numerical propagation (error on profile, err_{prof}). The second one is the relative error on the density peak height (err_{peak}) as explained more in detail in Section 2.5. Figure 2.13 shows that

the first approach (same number of fragment in each bin) has a lower error than the logarithmically spaced bins. Therefore, the first approach is used hereafter. Figure 2.13 allows the optimal number of bins to be chosen and this was set equal to 10: for this value there is a convenient reduction of the error compared to using a single value of ε for the whole cloud and the computational time is only slightly affected.

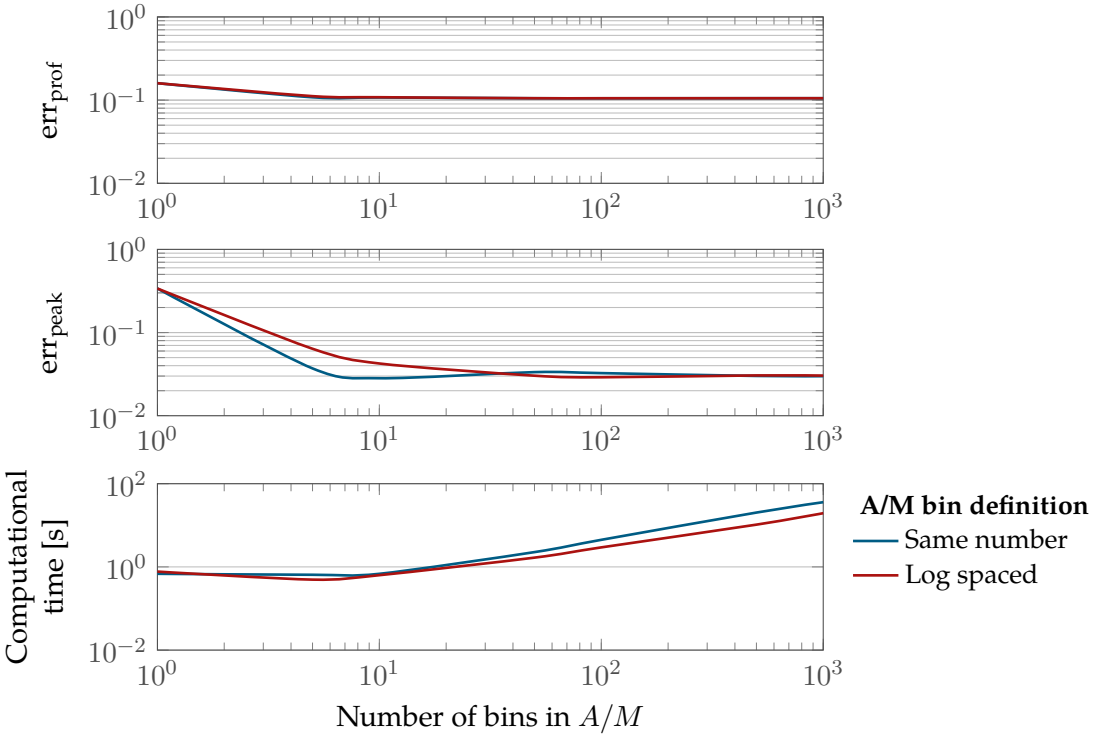

Figure 2.13: Relative error on density peak, relative error on the total number of fragments and computational time as a function of the number of the number of bins in A/M. The simulated period is equal to 1000 days.

2.5 Results for cloud propagation

In the remainder of the Chapter the proposed method will be applied to a specific fragmentation event. Then, the accuracy of the method for many initial conditions will be assessed and its computational time presented.

The results are expressed in terms of fragment spatial density with units km^{-3}. As discussed in Section 2.3, the analytical method provides directly the results in spatial density if Equation 2.24 is used to build the initial condition. The results of the numerical propagation are translated into a value of spatial density considering the number of fragments N_f in a spherical shell of radius r and width w, here set equal to $25\,\mathrm{km}$; it is equivalent to count the fragment distribution in altitude with histograms with width w. This output can be translated into fragment spatial density n with the following

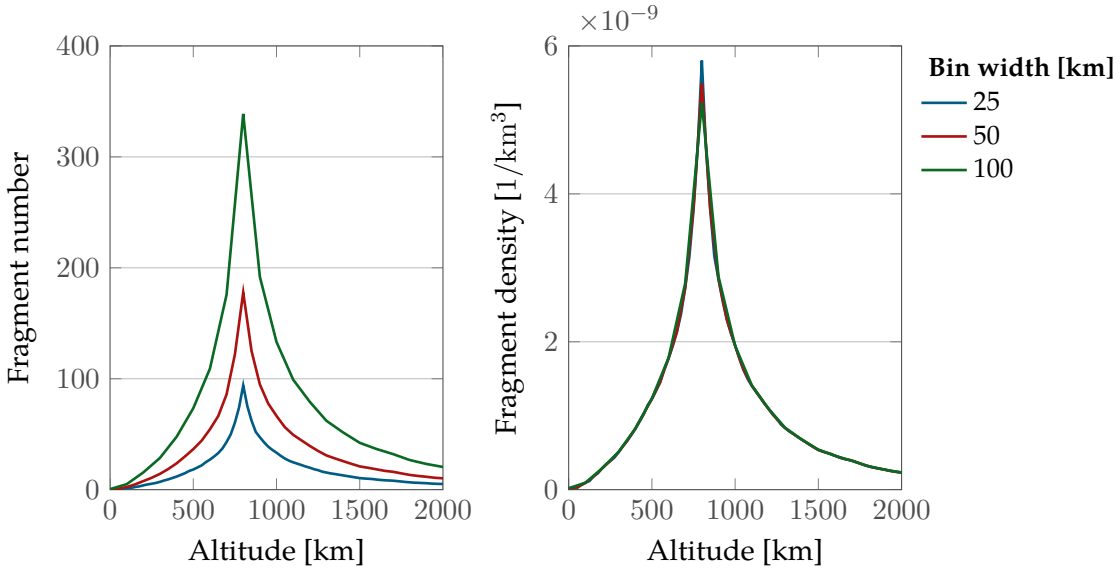

Figure 2.14: Alternative representation in terms of fragment number or spatial density for a fragmentation at $800\,\mathrm{km}$.

expression

$$n = \frac{N_f}{V} \qquad V = 4\pi w\left(\frac{w^2}{12} + r^2\right). \tag{2.49}$$

The representation with the number of fragments provides an easier physical interpretation, but the representation in terms of density is preferred because it is independent of the bin width (Figure 2.14), and it has a direct physical meaning, particularly important when the method is used to compute values of collision probability.

2.6 Propagation with CiELO

Most of the results in this Chapter refer to a fragmentation generated by a non catastrophic collision between a spacecraft and a projectile of $100\,\mathrm{g}$ with a collision velocity of $1\,\mathrm{km\,s^{-1}}$. In this Section, the parent orbit of the spacecraft is equatorial and circular, with altitude equal to $800\,\mathrm{km}$. The collision generates 2397 fragments, whose area-to-mass ratio ranges from 0.0298 to $15.4\,\mathrm{m^2\,kg^{-1}}$ in the specific run of the breakup model considered. In fact, one single run of the NASA breakup model is used to show an example of the output of the analytical method. Multiple runs of the breakup model are used to validate the analytical approach in Section 2.7.

The band is considered formed after almost 95 days and then the analytical propagation is applied, dividing the cloud in 10 bins of A/M. Figure 2.15 shows the cloud density, obtained with the analytical method, at the band formation (Figure 2.15a), and 1000 days later (Figure 2.15b). At the band formation, Figure 2.15a indicates a distinct peak (the dark red circle) in the cloud density at the altitude of the breakup. After 1000 days (Figure 2.15b) drag has reduced the peak and also the number of fragments at

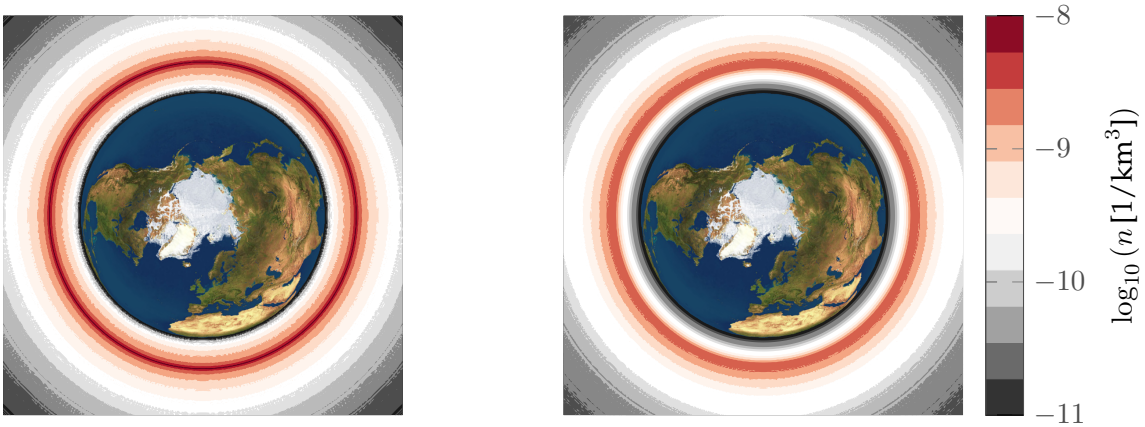

(a) $T_B + 0$ days

(b) $T_B + 1000$ days

Figure 2.15: Visualisation of cloud density at (a) the band formation and (b) after 1000 days. The plot is not in scale.

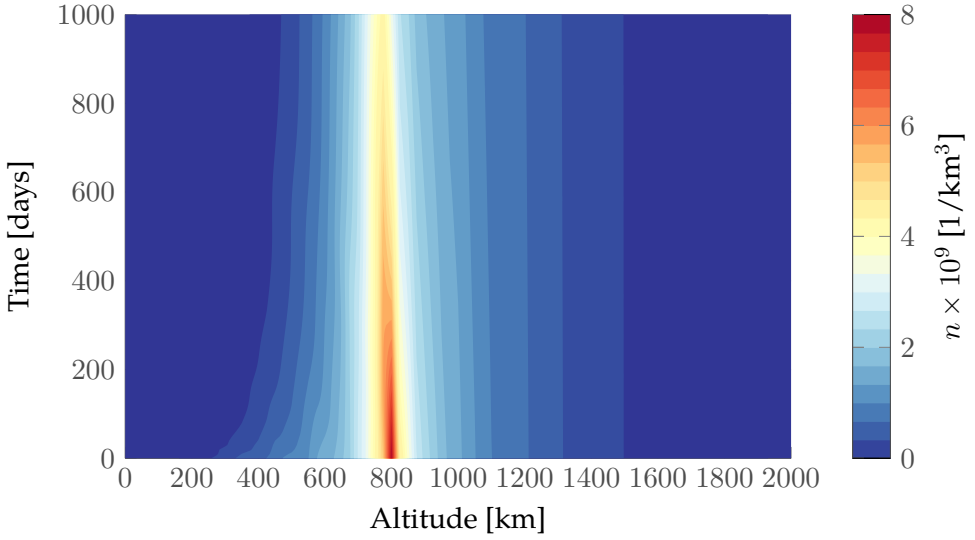

Figure 2.16: Visualisation of cloud density evolution for a fragmentation at 800 km.

low altitudes, below the fragmentation altitude; the density at high altitude is, instead, almost unchanged. This is shown more clearly in Figure 2.16, which gives an immediate representation of the persistence of the fragments in orbit. It also allows the estimation of how the altitude range affected by the fragmentation is reduced with time and this kind of plot can be used to compare different breakup events.

More in detail, the evolution of the density profile in time is shown in Figure 2.17, where the colours refer to different values of the area-to-mass ratio (A/M). For low A/M values there is always a distinct peak in the density profile and the peak shifts towards lower altitude with time. For high A/M, instead, the peak is quickly eroded and the fragments tend to be spread up to high altitudes. This is in agreement with the results by McInnes (2000). The number of fragments at the band formation is equal to 1740, which means that 27% of the fragments generated by the collision decay before the band

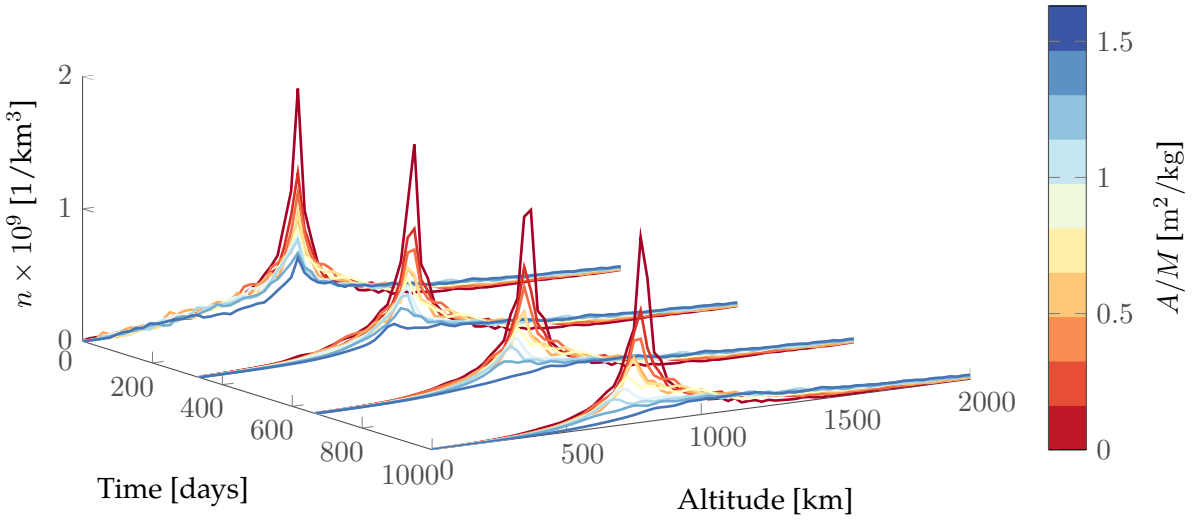

Figure 2.17: Evolution of the cloud density as a function of time after the band formation, for a fragmentation at 800 km.

formation. The analytical method predicts that after 1000 days, 1420 are still in orbit, against the result of 1357 obtained with the numerical integration: the relative error in the estimation of the fragment number is around 10%, so the analytical method can be considered a reasonable approximation.

Figure 2.18b presents an analysis of the peak height and location for each A/M bin. In Figure 2.18a the value of the peak height is normalised by the value at the band formation. In this way, the relative reduction of the peak for each A/M bin can be appreciated. During the 1000 days of propagation, the height of the density peak is reduced by 34% for the whole cloud, with the largest reduction for the bins with the largest A/M. The peak location is basically unchanged (Figure 2.18b) for the cloud globally, whereas it undergoes a large variation for fragments with high area to mass ratio A/M. This is due to the fact that, for the particular choice of the bin definition, the curves referring to high A/M values are flatter (Figure 2.17) and the altitude corresponding to the peak (i.e. the point with the highest density) changes discontinuously.

Further, the shape of the density function is affected by drag, which acts differently at low and high altitudes. For this reason, the fragment density is reduced by 33% in 1000 days at an altitude lower or equal to the parent altitude 800 km and only by 10% for higher altitudes. As the peak is reduced with time, the band of altitudes that contains 68.27%[8] of the population increases its amplitude with time (Figure 2.19).

[8]The specific value of the percentage is taken from the definition of normal distribution, where 68.27% of the values lie within one standard deviation from the mean

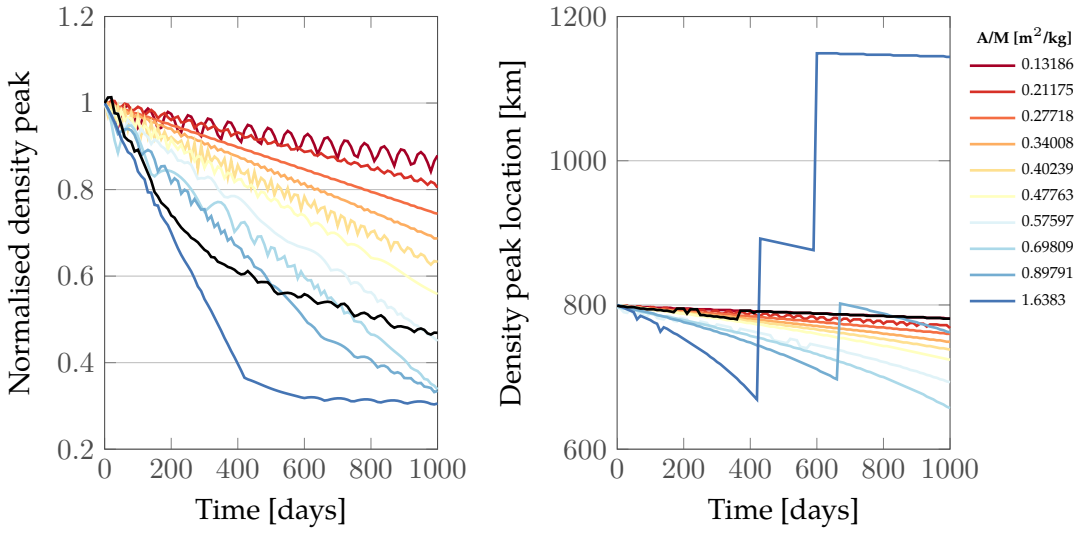

(a) Normalised peak height **(b)** Peak location

Figure 2.18: Evolution of the density peak height and location for a fragmentation at 800 km. The value of the peak height is normalised with the value at band formation. The colours refer to different values of the area-to-mass ratio and in black the value for the cloud globally is reported.

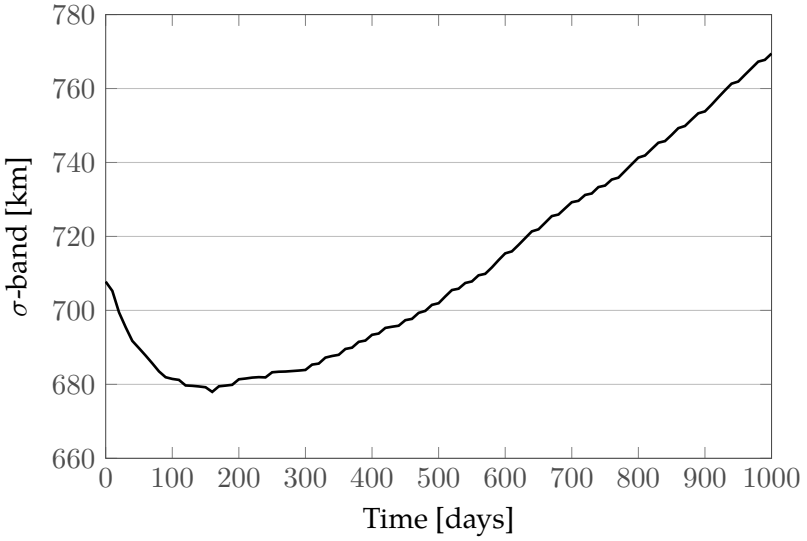

Figure 2.19: Evolution with time of the amplitude of the altitude band around the peak that contains 68.27% of the population for a fragmentation at 800 km.

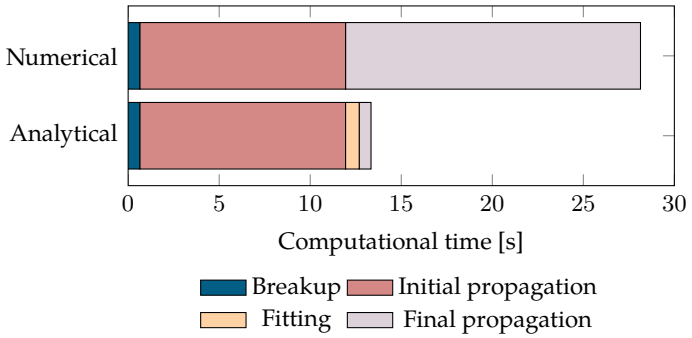

Figure 2.20: Computational time for a PC with 4 CPUs at 3.40 GHz.

2.7 Comparison with numerical propagation

The analytical method for the cloud propagation was compared in terms of computational time and accuracy. When the *numerical* propagation is used, the trajectory of each fragment is propagated individually using the semi-analytical propagator described in Section 2.2. It models the effect of the atmospheric drag, using the equations by King-Hele (1987), and of the Earth's oblateness considering only the term with J_2.

The numerical method used as a benchmark is certainly very simple, but this choice is motivated by wanting to study the error introduced by the continuity equation alone. This requires using the same models of perturbations for both cases. Future work will repeat the validation considering a more refined model of the atmosphere and additional perturbations such as solar radiation pressure, which can affect the fragments' trajectories at altitudes larger than $800\,\mathrm{km}$.

2.7.1 Computational time

The computational time for the numerical and the proposed analytical methods is presented in Figure 2.20: the intervals reported in the diagram refer to the fragmentation shown in Figure 2.16, which produces a cloud, composed initially by 2397 fragments and which is propagated up to five years after the band formation, with a time step of 1.5 days.

The measured computational times refer to a PC with 4 CPUs at 3.40 GHz; both codes are written in MATLAB and parallelised with MATLAB built-in functions. The values in Figure 2.20 are the average times obtained over twenty runs of the simulation. For both the analytical and the numerical propagator, the breakup model requires $0.64\,\mathrm{s}$ to generate the cloud. For the analytical method, the main contribution to the computational time is given by the numerical propagation until the band formation ($11.32\,\mathrm{s}$), while the time to build the initial condition ($0.75\,\mathrm{s}$) and the one for the final (analytical) propagation ($0.65\,\mathrm{s}$) are negligible. On the other hand, the full numerical propagation takes $28.15\,\mathrm{s}$ as

the simulation time for the numerical propagation depends on the number of fragments and the length of the simulated period[9]. In the case of the analytical method, these dependencies are still present, but in a weaker form. In fact, the number of fragments affects only the time for the propagation up to the band formation; the length of the simulation affects the computational time only if a certain time step is prescribed as in the case in Figure 2.20. This was done to measure the computational time with typical settings for the cases where the value of density is then used to compute the collision probability for a target crossing the cloud. As will be explained in Chapter 3, this requires dividing the studied time span into a convenient number of time steps. If, instead, the analytical method is used only to know the fragment density at a given time, a time step equal to the whole time span can be used, further reducing the time of the analytical propagation.

From the data in Figure 2.20 it is possible to observe a reduction of the computational time equal to 52% for a simulation of five years. This suggests the analytical approach can be an efficient tool to simulate different collision scenarios. In addition, it is important to highlight that the reduction in the computational time is only part of the advantages in terms of the use of computational resources. In fact, the formulation in spatial density allows the information of a fragmentation to be stored in a file of limited size compared to the case when the value of the orbital parameters of all the fragments need to be saved. This means that *expensive* cases with tens or hundreds of thousands of objects are generated on high performance computing systems but their results, expressed in spatial density, can be saved into file whose size is *manageable* on normal machines both in terms of RAM and physical memory. This allows the study of the impact of a simulated fragmentation on a different set of targets in a very fast way as it will be shown in Chapter 3.

2.7.2 Measure of the method accuracy

Four possible indicators of the method accuracy where considered:

- err_{peak}, which measures the relative error of the peak height, comparing the maximum density value for the analytical n_A and numerical propagation n_N,

$$\text{err}_{\text{peak}} = \frac{|\max(n_A) - \max(n_N)|}{\max(n_N)} \tag{2.50}$$

[9] Observe here that the numerical propagation has a large overhead as the time to launch the integration and propagate the fragments for 90 days up to the band formation requires a computational time (11.32 s) equal to 41.1% of the total computational time for five years of integration (28.15 s). In the case of the propagation up to band formation, 90% of the computational time is spent inside the MATLAB built-in function `ode45`. In general, the codes are only partially optimised in terms of performance as it was preferred to maintain a high level of readability (e.g. with an extensive use of structures).

- err_{tot}, which measures the relative error of the total number of fragments obtained by integrating the density curve

$$\text{err}_{\text{tot}} = \frac{|\int n_A \, dh - \int n_N \, dh|}{\int n_N \, dh}. \tag{2.51}$$

- err_{prof}, which measures the mean absolute error between the two density profiles

$$\text{err}_{\text{prof}} = \frac{\int |n_A - n_N| \, dh}{\int n_N \, dh}. \tag{2.52}$$

- R^2, the coefficient of determination, which in statistics indicate how well the data (n_N) fit a model (n_A); in formulas, indicating with n_F the number of fragments, and with j a point in the altitude grid

$$\begin{gathered} \bar{n}_N = \frac{1}{n_F} \sum_{j=1}^{n_F} n_{N,j} \quad SS_{\text{tot}} = \sum_j (n_{N,j} - \bar{n}_N)^2 \quad SS_{\text{res}} = \sum_j (n_{N,j} - n_{A,j})^2 \\ R^2 = 1 - \frac{SS_{\text{res}}}{SS_{\text{tot}}}. \end{gathered} \tag{2.53}$$

The first metric, err_{peak}, is a local property, whereas the other three consider the global shape of the density profile. This means that the error on on the peak in itself can be a misleading figure because it can be very low for curves with similar maximum value but different peak location. For this reason, its value is meaningful only when the global metrics are small. The second metric, err_{tot}, is the one with the strongest connection with the physics of the problem, but it also has the disadvantage that, in theory, it could be equal to zero even if the compared curves have different profiles, but the same integral. For this reason, the third metric was preferred to evaluate the method accuracy as errors in different directions do not compensate themselves. Observe that the indicator err_{prof}, differently from err_{peak} and err_{tot}, is not a relative error as its meaning is closer to a mean squared error. Finally, it was observed that R^2 and err_{prof} give consistent results, so only the former will be shown in the following. As it will be clarified later in this Section, the method is considered applicable when both the value of err_{peak} and the one of err_{prof} are below 0.2. This corresponds to a good visual agreement between the density profiles obtained with the two different propagation method and a value of err_{tot} lower than 5%. Alternative evaluations of the accuracy may be based on the estimation of the decayed objects.

It is important to highlight that the error between the analytical and the numerical propagation is due to two factors:

1. the difference between the spatial distribution of fragments and the density profile obtained from the *fitting* procedure (Section 2.3),
2. the error due to the propagation method in itself (Section 2.4).

Moreover, if the method is used to study a specific breakup, more runs of the NASA breakup model may be required to obtain a reliable representation of the initial condition. The next sections will try to highlight the contribution to the error from the different sources and the sensitivity of the results to the run of the NASA breakup model.

2.7.3 Example case: fragmentation at 800 km

The comparison presented here refers to the case studied in Section 2.6, a fragmentation generated by the non-catastrophic collision with energy of $50\,\mathrm{kJ}$, on an equatorial and circular parent orbit, with altitude equal to $800\,\mathrm{km}$. The collision generates 2397 fragments and the band is considered formed at $T_B = 95$ days; the analytical propagation is applied defining 10 bins in A/M.

Figure 2.21 compares the results between the numerical and the analytical propagation, using the expression of the spatial density introduced in Section 2.3. The grey bars indicate the distribution obtained from the numerical propagation of the fragment generated by averaging ten runs of the breakup model. The initial condition for the analytical method is built starting from the average distribution at the band formation. Figure 2.21 shows how the analytical propagation follows the evolution of the cloud density very well, correctly representing the reduction of the spatial density due to drag.

The results with a single run of the breakup model are very similar, as shown in Figure 2.22: also in this case, the analytical propagation follows the global evolution of the cloud very well. It is also possible to observe that the distribution obtained from the numerical propagation is less *smooth* than the one in Figure 2.21. This does not happen for the analytical method because, as explained in Section 2.3, building the initial condition with the expressions for the spatial density in Equation 2.24 makes the method less sensitive to the random parameters in the NASA breakup model. This result suggests that the density profile built on a single run of the breakup model can be considered representative of the fragmentation event without requiring to run the breakup model multiple times.

Figure 2.23 shows the evolution of the error defined in Section 2.7.2 for the case with a single run of the NASA breakup model. Focussing in particular on the evolution of $\mathrm{err}_{\mathrm{prof}}$, it is possible to notice that the error is already *high* at the band formation, meaning a major contribution to the error is given by the difference between the spatial distribution of the fragments and the density profile obtained with the *fitting*. This is related to the *smoothing* behaviour of the analytical method described in Figure 2.22 and it, therefore, suggests that a proper validation of the method should be done, using multiple runs of the NASA breakup model, as it will be shown later in this Section.

Finally, Figure 2.24 shows in detail the propagation of each A/M bin: for the sake of clarity, the number of A/M bins was reduced to four in this case. The colours refer to

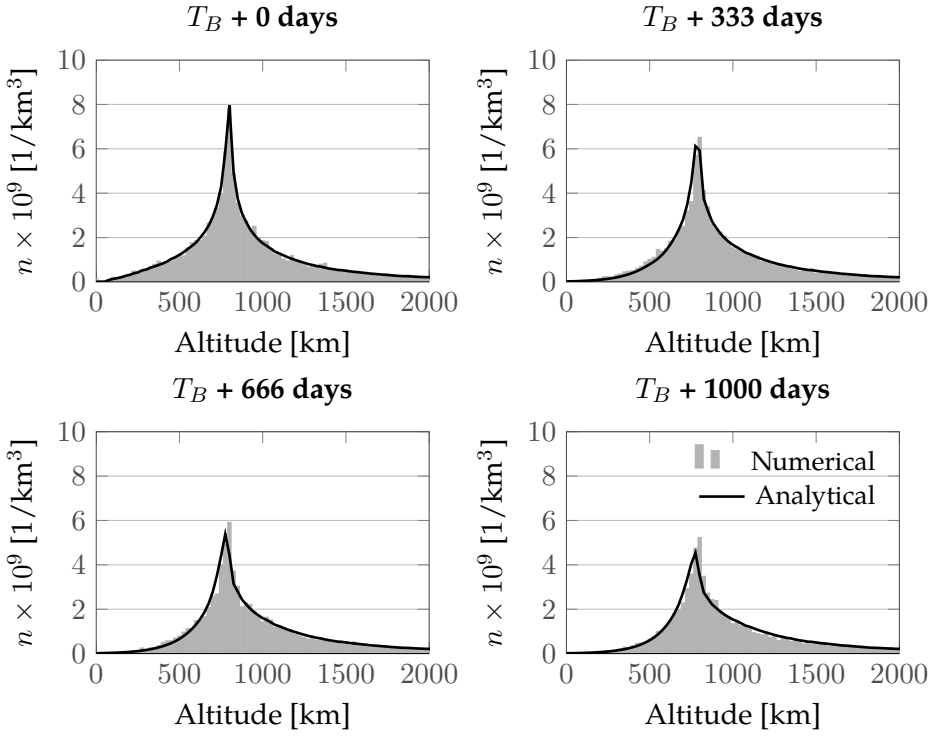

Figure 2.21: Fragment spatial density for a fragmentation at 800 km, for multiple runs of the NASA breakup model.

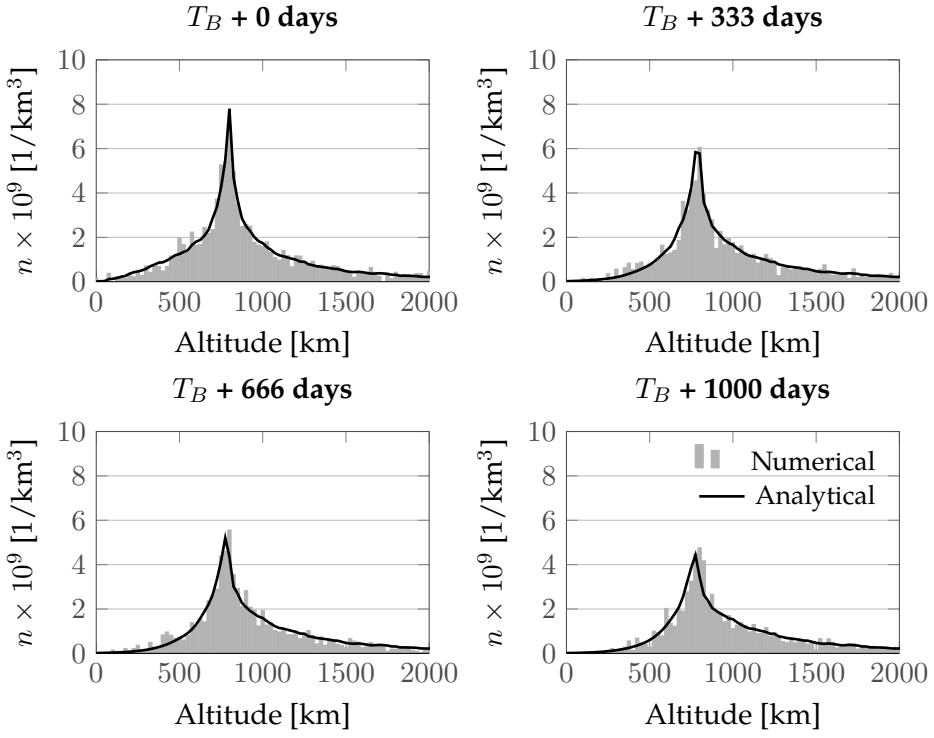

Figure 2.22: Fragment spatial density for a fragmentation at 800 km, for a single run of the NASA breakup model.

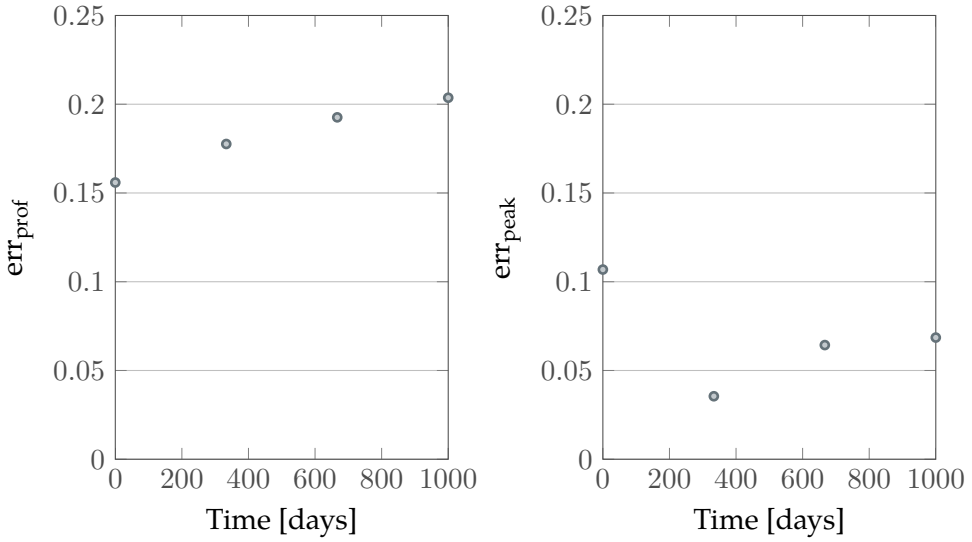

Figure 2.23: Evolution of the cloud density as a function of time after the band formation, for a fragmentation at $800\,\mathrm{km}$.

different values of the area-to-mass ratio; solid lines indicate the result of the numerical propagation, dashed lines the analytical one. It is possible to observe that the analytical model performs quite well in all the bins, even if its accuracy decreases for high A/M bins. This is due to the fact that high A/M bins correspond to a high mean eccentricity, so the hypothesis of circular orbits, required to write v_r as in Equation 2.37, introduces a certain level of error. The issues associated with this hypothesis are discussed in Chapter 2.8, but it is interesting to observe here that the dependency of mean eccentricity on the area-to-mass ratio is a product of how the velocity distribution is written in the NASA breakup model (Johnson and Krisko, 2001).

2.7.4 Range of applicability

The applicability of the method was tested varying the initial orbit of the impacted spacecraft, both in inclination and in altitude. When not differently specified, the results refer to ten runs of the NASA breakup model. The runs are averaged summing the number of fragments in the same altitude bin over the different runs and dividing the total number by the number of runs.

Figure 2.25 shows the value of errors after 1000 days from the band formation for inclinations ranging from 0 to 90 degrees: the value is always lower than 0.15, so the method follows correctly the cloud evolution for all the inclination values.

The applicability of the analytical method was also evaluated at different altitudes. For the validation, ten runs of the breakup model are used to simulate a fragmentation; the resulting debris cloud is followed up to 1000 days after the band formation, when the difference with the numerical propagation is measured.

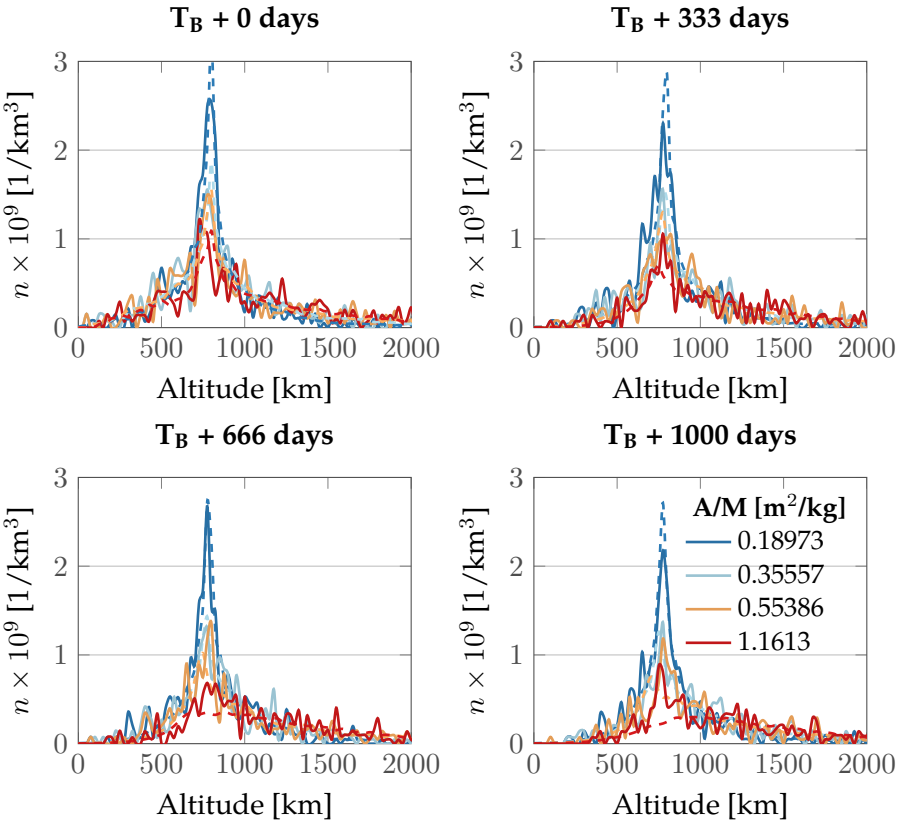

Figure 2.24: Evolution of the cloud density as a function of time after the band formation, for a fragmentation at 800 km. The colours refer to different values of the area-to-mass ratio; solid lines indicate the result of the numerical propagation, dashed lines the analytical one. Each bin contains the same number of fragments.

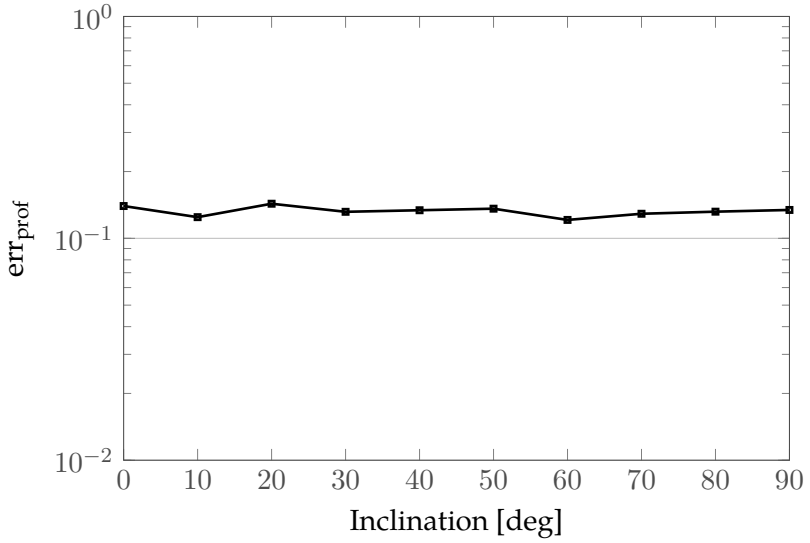

Figure 2.25: Accuracy of the method, measured by the relative error after 1000 days from the band formation, as a function of the inclination of the orbit where the fragmentation occurs (with fixed altitude equal to 800 km).

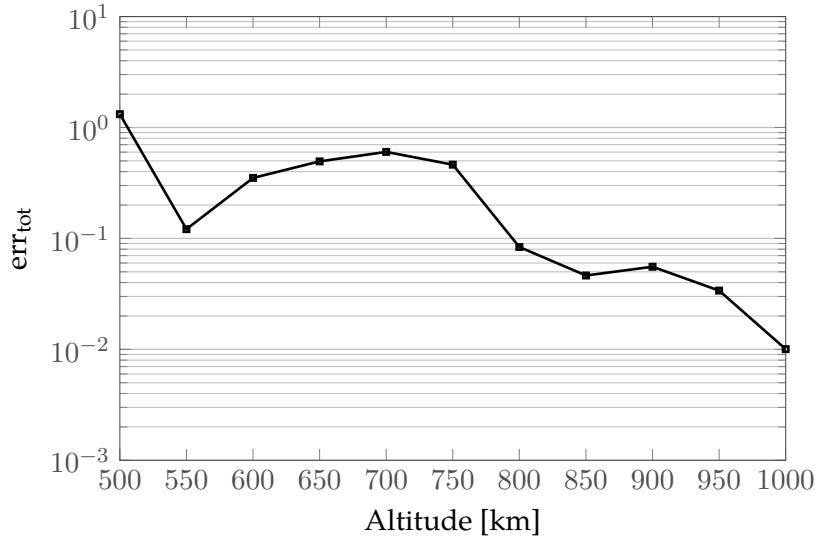

Figure 2.26: Accuracy of the method, measured by $\mathrm{err}_{\mathrm{tot}}$ after 1000 days from the band formation, as a function of the altitude of the orbit where the fragmentation occurs (with fixed inclination equal to 0°).

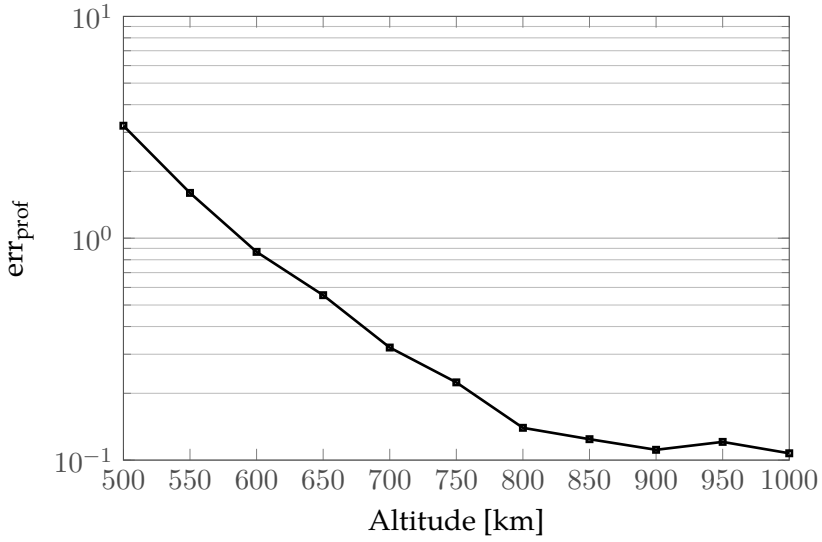

Figure 2.27: Accuracy of the method, measured by $\mathrm{err}_{\mathrm{prof}}$ after 1000 days from the band formation, as a function of the altitude of the orbit where the fragmentation occurs (with fixed inclination equal to 0°).

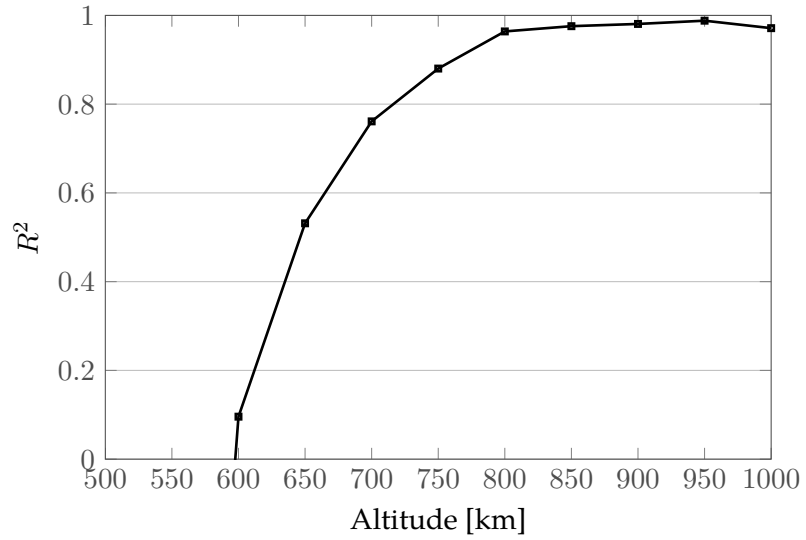

Figure 2.28: Accuracy of the method, measured by R^2 after 1000 days from the band formation, as a function of the altitude of the orbit where the fragmentation occurs (with fixed inclination equal to 0°).

The result of the validation is shown in the Figures 2.26, 2.27, 2.28 where, respectively, the value of err_{tot}, err_{prof}, and R^2 for different values of the collision altitude are shown to demonstrate the equivalence of their results as anticipated at the beginning of the Section. In particular, from Figures 2.27 and 2.28 one can observe how the accuracy of the method is good only for altitudes equal or larger than $800\,\text{km}$, where err_{prof} is always lower than 0.15 and R^2 above 0.95[10]. This region of LEO is actually very interesting for space debris studies as it is the one where the debris density is highest and where future events may be expected (Rossi et al., 2015a). The region is also where important remote sensing missions with large spacecraft are operating from sun-synchronous orbits. At these altitudes, the effect of solar radiation pressure also becomes relevant for the debris motion, therefore an extension of the present model may aim to include this effect in the analytical propagation.

At lower altitudes, even for very small values of eccentricity, the analytical method presents a large error. This is de to the fact that the hypothesis of circular orbits for the fragments introduces an unacceptable error on the results because the effect of drag is different along an orbit as will be discussed in Section 2.8. An extension of the method to include the effect of the eccentricity in the analytical propagation is presented in Chapter 4.

Focussing on the altitude range where the method accuracy is acceptable, it is interesting to study how the results of the analytical propagation depend on the breakup model. It was observed that, in the case of the analytical propagation, the results obtained with a single run of the breakup model seem very close to the ones obtained with multiple

[10]In the case of R^2, numbers close to 1 indicate that the profiles obtained with the two propagators are similar.

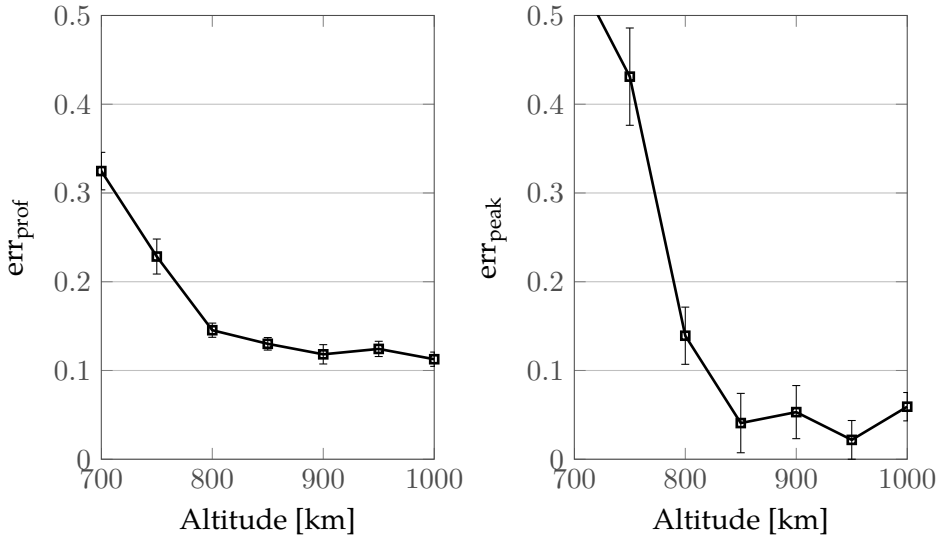

Figure 2.29: Relative error of the analytical model at different altitudes. The error is measured against the numerical propagation of a fragment cloud built averaging the output of ten runs of the breakup model; the initial condition for the analytical model is built using only the information in each single run of the breakup model. The error bars indicate, therefore, the variability of the error when different runs of the breakup model are used.

runs of the breakup model. This can be verified using the average results obtained from the multiple runs of the breakup model as a reference for the debris cloud evolution and comparing it with the predicted density profile obtained starting from a single run of the breakup model.

The results for this analysis are shown in Figure 2.29: the graph on the left refers to the error, $\mathrm{err}_{\mathrm{prof}}$, on the density profile in orbit after 1000 days; the curves on the right refer to $\mathrm{err}_{\mathrm{peak}}$. The error bars are defined by the maximum and the minimum error among the ten initial density distributions obtained with the analytical propagation and the initial condition set from only one run of the breakup model. The bars indicate, therefore, the variability of the error when different runs of the breakup model are used.

From the curve for $\mathrm{err}_{\mathrm{prof}}$ it is possible to observe that the variability with the run of the breakup model is very limited. For $\mathrm{err}_{\mathrm{peak}}$, instead, the variability seems larger, but the error is low in absolute terms. This demonstrates that the analytical model gives a reliable representation of the cloud evolution, even when a single run of the NASA breakup model is used.

Figure 2.30 shows a comparison of the density profile after 1000 days for six different collision altitudes: at low altitudes ($< 700\,\mathrm{km}$) the analytical method largely underestimates the drag effect, where the analytical method is expected to overestimate the collision probability. It is interesting to observe that the error is large in relative terms, but small in absolute terms as, for example, in the case at $500\,\mathrm{km}$ only 123 fragments are left after 1000 days and the error on the peak is of five fragments. The drag effect is,

instead, overestimated in the case at $700\,\mathrm{km}$. For all the cases at high altitudes ($\geq 800\,\mathrm{km}$) there is a very good agreement between the numerical and the analytical propagation.

As already mentioned, the threshold value for the errors was fixed at 0.2 and this limit can be used to estimate the maximum simulation time length at different altitudes. Figure 2.31 shows the result of this analysis: for a fragmentation at $500\,\mathrm{km}$ the errors are smaller than 0.2 for less than ten days; for the cases up to 700 km the maximum simulation length is always lower than six months, while for the cases at $850\,\mathrm{km}$ and higher altitudes the method is able to model the cloud evolution for more than 10 years.

In conclusion, the method accuracy is affected by the fragmentation altitude. Above $800\,\mathrm{km}$, it is accurate enough to predict the cloud evolution in the long term (more than some years); at lower altitudes, its applicability is limited to short times, but in any case it can be used as a preliminary tool to model collision scenarios as for low altitudes only a few fragments survive on the long term.

2.7.5 Results for different fragmentation energies

All the previous cases refer to a non-catastrophic collision of $50\,\mathrm{kJ}$ caused by the impact with a projectile of $100\,\mathrm{g}$ with a relative velocity of $1\,\mathrm{km/s}$ with respect to the target. These values of mass and relative velocity are on the low part of the possible values, so it is important to study the performance of the analytical method also for higher values of energy.

In particular, the case with collision energy equal to $50\,\mathrm{kJ}$ was compared with other three cases where the value of the projectile mass, its relative velocity or both were increased. The resulting density profiles are shown in Figure 2.32: the grey curve indicates the profile at the band formation, whereas the blue and the red one indicate the density profile after 1000 days from the band formation respectively using the numerical or the analytical propagation. In all cases it is possible to observe a good visual agreement between the numerical and the analytical propagation. Observe that for the case 2, with $M_p = 100\,\mathrm{g}$ and $v_c = 2\,\mathrm{km/s}$, and case 3, with $M_p = 400\,\mathrm{g}$ and $v_c = 1\,\mathrm{km/s}$, the value of fragment density is very similar because they have the same level of energy, expressed by the parameter M_e in the breakup model, and the same number of produced fragments ($N_f = 6781$). However, the collision velocity has a direct impact on the maximum variation of the fragment orbital parameters because of the saturation on the maximum ejection velocity that was set equal to 1.3 times the impact velocity (Section 2.1). For case 4, $M_p = 400\,\mathrm{g}$ and $v_c = 2\,\mathrm{km/s}$, 19179 fragments are generated.

It is useful to visualise the error for the four different cases to understand how the method accuracy depends on the fragmentation energy. Figure 2.33 shows the value of $\mathrm{err}_{\mathrm{prof}}$ at the band formation and 1000 days later for the four cases in Figure 2.32. In this case, a single run of the NASA breakup model was used and this explain why

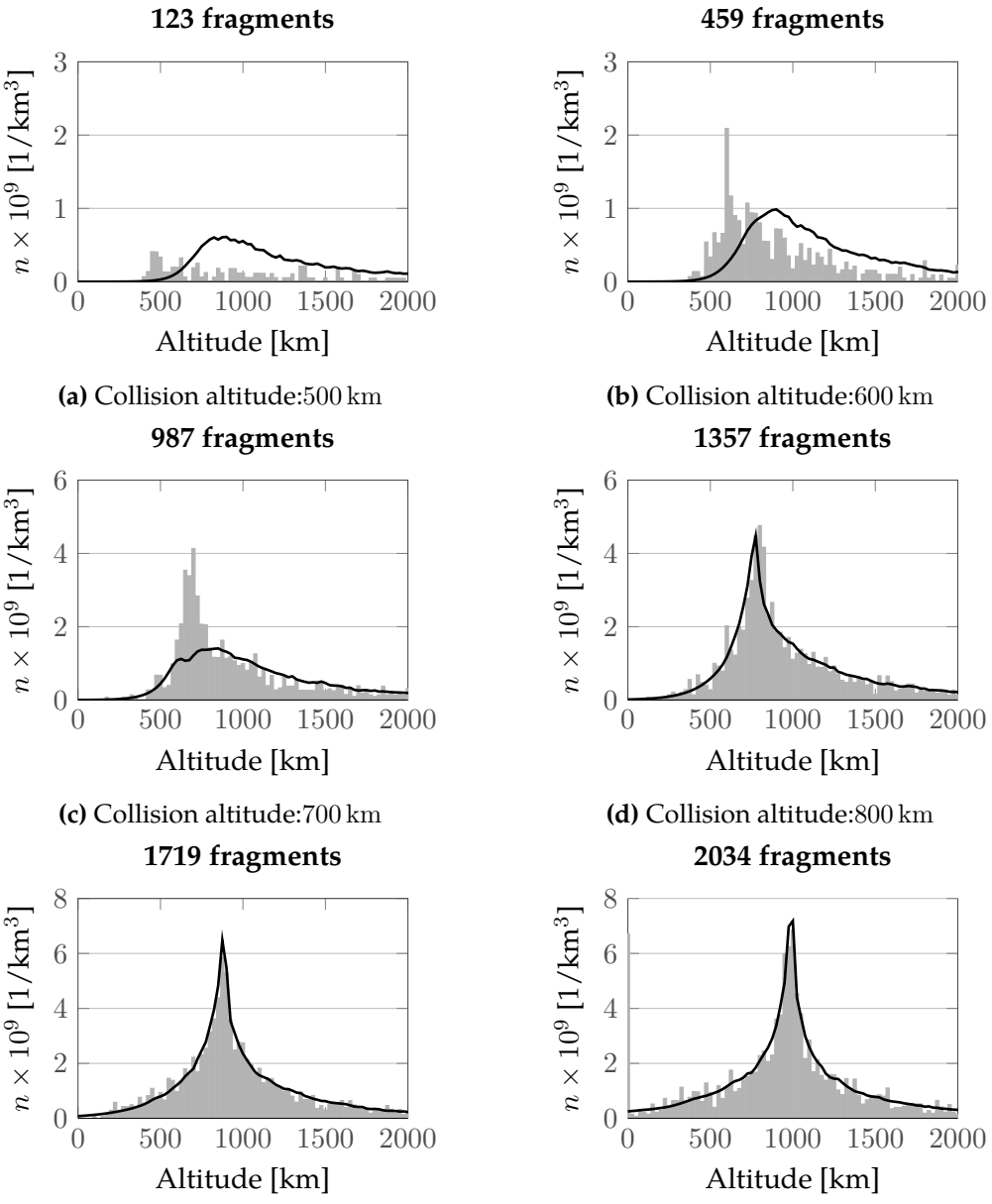

(a) Collision altitude:500 km

(b) Collision altitude:600 km

(c) Collision altitude:700 km

(d) Collision altitude:800 km

(e) Collision altitude:900 km

(f) Collision altitude:1000 km

Figure 2.30: Cloud density after 1000 days from the band formation for six different collision altitudes. The grey bar represent the result of the numerical propagation, the black line the result of the analytical propagation. The number of fragments still in orbit after 1000 days, according to the numerical propagation, is reported on top of each graph.

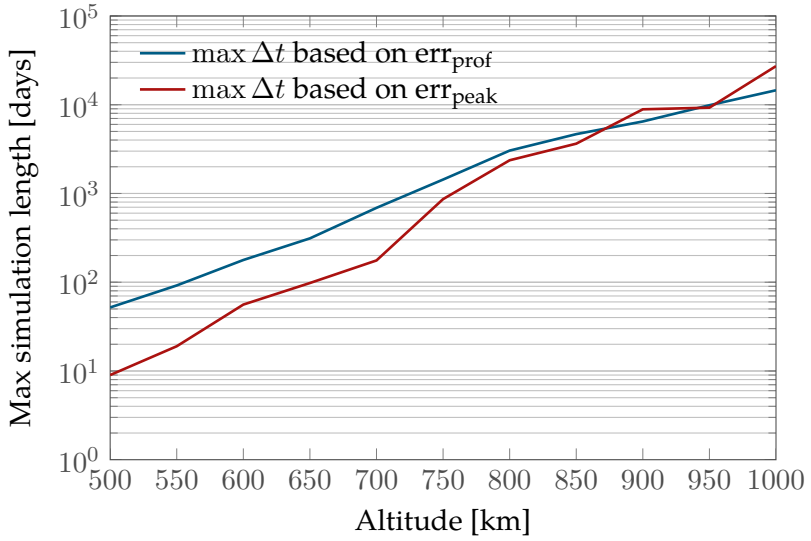

Figure 2.31: Applicability of the method, measured by the maximum simulation length, as a function of the fragmentation altitude. The maximum simulation length for each error is the one for which it becomes larger than the threshold value of 0.2.

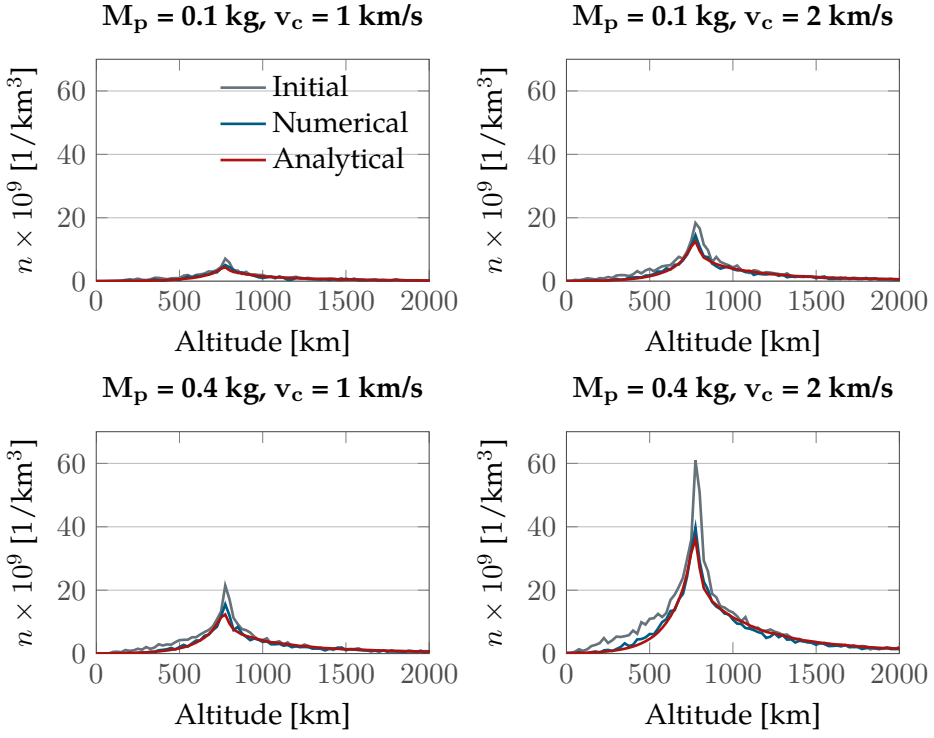

Figure 2.32: Cloud density profiles after 1000 days from the band formation for four different fragmentations at 800 km.

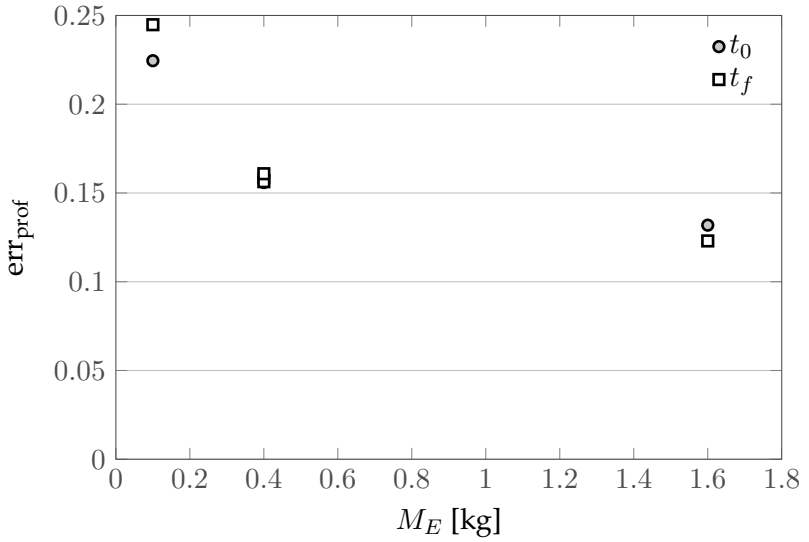

Figure 2.33: Dependence of $\mathrm{err}_{\mathrm{prof}}$ on the collision energy M_e at the time of band formation (t_0) and after 1000 days (t_f). Single run of the breakup model.

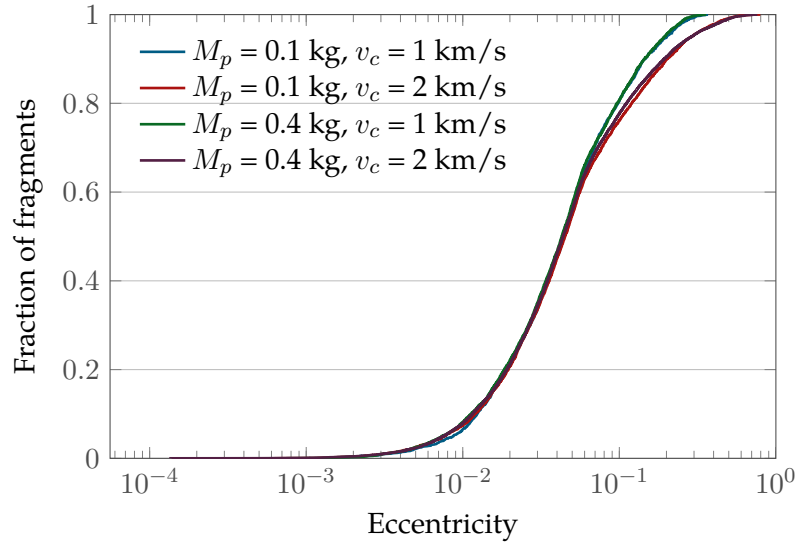

Figure 2.34: Eccentricity distribution among the fragments after the breakup for four different fragmentations.

the error for the case with $M_e = 0.1\,\mathrm{kg}$ is higher than the values in Figure 2.27. From Figure 2.33 one can observe a clear dependence of the error on the fragmentation energy; in particular, the higher the energy, the lower the error. This can be explained by the fact that the higher the energy the larger the number of produced fragments, and so the analytical method is more efficient in representing the fragment distribution. The role of the number of fragments is confirmed by two factors:

- the two cases with the same energy (and then same fragment number), but different projectile mass and velocity have the same level of error,
- the dependence of the error on the energy is already present at the band formation.

The result that the method accuracy improves for larger values of energy was not fully expected. In fact, if the collision velocity increases, also the maximum variation of the orbital parameters, including the eccentricity, increases. If a large fraction of the fragments have eccentricity very different from zero, then the accuracy of the method could be affected as the long term propagation of the cloud density is obtained with the hypothesis that the fragments are on circular orbits.

However, Figure 2.34 shows that the eccentricity distribution among the fragments is quite similar for the four tested cases. Even if the maximum value of eccentricity depends on the impact velocity (0.8 for $v_p = 2\,\mathrm{km/s}$, 0.4 for $v_p = 1\,\mathrm{km/s}$), the empirical cumulative distribution functions of the studied cases are practically identical up to $e = 0.06$, so up to 60% of the fragments in the cloud. The fraction of fragments with $e > 0.1$ is around 20% for all the cases; in the case with $v_p = 2\,\mathrm{km/s}$ just a small 3% of the fragments have eccentricity between 0.4 and 0.8, and this percentage does not seem to affect the accuracy of the method. Future work may investigate if there is a limit in the increment of energy so that the large variation of the orbital parameters start to become detrimental to the method accuracy.

2.7.6 Results for an explosion case

Finally, the analytical method was applied to describe a different kind of fragmentation event, an explosion. According to the NASA breakup model (Johnson and Krisko, 2001), the number of fragments larger than a certain size L_c is equal to

$$N_f(L_c) = 6S\left(L_c[\mathrm{m}]/1[\mathrm{m}]\right)^{-1.6} \tag{2.54}$$

where S is a non-dimensional empirical factor between 0.1 and 1. $S = 1$ is used to model the explosions of upper stages with masses between 600 and $1000\,\mathrm{kg}$; $0.1 < S < 1$ is used to model other explosions, but no further details on the value of S are available in literature.

$S = 1$ was used in this application, so the resulting number of generated fragments with size between $1\,\mathrm{mm}$ and $10\,\mathrm{cm}$ is equal to $378\,335$. This number is much larger than in the case of the *weak* non-catastrophic collision studied in Sections 2.7.3 and 2.7.4 and this caused some issues in terms of the numerical simulation of the trajectory of each fragments. This process requires, in fact, a large amount of RAM and it was not possible to run the simulation on a standard workstation equipped with 16GB of RAM. Instead, IRIDIS, the high performance computing facility of the University of Southampton, was used for this simulation. The full numerical propagation of the cloud required 40 minutes on IRIDIS using 12 processors with 4GB of RAM each; the computational time for the analytical method is instead less than two minutes, with 1.6

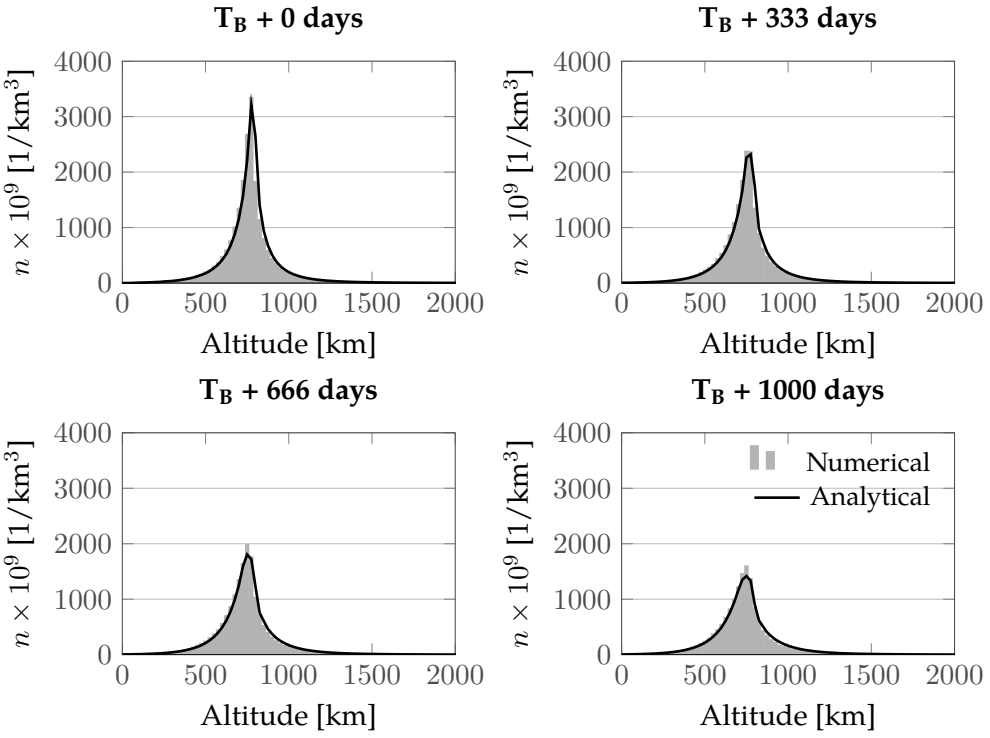

Figure 2.35: Fragment spatial density for an explosion at 800 km. The grey bar represent the result of the numerical propagation, the red line the result of the analytical propagation.

minutes for the propagation up to the band formation and 1.46 seconds for the long term propagation.

The results for this case are shown in Figure 2.35: also in this case the analytical method matches very well with the output from the numerical propagation. In particular, both err_{prof} and err_{peak} are equal to 0.11 after 1000 days from the band formation. This low level of error can be explained by two factors, each one connected to the two sources of error discussed in Section 2.7.2. First, as anticipated in Section 2.1, explosions tend to produce fragments with lower relative velocity than collisions. In particular, the peak in the velocity distribution is at $60\,\mathrm{m/s}$ for the explosion in Figure 2.35, whereas it is around $380\,\mathrm{m/s}$ for the non-catastrophic collisions studied in Sections 2.7.3 and 2.7.4. A lower relative velocity means that the fragments are in orbits with lower eccentricity and so they are closer to the hypothesis of circular orbits introduced in the analytical propagation. The second factor that explains the low level of error is the high number of fragments generated by the explosion; this contributes to reduce the difference between the spatial distribution of the fragments and the density profile obtained from the *fitting* process.

In conclusion, the results for the explosion case are important because they demonstrate that the analytical approach can be applied to any fragmentation event; they also show that the analytical approach is robust to the choice of the breakup model as similar level

of accuracy are reached for different fragment distributions. Moreover, this analysis confirms that the modelling of a non-catastrophic collision of $50\,\mathrm{kJ}$ is the most demanding scenario among the tested ones. For this reason, the *weak* non-catastrophic collision is used also in the following as a benchmark to evaluate the method applicability.

2.8 Effect of the model hypotheses

The results in Section 2.7.4 clearly show that the method accuracy reduces for low fragmentation altitudes and this practically sets a limit on the method applicability. Considering a limit of 0.2 on accuracy indicators, the analytical approach is applicable at altitudes higher than $800\,\mathrm{km}$. To understand what affects the method's accuracy at low altitudes, it is useful to analyse the method hypotheses and their effect. Based on this analysis, an improvement to the method will be developed in Chapter 4.

Two assumptions were introduced to obtain the analytical solution in Equation 2.43:

1. the fragments are on circular orbits (Equation 2.37),
2. the radial distance of the fragments can be approximated with a fixed distance in the square root in the expression for the radial velocity (Equation 2.42).

The contribution of each hypothesis is studied in Figure 2.36, where the variation in the semi-major axis after one period due to drag is plotted as a function of the semi-major axis. The plot is obtained considering that, starting from the altitude where the fragmentation occurs (in this case $R_h = R_E + 500\,\mathrm{km}$), it is possible to compute the maximum eccentricity that a fragment can have, given the semi-major axis of its orbit. In fact, all the fragments' orbits must include the point of fragmentation, which, in the two extreme cases, can be the apogee (Figure 2.36a) or the perigee (Figure 2.36b) of the fragment orbit. The maximum eccentricity is then the one associated with one of these two extreme cases: the fragmentation altitude is at the apogee for fragments with semi-major axis lower than the one of the parent orbit, whereas the fragmentation altitude is at the perigee for fragments with semi-major axis higher than the initial one

$$e_{\max} = \begin{cases} 1 - \frac{R_h}{a}, & a \geq R_h \\ \frac{R_h}{a} - 1, & a < R_h \end{cases}. \tag{2.55}$$

Knowing both the initial semi-major axis and the eccentricity, the altitude decay of the fragment in one period can be computed (Equations 2.2), using as a reference a value of the area-to-mass ratio equal to $0.5\,\mathrm{m^2\,kg^{-1}}$. Figure 2.36 shows the variation of the semi-major axis in one orbit as a function of the orbit semi-major axis for the fragments produced by a fragmentation at $500\,\mathrm{km}$; the vertical lines indicate the eccentricity.

The different colours indicate different hypotheses in the computation of the fragment decay, whereas the dashed/solid lines refer to different hypotheses on the atmospheric

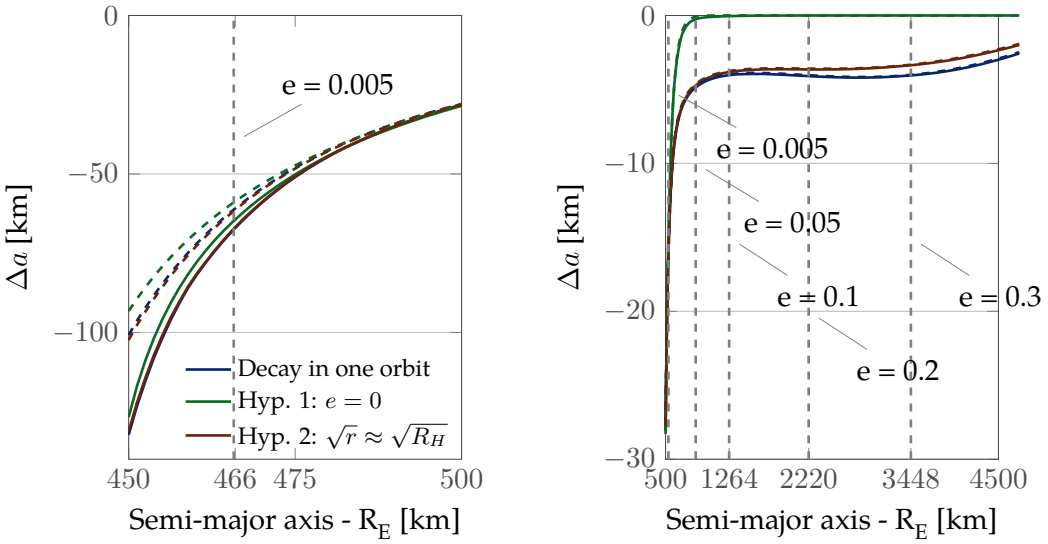

Figure 2.36: Variation of the semi-major axis in one orbit as a function of the orbit semi-major axis with different hypotheses for the integration, considering a fragmentation at $500\,\mathrm{km}$. The vertical lines refer to eccentricity values. (a) refers to semi-major axis values lower than the fragmentation altitude, (b) to higher semi-major axis values. The vertical lines refer to eccentricity values.

model. The dashed lines are obtained with the hypothesis that R_h, ρ_0, H are computed at the fragmentation altitude and then kept constant for the whole simulation, as explained in the method description in Chapter 2. The solid lines refer to the integration updating at each time step the parameters of the atmosphere, considering the actual value of the fragment altitude.

The blue curve indicates the variation of the semi-major axis a obtained through numerical integration of Gauss' equations for a and the eccentricity e. The blue dashed line is, therefore, the reference curve that represents the results of the numerical propagation used to validate the analytical one.

The red curve is obtained through numerical integration of Gauss' equations for a and the eccentricity e, but assuming $\sqrt{r} \approx \sqrt{R_h}$: as shown in Figure 2.36, this hypothesis introduces a small but acceptable error as already found by McInnes (2000), who estimated that the expression of the characteristic lines is accurate to order 1×10^{-2} for altitudes below $1000\,\mathrm{km}$.

The green curve represents the effect of the hypothesis $e = 0$, which is the integration only of

$$v_r = -\varepsilon\sqrt{a}\exp\Big(-\frac{a - R_h}{H}\Big), \tag{2.56}$$

and it is possible to observe that the fragment decay is underestimated, both at high and at low altitude. This is due to the fact that neglecting the eccentricity in the exponential term corresponds to applying an incorrect value of the density to compute the drag effect.

In fact, using only the value of the semi-major axis, the information on the passage with low perigee, given by the eccentricity, is lost and the predicted decay is zero.

For example, for a fragment with semi-major axis equal to $R_E + 1000\,\mathrm{km}$ and corresponding eccentricity equal to 0.007, Gauss's equations estimate a reduction of the semi-major axis of $4.40\,\mathrm{km}$ in 94 minutes. Introducing the approximation $\sqrt{r} \approx \sqrt{R_h}$, the predicted decay is $4.24\,\mathrm{km}$, so the relative error is less than 4%. On the other end, with the hypothesis of circular orbits, the predicted decay is almost zero ($0.11\,\mathrm{km}$) and so the effect of drag on the cloud is largely underestimated.

This effect is stronger at low altitudes where a small variation in altitude results in a larger variation in density compared to what happens at higher altitude; in other words, at low altitudes the eccentricity value above which the decay is strongly underestimated is lower than at high altitude.

This can be verified by plotting the variation of the atmospheric density ρ for two orbits with the same low eccentricity (e.g., $e = 0.01$) and different semi-major axes, as shown in Figure 2.37. The x-axis represents the angular coordinate from the perigee to apogee; the y-axis indicates the relative error between the actual density value computed with the exponential model and the value of ρ at an altitude equal to the semi-major axis, such as it is done in the analytical model with the hypothesis of circular orbit. For the case at low altitude, the relative error arrives up to 2, so Equation 2.56 cannot be considered a good representation of the cloud evolution.

One could expect drag to affect the eccentricity distribution in such a way that the average eccentricity is reduced with time because of the progressive circularisation of the orbits. Actually, as shown in Figure 2.38, drag reduces the number of fragments, but especially

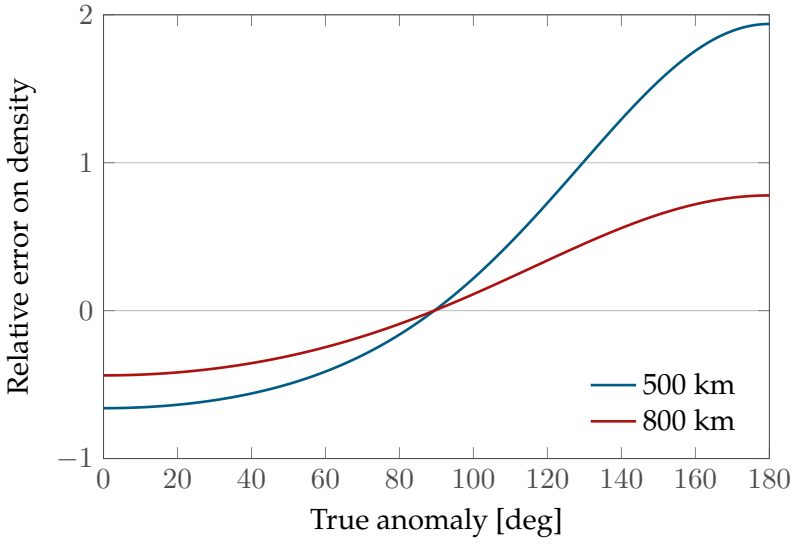

Figure 2.37: Relative error on the atmospheric density along one orbit for two non-circular orbits ($e = 0.01$).

those with low eccentricity as they also have low semi-major axis. The fragments with high eccentricity instead also have high energy and their decay is slow; their presence drives the average eccentricity to increase (for example, in the case in Figure 2.38 from 0.05 to 0.08). This means that the error due to eccentricity always increases with the simulation time.

This observation can be extended to all altitudes value; moreover, it is also interesting to observe how the eccentricity distribution is affected by the fragmentation altitude. Figure 2.39 shows the quantiles of the eccentricity distribution for different altitudes after 1000 days since the band formation. In general, 75% of the fragments have an eccentricity value lower than 0.15, but the value is dependent on the altitude as at low altitudes, as seen in the previous case in Figure 2.38, the fragments with low eccentricity decay more quickly.

Summary

The proposed analytical method, CiELO, is formed by four main building blocks. The generation of the fragments due to a collision or an explosion is described through a breakup model that defines how the energy of the fragmentation event is distributed among the fragments and specifies their characteristics (e.g. mass, size). In this work,

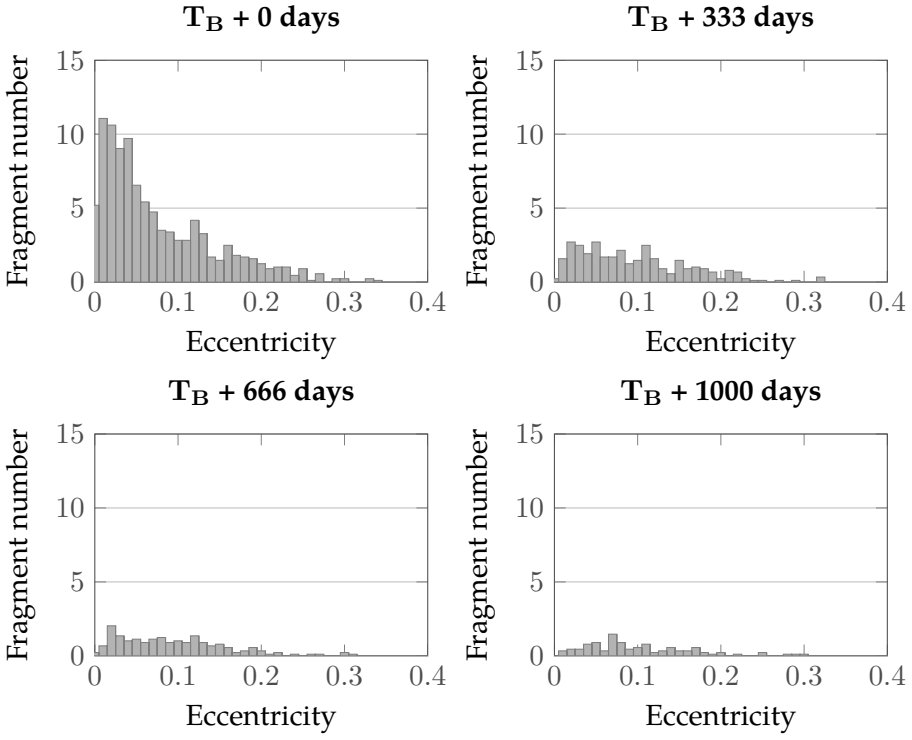

Figure 2.38: Evolution of the eccentricity distribution as a function of time, after the band formation, for a fragmentation at $500\,\mathrm{km}$.

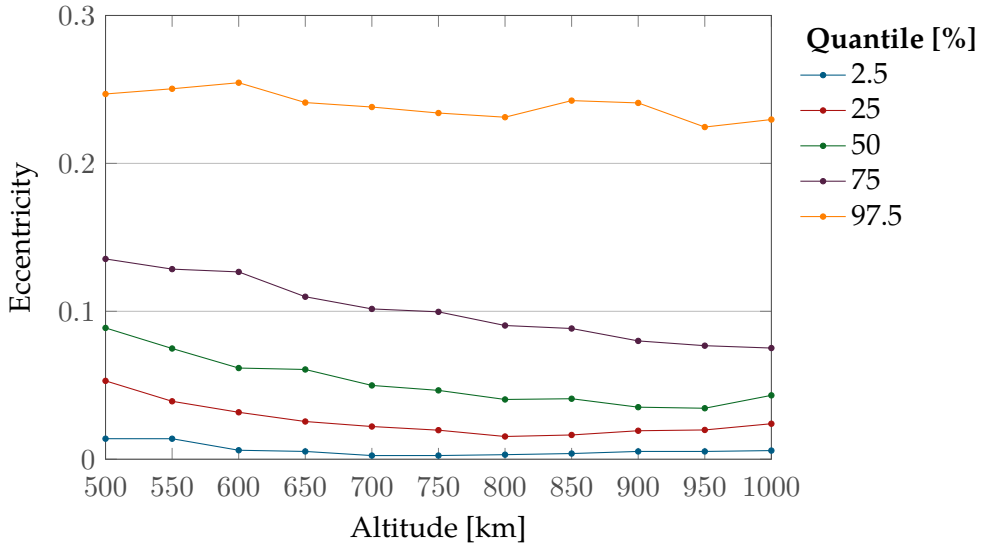

Figure 2.39: Quantiles of the eccentricity distribution as a function of the altitude, 1000 days after the band formation, for a fragmentation at 500 km.

the NASA breakup model (block 1) is used considering only the fragment with size between 1 mm and 10 cm. Once the fragments are generated, their orbital parameters are numerically propagated (block 2) to model the short initial phase of the cloud evolution when the Earth's oblateness has the dominant effect. The numerical propagator is based on semi-analytical techniques and each fragment trajectory is considered separately. The numerical propagation implemented in the code models the secular effect of the Earth's oblateness, considering the J_2 term only, and the effect of the atmospheric drag, considering the average variation of the parameters along one orbit. In particular, the effect of drag is implemented on different orbital regimes in terms of eccentricity. The numerical propagation is stopped once the fragments are spread and form a band around the Earth. The time required to form a band around the Earth can be estimated through some expressions available in literature that provide a stop criterion that does not require any continuous check on the fragment propagation. Once the fragments form a band around the Earth, it is possible to change the point of view from the single fragments to the whole cloud. This requires the conversion of the information on the position of all the fragments into a continuous density function (block 3). Different approaches are possible here, depending on the use of distribution functions or fitting functions, which give the best results. The long term evolution of the cloud is obtained by applying the continuity equation to model the effect of the atmospheric drag (block 4). Assuming that the system can be considered spherically symmetrical, it can be studied through only one coordinate, the radial distance from the Earth r. Using an exponential model for the atmosphere and assuming that the fragments are in quasi-circular orbits it is possible to obtain an analytical formulation for the evolution of the fragment spatial density with time. The analytical method was used to model the resulting fragment spatial density after a collision. It allows the effective visualisation of the persistence of the fragments

in orbit depending on their initial energy. It is also able to show the different evolution of the profile density for low and high values of area-to-mass ratios.

The performance of the analytical model was assessed through the comparison with the results obtained using a numerical propagator such as the one used to follow the fragments' trajectories from the breakup to the band. The performance was evaluated both in terms of computational time and accuracy. For what concerns the computational time, a reduction larger than 50% was observed for the simulated case. Moreover, the formulation in spatial density allow the information on the fragmentation to be stored in a more efficient way than saving the state of each fragment at each time step. Therefore, the analytical method requires not only less computational time, but also less memory. The accuracy of the method was measured by two indicators. The first, $\mathrm{err}_{\mathrm{prof}}$, measures the mean error between the integral of the density profile obtained with the analytical approach and the numerical one. The second indicator, $\mathrm{err}_{\mathrm{peak}}$, measures, instead, measures the relative error between the peaks of the two curves. These indicators were chosen because together they provide information on the ability of the analytical method to capture both the global shape of the density profile and its most important local feature.

Different fragmentations were simulated to assess the method accuracy. Different values of the collision energy were also simulated as well the case of an explosion: for all these cases the larger the number of fragments, the lower the error. It was found that the fragmentation inclination has no substantial influence on the accuracy whereas the fragmentation altitude has a large impact. In fact, the error becomes large at low altitude, limiting the method applicability to fragmentations at $800\,\mathrm{km}$ and above. It was shown how this error is related to the hypothesis that all fragments are on circular orbits.

Part of the content of this Chapter was published in F. Letizia, C. Colombo, and H. G. Lewis. Collision probability due to space debris clouds through a continuum approach. Journal of Guidance, Control, and Dynamics*, 2015i. doi: 10.2514/1.G001382. Accessed 10 September 2015.*

3

Collision probability through a fragment cloud

The analytical approach can be used to describe the evolution of a fragment cloud, so it can be applied to study how the cloud affects the collision probability for near spacecraft. In particular, the proposed analytical method will be applied to study the consequences of fragmentations occurring on orbits with any inclination and altitude between 800 and $1000\,\mathrm{km}$. The comparison with the numerical propagation, described in Section 2.7, has shown that this is the region where the analytical method can be applied with a good level of accuracy for simulations over several years. This region of space is particularly interesting because it presents the highest density of space debris population (so it is reasonable to study fragmentations originating from this region).

The consequences of a fragmentation are evaluated considering the resulting collision probability for spacecraft crossing the cloud. This requires a way to relate the fragment spatial density to the collision probability for the target spacecraft and it will imply estimating the relative velocity between the target and the fragment cloud. Most of the following analysis will consider only cases when the fragment band has already reached the band configuration and, therefore, the long term effect of a fragmentation is here studied. Moreover, only the debris density related to small fragments, between $1\,\mathrm{mm}$ and $10\,\mathrm{cm}$, is considered.

3.1 Analogy with gas kinetic theory

The collision probability for a spacecraft crossing a fragment cloud can be computed following the analogy with the kinetic gas theory (McKnight, 1990; Su and Kessler, 1985a). According to this analogy, the collisions between a target and a background population, such as fragments in a cloud, can be modelled similarly to the collisions among molecules within an inert gas (Jenkin, 1996). The collision probability is then obtained by modelling the collisions as a Poisson process.

The use of Poisson process to model *rare events* is very common as it can be demonstrated that the probability that an event with low success probability occurs in a given interval of time Δt is a Poisson process with rate λ, if certain hypotheses are respected (Ross, 2013). Using N_E to indicate the number of events in the time interval $\Delta t = [0, t]$ (divided in subintervals Δt_H), the hypotheses are the following:

1. $N_E(0) = 0$,
2. the numbers of events occurring in non-overlapping time intervals are independent or, in other words, what happens in a time interval has no impact on what happens in another non-overlapping time interval,
3. the probability of collision during a certain time interval is proportional to the length of the time interval and not on its position along the considered time span,
4. $P\{N_E(\Delta t_H) = 1\} = \lambda \Delta t_H + o(\Delta t_H)$, the probability of exactly one event occurring in a given time interval of length Δt_H is equal to $\lambda \Delta t_H$ plus a quantity that is *small* compared to Δt_H,
5. $P\{N_E(\Delta t_H) \geq 2\} = o(\Delta t_H)$, the probability of multiple events happening in a certain time interval is *small*.

In the case of a debris cloud, hypothesis 2 can be translated into assuming that the motion of the fragments is random. This means, as highlighted by Jenkin (1996), that this method should not be used in the first phases of the cloud evolution, when the fragments' trajectories are highly correlated. In this application, as anticipated, the focus will be mostly on the phase when the fragments have reached the band configuration, so the analogy is applied at a late stage of the cloud evolution, when the motion of the fragments has already been randomised. Hypothesis 3 can be related with having a large enough number of fragments, so that the cloud can be considered as a continuum.

The parameter λ is a constant that needs to be determined and it is set in such a way that $\lambda \Delta t$ is equal to number of collisions N in the time interval Δt. It is computed similarly to what is done for inert gases, considering the volume swept by the target in a given Δt

$$N = n(r, t) \Delta v \sigma_c \Delta t \tag{3.1}$$

where $n(r,t)$ is the value of the fragment spatial density, Δv is the average relative velocity between the targets and the fragments, and σ_c the collisional cross-sectional area (Chobotov, 2002; Jenkin, 1996; Kessler, 1981). The product $\Phi = n(r,t)\Delta v$ is often indicated as the flux of particles. The approach in Equation 3.1 has been criticized, for example by Chan (2008), who observed that the spatial density of the fragments and the mean free path of the target have a very different ratio in the case of gases and in the one of space debris. In any case, other approaches to compute of collision probability, such as the one proposed by Chan (2008), are applicable if they are based on a dependence of the number of collisions on the fragment spatial density.

Observe that this method also assumes that there is no interaction among the objects in the cloud. In particular, collisions among the fragments in the cloud are not considered. It is useful to remind that the propagation method based on the continuity equation may take into account this contribution through the term $\dot{n}^+$ in Equation 2.28 as done by McInnes (1993).

Once that an expression for the rate $\lambda = N/\Delta t$ of the Poisson process is obtained, it is possible to write the probability of collision considering that for a Poisson process

$$P\{N_E(\Delta t) = 0\} = \mathrm{e}^{-N}, \tag{3.2}$$

which expresses the probability that no event (collision) occurs in the considered time interval. Therefore, the cumulative collision probability for the target spacecraft in the time interval Δt is equal to

$$p_c(t) = 1 - \exp(-N) = 1 - \exp(-n(r,t)\Delta v \sigma_c \Delta t). \tag{3.3}$$

The parameter σ is usually defined considering the dimensions of both the colliding objects (Kessler, 1981), but here only the target spacecraft area A_T is considered because the fragments are much smaller than it, so $\sigma_c \approx A_T$. The relative velocity Δv needs to be estimated without having information on the orbital parameters of the single fragments, but knowing only their spatial density $n(r,t)$, obtained with the CiELO method described in Chapter 2, and the fact that the fragments are randomised in ν, ω, Ω. A method to estimate the relative velocity Δv is discussed in detail in Section 3.3. For what concerns the spatial density $n(r,t)$, as anticipated, it is obtained from the analytical propagation, so only its dependence on the altitude is retained, whereas, in reality, the distribution of fragments may depend also on the latitude. Section 3.2 explains why the dependence on the latitude can be neglected for long term studies of the collision probability.

3.2 The role of latitude in the long term propagation

As stated in Section 2.3, the correct representation of the cloud spatial density also requires to consider the distribution in latitude. However, in this work a constant distribution in latitude is assumed, similarly to what was done by Kessler (1990). This approximation is chosen because the purpose of this method is to study the long term (i.e. years) effect of a fragmentation, whereas the latitude of a target spacecraft crossing the cloud evolves in a much shorter time scale (i.e. hours). Following the target latitude would require very short time steps for the integration, vanishing or reducing the advantage of having a fast propagator for the fragment cloud.

This approach was criticised by Hujsak (1993) as it masks the difference between two satellites crossing the same fragment cloud, but having different orbital inclinations. Assuming that both the orbits are completely inside the fragment cloud, the spacecraft with the highest inclination will spend a longer time in zones with high spatial density, compared to the one with low inclination. It is, therefore, important to note that the analytical method is also able to deal with the distribution in latitude. In fact, applying the general solution for a 2D formulation of a continuity equation problem to the current application, the expression for the density (Equation 2.43) can be written as

$$\tilde{n}(r,\beta,t) = \tilde{n}_0(r_i,\beta_i)\frac{v_r(r_i,\beta_i)v_\beta(r_i,\beta_i)}{v_r(r,\beta)v_\beta(r,\beta)} \tag{3.4}$$

where $\tilde{n}_0$ is the initial distribution, r_i, β_i are functions obtained by inverting the characteristic lines at initial time $t = 0$, v_r, v_β are respectively the expression of dr/dt and $d\beta/dt$ due to the effect modelled by the continuity equation, i.e., drag. Therefore in this case, where the effect of drag on quasi-circular orbits is considered,

$$\frac{dr}{dt} = -\varepsilon\sqrt{R_H}\exp\left(\frac{r-R_H}{H}\right) \tag{3.5}$$

$$\frac{d\beta}{dt} = 0 \tag{3.6}$$

meaning that v_r depends only on r and the distribution in latitude is not directly affected by drag. As a result, Equation 3.4 can be written as

$$\tilde{n} = \tilde{n}_0(r_i,\beta)\frac{v_r(r_i)}{v_r(r)}. \tag{3.7}$$

The expression for $\tilde{n}_0(r_i,\beta_i)$ is simply the ones discussed in Section 2.3, given, among others, by Kessler (1981) and Sykes (1990)

$$\tilde{n}_0(r_i,\beta_i) = S(r_i,\beta) = s(r_i)f(\beta) \tag{3.8}$$

and finally

$$\tilde{n}(r,\beta,t) = f(\beta)\frac{s(r_i)v_r(r_i)}{v_r(r)}. \tag{3.9}$$

Similarly to what is done for $s(r)$ in Section 2.3, $f(\beta)$ can be built from the distribution of the fragments at the time of band formation.

In this work, as explained before, the choice was not to follow the evolution of the target latitude: what is relevant for the study is knowing if the target spacecraft is inside or outside the fragment band, as visualised in Figure 3.1a; if the spacecraft is inside, the collision probability is computed using an average value of the fragment density, which depends only on the distance and not on the latitude.

Initially, the average density value was computed through the integral average of $f(\beta)$ on its domain

$$\begin{aligned}\bar{f}_{\text{lin}} &= \frac{1}{2\beta_{\text{max}}}\int_{-\beta_{\text{max}}}^{\beta_{\text{max}}} f(\beta)\,\mathrm{d}\beta \\ &= \frac{1}{2\beta_{\text{max}}}\int_{-\beta_{\text{max}}}^{\beta_{\text{max}}} \frac{2}{\pi}\frac{1}{\sqrt{\cos^2\beta - \cos^2\beta_{\text{max}}}}\,\mathrm{d}\beta\end{aligned} \tag{3.10}$$

where β_{max} is the maximum latitude covered by the band, which, as will be shown later, is related to the fragmentation inclination. This integral can be solved using the non-diverging expression for f proposed Kessler (1981) and so

$$\bar{f}_{\text{lin}} = \frac{1}{\sin\beta_{\text{max}}}. \tag{3.11}$$

This value can be alternatively obtained considering the geometry of the problem. In fact, the volume of the band can be obtained by subtracting from the volume of the sphere ($V_{\text{sph}} = \frac{4}{3}\pi r^3$) two spherical sectors whose spherical caps have height equal to η ($V_{\text{sec}} = \frac{2}{3}\pi r^2\eta$). η can be related to the angle β_{max} (Figure 3.1b)

$$\eta = r - r\sin(\beta_{\text{max}}) \tag{3.12}$$

so that the final expression for the band volume is

$$\begin{aligned}V_{\text{band}} &= \frac{4}{3}\pi r^3 - 2\frac{2}{3}r^2 r(1-\sin\beta_{\text{max}}) = \frac{4}{3}\pi r^3\sin\beta_{\text{max}} \\ &= V_{\text{sph}}\sin\beta_{\text{max}}.\end{aligned} \tag{3.13}$$

At this point, $\bar{f}_{\text{lin}}$ can be computed again, now with the meaning of a scaling factor between the two volumes,

$$\frac{V_{\text{sph}}}{V_{\text{band}}} = \frac{1}{\sin\beta_{\text{max}}} = \bar{f}_{\text{lin}}. \tag{3.14}$$

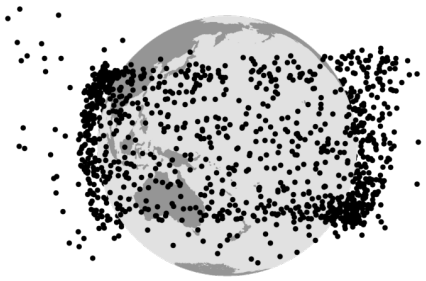

(a) Fragment band

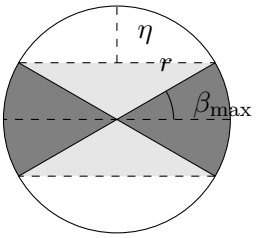

(b) Geometry of the band volume

Figure 3.1: Fragment band and its geometrical description.

This approach, which seems validated by the geometrical observation in Equation 3.14, would give a correct scaling factor only if β had a linear evolution with time. As this is not true, the correct dependence of β on time should be considered and the average density value should be found by computing once the integral average of $f(\beta)$ over one orbital period. This factor can then be used to rescale the spatial density at any time, applying again the hypothesis that the fragments' and the target's inclinations are not changing. The dependence of the latitude β on the orbital parameters is expressed by

$$\beta = \arcsin\left(\sin\left(\omega + \nu\right)\sin i\right) \tag{3.15}$$

where ω, ν, i refer to the argument of perigee, the true anomaly and the inclination of the target spacecraft crossing the cloud. Introducing the argument of latitude $u = \omega + \nu$ and writing the expression for the case of circular orbit, the scaling factor of the spatial density can be computed as

$$\bar{f} = \frac{1}{\pi^2}\int_{-u_{\max}}^{u_{\max}} \frac{\mathrm{d}u}{\sqrt{\cos^2\left(\beta(u)\right) - \cos^2\left(\beta_{\max}\right)}} \tag{3.16}$$

where $\beta(u)$ is given by Equation 3.15. $\beta_{\max}$ is the maximum latitude covered by the band. For non-equatorial orbits, $\beta_{\max}$ is set equal to the inclination where the fragmentation occurs i_F if $i_F \leq \pi/2$ and equal to $\pi - i_F$ otherwise. This follows from the band characterisation proposed by McKnight (1990) and the observation that, with the current hypotheses (e.g. non-rotating atmosphere), the fragment inclination is not affected by drag and is thus constant. For equatorial orbits, $\beta_{\max}$ is set equal to the maximum inclination reached by the fragments due to the breakup.[1] $u_{\max}$ is equal to π if $i_T \leq i_F$; $u_{\max} = \arcsin\left(\sin(\beta_{\max})/|\sin i_T|\right)$ otherwise.

This approach was tested by performing a simulation where the spatial density and the collision probability ($p_{c,f(\beta)}$) are computed considering the dependence on the latitude

[1] This can be done for any inclination of the parent orbit. This approach was compared, for different inclinations, with the results obtained setting the maximum covered latitude equal to the parent orbit inclination. The latter gives actually a distribution closer to the observed one and is, therefore, implemented.

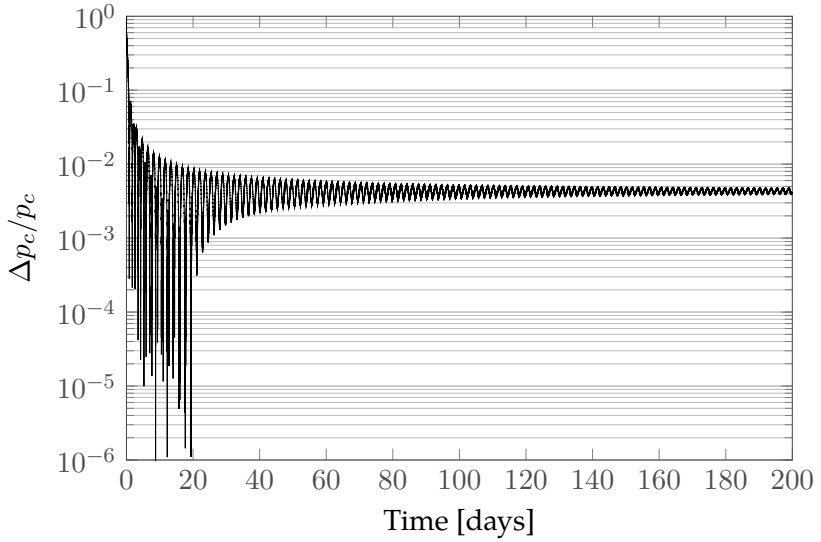

Figure 3.2: Relative error on the collision probability due to the averaging in latitude for a simulation case with $i_T = i_F = 60$ degrees.

and using a very short time step, equal to five minutes.[2] In this way, for each target orbit there are at least 20 integration points and the value of β can be considered representative of the time-step. This result is compared to the simulation run with a time step equal to one day, where only the dependence on the geocentric distance is considered and the scaling factor from Equation 3.16 is applied. The collision probability obtained in this way is indicated with $p_{c,\bar{f}}$.

The result of the comparison is presented in Figure 3.2: it shows the relative error

$$\frac{\Delta p_c}{p_c} = \frac{|p_{c,\bar{f}} - p_{c,f(\beta)}|}{p_{c,f(\beta)}} \tag{3.17}$$

introduced by Equation 3.16 on the collision probability. The simulation refers to a target with inclination equal to $i_T = 60$ degrees crossing a cloud generated from an orbit with equal inclination ($i_F = 60$ degrees). It is possible to observe how the difference between the two methods is limited, with the relative error that oscillates around a value equal to 0.004. Therefore, Equation 3.16 is an effective way to model the long term evolution of the collision probability without following the target latitude. This is shown in Figure 3.3 where the evolution of $\bar{f}$ as a function of i_F, for a fixed i_T, is shown. When $i_T > i_F$, the target spends only a part of its orbit within the cloud; the part is lower and lower for decreasing values of the inclination of the orbit where the fragmentation occurred. In this configuration, the target always crosses the part of the cloud with the highest density (with respect to the variation in latitude). When $i_T < i_F$ the target is always inside the fragment band, but as i_F increases, the target is farther from the region with

[2]Observe that using this large number of points results in a remarkable increase in the RAM required to run the simulation in a such a way that a high-performance computing cluster was required for this validation. If the analytical method is instead used on a normal machine, then a reasonable, higher, time-step needs to be chosen.

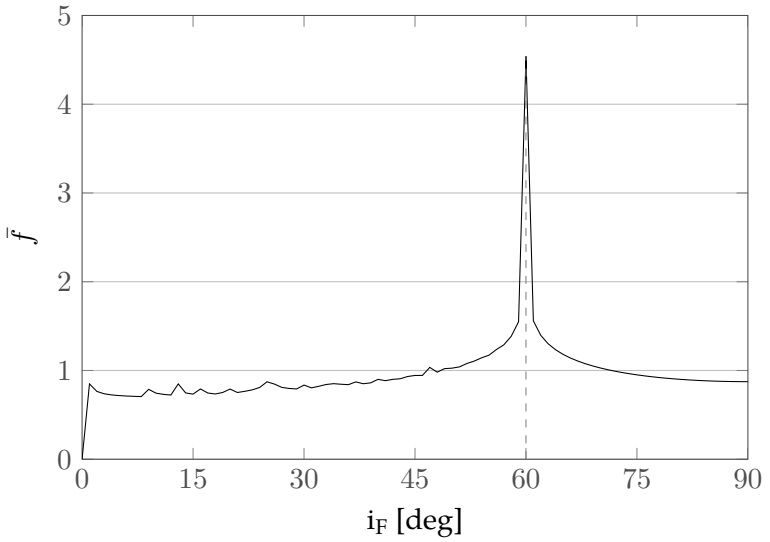

Figure 3.3: Variation of $\bar{f}$ with the fragmentation inclination i_F for a fixed target inclination equal to 60 degrees.

the highest fragment density. When $i_F = i_T$ the target is always inside the fragment band and it crosses the region with the maximum density, so $\bar{f}$ reaches the highest value. In this way, the remark by Hujsak (1993) on how the target inclination affects its collision probability is addressed. For this reason, this approach will be used in the following results where the spatial density is always computed as $S(r) = \bar{f}s(r)$.

3.3 Collision velocity estimation

To keep the formulation simple and dependent only on the radial distance, a set of hypotheses is introduced to obtain the expression of the relative velocity Δv. If a single fragment is considered, Δv can be obtained from the rule of cosines

$$\Delta v^2 = v_T^2 + v_F^2 - 2v_T v_F \cos\phi \tag{3.18}$$

where v_T and v_F are respectively the orbital velocities of the target and of the fragment with respect to the central body; ϕ is the angle between the two vectors $\mathbf{v_T}$ and $\mathbf{v_F}$. v_T is known from the propagation of the target trajectory; v_F is a piece of information that is lost with the analytical propagation. However, the propagation of the fragment cloud is done under the hypothesis of quasi-circular orbits, so

$$v_F \approx v_{\text{circ}} = \sqrt{\frac{\mu_E}{r}}. \tag{3.19}$$

The angle ϕ can be related to the geometry of the two orbits. In fact, the intersection between two circular orbits with the same radius can be represented by the spherical triangle in Figure 3.4 where B is the ascending node of the target orbit and C the ascending

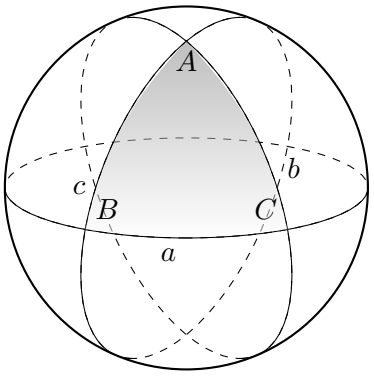

Figure 3.4: Generic spherical triangle.

node of the fragment orbit. Therefore,

$$B = i_T \quad C = \pi - i_F; \tag{3.20}$$

also $a = \Delta\Omega$, so the spherical triangle can be solved with the law of cosines to find the angle A

$$\cos A = \sin B \sin C \cos a - \cos B \cos C \tag{3.21}$$

$$= \sin(i_T) \sin(i_F) \cos(\Delta\Omega) + \cos(i_T) \cos(i_F) \tag{3.22}$$

Equation 3.22 can be used to provide a unique value of ϕ for a given configuration of target and fragments in terms of their inclinations. Given that Ω is uniformly distributed among the fragments, the average relative velocity $\Delta\bar{v}$, can be found computing the integral mean of the function

$$\Delta v = \sqrt{v_T^2 + v_F^2 - 2v_T v_F \left[\sin(i_T) \sin(i_F) \cos(\Delta\Omega) + \cos(i_T) \cos(i_F)\right]} \tag{3.23}$$

for $\Delta\Omega$ from 0 to 2π. By setting

$$\chi = v_T^2 + v_F^2 - 2v_T v_F \cos(i_T) \cos(i_F) \qquad \eta = 2v_T v_F \sin(i_T) \sin(i_F) \tag{3.24}$$

the average value of the relative speed can be written as

$$\Delta\bar{v} = \frac{2}{\pi}\sqrt{\chi + \eta}\, \mathrm{E}\left[\frac{2\eta}{\chi + \eta}\right], \tag{3.25}$$

where $\mathrm{E}[x]$ is the complete elliptic integral of the second kind. $\mathrm{E}[x]$ is implemented in MATLAB by the function `ellipke`, which can be evaluated with different values of tolerance. A trade-off analysis between the computational time and the accuracy was performed leading to the choice of the tolerance equal to 1000ϵ, with ϵ the machine epsilon. For this value of tolerance, a single evaluation of $\mathrm{E}[x]$ requires 3.8×10^{-5} s and the relative error compared to the value with tolerance equal to ϵ is lower than 0.9×10^{-12}.

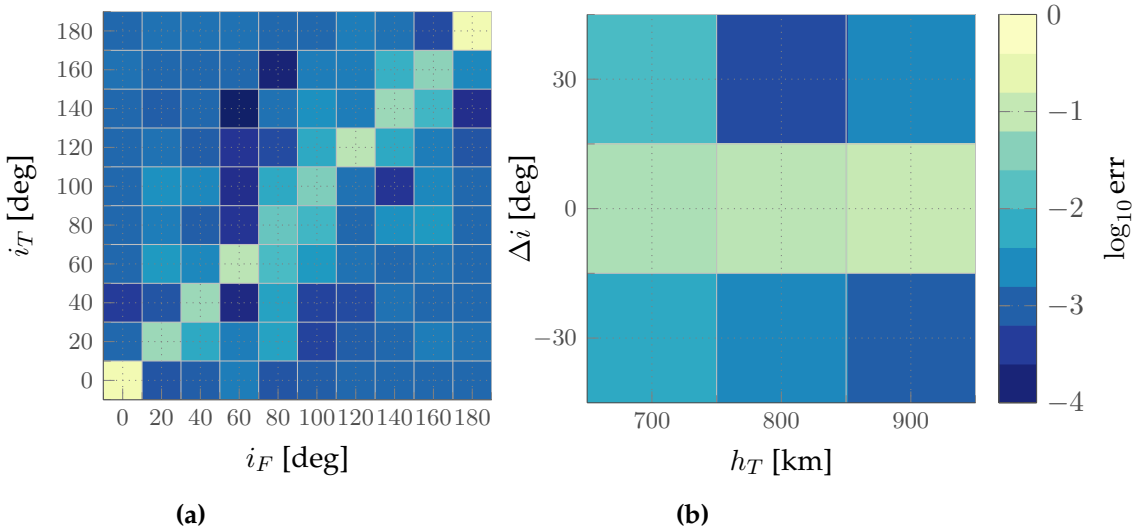

Figure 3.5: Relative error in the estimation of the relative velocity between target and fragments for several configurations with variation (a) in inclination and (b) in altitude.

The approximation for Δv was validated for different geometries of the target and fragment orbits. The results of the validation are shown in Figure 3.5, where the metric used to measure the method accuracy is

$$\overline{\text{err}}_{\text{rel}} = \frac{\int |\Delta v_A - \Delta v_N| \, \mathrm{d}t}{\int \Delta v_N \, \mathrm{d}t}, \tag{3.26}$$

where Δv_N is the estimation of the velocity obtained using a numerical procedure that computes the distance and the relative velocity between the target and each fragment as explained in Appendix A.3; Δv_A is the analytical estimation obtained from Equation 3.25. Basically, Equation 3.26 measures if the analytical approximation is able to capture the average value of the relative velocity, which is considered to be the most relevant parameter in a long-term study of the collision probability.

Figure 3.5a refers to different combinations of inclinations for the target (i_T) and the fragments (i_F), while their initial altitude is the same and equal to 800 km. As one could expect, Equation 3.25 does not work for equatorial orbits, where $\Delta\Omega$ is not defined; for those cases $\overline{\text{err}}_{\text{rel}} \approx 0.3$, whereas it is lower than 0.08 for all the other cases.

Figure 3.5b shows the results for different choices of the orbit inclinations, with $\Delta i = i_F - i_T$, and of the target altitude, with the fragmentation starting again at 800 km. Also in this case the error is generally low, but it tends to increase with the altitude difference for orbits with the same inclination. In addition, it was verified that $\overline{\text{err}}_{\text{rel}}$ is lower than 10% for all cases discussed in the rest of the Chapter.

Finally, it is interesting to compare the numerical and the analytical methods for the relative velocity also in terms of computational time. The numerical procedure is explained in details in Appendix A.3, but it can be summarised by saying that, at each time step,

the code identifies which fragments can intersect the target orbit based on a filter that computes their perigee and apogee. Then the geometrical intersection between the two orbital planes is derived, finding the nodal line, where the velocity of the two objects is measured. In other words, the used *numerical* procedure approximates the search for the minimum distance between two orbits checking only along the nodal line. This avoids introducing any numerical algorithm to find the zero (or the minimum) of a function, keeping the method purely geometrical. Nevertheless, checking the intersections between the target orbit and the thousand fragment orbits requires around $0.5\,\mathrm{s}$ at each time step for a fragmentation with 2397 fragments[3]. This means that when the relative velocity is computed for simulations for five years with a time step equal to 1.5 days, the numerical method requires around $647\,\mathrm{s}$, whereas the analytical method uses only $0.17\,\mathrm{s}$[4]. In other words, the time required by the numerical method for one step is the same that would be required by the analytical one to estimate the relative velocity for 15.5 years of simulation with a time step of 1.5 days. These figures demonstrate very clearly the advantage of adopting an analytical method based on a formulation in terms of spatial density: whereas for the propagation of a fragment cloud the difference in the computational time between the numerical and the analytical methods is small in absolute terms, but when the collision probability is computed the difference becomes noticeable.

3.4 Collision probability computation

Thanks to the analytical estimation of the relative velocity, it is now possible to compute the average number of collisions N in a time interval Δt as in Equation 3.1

$$N = n\Delta v A_T \Delta t$$

and the resulting collision probability as in Equation 3.3

$$p_c = 1 - \exp(-N).$$

The target mass and size were set considering the average values among possible targets (Rossi et al., 2013); in particular,

$$A_T = 11\,\mathrm{m}^2 \quad M_T = 2322\,\mathrm{kg}.$$

The propagation of the target starts from the moment when the fragment band is formed. Some examples of the results obtained during the validation process are presented in

[3] on a PC with 4 CPUs at 3.40 GHz; in this case the code is not parallellised

[4] both the values are obtained as average on five cases and refer to the time for the computation of the relative velocity only, not considering the time for the density propagation.

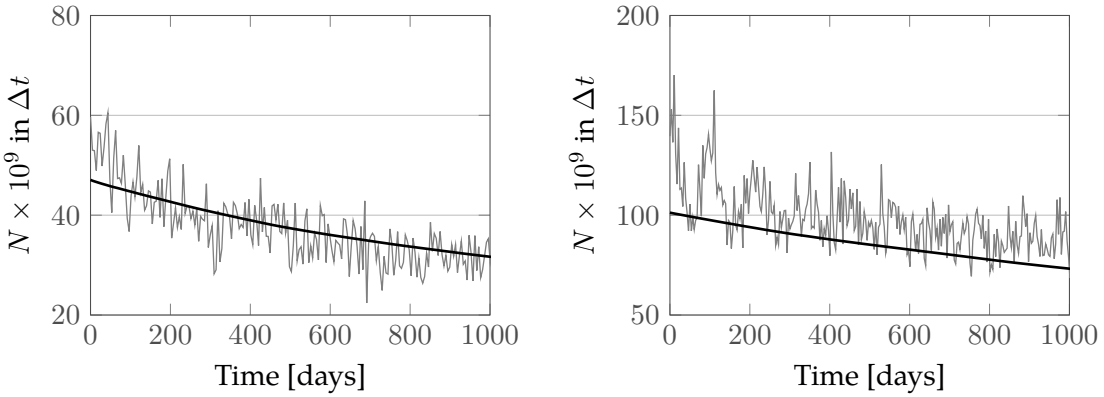

(a) F(30,800)T(30,800), $\Delta v = 4.744\,\mathrm{km/s}$.

(b) F(60,800)T(90,800), $\Delta v = 9.905\,\mathrm{km/s}$.

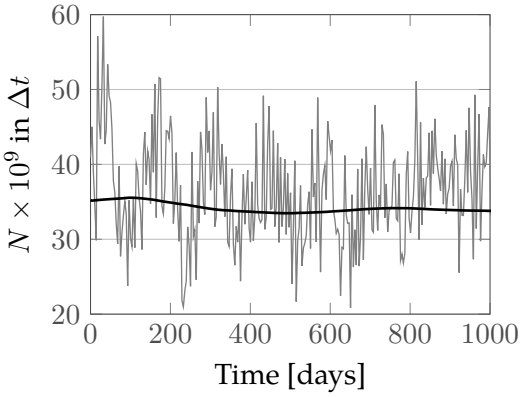

(c) F(60,800)T(30,700), $\Delta v = 7.618\,\mathrm{km/s}$.

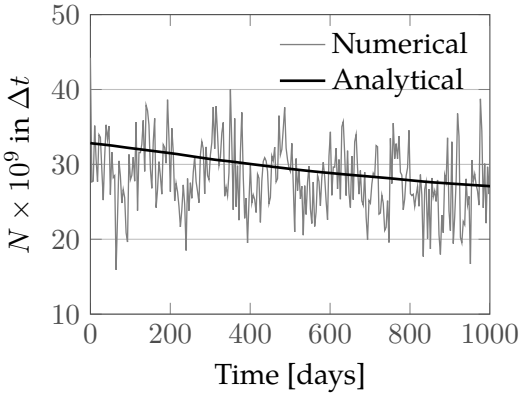

(d) F(60,800)T(30,900), $\Delta v = 7.565\,\mathrm{km/s}$.

Figure 3.6: Comparison between the number of collisions estimated with the numerical propagation (in grey) and with the analytical one (in black). The time is measured from the instant of band formation.

Figure 5.4, which shows the distribution of the relative velocity Δv among the fragments for different cases, indicated with the notation

$$\mathrm{F}(i_F,a_F - R_E)\mathrm{T}(i_T,a_T - R_E),$$

where F refers to the orbital parameters of the fragmentation parent orbit and T to the ones of the target spacecraft crossing the cloud.

Figure 3.6 shows the number of collisions N predicted by applying the analogy with the kinetic theory of gases using the value of density n and relative velocity Δv obtained from the numerical propagation (in grey) and the analytical one (in black), where the average velocity is used. Four cases with different inclinations and altitudes are shown. In all cases, as a result of the approximation of the velocity, the analytical method is able to capture the average behaviour, but not the high frequency oscillations. The oscillations derive from the relative velocity and are due to the fact that Ω is not uniformly distributed among the fragments that intersect the target orbit. The resulting difference in the cumulative collision probability is in any case minimal.

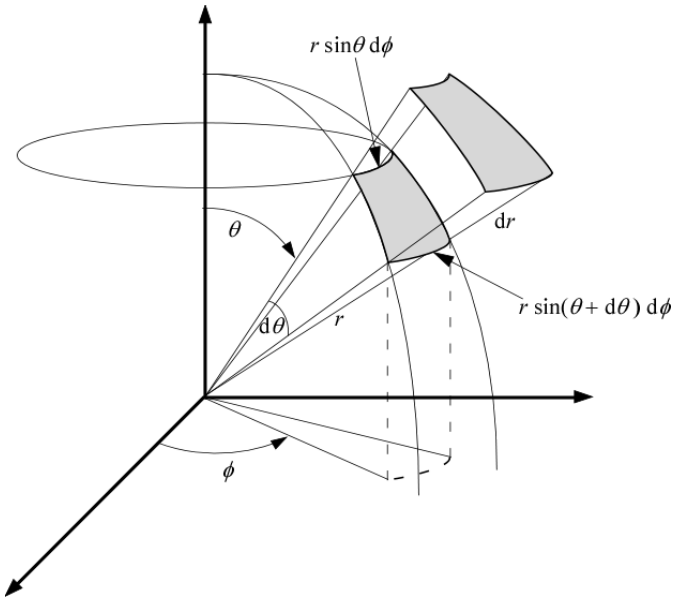

Figure 3.7: Notation and definition of the reference volume.

3.5 Collision probability before the band formation

Equation 3.3 is used to compute the collision probability after the band is formed, but one may want to apply it also in the previous phase of the debris cloud evolution. It is important to remember the recommendation from Jenkin (1996) against using the analogy with the kinetic theory of gases in the early phase of the cloud evolution, when the motion of the fragments is still highly correlated. Therefore, the results in this section will require further analysis to understand if the analogy is applicable and, if not, to identify a more suitable formulation. In this work, the interest is in understanding how to express a value of spatial density from the numerical propagation and whether the method to compute the relative velocity is applicable also before the band formation.

The value of spatial density can be obtained from the numerical propagation in the following way. As the numerical propagation of the fragments is performed in terms of the evolution of their orbital parameters, the first step is to convert the orbital parameters into spherical coordinates (r, φ, β). The domain of integration is then divided in a grid in (r, φ, β) and the number of fragments in each cell of the domain is computed. Finally, the value of spatial density is obtained by dividing the number of fragments in a cell by the volume of the cell itself.

Adopting the notation as in Figure 3.7, where $\theta = \pi/2 - \beta$, the volume of a cell is given by

$$V = \int_{\theta_-}^{\theta_+} \int_{\varphi-}^{\varphi+} \int_{r_-}^{r_+} r^2 \sin\theta \, \mathrm{d}r\mathrm{d}\theta\mathrm{d}\varphi = \left[\frac{r^3}{3}\right]_{r_-}^{r_+} [\varphi]_{\varphi-}^{\varphi+} [-\cos\theta]_{\theta_-}^{\theta_+} \tag{3.27}$$

where $\theta = \frac{\pi}{2} - \beta$ and the values of the extremes of integrations depend on the grid used to discretise the domain.

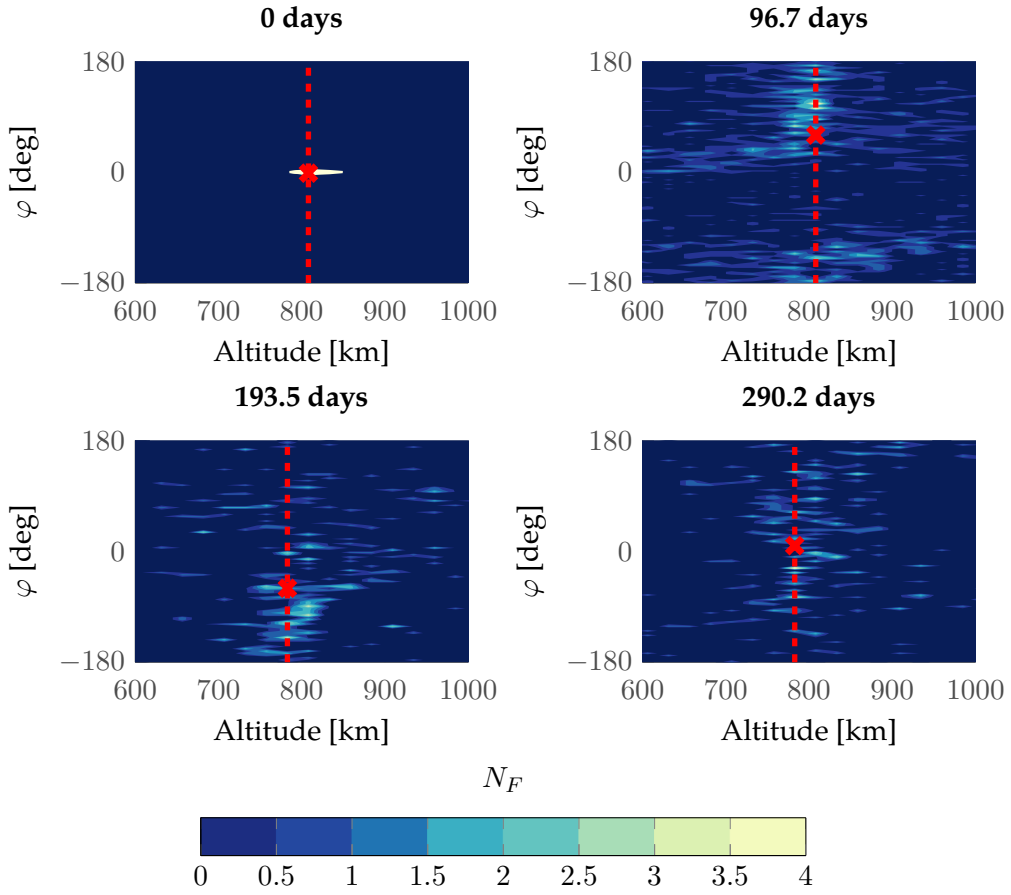

Figure 3.8: Representation of the cloud in the plane (r, ϕ). The red cross represent the position of the target and the dashed line the possible values of the longitude during the time step. Fragmentation and target are initially at $800\,\mathrm{km}$ and their inclinations are respectively 60 and 20 degrees.

This method could be adopted directly to obtain the value of n in Equation 3.3, choosing the value of density in the cell occupied by the target at a certain time. This is represented in Figure 3.8, where the cross indicates the position of the target at a certain time in the space of altitude and longitude φ. However, it was observed in Section 3.2 that the value of latitude (and in this case also of longitude) are not representative of the whole time step as they evolve in a much shorter time scale. For this reason, at each time step, the full osculating orbit of the target is reconstructed and the value of the fragment density is evaluated (and averaged) for different values of true anomaly. This means that in Figure 3.8 the value of spatial density should be evaluated along the dashed line (variation of φ) and its average used for the computation of the collision probability.

For the velocity, Equation 3.23

$$\Delta v_{\Delta\Omega} = \sqrt{v_T^2 + v_F^2 - 2v_T v_F \left[\sin\left(i_T\right)\sin\left(i_F\right)\cos\left(\Delta\Omega\right) + \cos\left(i_T\right)\cos\left(i_F\right)\right]}$$

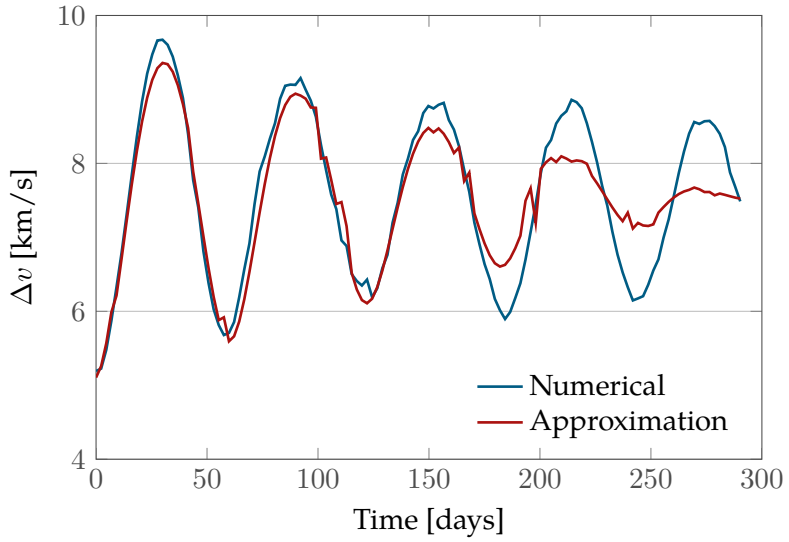

Figure 3.9: Relative velocity between the target and the fragment cloud before the band formation. The band is considered formed at around 290 days.

is still applied, but, in this case, it is not possible to assume that $\Delta\Omega$ is uniformly distributed between $-\pi$ and π. Therefore, Equation 3.23 is applied using for $\Delta\Omega$ the difference between the target longitude of the ascending node Ω_T and the value of Ω corresponding to the peak in the distribution in Ω_F. To obtain a gradual transition towards the value of the relative velocity adopted when the fragments are distributed (Δv_{dis}), the relative velocity is computed as

$$\Delta v = \alpha_{\text{dis}} \Delta v_{\text{dis}} + (1 - \alpha_{\text{dis}}) \Delta v_{\Delta\Omega} \tag{3.28}$$

where α_{dis} is a factor that measures how distributed the fragments are and, for the moment, it is simply set proportional to the elapsed time from the fragmentation $\alpha_{\text{dis}} = t/T_B$. The validation for this approach to the velocity estimation is shown in Figure 3.9, which presents in blue the value of the average relative velocity obtained with the numerical procedure, and in red the approximation obtained with the assumptions introduced in this Section. Figure 3.9 refers to a fragmentation on an orbit with inclination equal to 60 degrees and inclination of the target orbit equal to 20 degrees; for both the fragmentation and the target the initial altitude is equal to $800\,\text{km}$. Similar results were found also with different inclination and altitude combinations. In all cases, knowing the distribution of Ω among the fragments allows the oscillations in Δv to be followed. Whereas the average behaviour of the relative velocity is well captured, the damping of the oscillations (due to the progressive distribution of the fragments) is overestimated by the analytical approach. Future work will focus on an improvement of the description of the evolution of the cloud before the band formation to derive a more accurate estimation of the relative velocity.

Finally, Figure 3.10 shows the resulting collision probability for the target both before

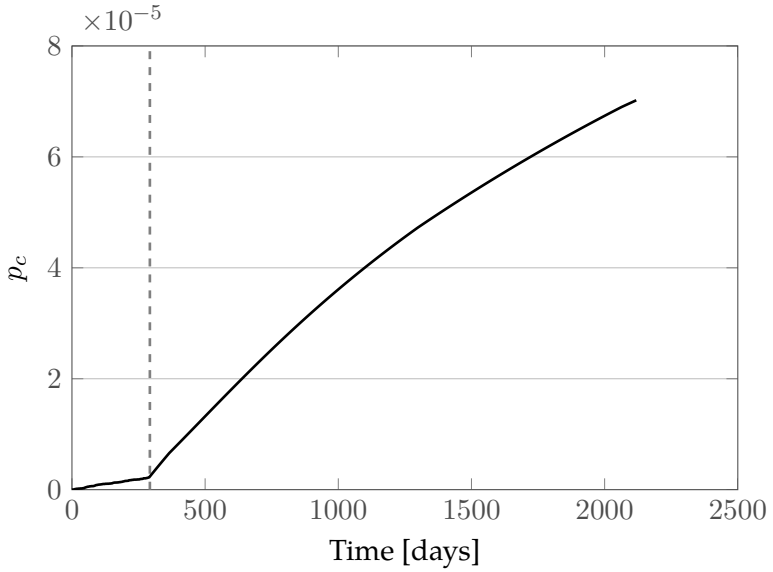

Figure 3.10: Resulting cumulative collision probability for a target at 800 km and orbital inclination equal to 20 degrees crossing a cloud generated by a fragmentation at $800\,\mathrm{km}$ and 60 degree of orbital inclination.

and after the band formation. The change in the slope of the curve when switching from one formulation to the other is very evident and unnatural. This behaviour is due to a difference of around one order of magnitude in the fragment density encountered by the target. This suggests that the computation of the fragmentation density in the first phase should be improved. Techniques available in literature may be adopted, such as the description of the cloud volume or of the position of its edges or the approach to compute the collision probability within a pinched torus proposed by Jehn (1996). As further investigation on this point is required, in the following we will always refer only to the computation of the collision probability after the band is formed.

A final comment on the computational time can clarify the advantage, given by the analytical method, of working directly with the spatial density. The time required for the numerical propagation is around $33\,\mathrm{s}$ on a machine with 4 CPUs and for a fragmentation of around 3000 fragments, plus $29\,\mathrm{s}$ to convert the information on the orbital parameters into the value of spatial density measured on a grid $100\times100\times100$ in r, ϕ, β. On the other hand, the propagation with the analytical equation requires only $2.64\,\mathrm{s}$ and the output is in spatial density, so it can be directly used to compute the collision probability. This suggests the interest in extending the applicability of the analytical method to earlier stages of the cloud evolution. Some results on this point will be shown in Section 4.2 and Chapter 6.

3.6 Collision scenarios

Thanks to its limited computational time and its good accuracy, the proposed method can be applied to study the collision probability due to small fragments in many different scenarios. The method is applied to three different cases

- to study the impact of a breakup on different target spacecraft,
- to build, for each target spacecraft or for a whole set of targets, a *map* of collision probability, by varying the inclination and the altitude of the simulated breakup,
- to generate a *matrix of influence* among a set of targets.

The results presented in this work are obtained using as targets the one listed in Table 3.1. They were extracted from a list prepared by IFAC-CNR, ISTI-CNR and University of Southampton for a study sponsored by ESA (Rossi et al., 2013). The objects in Table 3.1 are the ten spacecraft with the largest collision probability, sorted by their semi-major axis.

Table 3.1: List of target spacecraft (Rossi et al., 2013) for the analysis of the collision probability.

ID	Target	h_p [km]	h_a [km]	i [deg]	Mass [kg]	Size [m]
SC1	ESA-4419	816.0959	818.9741	98.73	4090	6.91
SC2	ESA-3308	818.5311	832.9389	98.83	2490	5.17
SC3	ESA-3331	804.0385	858.8315	98.83	1000	4.46
SC4	ESA-2218	822.4681	865.8019	70.90	3220	4.49
SC5	ESA-1761	946.4051	986.0649	82.91	1420	4.06
SC6	ESA-2332	934.9528	998.1172	82.95	1420	4.06
SC7	ESA-1291	964.0951	990.5749	82.95	1420	4.06
SC8	ESA-2172	960.1156	1005.754	82.93	1420	4.06
SC9	ESA-2961	968.9735	999.8965	82.94	1420	4.06
SC10	ESA-115	1099.8350	1099.8350	63.00	1000	2.41

3.6.1 Single event simulation

The first application of the method is the evaluation of the consequences of a breakup on the target list in Table 3.1, considering the collision probability associated with fragments larger than $1\,\mathrm{mm}$ and smaller than $10\,\mathrm{cm}$.

For this application, two recent small breakups are considered (NASA Orbital Debris Program Office, 2014), whose parameters are reported in Table 3.2. The value in the last column is an estimation of the parameter M_e used in the NASA breakup model as a measure of the energy of the breakup (Johnson and Krisko, 2001). For non-catastrophic collisions, M_e is defined as the product of the mass of the smaller object M_p and the

Table 3.2: Parameters of two recent small breakups (NASA Orbital Debris Program Office, 2014).

Spacecraft	h_p [km]	h_a [km]	i_0 [deg]	$N_{L_c>5\,\mathrm{cm}}$	M_e [kg]	N_F
Cosmos 1867	775	800	65	35	2.665	28138
Cosmos 2428	845	860	71	9	0.436	7235

square of the collision velocity v_c (Krisko, 2011)

$$M_e[\mathrm{kg}] = M_p[\mathrm{kg}]v_c^2[\mathrm{km/s}]/1[\mathrm{km/s}].$$

From this parameter, the fragment size distribution for a collision can be described by the expression

$$N_f(L_c) = 0.1(M_e)^{0.75}L_c^{-1.71} \tag{3.29}$$

where L_c is the fragment characteristic length and $N_f(L_c)$ the number of fragments of size equal or larger than L_c. If v_c is unknown, the parameter M_e can be estimated considering that the number of fragments added to the debris population catalogue is known for the two breakups (respectively 35 objects for Cosmos 1867 and 9 objects for Cosmos 2428)[5]. Therefore, assuming that the tracked fragments are larger than $5\,\mathrm{cm}$, the value of M_e is obtained inverting Equation 3.29 and the number of fragments N_F in the desired size range ($1\,\mathrm{mm}$-$10\,\mathrm{cm}$) is then obtained applying again Equation 3.29 with the computed value of M. Observe that the total number of fragments shown in Table 3.2 is very large and there is not a general consensus on the reliability of the NASA breakup model in the studied size range. Some modifications of the model are available in literature (Hanada et al., 2009), but the original NASA model is used because the purpose of this work is not to develop a new breakup model, but rather to show the possible applications and the advantages of using an analytical formulation based only on the spatial density. The implementation of the NASA model used in this work was validated with the comparison to the available data on other implementations (Rossi et al., 2006) as shown in Appendix A.1.

The effect of the breakups on the target in the list is shown in Figure 3.11, which shows the cumulative collision probability caused by fragments larger than $1\,\mathrm{mm}$ from the time of band formation up to five years afterwards. The study of a single case in Figure 3.11 for the Cosmos 1867 event was obtained with an average computational time equal to 9.45 minutes on a cluster with 4 processors; the average computational time is equal to 7 minutes for the Cosmos 2428 cases. Most of the propagation time is required for the propagation of the fragments from the breakup to the band, so the computational effort is required only once to generate the fragment cloud, which can be saved and superimposed on each target spacecraft trajectory.

[5]Values updated from `https://www.space-track.org/` in July 2015.

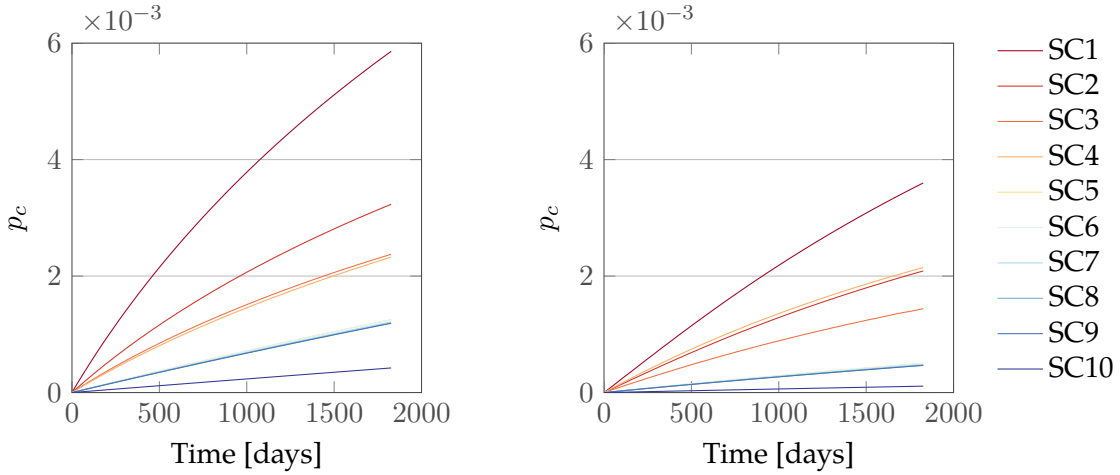

(a) Cosmos 1867 **(b)** Cosmos 2428

Figure 3.11: Resulting cumulative collision probability from the two breakups on the targets in Table 3.1. The time is measured from the instant when the band is considered formed.

For the first breakup (Cosmos 1867), the resulting collision probability p_c is shown in Figure 3.11a: it is possible to observe that the first four spacecraft in the list are the most affected by the fragmentation. This is explained by two factors: firstly, SC1 and SC2 have the largest cross-sectional area, and secondly the first four spacecraft are both at the lowest altitudes and the shortest radial distance from the fragmentation location. A similar behaviour can be observed for the second breakup (Cosmos 2428) in Figure 3.11b, which shows the effect of inclination. In fact, the inclination of Cosmos 2428 is very similar to the one of SC4, which, in this case, has a slightly higher collision probability than SC2 even if the latter has a larger cross-sectional area.

3.6.2 Maps of collision probability

The collision risk for a spacecraft can also be studied from a different point of view: instead of focussing on a single breakup, the location of the simulated breakup is changed to highlight the effect of the breakup conditions on the collision probability. In particular, here the altitude and the inclination of the fragmentation are varied and this allows defining the most dangerous regions for a collision to occur for all the targets in Table 3.1. Other parameters (e.g. time, fragmentation energy) may be considered with the same approach for a sensitivity study.

Figure 3.12 shows, for example, the result of a study performed for the spacecraft SC4 for fragmentations of $50\,\mathrm{kJ}$, including all the fragments down to $1\,\mathrm{mm}$. The peak in the collision probability is slightly above the altitude of the spacecraft semi-major axis ($a_{\mathrm{SC4}} = R_E + 844\,\mathrm{km}$) and for inclinations i_F where $\sin(i_F) = \sin(i_{\mathrm{SC4}})$. Under this condition, the spacecraft will spend a part of its orbit at latitudes where the cloud density

is maximum. The collision probability is high also for inclinations where $\sin(i_F) > \sin(i_{SC4})$ because in these cases the spacecraft is always inside the band formed by the fragments. As expected, fragmentations at higher altitudes than SC4 have a larger effect than the ones at lower altitudes. In fact, over time drag tends to reduce the fragments' altitude and the fragments initially at altitudes higher than SC4 decay towards the target orbit.

The same analysis was performed for all the targets in Table 3.1: for each spacecraft a map such as the one in Figure 3.12 for SC4 is computed and then they are summed to obtain the global map in Figure 3.13, where the markers indicate the targets. It is possible to observe two peaks in the collision probability, corresponding to the two bands in altitude where the targets are grouped: the first from 817 to $844\,\mathrm{km}$ for SC1-4, the second from 966 to $984\,\mathrm{km}$ for SC5-9. Observing the first peak in altitude ($h \approx 840\,\mathrm{km}$), it is possible to notice that the distribution of collision probability is not symmetrical around the peak: in fact, fragmentations at higher altitudes (e.g. $880\,\mathrm{km}$) have a larger effect than the ones at lower altitudes (e.g. $800\,\mathrm{km}$) as already discussed for Figure 3.12. It is also possible to observe that the collision probability is still relatively high around $h = 820\,\mathrm{km}$, mainly because of the presence of SC1, whose large cross-sectional area has a large influence on the total collision probability.

As observed in Figure 3.11b and Figure 3.12, the fragmentations with $\sin(i_F) = \sin(i_T)$ have a large effect on the total collision probability because of the distribution of objects with latitude. Eight out of ten spacecraft in Table 3.1 have $\sin(i_T) \approx \sin(82°) = \sin(98°)$, so at these inclinations two clear bands of high collision probability are present. Similar to Figure 3.12, the collision probability is high also in the whole inclination band between 80 and 100 degrees, which corresponds to fragmentations for which all the targets are always inside the fragment band.

A map such as the one in Figure 3.12 is obtained with a computational time equal to 3.66 hours in average, over the ten cases, on a cluster with 4 processors. The process can be easily automated and parallelised to study a list of targets and obtain a global map as the one in Figure 3.13. These maps may be useful to study both operational and non-operational targets to understand under which conditions a fragmentation has the largest effect on the spacecraft. Moreover, the global maps can highlight the most critical areas in terms of influence on the whole spacecraft population or on the satellites of an operator. For example, an operator may use this visualisation to understand the vulnerability of their fleet to fragmentations in specific orbital regions. Large operators may also be interested in evaluating if these orbital regions are populated by spent satellites or rocket bodies and get an insight on which objects would be the most beneficial to remove from the operators perspective. A development on this idea is presented in Chapter 6 where an environmental index for spacecraft is presented. Note that the number of targets used to build the global map can be increased or some representative objects of the whole population can be chosen. Whenever the list of targets is updated,

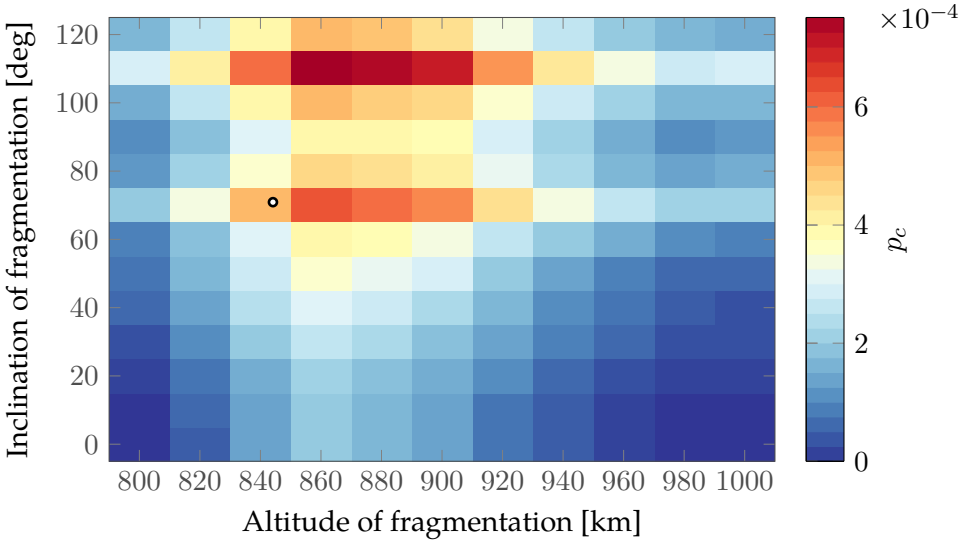

Figure 3.12: Cumulative collision probability map for SC4 for fragmentations of 50 kJ, including all the fragments down to 1 mm. The marker indicates the orbital parameters of SC4. Simulated period equal to five years.

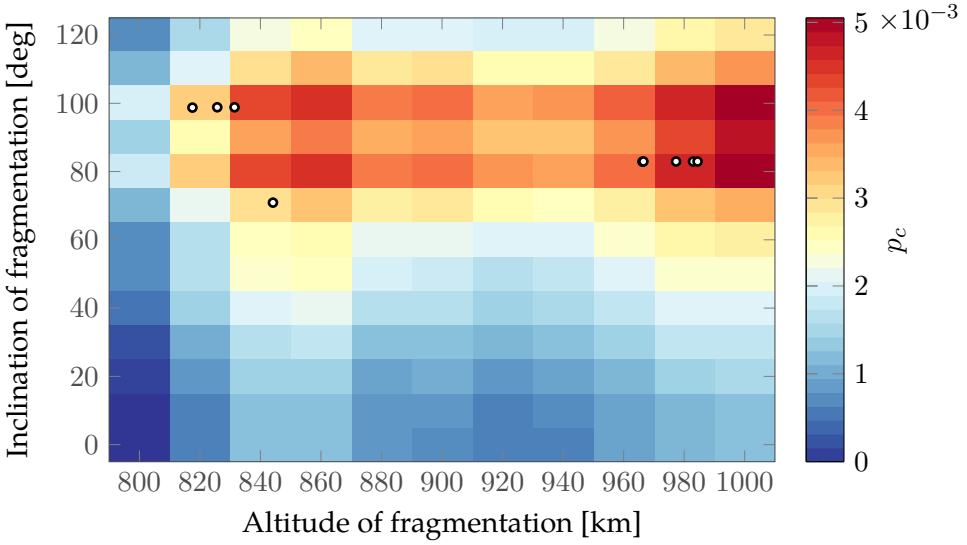

Figure 3.13: Total cumulative collision probability map for the targets in Table 3.1 for fragmentations of 50 kJ, including all the fragments down to 1 mm. The markers indicate the targets. Simulated period equal to five years.

the map needs to be computed again because the terms in the equation for the collision probability depend on the selected targets. In contrast, the propagation of the debris clouds, resulting from the breakups defined by the grid in semi-major axis and inclination, can be saved and stored. In this way, the computational time required to study a different target on the same grid is strongly reduced.

3.6.3 Influence matrix

Finally, similarly to what was done by (McKnight and Lorenzen, 1989), an *influence matrix* is proposed to study the following situation: a small breakup caused by a non-catastrophic collision with one of the spacecraft in Table 3.1, generates a fragment cloud that can interfere with other spacecraft. Each spacecraft in Table 3.1 is treated as a potential target and its collision probability due to the fragment cloud is computed after a certain time. This process is repeated running through the whole list of spacecraft in Table 3.1 to obtain a picture of how each spacecraft affects the collision probability of the other ones in the list. In the whole analysis, it is assumed that the collision probabilities are independent and each case is studied separately.

Figure 3.14 shows the resulting influence matrix for the spacecraft in Table 3.1 considering a fragmentation of $50\,\mathrm{kJ}$ and plotting the resulting collision probability after five years. It is important to specify that, as the proposed method is able to provide an analytical expression for the density only after the band is formed, the collision probability is computed starting from that moment. This means that the collision probability may be underestimated for satellites such as SC5-SC9 that have very similar orbits and that may start to interact before the band is formed.

The sum of the collision probabilities, over all the targets, due to the same source can be used as an index of the spacecraft *influence*; similarly, the sum of the collision probabilities for one target from all the sources can be used as an index of its *vulnerability*. In formulas, $I(i,j)$ is the element of the influence matrix that expresses the cumulative collision probability of the object j due to a fragmentation starting from the object j. For a generic object k, the two indices are obtained from

$$\text{Influence}(k) = \sum_{j=1}^{N_{\text{tot}}} I(k,j)$$
$$\text{Vulnerability}(k) = \sum_{i=1}^{N_{\text{tot}}} I(i,k).$$

Both these values are shown in Figure 3.15. As one can expect, the influence is very strong among satellites on similar orbits such as the already cited group SC5-SC9 and the group SC1-SC4. SC10 has, instead, the lowest influence because it is in an orbit with lower inclination than the other objects and, therefore, its fragmentations affect a smaller

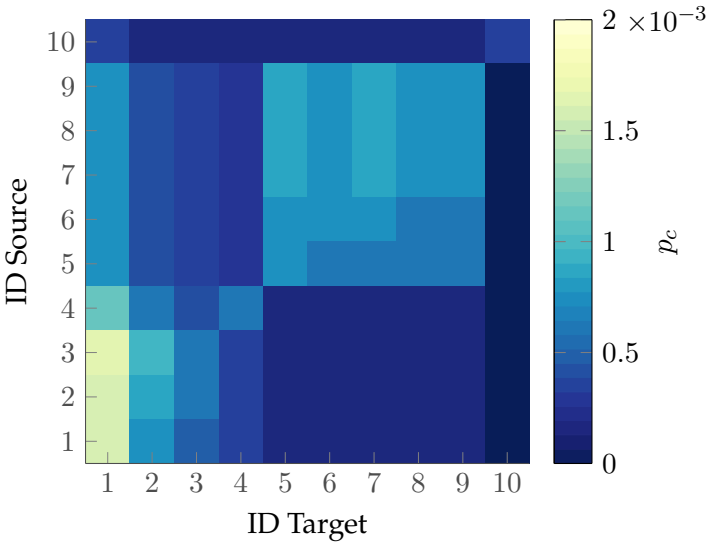

Figure 3.14: Influence matrix showing the cumulative collision probability for ten studied spacecraft.

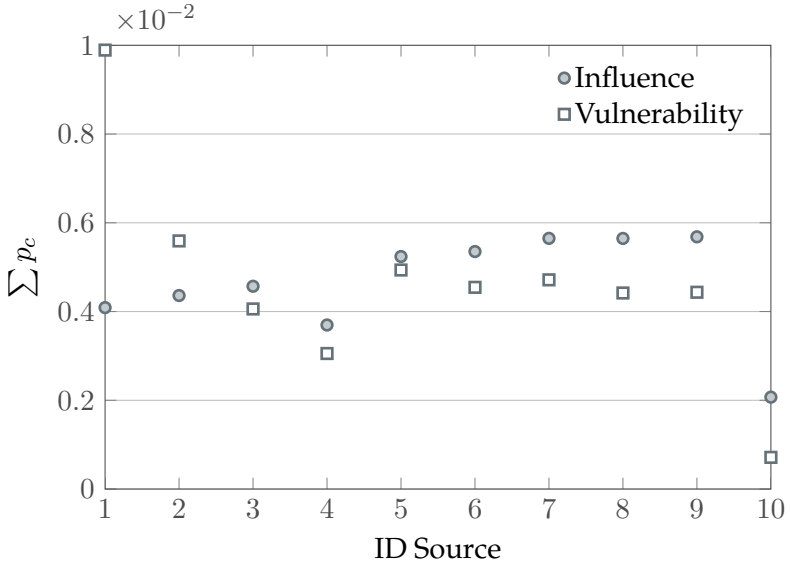

Figure 3.15: Sum of the generated collision probability for the scenarios in Figure 3.14.

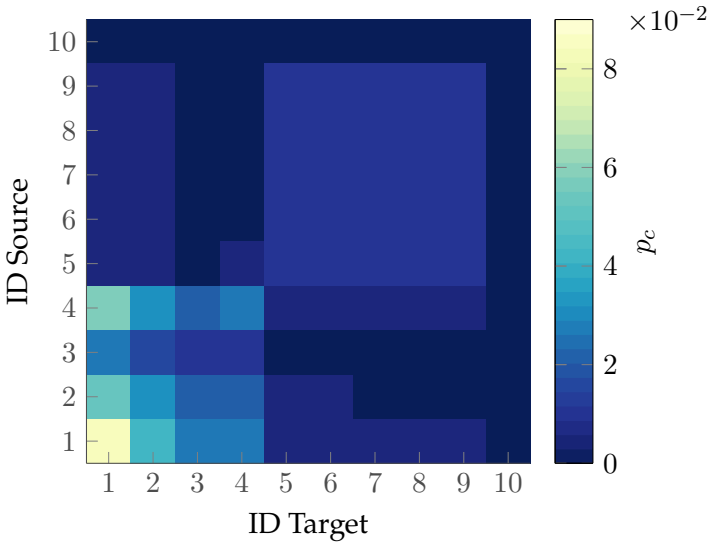

Figure 3.16: Influence matrix showing the cumulative collision probability for ten studied spacecraft in case of catastrophic collisions.

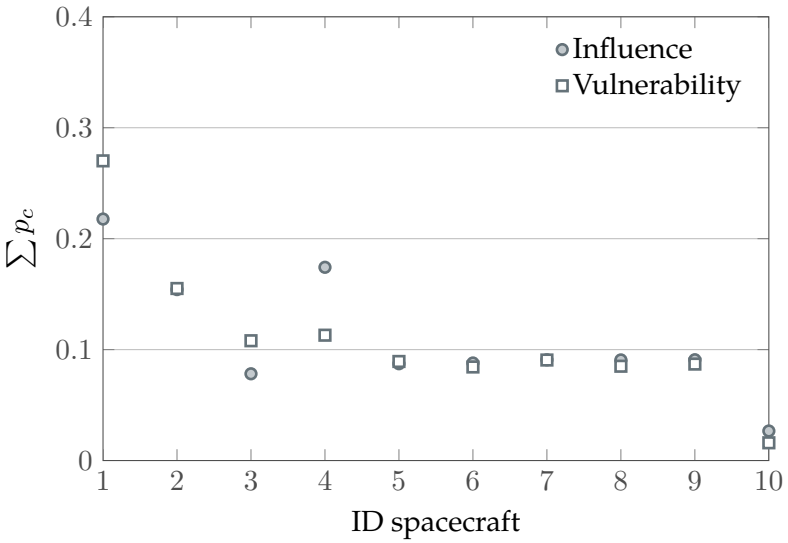

Figure 3.17: Sum of the generated collision probability for the scenarios in Figure 3.16 (catastrophic collisions) considering fragments larger than 1 cm.

range of latitudes. A high vulnerability is registered for SC1, which is in a lower orbit than the other spacecraft and which has a much larger cross-sectional area. This explains why it is affected by all the fragmentations originating from the other spacecraft. On the other hand, SC10 is the least vulnerable target because of its high altitude (with more than $115\,\mathrm{km}$ of separation between its semi-major axis and the one of the closest object) and because of its small cross-sectional area.

The computational time required to generate Figure 3.14 is equal to $645\,\mathrm{s}$ on a PC with 8 CPUs at 3.40 GHz. The process is fully automatic and parallelised, so the number of spacecraft in the list can be extended to obtain a more complete picture of the mutual influence among what are considered the most critical objects in the debris population in LEO.

Similar results can be obtained also simulating catastrophic collisions instead of non-catastrophic ones, as shown in Figures 3.16 and 3.17. In these simulations, a fixed impact velocity equal to $10\,\mathrm{km/s}$ is set as input of the breakup model and the mass of the projectile is neglected. In addition, the threshold on the fragment size was changed from $1\,\mathrm{mm}$ to $1\,\mathrm{cm}$: this was done because the number of fragments generated by a catastrophic collision according to the NASA breakup model is extremely large. For example, if the fragmenting satellite has a mass equal to $1000\,\mathrm{kg}$, more than two million objects larger than $1\,\mathrm{mm}$ are generated. Increasing the threshold size to $1\,\mathrm{cm}$, *only* $40\,000$ are generated. This number is still much larger than the number of fragments in the cloud created by the non-catastrophic collision studied in Figure 3.14 and this explains why the cumulative collision probability is still higher than the previous case. The results in Figure 3.16 are interesting because they show how the kind of fragmentation affects the ranking of the analysed spacecraft. When catastrophic collisions are considered, the driving factor for the *influence* is the mass, as can be seen from the results of the two spacecraft with the largest mass (i.e. SC1 and SC4).

Summary

The results obtained with the analytical method can be used to estimate the additional collision probability for a spacecraft due to the objects produced by the studied fragmentation. For this purpose, the analogy with the kinetic theory of gases can be applied: according to this theory, the collision probability can be modelled as a Poisson process with the number of collisions per unit of time proportional to the fragment spatial density and to the average relative velocity between the target and the fragments. The value of density is known from the analytical propagation, so the method described here can be applied only after the fragments have dispersed and formed a band around the Earth. For the velocity, an additional analytical method was introduced. The method is based on computing the relative velocity between the target and a single fragment assuming

that both are on circular orbits. In this case, their relative velocity depends on their inclinations, which are known, and on the difference in the longitude of the ascending node Ω between the two orbits. This last value is not known for the single fragment, but the fact that the fragments within the cloud are uniformly distributed in Ω can be used to obtain the average value of the relative velocity. This approach was tested in many different orbital configurations for the target and the fragmentation, changing their orbital inclination and altitude. Except for the cases where both the target and the fragmentation are on equatorial orbits, the method works well with an average relative error lower than 10%. As the analytical method for the velocity relies only on the information available from the analytical propagation, they can be combined to obtain a fast way to evaluate the collision probability for a spacecraft crossing a fragment cloud. As the collision probability is studied on a time span of some years, the latitude of the target is not followed and, therefore, the variation on the cloud density with latitude is not considered. Instead, an average value across the latitude range is used. The proposed analytical method was applied to study three different cases and demonstrate the flexibility of the approach. For all the applications, a set of *interesting* targets was selected; in particular, the targets were chosen among the catalogue of space debris objects, picking the ones with the highest collision probability. It is important to remark that the purpose of this chapter was not to identify the most critical objects in the debris population, but rather to show how the analytical method can be used in some real-world application. In the first case, the data from some recent breakups was used to simulate the produced fragment clouds and the resulting collision probability for the studied targets. The purpose of these simulations was to understand which objects, among the monitored ones, were the most exposed in the occurrence of a fragmentation events and which parameters have the largest impact on the collision probability. For the second application, a large number of fictitious fragmentations was simulated, changing in each case the altitude or the inclination of the orbit where the fragmentation occurs. The collision probability for each target and the cumulative probability were then computed obtaining what was called a *collision map*. These maps are effective in visualising the most critical conditions for a fragmentation to happen considering its effect on one or more targets. These maps can be used, for example, to suggest areas in the LEO region to keep as *clean* as possible because a fragmentation originating there would have a large impact on the existing debris population. Finally, in the last application, the selected objects from the debris catalogue were used both as sources and targets of fragmentations. In fact, as these objects have the highest collision probability, they are the ones more likely to be hit by another piece of debris generating a new debris cloud. The effect of these clouds on the other objects in the set was simulated to study the mutual influence among the targets. In this way, it was possible to identify the most exposed object and the one with the largest influence. These analyses may be useful to rank potential targets of active debris removal missions. In all the three cases, the analytical method presents a much lower computational time than a fully numerical simulation. For this reason, a large

number of collision scenarios could be launched (and stored), enabling new analyses on the resulting collision probability considering the contribution of small fragments.

Part of the content of this Chapter was submitted to publication in F. Letizia, C. Colombo, and H. G. Lewis. Multidimensional extension of the continuity equation method for debris clouds evolution. Advances in Space Research, *2015b. doi:10.1016/j.asr.2015.11.035. Accessed 8 December 2015.*

4

Density propagation with multiple variables

As shown in Chapter 2, the proposed approach based on the continuity equation provides an accurate description of the evolution of clouds produced by fragmentation events at different inclinations. Therefore, it was applied in Chapter 3 to study many different scenarios of collisions to understand, for example, which objects, in case of fragmentation, are more likely to have a large impact on the global collision risk for operational satellites.

However, the current formulation of the method can only be applied to fragmentation events at $800\,\mathrm{km}$ or higher, because at lower altitudes the hypothesis of circular orbits in Chapter 2 introduces a large error on the evolution of the cloud density. This limit can be relaxed by switching to a multi-dimension formulation of the problem. This will also allow other limitations of the proposed model to be dealt with, such as the need of the numerical propagation to model the fragment spreading due to the Earth's oblateness, and the division of the cloud in area-to-mass bins.

Following the approach by Gor'kavyi et al. (1997), the continuity equation can be written in any phase space by simply writing the divergence in rectangular coordinates, regardless the nature of the phase space variables. This approach is chosen because the effect of perturbations is usually described in terms of their impact on the orbital parameters (through Gauss' equations). Therefore, the problem is written in the space defined by the relevant orbital parameters to use the expression directly on the variation of the orbital parameters and to avoid complex transformations to a physical 3D space. The

results can then be translated into physical coordinates by using expressions such as the equation of the spatial density as a function of the orbital parameters in Equation 2.24.

4.1 Formulation of the continuity equation in multiple dimensions

The continuity equation is written as

$$\frac{\partial n}{\partial t} + \nabla \bullet \mathbf{f} = \dot{n}^{+} - \dot{n}^{-}; \tag{4.1}$$

writing the divergence in rectangular coordinates and considering m generic variables $(\alpha_1, \ldots, \alpha_m)$, the Equation 4.1 becomes

$$\frac{\partial n}{\partial t} + \frac{\partial n}{\partial \alpha_1} v_{\alpha_1} + \cdots + \frac{\partial n}{\partial \alpha_m} v_{\alpha_m} + \Big[\frac{\partial v_{\alpha_1}}{\partial \alpha_1} + \cdots + \frac{\partial v_{\alpha_m}}{\partial \alpha_m}\Big] n = \dot{n}^{+} - \dot{n}^{-}, \tag{4.2}$$

where v_{α_j} is the rate of variation of the variable α_j. The sink and source terms are neglected also in this case ($\dot{n}^{+} - \dot{n}^{-} = 0$), so applying the method of characteristics the following system of ODEs is obtained

$$\begin{cases} \dfrac{dt}{ds} = 1 & (4.3) \\ \dfrac{d\alpha_1}{ds} = v_{\alpha_1}(\alpha_1, \ldots, \alpha_m) & (4.4) \\ \quad \vdots & \\ \dfrac{d\alpha_j}{ds} = v_{\alpha_j}(\alpha_1, \ldots, \alpha_m) & (4.5) \\ \quad \vdots & \\ \dfrac{d\alpha_m}{ds} = v_{\alpha_m}(\alpha_1, \ldots, \alpha_m) & (4.6) \\ \dfrac{dn}{ds} = -\Big[\dfrac{\partial v_{\alpha_1}}{\partial \alpha_1} + \cdots + \dfrac{\partial v_{\alpha_m}}{\partial \alpha_m}\Big] n(\alpha_1, \ldots, \alpha_m, t). & (4.7) \end{cases}$$

The characteristic lines of the problem are obtained by solving the Equations 4.3-4.6, which depend on the specific formulation of the problem (which gives the actual expressions for $v_{\alpha_1}, \ldots, v_{\alpha_m}$). On the other hand, the formal expression of $n(\alpha_1, \ldots, \alpha_m, t)$ can be written for any problem. It can be obtained by dividing Equation 4.7 by any of the Equations 4.4-4.6. For example, dividing by Equation 4.4, the result is

$$\frac{dn}{d\alpha_1} = -\frac{1}{v_{\alpha_1}}\Big[\frac{\partial v_{\alpha_1}}{\partial \alpha_1} + \cdots + \frac{\partial v_{\alpha_j}}{\partial \alpha_j} + \cdots + \frac{\partial v_{\alpha_m}}{\partial \alpha_m}\Big] n \tag{4.8}$$

where it is possible to separate the variables, so that

$$\frac{dn}{n} = -\frac{1}{v_{\alpha_1}}\left[\frac{\partial v_{\alpha_1}}{\partial \alpha_1}\right] d\alpha_1 + \cdots - \frac{1}{v_{\alpha_1}}\left[\frac{\partial v_{\alpha_j}}{\partial \alpha_j} + \cdots - \frac{1}{v_{\alpha_1}}\left[\frac{\partial v_{\alpha_m}}{\partial \alpha_m}\right] d\alpha_1. \tag{4.9}$$

In the right hand side, in each term starting from the second one $d\alpha_1/v_{\alpha_1}$ can be rewritten using Equation 4.5

$$\frac{d\alpha_1}{v_{\alpha_1}} = \frac{d\alpha_j}{v_{\alpha_j}},$$

with α_j one of the m coordinates. Equation 4.9 becomes

$$\frac{dn}{n} = -\frac{1}{v_{\alpha_1}}\left[\frac{\partial v_{\alpha_1}}{\partial \alpha_1}\right] d\alpha_1 + \cdots - \frac{1}{v_{\alpha_j}}\left[\frac{\partial v_{\alpha_j}}{\partial \alpha_j}\right] d\alpha_j + \cdots - \frac{1}{v_{\alpha_m}}\left[\frac{\partial v_{\alpha_m}}{\partial \alpha_m}\right] d\alpha_m, \tag{4.10}$$

that can be easily integrated into

$$\log(n) = -\log(v_{\alpha_1}) + \cdots - \log(v_{\alpha_j}) + \cdots - \log(v_{\alpha_m}) + k \tag{4.11}$$

where k is a constant of integration. Finally,

$$n = \frac{K^*}{\prod_j^m v_{\alpha_j}}. \tag{4.12}$$

K^* is a constant ($K^* = \exp k$) that is obtained from the initial condition at $t = 0$

$$n_0(\alpha_1, \ldots, \alpha_m) = n(\alpha_1, \ldots, \alpha_m, t = 0) \tag{4.13}$$

as

$$K^* = n_0(\tilde{\alpha}_1, \ldots, \tilde{\alpha}_m) \prod_j^m v_{\alpha_j}(\tilde{\alpha}_1, \ldots, \tilde{\alpha}_m). \tag{4.14}$$

In Equation 4.14 $\tilde{\alpha}_j$ indicates the function obtained by inverting the characteristic lines G at initial time $t = 0$. So, for example, if from Equations 4.3-4.4 it is possible to write the characteristic line for α_j as

$$G(\alpha_j, t) = f(\alpha_j) + g(t) \tag{4.15}$$

with $g(0) = 0$, then

$$\tilde{\alpha}_j = f^{-1}(G(\alpha_j, t)), \tag{4.16}$$

with f^{-1} inverse of f.

In the next Sections, this formulation will be applied to three different cases to

- model the effect of the Earth's oblateness, i.e. the evolution from the ellipsoid phase (Figure 1.4a) to the band phase (Figure 1.4c),
- include the distribution in area-to-mass ratio A/M of the fragments for the propagation under the drag effect, once the band is formed (Figure 1.4c),

- include the distribution in eccentricity in the propagation under the drag effect, once the band is formed (Figure 1.4c).

4.2 Modelling of the effect of the Earth's oblateness

As discussed in the previous sections, the Earth's oblateness is the dominant perturbation on the fragment cloud evolution before the band formation (Figure 1.4). The secular and long-term effect of zonal spherical harmonics of the second order J_2 on the orbital parameters can be written as (Vallado, 2013)

$$\dot{\Omega} = -\frac{3}{2} J_2 \frac{R_E^2}{p^2} \bar{n} \cos i \tag{4.17}$$

$$\dot{\omega} = \frac{3}{2} J_2 \frac{R_E^2}{p^2} \bar{n} \left(2 - \frac{5}{2} \sin^2 i \right). \tag{4.18}$$

where R_E is the Earth's radius, p is the semi-latus rectum of the orbit $p = a(1 - e^2)$, $\bar{n}$ is the mean motion $\bar{n} = \sqrt{\mu_E / a^3}$, and i is the orbit inclination.

The continuity equation can be applied to model this phase of the cloud evolution by writing the problem in the phase space defined by the semi-major axis (a), the longitude of the ascending node (Ω) and the argument of the perigee (ω). Three possible formulations are possible. In the first case, it is assumed that the effect of drag can be neglected and the spreading of the cloud is evaluated only on the angles ω and Ω, considering that the distribution in a is constant. In the second case, the effect of drag is considered, so that the cloud density is a function not only of the two angles, but also of the semi-major axis. Finally, a third approach is presented where only one angle and the semi-major axis are used as variables of the problem.

4.2.1 Earth's oblateness only

For simplicity, it is assumed that the effect of drag can be neglected during the initial phase of the cloud evolution, which usually lasts a couple of months. This assumption follows the *phased approach* proposed by McKnight (1990) to study space debris cloud evolution as explained in Chapter 1. This approach was adopted, for example, by Jehn (1991) and Ashenberg and Broucke (1993) to describe how the debris cloud spreads under the effect of the Earth's oblateness, without considering other perturbations. Introducing the approximation that drag can be neglected, the variation of the semi-major axis is null ($v_a = 0$). Nevertheless, the information on the distribution of a is required to calculate the variation of Ω and ω as in Equations 4.17 and 4.18. Introducing

$$\lambda = \frac{3}{2} \sqrt{\mu_E} J_2 R_E^2,$$

the expressions of the variation of the parameters are

$$\begin{cases} v_{\alpha_1} = v_a = 0 & (4.19) \\ v_{\alpha_2} = v_\Omega = -\dfrac{\lambda}{a^{7/2}} \cos i & (4.20) \\ v_{\alpha_3} = v_\omega = \dfrac{\lambda}{a^{7/2}} \left(2 - \dfrac{5}{2} \sin^2 i\right), & (4.21) \end{cases}$$

Since a is constant, the characteristic lines are easily found as

$$\begin{cases} G_a(a,t) = a & (4.22) \\ G_\Omega(\Omega,t) = \Omega + \dfrac{\lambda}{a^{7/2}} \cos(i)\, t & (4.23) \\ G_\omega(\omega,t) = \omega - \dfrac{\lambda}{a^{7/2}} \left(2 - \dfrac{5}{2} \sin^2 i\right) t & (4.24) \end{cases}$$

that are of the form

$$G(\alpha,t) = f(\alpha) + g(t), \quad g(0) = 0$$

as introduced in Section 4.1. As f, in this case for all the three variables, is simply the identity, the expressions obtained inverting the characteristics at the initial time are identical to the characteristics, so

$$\begin{cases} \tilde{a} = G_a(a,t) & (4.25) \\ \tilde{\Omega} = G_\Omega(\Omega,t) & (4.26) \\ \tilde{\omega} = G_\omega(\omega,t) & (4.27) \end{cases}$$

The density of the cloud can be written as in Equation 4.12

$$n(a,\Omega,\omega,t) = n_0(\tilde{a},\tilde{\Omega},\tilde{\omega}) \frac{v_\Omega(\tilde{a}) v_\omega(\tilde{a})}{v_\Omega(a) v_\omega(a)}; \tag{4.28}$$

as a is constant, also v_Ω and v_ω can be simplified and therefore

$$\begin{aligned} n(a,\Omega,\omega,t) &= n_0(a,\tilde{\Omega},\tilde{\omega}) & (4.29) \\ &= n_0 \left[a, \Omega + \frac{\lambda}{a^{7/2}} \cos(i)\, t, \omega - \frac{\lambda}{a^{7/2}} \left(2 - \frac{5}{2} \sin^2 i\right) t\right]. & (4.30) \end{aligned}$$

The dependence of $\tilde{\Omega}$ and $\tilde{\omega}$ on t is linear, so n is computed extremely easily as it corresponds to a simple translation of the domain of the initial conditions.

4.2.2 Earth's oblateness and atmospheric drag (3D)

If the drag effect is considered, the variation of the semi-major axis is not zero. As explained in Chapter 2, the radial velocity of a fragment due to drag can be expressed as in Equation 2.37

$$v_r = -\varepsilon\sqrt{r}\exp\Big(-\frac{r-R_h}{H}\Big);$$

also in this case, the hypothesis of circular or quasi circular orbits is kept, so $r \approx a$. Therefore, Equation 2.37 can be used to express the variation of the semi-major axis substituting r with a. The expressions for the other parameters (Ω, ω) are unchanged with respect to Equations 4.20 and 4.21, so the system of ODEs is

$$\begin{cases} \dfrac{dt}{ds} = 1 & (4.31)\\ \dfrac{da}{ds} = -\varepsilon\sqrt{a}\exp\Big(-\dfrac{a-R_h}{H}\Big) & (4.32)\\ \dfrac{d\Omega}{ds} = -\dfrac{\lambda}{a^{7/2}}\cos(i) & (4.33)\\ \dfrac{d\omega}{ds} = \dfrac{\lambda}{a^{7/2}}\left(2-\dfrac{5}{2}\sin i^2\right) & (4.34)\\ \dfrac{dn}{ds} = -\left[\dfrac{\partial v_a}{\partial a}+\dfrac{\partial v_\Omega}{\partial \Omega}+\dfrac{\partial v_\omega}{\partial \omega}\right] n(a,\Omega,\omega,t). & (4.35) \end{cases}$$

The characteristic for a is the one already obtained for r starting from the expression for v_r as in Equation 2.37, so

$$G_a(a,t) = \exp\Big(\frac{a-R_h}{H}\Big) + \varepsilon\frac{\sqrt{R_h}}{H}t;$$

obtained, as before, with the approximation $\sqrt{a} \approx \sqrt{R_h}$.

The second characteristic of the system is obtained by dividing Equation 4.33 by Equation 4.32

$$\frac{d\Omega}{da} = \frac{v_\Omega}{v_a} = \frac{\lambda\cos i}{\varepsilon}\frac{\exp\left(\frac{a-R_H}{H}\right)}{a^4} \tag{4.36}$$

whose solution can be expressed as

$$G_\Omega(\Omega, a) = \Omega - \frac{\lambda}{\varepsilon}\cos i\Big[\Gamma(a) - \Gamma(a_0)\Big] \tag{4.37}$$

as already obtained by McInnes (1994). We take here the occasion to explicitly write $\Gamma(a)$ to amend a typo in the original paper

$$\Gamma(a) = \frac{-\exp\left(\frac{a-R_H}{H}\right)H\left(2H^2+Ha+a^2\right) + r^3\exp\left(-\frac{R_H}{H}\right)\mathrm{Ei}\left[\frac{a}{H}\right]}{6H^3a^3} \tag{4.38}$$

where $\mathrm{Ei}(z)$ is the exponential integral function, defined as

$$\mathrm{Ei}(z) = -\int_{-z}^{\infty} \frac{\exp(-u)}{u}\, du. \tag{4.39}$$

As ω and Ω have the same dependence on a, also the characteristic for ω is expressed through the function Γ and only the constant factor is different. In particular, the expression for ω is

$$G_\omega(\omega, a) = \omega + \frac{\lambda}{\varepsilon}\left(2 - \frac{5}{2}\sin i^2\right)\Big[\Gamma(a) - \Gamma(a_0)\Big].$$

Therefore, also in this case is possible to write an explicit expression for n

$$n(a, \Omega, \omega, t) = n_0(\tilde{a}, \tilde{\Omega}, \tilde{\omega})\frac{v_a(\tilde{a})v_\Omega(\tilde{a})v_\omega(\tilde{a})}{v_a(a)v_\Omega(a)v_\omega(a)} \tag{4.40}$$

with

$$\begin{cases} \tilde{a} = R_h + H\log\left(G_a(a,t)\right) & (4.41)\\ \tilde{\Omega} = G_\Omega(\Omega, \tilde{a}) & (4.42)\\ \tilde{\omega} = G_\omega(\omega, \tilde{a}). & (4.43) \end{cases}$$

Note that in this case the initial condition is not simply translated across the domain, but, as the semi-major axis decreases with time, the initial distribution is modified with time as expressed by Equation 4.40.

4.2.3 Earth's oblateness and atmospheric drag (2D)

If the purpose of the method is to obtain the long term evolution of the cloud, the scope of the description of the effect of the Earth's oblateness is to estimate when the band (Figure 1.4c) is formed and to have at the time a faithful representation of the fragment distribution with the orbital parameters. This can be achieved with a simplified expression of Equation 4.40 that considers the semi-major axis a and only one angle between Ω and ω. The angle to be chosen is the slowest in spreading during the band formation. Following (Ashenberg, 1994), for each altitude and inclination of the parent orbit is possible to know *a priori* which angle drives the band formation. For example, if Ω is the relevant angle to determine the time for band formation, the equations for this case are the same as the 3D case, but as ω can be disregarded, the expression for n is simplified to

$$n(a, \Omega, t) = n_0(\tilde{a}, \tilde{\Omega})\frac{v_a(\tilde{a})v_\Omega(\tilde{a})}{v_a(a)v_\Omega(a)}.$$

4.2.4 Results

The analytical modelling of the initial phase of the cloud evolution was validated through the comparison with the results obtained with the numerical integration. The domain

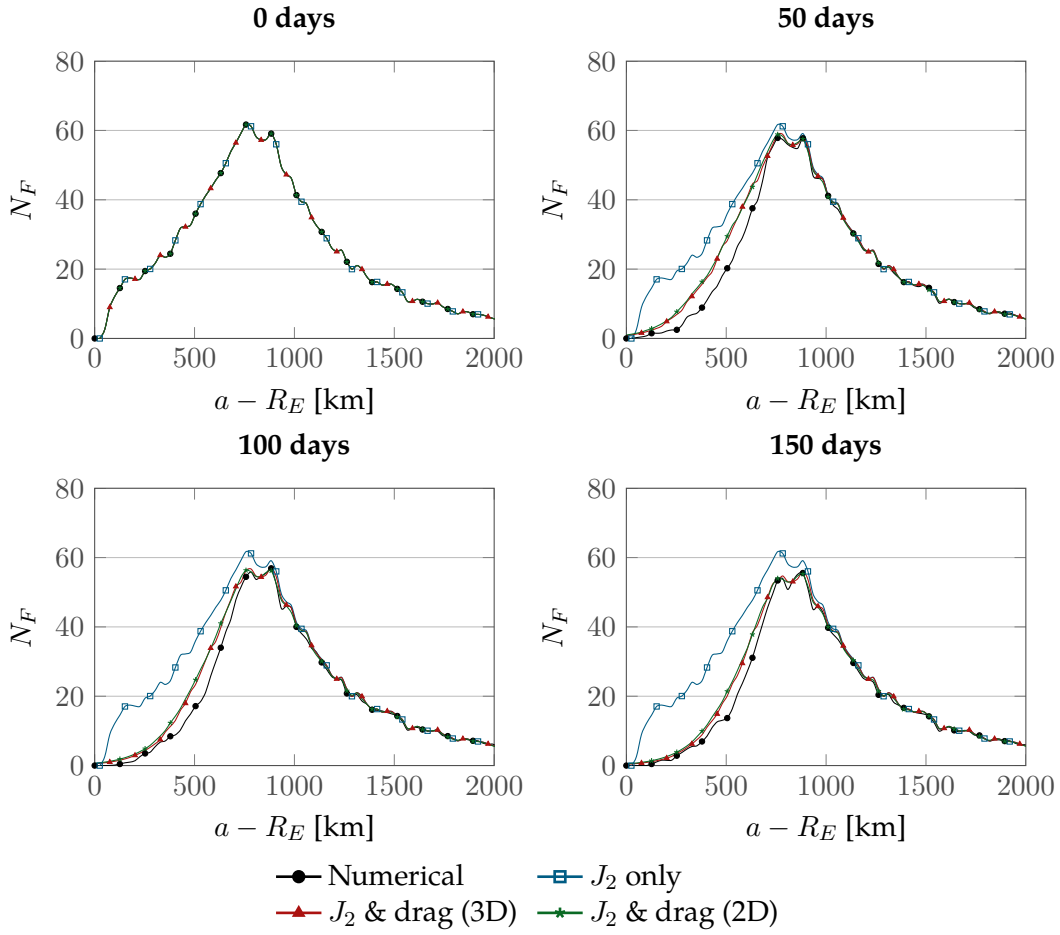

Figure 4.1: Evolution of the distribution of the semi-major axis, for a fragmentation at $800\,\mathrm{km}$ and $i = 30°$, from the fragmentation to 150 days after the event.

is divided into cells with width equal to $25\,\mathrm{km}$ in semi-major axis and 3.6 degrees in the two angles ω and Ω. The number of fragments N_F in each cell, according to the different propagator, is counted and compared. The cloud analysed in the following is generated by a breakup in a circular orbit with altitude equal to $800\,\mathrm{km}$ and inclination equal to 30 degrees. The cloud evolution is followed from the breakup up to 150 days later, when the transition to the band can be considered complete.

Figures 4.1, 4.2, 4.3 show respectively the evolution of the distributions in a, ω, Ω for the proposed analytical methods and for the numerical propagation. The accuracy in the description of the distribution in a is the most relevant figure to consider as it has a direct impact on the estimated value of the spatial density. From Figure 4.1 one can observe how neglecting the effect of drag leads to an overestimation of the number of objects with low semi-major axis. The same two indicators introduced in Section 2.7 are used to estimate the method accuracy. The first, $\mathrm{err}_{\mathrm{prof}}$ (Equation 2.52), measures the mean error on the density profile along the altitude (h)

$$\mathrm{err}_{\mathrm{prof}} = \frac{\int |n_A - n_N|\, dh}{\int n_N\, dh}.$$

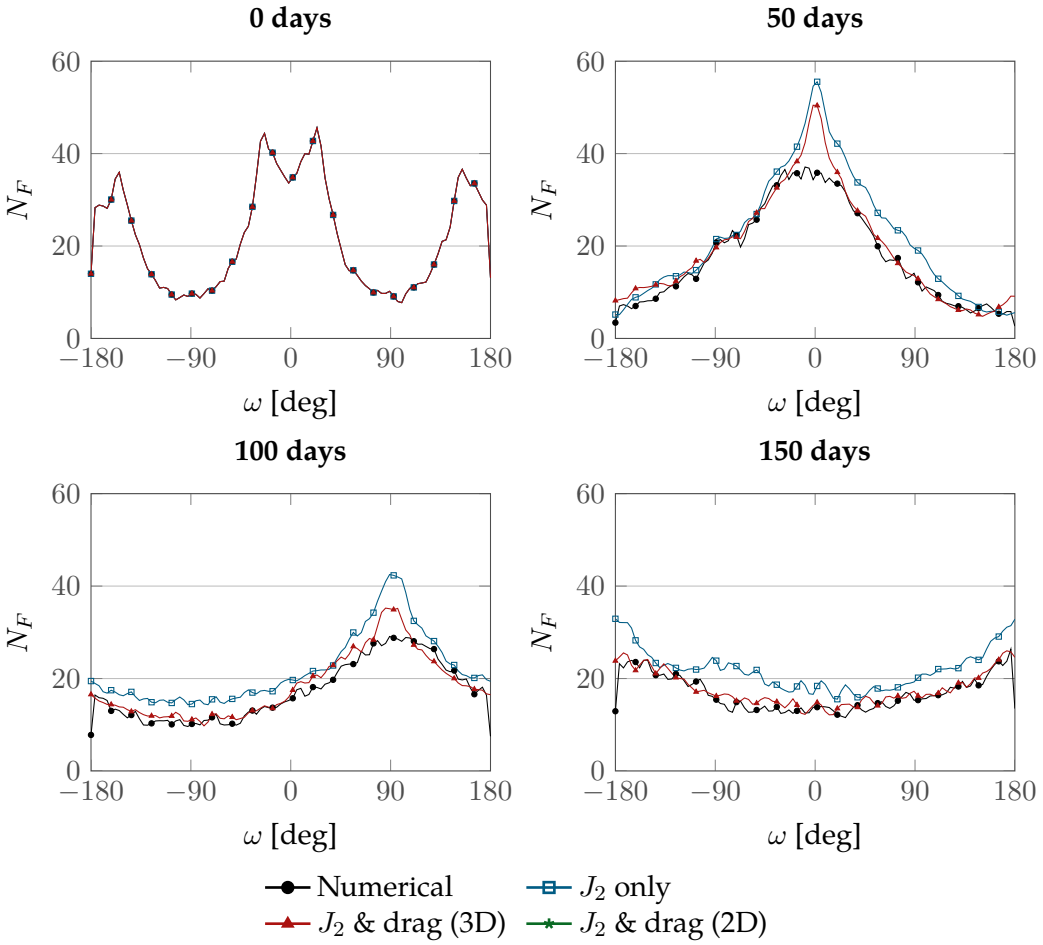

Figure 4.2: Evolution of the distribution of the argument of the perigee, for a fragmentation at 800 km and $i = 30°$, from the fragmentation to 150 days after the event.

Table 4.1: Accuracy and computational time t_c for the three approaches to the modelling of the initial evolution of a fragment cloud. $\Delta t = 150$ days. Errors measured on the distribution of the semi-major axis.

Method	err_{prof}	err_{peak}	t_c [s]
Earth's oblateness only	0.33	0.38	0.18
Earth's oblateness + atmospheric drag (2D)	0.07	0.11	0.08
Earth's oblateness + atmospheric drag (3D)	0.06	0.08	0.37

The second, err_{peak} (Equation 2.50), measures the relative error on the peak height, comparing the maximum density value for the analytical n_A and numerical propagation n_N,

$$\text{err}_{\text{peak}} = \frac{|\max(n_A) - \max(n_N)|}{\max(n_N)}.$$

Table 4.1 shows the value of the two indicators for the different propagation methods. It appears clearly that the assumption that drag can be neglected in the first phase of the cloud evolution is not valid.

Figure 4.2 shows how the spreading of ω is well captured, but, as expected, neglecting

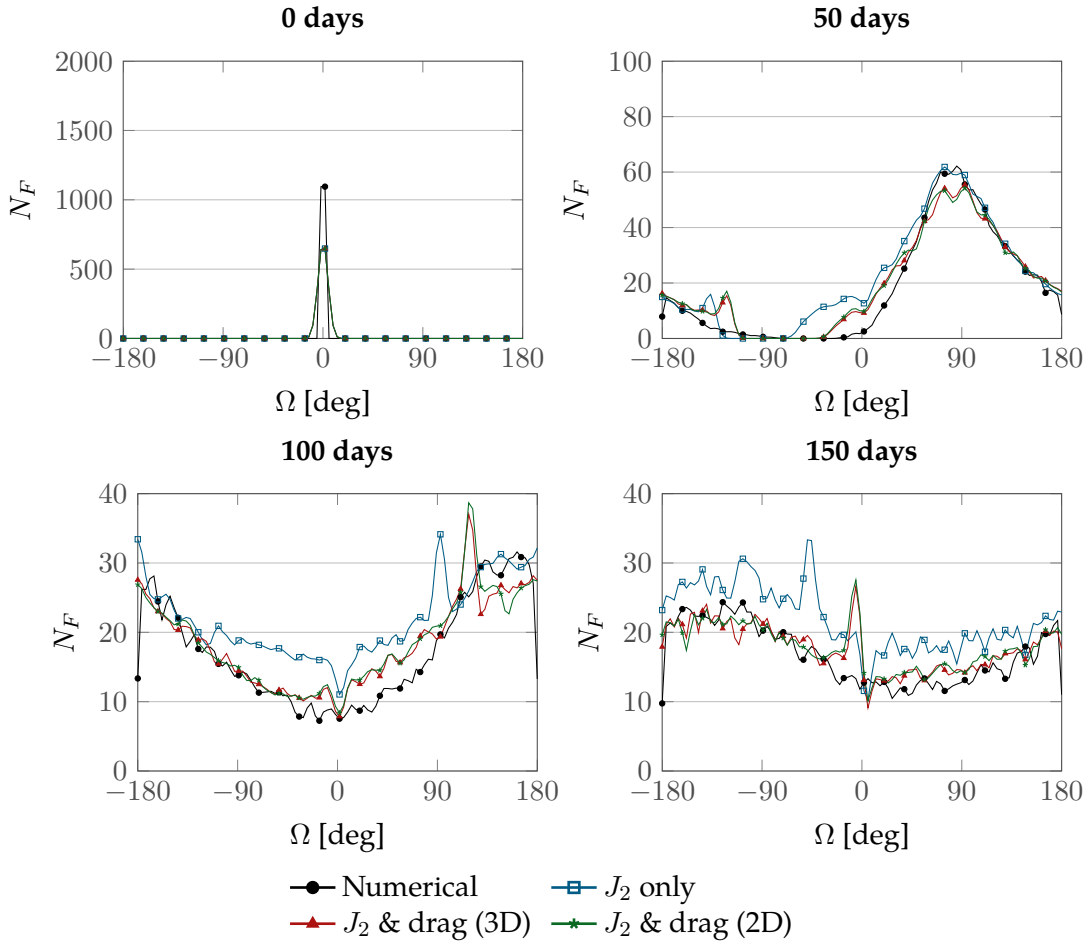

Figure 4.3: Evolution of the distribution of the longitude of the ascending node, for a fragmentation at 800 km and $i = 30°$, from the fragmentation to 150 days after the event.

drag leads also in this case to an overestimation of the number of fragments. Figure 4.3 shows the evolution of the distribution of Ω. Observe that in this case the initial condition was modified substituting the real initial distribution where all fragments have $\Omega = 0$ with a Gaussian distribution. This was done to avoid numerical issues such as instabilities, even if some anomalous peaks are still presents (e.g. the one at -5 degrees at $t = 150$ days). In fact, the method of characteristics derives the state at a given time by checking the value of the initial condition along the corresponding characteristic, so, with the current implementation, numerical instabilities may arise if the initial condition is equal to zero in all the domain expect in one point.

In terms of computational time, all the analytical approaches are much faster than the numerical propagation. The average running time over ten simulations, as measured by MATLAB built-in functions and for a PC with 4 CPUs at 3.4GHz, is reported in Table 4.1;

for the numerical propagation the average computational time is equal to $55\,\mathrm{s}$[1]. Including drag doubles the computational time, but the numbers are so low that there is no practical convenience in using the model with the Earth's oblateness only. On the other hand, reducing the number of parameters gives a larger speed-up while keeping a better level of accuracy.

Given the performance both in terms of accuracy and computational time, the application of the continuity equation to the initial phase of the cloud evolution appears promising. Future work will aim to use the analytical propagation to describe the spreading of the angles ω and Ω and asses when the band is formed. Another application could be the description of the cloud density in coordinates such as geocentric distance, longitude and latitude to allow for an analytical estimation of the collision probability also before the band formation.

4.3 Modelling of the area-to-mass distribution

In the 1D approach with the continuity equation for the description of drag effect proposed by McInnes (1993), all the constants of the problem are collected in the parameter ε defined in Equation 2.36

$$\varepsilon = \sqrt{\mu_E}\frac{c_d A}{M}\rho_{\text{ref}};$$

however, A/M is not the same for all the fragments in a debris cloud. Figure 4.4 shows the distribution of A/M obtained by one simulation, with the NASA breakup model, of a non-catastrophic collision with energy equal $50\,\mathrm{kJ}$. According to the model, the distribution of A/M is a log-normal distribution with mean value and standard deviation that depend on the fragment size (Johnson and Krisko, 2001). In particular, the simulated case presents a minimum value equal to $0.0288\,\mathrm{m^2\,kg^{-1}}$, a maximum value of $15.3978\,\mathrm{m^2\,kg^{-1}}$ and a peak of the distribution around $0.4\,\mathrm{m^2\,kg^{-1}}$.

The formulation by (McInnes, 1993) does not consider this distribution of A/M, which has instead a large impact on the fragment evolution. The novel extension to 2D explained in Section 4.1 can be applied to consider the area-to-mass ratio as an additional parameter in the continuity equation, thus improving the description of the drag effect. The equation that describes the evolution of A/M is simply

$$\frac{d(A/M)}{dt} = 0,$$

which means that the shape and the attitude of the fragments do not change with time, while the evolution of the fragment distance is described by Equation 2.37.

[1]The fact that the computational time is longer in this case than for the long term simulations studied in Section 2.8 is due to the fact that in the short time simulated here only a few fragments decay.

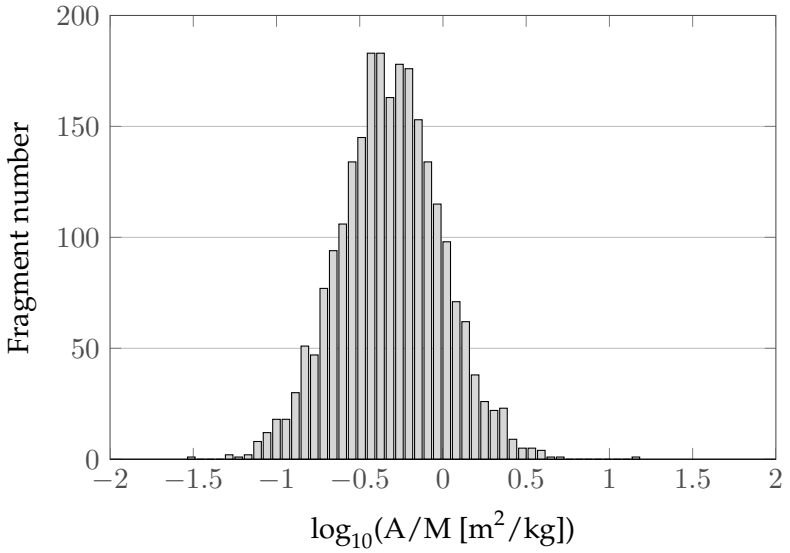

Figure 4.4: Area-to-mass ratio distribution for a non-catastrophic collision of $50\,\mathrm{kJ}$.

In this case, using the same notation as in Section 4.1,

$$\begin{aligned}
\alpha_1 &= r \\
\alpha_2 &= \frac{A}{M} \\
v_{\alpha_1} &= v_r = -\varepsilon\sqrt{R_h}\exp\Big(-\frac{r-R_h}{H}\Big) \\
v_{\alpha_2} &= v_{A/M} = 0 \\
\tilde{\alpha}_1 &= \tilde{r} = R_h + H\log\left(G(r,t)\right) \\
\tilde{\alpha}_2 &= \left(\frac{\tilde{A}}{M}\right) = \frac{A}{M}
\end{aligned}$$

where the expression of the characteristic for r, $G_r(r,t)$, is the same as in Equation 2.41

$$G_r(r,t) = \exp\Big(\frac{r-R_h}{H}\Big) + \varepsilon\frac{\sqrt{R_h}}{H}t$$

and v_r depends on A/M through ε as shown in Equation 2.36. The final expression for the fragment density, applying Equation 4.12, is

$$n(r, A/M, t) = n_0(r, A/M)\frac{v_r(\tilde{r}, A/M)}{v_r(r, A/M)}.$$

4.3.1 Results

Figure 4.5 compares the results of the analytical propagation with the output of the numerical one. The results are expressed in terms of spatial density, which, in the case of the numerical propagation, is obtained by counting the number of objects in spherical

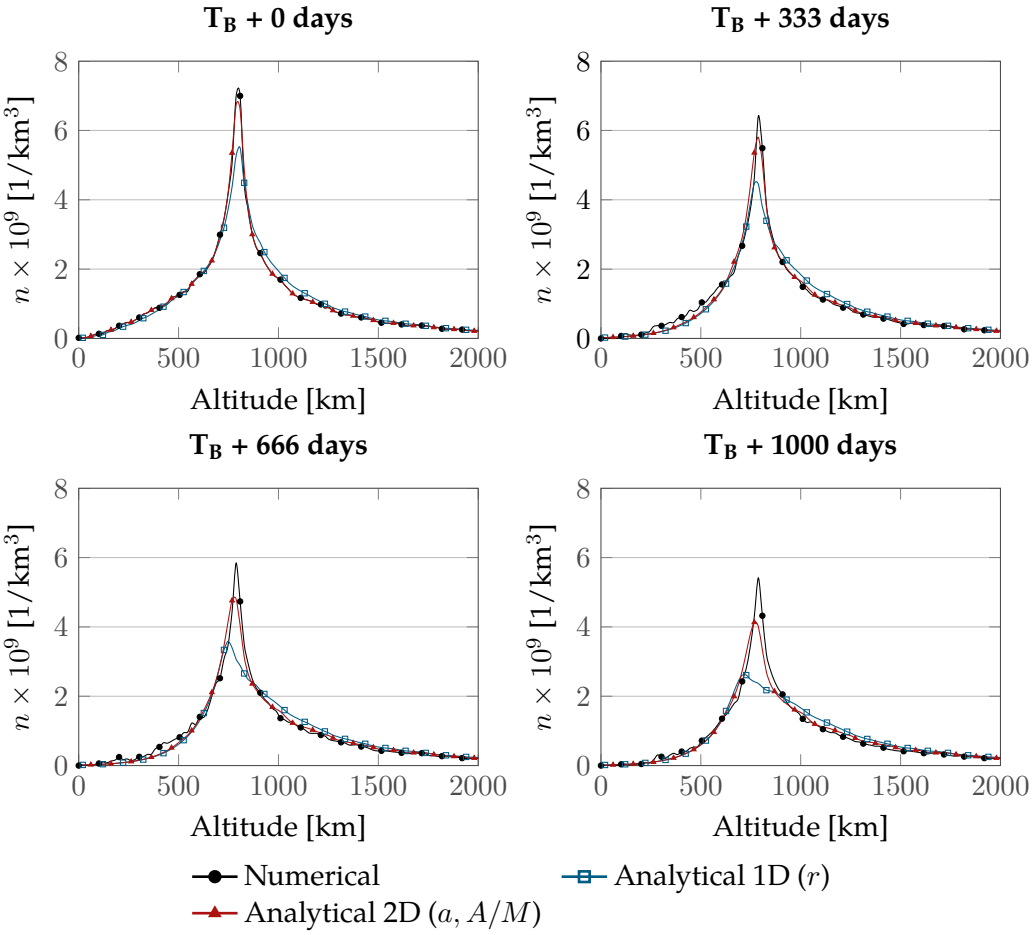

Figure 4.5: Evolution of the cloud density (n) profile as a function of time after the band formation T_B (T_B = 95 days) for a fragmentation at $800\,\mathrm{km}$, $i = 0$ degrees.

shells with thickness equal to $20\,\mathrm{km}$. Figure 4.5 shows how the 2D formulation follows the evolution of the cloud well and represents a significant improvement of the 1D approach for treating A/M: after 1000 days from the band formation, the relative error on the peak ($\mathrm{err}_{\mathrm{peak}}$) is equal to 49% for the 1D method and 20% for the 2D one.

However, it has to be noted that treating A/M as an additional dimension of the problem increases its complexity and the required computational time. In particular, it is possible to keep the 1D formulation of the problem and divide the fragments into N_b bins in area-to-mass ratio, as introduced in Chapter 2. Figure 4.6 shows the density at 1000 days for a fragmentation at $800\,\mathrm{km}$ for different formulations of the problem: both including 5 and 10 bins is possible to obtain a result similar to the 2D approach around the peak area.

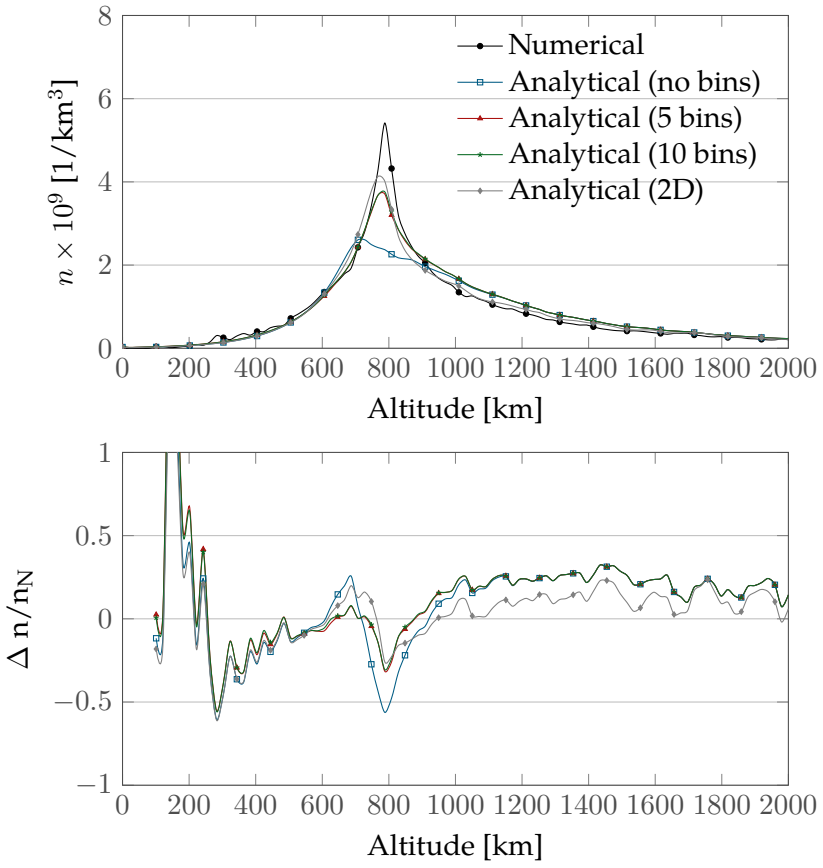

Figure 4.6: Density profile at 1000 days after the band formation T_B (T_B = 95 days) for a fragmentation at $800\,\mathrm{km}$, $i = 0$ degrees for different propagators and relative error measured with respect to the value obtained with the numerical propagation n_N.

4.4 Modelling of the eccentricity distribution

The method explained in Chapter 2 is based on the hypothesis that the fragments are on circular orbits: this allows a full analytical solution for the spatial density evolution under the drag effect to be obtained. However, this also limits the applicability of the method to altitudes equal to and higher than $800\,\mathrm{km}$. In fact, at lower altitudes, even in the case of a small value of eccentricity, the atmosphere density changes so largely along one single orbit that Equation 2.37 is not accurate anymore. For this reason, the eccentricity should be included as a variable in the propagation. In particular, the problem is formulated here in terms of the evolution of the debris cloud in the phase space defined by the semi-major a and the eccentricity e. In this case, the cloud spatial density, in $[1/\mathrm{km}^3]$, is computed *a posteriori* with the expressions , such as Equation 2.24, that express the probability of finding a fragment at a certain distance given its orbital parameters and that were used in the fitting process explained in Section 2.3.

In order to study the debris cloud density as a function of a and e, an expression of their rate of variation, respectively v_a and v_e, is required. They both can be obtained from the

expression for the variation of the orbital parameters in one orbit

$$\Delta a = -2\pi \frac{c_d A}{M} a^2 \rho_{\text{ref}} \exp\Big(-\frac{a - R_H}{H}\Big)\Big[I_0 + 2eI_1 + O(e^2)\Big] \tag{4.44}$$

$$\Delta e = -2\pi \frac{c_d A}{M} a \rho_{\text{ref}} \exp\Big(-\frac{a - R_H}{H}\Big)\Big[I_1 + \frac{e}{2}(I_0 + I_2) + O(e^2)\Big]; \tag{4.45}$$

derived by King-Hele (1987) for orbits whose eccentricity is between 0.01 and 0.1. It is assumed that the other orbital parameters are unchanged under the hypothesis the Earth's rotation is neglected. I_n indicates the modified Bessel function of the first kind and order n with argument $z = ae/H$, where H is the scale height coming from the exponential model of the atmosphere; $I_k(z)$ can be defined by the contour integral

$$I_k(z) = \frac{1}{2\pi \mathrm{i}} \oint \mathrm{e}^{(z/2)(t+1/t)} t^{-k-1}\, dt; \tag{4.46}$$

for $k \in \mathbb{Z}$ the definition can be simplified in

$$I_k(z) = \frac{1}{\pi} \int_0^{\pi} \mathrm{e}^{z\cos\theta} \cos k\theta \, d\theta. \tag{4.47}$$

Therefore, the expression of the velocities is

$$\begin{aligned} v_a &= -\sqrt{\mu_E a}\frac{c_d A}{M}\rho_0 \exp\Big(-\frac{a - R_H}{H}\Big) f(a, e, H) \\ v_e &= -\sqrt{\frac{\mu_E}{a}}\frac{c_d A}{M}\rho_0 \exp\Big(-\frac{a - R_H}{H}\Big) g(a, e, H) \end{aligned} \tag{4.48}$$

where

$$\begin{aligned} f(a, e, H) &= I_0 + 2eI_1 + O(e^2) \\ g(a, e, H) &= I_1 + \frac{e}{2}(I_0 + I_2) + O(e^2). \end{aligned} \tag{4.49}$$

Introducing the parameter ε as in Equation 2.36, the resulting system of equations is

$$\begin{cases} \dfrac{dt}{ds} = 1 & (4.50) \\ \dfrac{da}{ds} = -\varepsilon\sqrt{a}\exp\Big(-\dfrac{a - R_H}{H}\Big) f(a, e, H) & (4.51) \\ \dfrac{de}{ds} = -\dfrac{\varepsilon}{\sqrt{a}}\exp\Big(-\dfrac{a - R_H}{H}\Big) g(a, e, H) & (4.52) \\ \dfrac{dn}{ds} = -\Big[\dfrac{\partial v_a}{\partial a} + \dfrac{\partial v_e}{\partial e}\Big] n(a, e, t) & (4.53) \end{cases}$$

that, however, does not admit an analytical solution. Two approximations are, therefore, introduced:

$$\sqrt{a} \approx \sqrt{R_H} \tag{4.54}$$

and

$$f(a, e, H) \approx f(R_H, e, H) \qquad g(a, e, H) \approx g(R_H, e, H); \tag{4.55}$$

the impact of these approximations on the accuracy of the trajectory evolution was verified and considered acceptable, as shown in Figure 4.7. It shows the relative error on the semi-major axis err_a and on the eccentricity err_e

$$\text{err}_a = \frac{\tilde{a} - a_N}{a_N} \qquad \text{err}_e = \frac{\tilde{e} - e_N}{e_N}$$

where $(\tilde{a}, \tilde{e})$ are the values of the orbital parameters obtained by introducing the approximations in Equations 4.54 and 4.55, and (a_N, e_N) are the values obtained from the numerical propagation, without any approximation. In all cases shown in Figure 4.7, the semi-major axis is set equal to R_E + 700 km while four different values of eccentricity are considered. The error is very low for the first two cases ($e = 0.010$ and $e = 0.037$), whose curves lay on the x-axis in Figure 4.7. In general, the error is lower than 1% both for the semi-major axis and for the eccentricity for all the cases except the one with $e = 0.092$, whose perigee is equal to $50\,\text{km}$, the threshold value below which the fragments are considered to be re-entering. These fragments are likely to re-enter much faster than the other ones, so also their impact on the propagation of the cloud is limited in time.

Even with the approximations in Equations 4.54 and 4.55 it was not possible to obtain an analytical solution as the complexity of the problems derives from the fact that the evolution in a and e are coupled through the Bessel functions. A detailed discussion on the issues related to find a solution for the system can be found in Appendix B.5. One attempt to approximate the problem is to decouple the equations by assuming a constant eccentricity $v_e = 0$. This is still a strong hypothesis on the eccentricity, but compared to the 1D approach, the 2D formulation takes into account the eccentricity distribution and uses this information to correct the evolution of the semi-major axis, although its derivative is considered to be zero. On the other hand, neglecting the evolution of the eccentricity and setting $e = e_0$ implies that the effect of drag is overestimated. In fact, drag gradually reduces the orbit eccentricity and keeping a constant value is equivalent to predicting a higher velocity at the perigee and so a larger reduction of the semi-major axis.

The impact of this approximation is evaluated in Figure 4.8, which shows the evolution of the semi-major axis as a function of a time according to Equation 4.45, in blue, the approximation in Equation 4.55 in red, the evolution of the semi-major axis for a constant value of $e = e_0$ in $f(R_H, e, H)$ in green and the circular orbit case in purple. In the case of perigee altitude equal to $500\,\text{km}$, the relative error introduced by setting $e = e_0$ is around 0.5% so still much lower than the one with hypothesis of circular orbit.

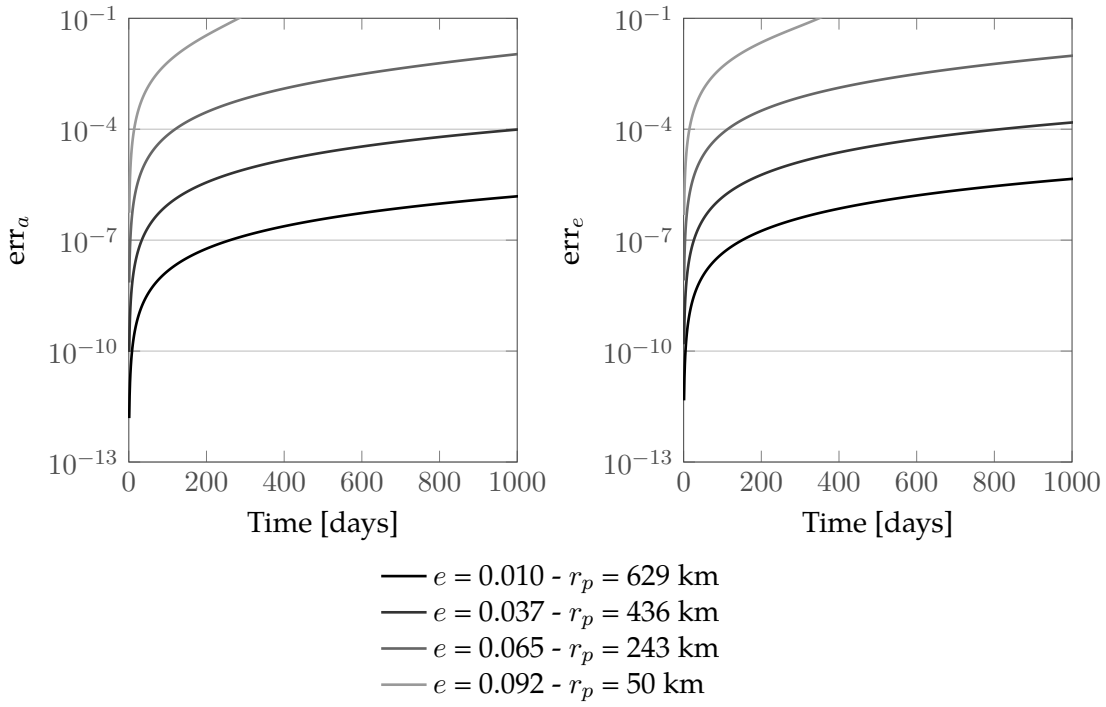

Figure 4.7: Relative error on the semi-major axis a and on the eccentricity e resulting from the approximation in Equation 4.55 for fixed semi-major axis equal to R_E + 700 km and different values of eccentricity.

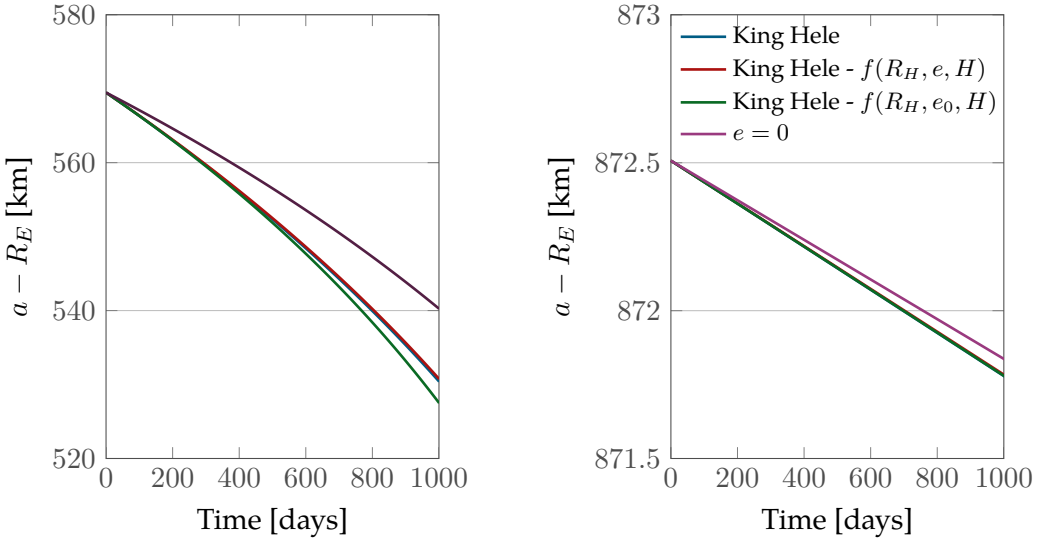

(a) Perigee altitude: 500 km

(b) Perigee altitude: 800 km

Figure 4.8: Evolution of the semi-major axis in time with different approximations of Equation 4.44 for two different perigee altitudes and initial eccentricity of $e_0 = 0.01$.

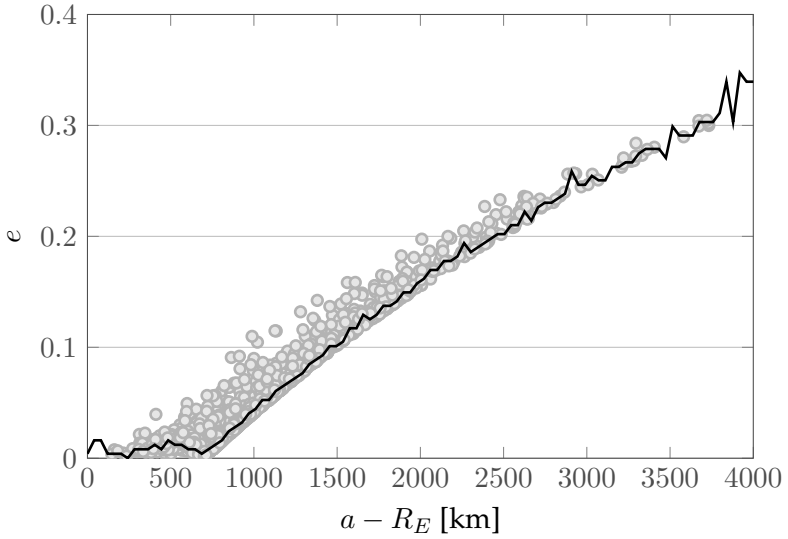

Figure 4.9: Distribution of semi-major axis and eccentricity, for a fragmentation at $700\,\mathrm{km}$, at the band formation (92 days after the fragmentation).

The equations used to model the cloud evolution are

$$\alpha_1 = a \tag{4.56}$$

$$\alpha_2 = e \tag{4.57}$$

$$v_{\alpha_1} = v_a = -\sqrt{\mu R_H}\frac{c_d A}{M}\rho_0 \exp\Big(-\frac{a - R_H}{H}\Big) f(R_H, \tilde{e}(a), H) \tag{4.58}$$

$$v_{\alpha_2} = v_e = 0 \tag{4.59}$$

$$\tilde{\alpha}_1 = \tilde{a} = H \log\Big[(\exp\Big(\frac{a - R_H}{H}\Big) + \varepsilon f(R_H, \tilde{e}(a), H)\frac{\sqrt{R_H}}{H}t\Big] \tag{4.60}$$

$$\tilde{\alpha}_2 = \tilde{e} = e. \tag{4.61}$$

Note that an heuristic was adopted in Equation 4.58, introducing $\tilde{e}(a)$ that expresses a reference value of the eccentricity for each value of the semi-major axis. This means that, given a value of the semi-major axis a_j, $\tilde{e}(a_j)$ is the constant value associated with it. The value of $\tilde{e}(a)$ can be obtained starting from the initial distribution $n_0(a, e)$ at the band formation: the function e_0 is built assigning to each value of the semi-major axis the value of eccentricity where the density is maximum; for example, for $a = a_j$

$$\tilde{e}(a_j) = e_j : n_j = n_0(a_j, e_j) = \max\left(n_0(a_j, e)\right).$$

The resulting function for the case at 700 km is shown in Figure 4.9. This approximation is kept for the whole simulation.

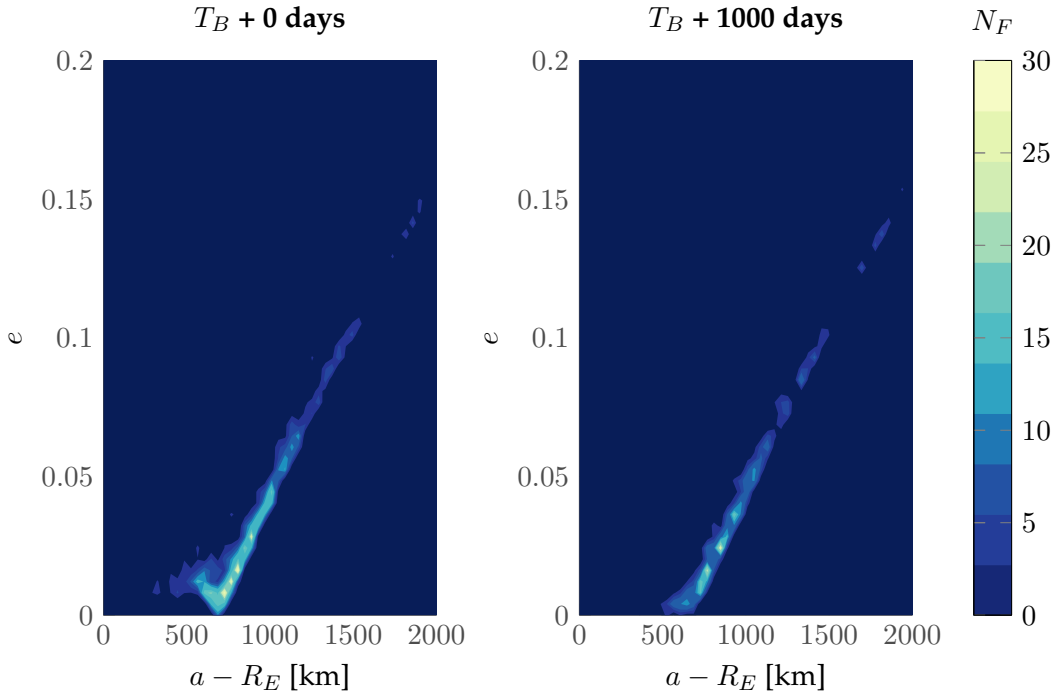

(a) Numerical propagation

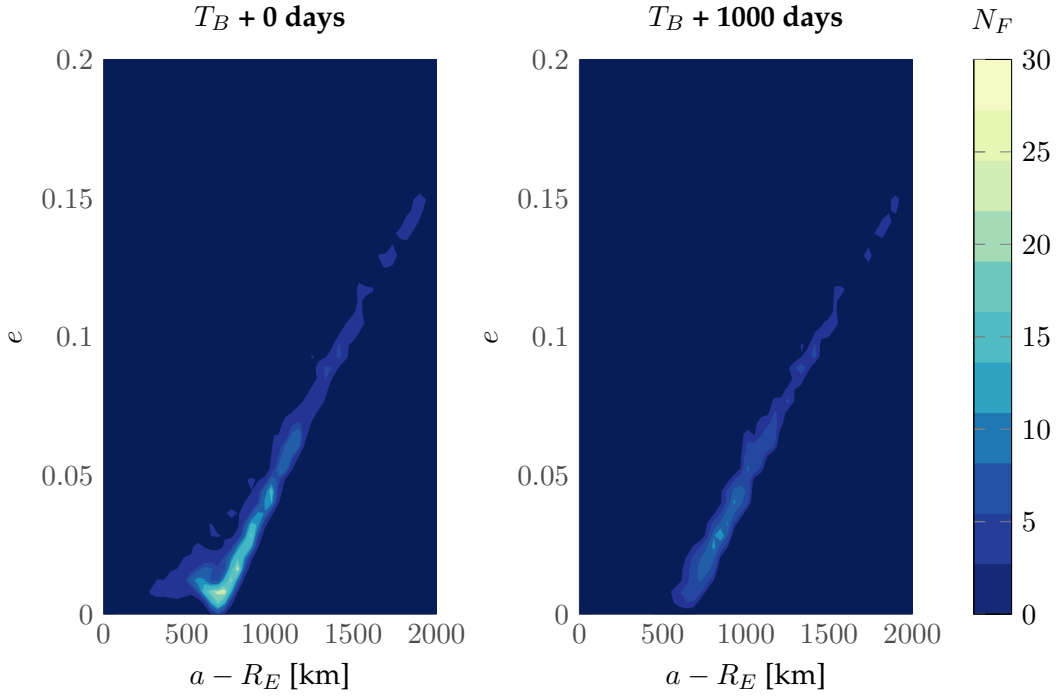

(b) Analytical propagation

Figure 4.10: Visualisation of cloud density (in number of fragments) at the band formation ($T_B = 92$ days) and after 1000 days for two propagation methods.

4.4.1 Results

The result of the numerical propagation in terms of density in the phase space of a and e is shown in Figure 4.10a: the domain is divided into cells with width equal to $25\,\mathrm{km}$ in semi-major axis and 0.005 in eccentricity; the plot shows the number of fragments N_F in each cell. The plot on the left refers to the moment of band formation; it is easy to recognise the v-shaped distribution of eccentricity with semi-major axis, which is an alternative representation of the well known Gabbard diagram (Portree and Loftus, 1999). The v-shaped curve is centred on the altitude of the parent orbit: the leg on the left represents the fragments whose orbits have the fragmentation location as apogee, the leg on the right those with the fragmentation location as perigee. The plot on the right refers instead to the cloud density at 1000 days after the band formation: the number of fragments is reduced and the fragments with low semi-major axis are on circular orbits, therefore one leg of the v-shaped distribution disappears. The same plots can be obtained also with the analytical approach in 2D (Figure 4.10b) which provides a distribution of fragments that is extremely similar to the numerical simulation. The most evident difference in the density after 1000 days from the band formation is that the analytical approach underestimates the number of fragments with $e \approx 0$.

This is even clearer from Figure 4.11 that shows the distributions of semi-major axis and eccentricity for the numerical propagation and for the 2D analytical approach at the different time instants. After 1000 days from the band formation, the distribution of the semi-major axis is well captured (Figure 4.11); on the other hand, the analytical approach is not able to represent the peak at $e \approx 0$ in the eccentricity distribution. This happens because the analytical propagation is obtained starting from the equation

$$\frac{de}{dt} = 0$$

so the progressive reduction of eccentricity is lost.

Despite this error, it is possible to see from Figure 4.12 how the 2D approach represents in any case a remarkable improvement compared to the 1D method described in Chapter 2. Figure 4.12 shows the evolution with time of the spatial density different altitudes, normalised by the value at the initial time, for a fragmentation at $800\,\mathrm{km}$. The results obtained with three different propagation techniques are shown: the numerical propagation (solid line), the 1D analytical propagation (dashed line), and the 2D analytical propagation (dotted line). The main difference among the propagation methods is visible at the fragmentation altitude (in blue). Whereas the 2D analytical method is able to follow the rate of variation obtained with the numerical propagation, the 1D method predicts a much steeper reduction of the density. This happens because the 1D approach assumes that all fragments are on circular orbits, so the contribution of the objects with semi-major axis larger than the one of the parent orbit is not well modelled.

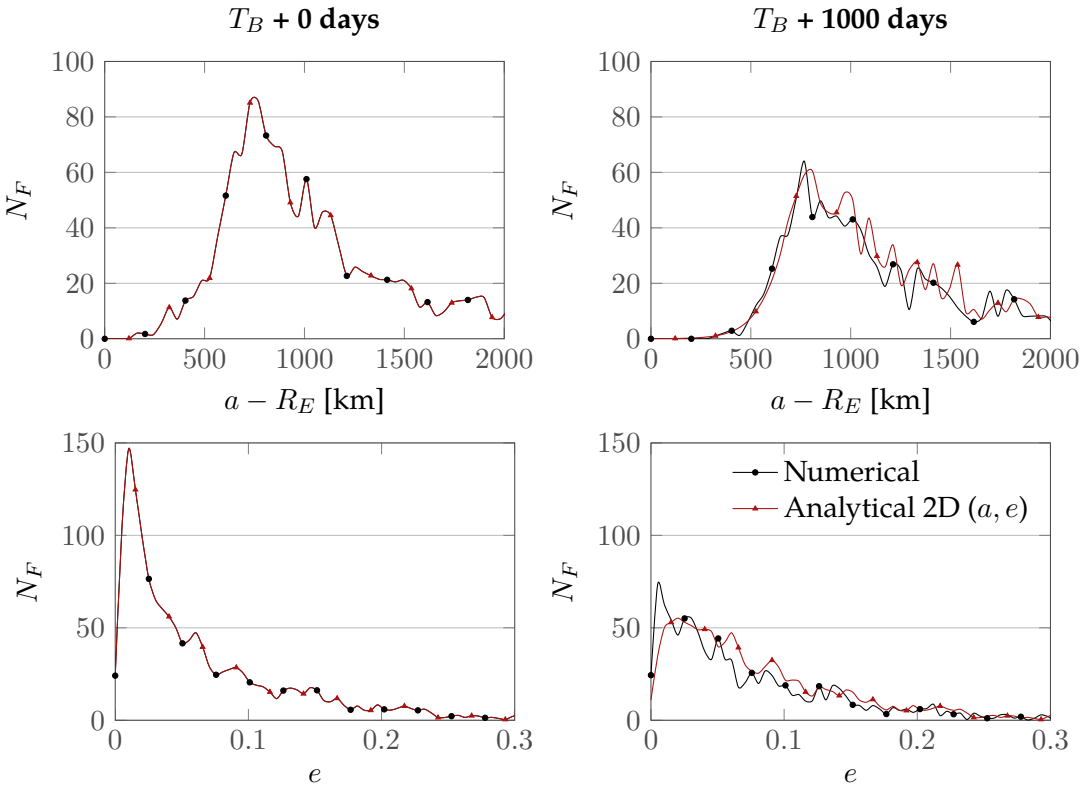

Figure 4.11: Distribution of semi-major axis and eccentricity, for a fragmentation at 700 km, at the band formation ($T_B = 92$ days) and after 1000 days.

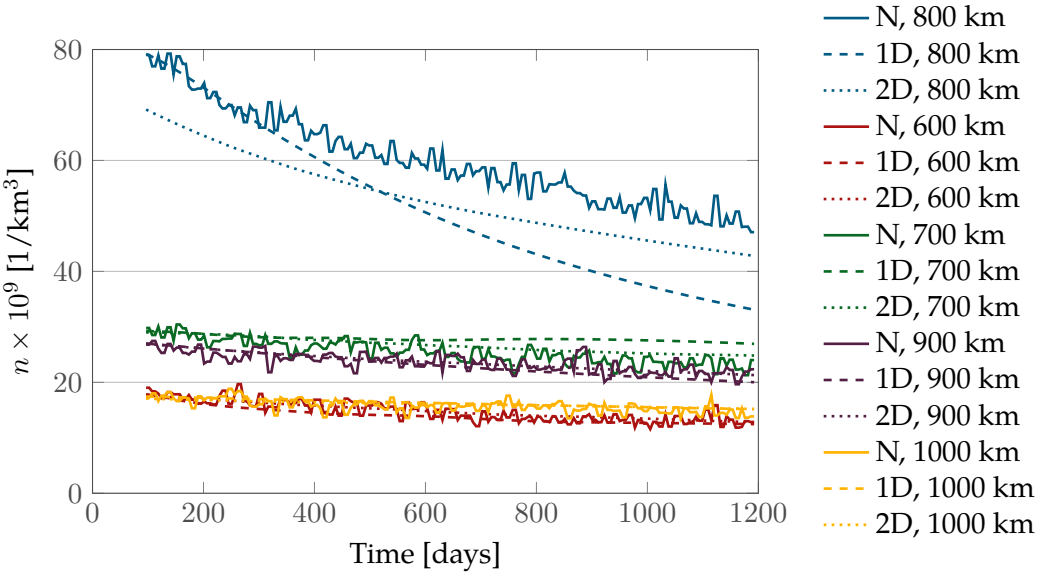

Figure 4.12: Evolution of the spatial density with time for different propagators and at different altitudes. N indicates the numerical propagation, 1D the analytical propagation based only on the geocentric radius, 2D the analytical propagation in semi-major axis and eccentricity.

These fragments, which represent the right branch of the v-shaped distribution in Figure 4.10, have the perigee of their orbits close to the breakup location, so they contribute to the density at the fragmentation altitude. With the 1D approach all the fragments at the peak location are treated in the same way because of the hypothesis $e = 0$, so the peak appears to move towards lower altitudes. With the 2D approach the information on the eccentricity is kept, so the method can distinguish between the fragments that have the breakup location closer to their perigee, which are less affected by atmospheric drag. In this way, the correct rate in the peak evolution is obtained.

Figure 4.13 shows the cloud density profile after 1000 days from the band formation for a fragmentation at six different altitudes. The value of spatial density for the numerical propagation is obtained dividing the altitude in bins with width equal to $25\,\mathrm{km}$, counting the number of fragments in each bin and dividing by the volume of the corresponding spherical shell. For the numerical propagation ten runs of the breakup model were performed to take into account the random parameters within the model. At high altitudes the accuracy of the 1D and the 2D formulation is similar. At $700\,\mathrm{km}$ only the 2D method is able to identify the correct peak location and the relative error on the peak height ($\mathrm{err}_{\mathrm{peak}}$) is halved. The case of a fragmentation at $600\,\mathrm{km}$ shows that even the 2D approach is not able to obtain an accurate prediction of the cloud evolution at such low altitudes. Note, however, that, if the fragmentation happens at very low altitude, the number of fragments after 1000 days is very low, so even the use of a continuum approach is questionable for such a limited number of samples.

Using the same measure of the method accuracy introduced in Section 2.7.2, the relative error on the density peak ($\mathrm{err}_{\mathrm{peak}}$) and on the mean error along the profile ($\mathrm{err}_{\mathrm{prof}}$) for the methods are plotted in Figure 4.14. Setting also in this case a threshold value at 0.2, which corresponds to a good visual agreement between the density profile obtained with the numerical propagation and the one with the analytical one, the 1D approach is applicable above $800\,\mathrm{km}$ and the 2D approach instead can be applied from $700\,\mathrm{km}$ and the average error on the respective ranges of applicability is similar. This extends the applicability of the method in a such a way that it can be applied along most of the altitude range of the sun-synchronous orbits, where the debris density is the highest and where there are many critical objects in terms of possible future fragmentations.

An important consequence of this improvement in the modelling is that, when the 2D formulation is adopted, the propagation with the continuity equation can be applied to study the evolution of a debris cloud for longer time periods. Figures 4.15 and 4.16 show an example of the results obtained, with a single run of the NASA breakup model, for a fragmentation at $700\,\mathrm{km}$ and one at $800\,\mathrm{km}$. For the second case, the agreement is still very good, whereas for the case at $700\,\mathrm{km}$ there is clear discrepancy between the numerical and the analytical method. However, in contrast from what happens using the 1D approach at $700\,\mathrm{km}$, the analytical propagation now overestimates the value of

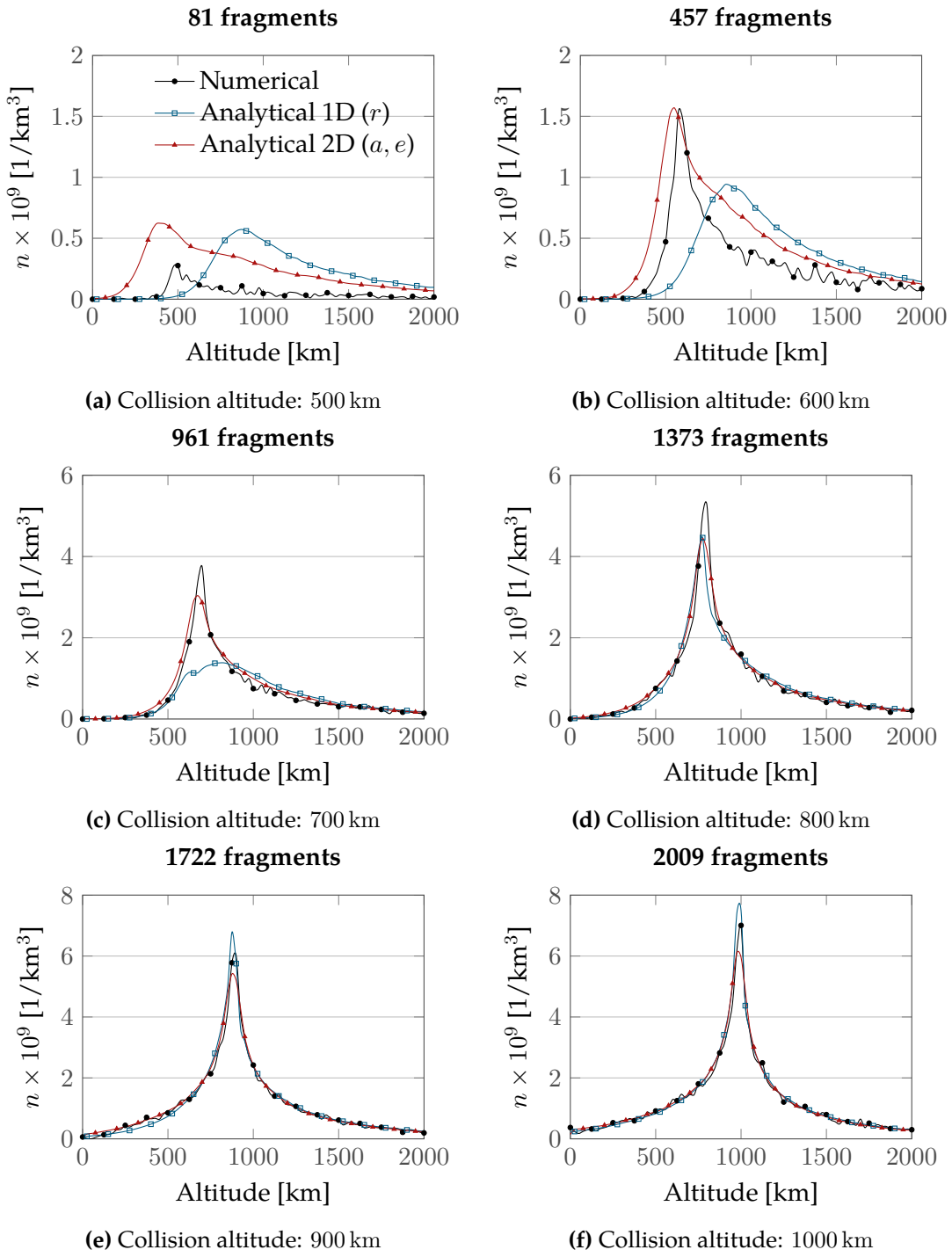

(a) Collision altitude: 500 km

(b) Collision altitude: 600 km

(c) Collision altitude: 700 km

(d) Collision altitude: 800 km

(e) Collision altitude: 900 km

(f) Collision altitude: 1000 km

Figure 4.13: Cloud density after 1000 days from the band formation for six different collision altitudes.

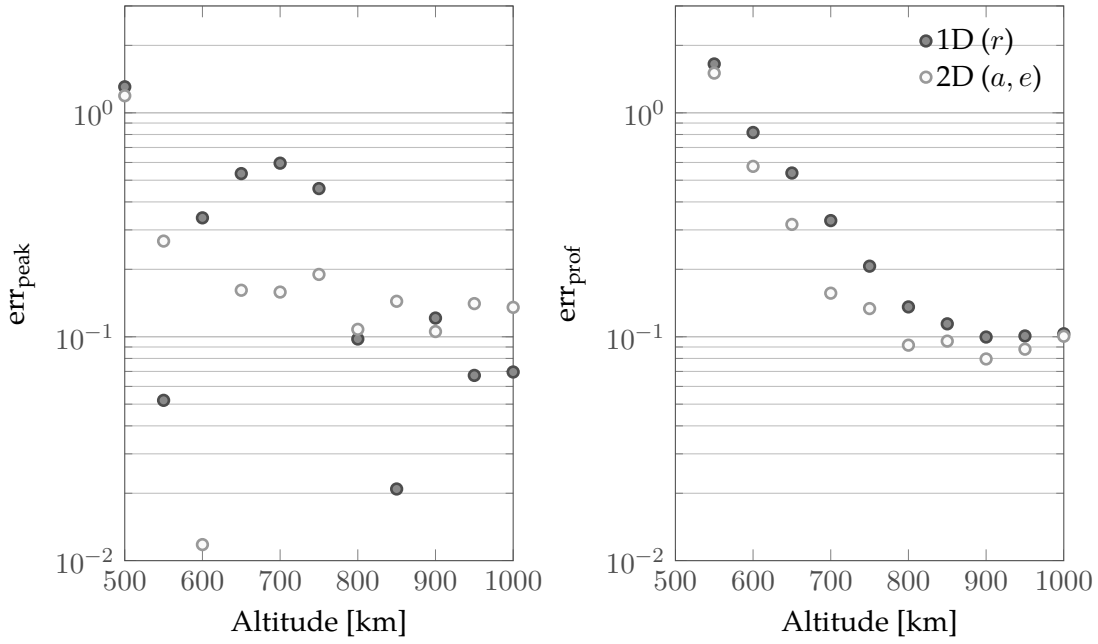

Figure 4.14: Accuracy of the method, measured by the relative error on peak (err_{peak}) and mean error along the density profile (err_{prof}) after 1000 days from the band formation, as a function of the fragmentation altitude, for analysed propagation techniques.

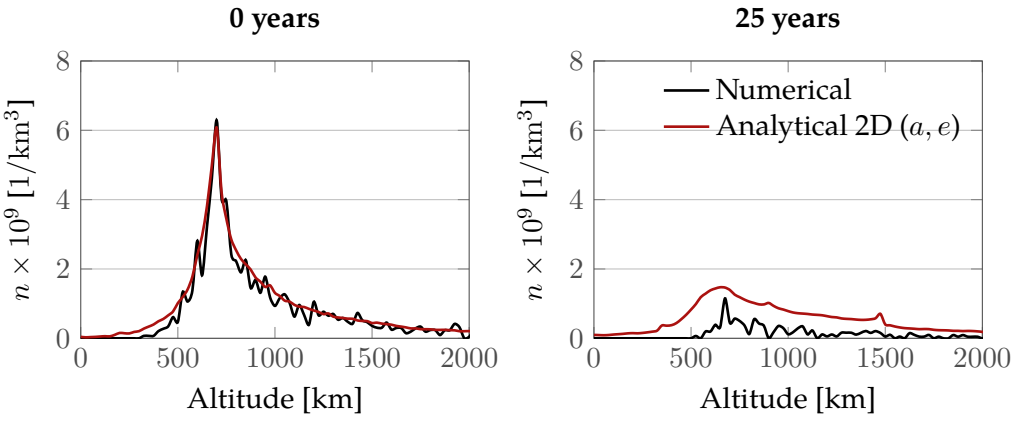

Figure 4.15: Comparison between the density profile obtained with the numerical propagation and the one from the analytical one for a fragmentation at 700 km.

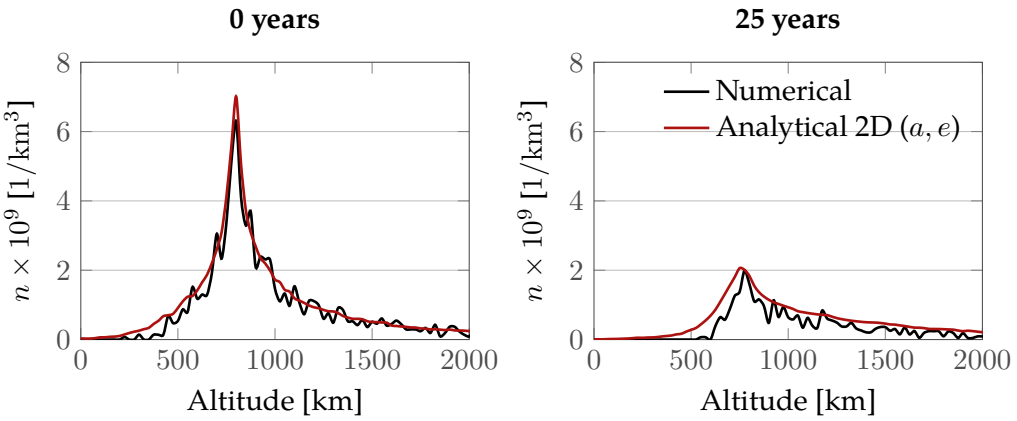

Figure 4.16: Comparison between the density profile obtained with the numerical propagation and the one from the analytical one for a fragmentation at 800 km.

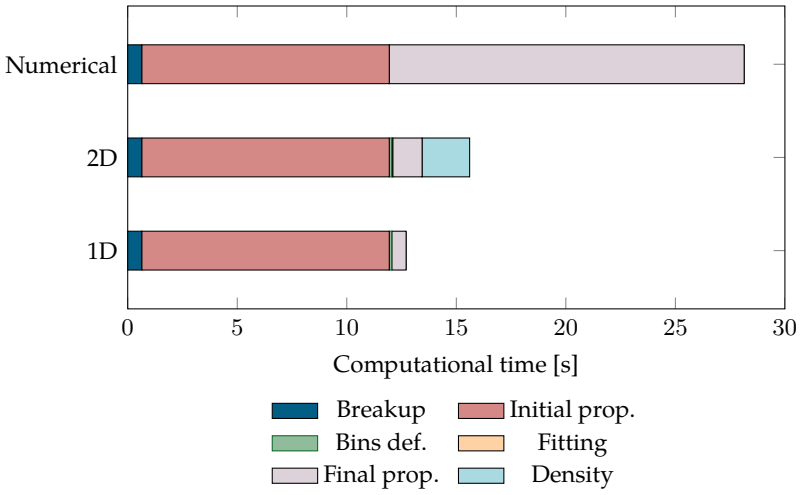

Figure 4.17: Computational time for a PC with 4 CPUs at 3.40 GHz and the division of the cloud into ten bins in A/M.

the spatial density. This means that the method will give a conservative estimation of the collision probability for a spacecraft crossing the debris cloud.

The improvement in the results is associated with an increase in the computational time that can be evaluated from Figure 4.17, which shows the time required to estimate the cloud density 1000 days after the band formation. The measured computational times refer to a PC with 4 CPUs at 3.40 GHz and the numbers in Figure 4.17 represent to the average time over ten runs. All the codes are written in MATLAB and parallelised. The propagation with the 2D formulation requires more than double the time of the 1D ($1.34\,\mathrm{s}$ compared to $0.66\,\mathrm{s}$), but the computational time is still lower than the numerical propagation. The final step of conversion from the density in the (a, e)-plane into the spatial density in $1/\mathrm{km}^3$ appears quite expensive ($2.17\,\mathrm{s}$). One can observe that, for applications when the propagation method is used to compute the collision probability for a spacecraft crossing the cloud, the value of n is required only at the target altitude, so the computation would be faster. On the other hand, when the cloud propagation is used for such application, it is not sufficient to know the state of the cloud at the final time, but a fine time step should be adopted. As at each time step the fit of a 2D function is performed, the operation could be expensive, so future work will investigate alternative implementations. In any case, it is important to highlight that the running time is only a part of the computational effort required by a simulation. The main advantage of the proposed approach is that describing the problem in terms of spatial density instead of studying the position of each objects reduces the required RAM. This means that large fragmentations (e.g. with more than 10000 fragments) can be simulated on normal PCs, without the use of supercomputers.

The saving in the computational time achieved also with the 2D approach suggests that it also can be applied to study many different fragmentation scenarios to understand which conditions affect the most the debris environment and the collision probability for operational spacecraft.

Summary

The proposed method based on the continuity equation was originally formulated in one dimension, considering only the dependence of the debris fragment density on the distance from the Earth. Actually, the method can be easily extended to multiple dimensions, using as additional variables physical parameters (such as the area-to-mass ratio) or orbital parameters. This last case is particularly interesting because it allows the effect of perturbations to be included through the classical formulation derived from Gauss' equations. The multi-dimensional formulation of the continuity equation was applied to three cases. Firstly, it allows the modelling the effect of the Earth's oblateness on the debris cloud in the first phase of its evolution. Different options for the modelling

were discussed and the following conclusions were drawn: firstly, the effect of drag should also be included in the first phase of the cloud evolution; secondly, depending on the application, it is possible to model the problem using the semi-major axis as variable and only one angle, either ω or Ω, choosing the one with the slowest dispersion. These two observations allow the optimal balance to be obtained in the trade-off between accuracy and computational time. Secondly, the 2D formulation of the method was used to describe the effect of the atmospheric drag on the debris cloud considering the distribution of the area-to-mass ratio across the cloud. This is done by treating this parameter as an additional variable of the propagation. The obtained results are coherent with the ones from the 1D formulation with the division in area-to-mass bins, proving the validity of the approach. However, the previous 1D formulation is more convenient in terms of computational time and it is therefore preferred. Finally, the method was used to include the dependence on eccentricity in the modelling of the atmospheric drag. A very simple model was formulated assuming a constant distribution of the eccentricity. It was observed that this already improves the results in such a way that the applicability of the analytical method can be extended to $700\,\mathrm{km}$. In this way, the proposed continuous approach can be applied to study the whole region of space where the debris density is maximum.

Part of the content of this Chapter is included in F. Letizia, C. Colombo, and H. G. Lewis. Improved continuity equation method for space debris cloud collision analysis, 2015e. Manuscript in preparation.

5

Collision probability with the formulation in multiple variables

The propagation method based on the 2D formulation of the continuity equation, outlined in Section 4.4, can be used for the long term evolution of the spatial density of a cloud generated by a breakup occurred between 700 and $1000\,\mathrm{km}$ in altitude. As in the 1D case, the information on the spatial density can be used to assess the collision probability for spacecraft crossing the fragment cloud.

Also in this case, the collision between a spacecraft and the fragments in a cloud is modelled as a Poisson process, so that the cumulative collision probability can be written as in Equation 3.3

$$p_c = 1 - \exp\left(-N\right) = 1 - \exp\left(-n\sigma_c\Delta v\Delta t\right)$$

where $n(r,t)$ is the fragment spatial density derived from $n(a,e,t)$, σ_c is the collisional cross sectional area, and Δv the average relative velocity between the target and the fragments.

The fragment spatial density is known thanks to the analytical method explained in Section 4.4; as with the 1D formulation, an analytical expression is available only after the fragment band is formed, so the collision probability will be studied from that moment onwards. Similarly to the 1D case, an analytical expression is sought for the relative velocity: it should be based only on the knowledge of the distribution of the fragments in the phase space (a,e), given by the analytical propagation, and it should exploit the fact that the fragments are uniformly distributed in M,ω,Ω.

5.1 Collision velocity estimation

The 2D analytical expression for the velocity can be obtained in a similar way to the one for the 1D version of the method, which was explained in Chapter 3. The same steps are retraced to understand how to include the additional information on the eccentricity.

5.1.1 Relative velocity between the target and a single fragment

To understand how the relative velocity can be estimated, it is useful to start from a simplified case with only one fragment. The relative velocity between two objects can be written with the law of cosines as

$$\Delta v = \sqrt{v_T^2 + v_F^2 - 2 v_T v_F \cos\phi} \tag{5.1}$$

where v_T and v_F indicate the magnitude of the two velocity vectors, respectively for the target and for the fragment, with respect to the central body. For the moment it is assumed that v_T and v_F are known and the attention is focussed on ϕ, which is the angle between the two vectors. Kessler (1981) provides a way to estimate this angle starting from the orbital parameters of the two objects exactly in the same situation studied in this work, i.e. one object is a target object whose orbital parameters are completely known and the second object is part of a set where ν, ω, Ω were randomised by the effect of perturbations. It is important to highlight that not knowing all the parameters for the second object means that multiple solutions for ϕ should be expected. In particular, according to Kessler (1981), ϕ can be obtained by solving the spherical triangle in Figure 5.1

$$\cos\phi = \sin\gamma_T \sin\gamma_F + \cos\gamma_T \cos\gamma_F \cos(\alpha_T - \alpha_F) \tag{5.2}$$

where the subscript T refers to the target and F to the fragment. The two angles γ and α are defined respectively as

$$\cos^2\gamma = \frac{a^2(1-e^2)}{r(2a-r)} \quad \cos\alpha = \frac{\cos i}{\cos\beta} \tag{5.3}$$

where r and β are the altitude and the latitude where we would like to estimate ϕ, that is at the target location.

Considering all possible choices for the signs of γ and α, there are 16 possible combinations that can be reduced to eight considering the property of symmetry of the trigonometric functions (Kessler, 1981). These eight possible combinations can all be described by

$$\cos\phi = \pm\sin\gamma_T \sin\gamma_F \pm \cos\gamma_T \cos\gamma_F \cos(\alpha_T \mp \alpha_F) \tag{5.4}$$

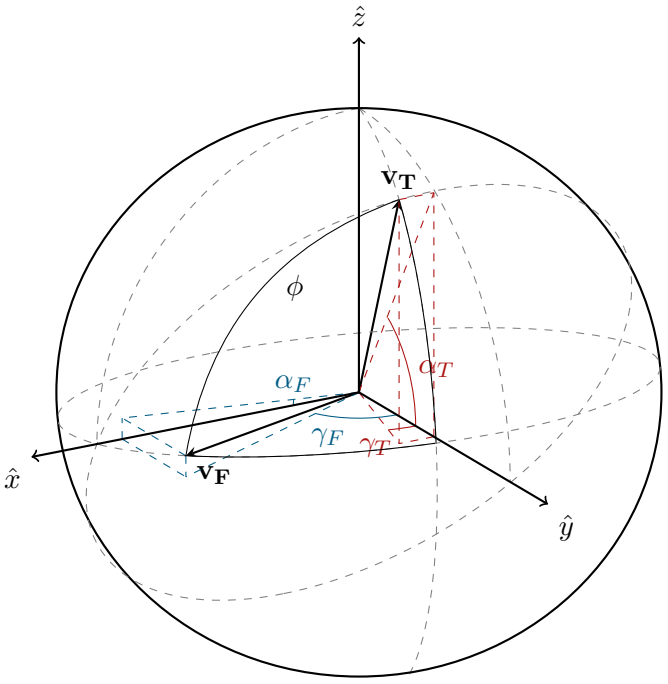

Figure 5.1: Definition of the angles between the velocity vectors according to Kessler (1981).

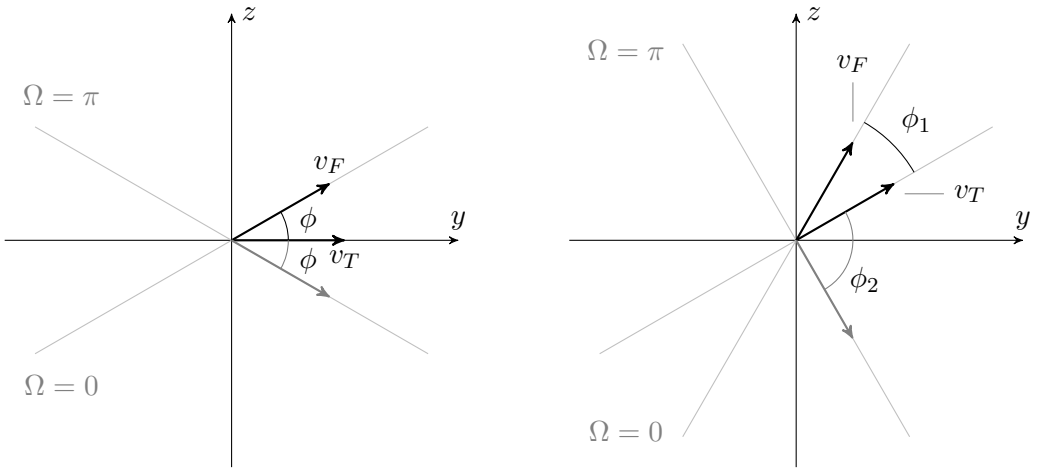

(a) Equatorial target orbit

(b) Non-equatorial target orbit

Figure 5.2: Velocity diagrams

where now the angles are always taken in absolute value. Out of the eight combinations, only four are compatible with the geometry of the problem. Note that, since no information is available on ν, ω, Ω, it is not possible to further reduce the number of solutions, except for simple equatorial, circular cases. Therefore, with this method, the relative velocity between the target and a fragment is the average among the four possible values associated with the four possible values of ϕ.

To understand how to reduce Equation 5.4 to only four possible solutions, it is convenient to consider a simplified case when the target is on a circular and equatorial orbit, and

the fragment is on a circular orbit with the same radius as the target. In this case

$$\cos^2 \gamma_T = 1 \quad \sin \gamma_T = 0 \quad \alpha_T = 0 \quad \alpha_F = \pm i_F$$

and

$$\cos \phi = \pm \cos i_F. \tag{5.5}$$

It is easy to observe that only one sign of $\cos \phi$ in Equation 5.5 is admissible, depending on the direction of motion of the target and of the fragment along their orbits. For example, Figure 5.2a shows the two vectors $\mathbf{v_T}$ and $\mathbf{v_F}$ on the (y, z)-plane in the case that Ω_F = 0; the angle ϕ is equal to the inclination of the fragment orbit. This is true also for the case with $\Omega_F = \pi$ (shown in grey in Figure 5.2a) and so, in this situation, the correct choice is the positive sign for $\cos \phi$ in Equation 5.5.

Also relaxing the hypothesis on $i_T = 0$, it is possible to obtain a similar velocity diagram, as shown in Figure 5.2b. In this case

$$\cos \phi = \pm \cos \left(i_T \mp i_F \right) \tag{5.6}$$

and also here only the positive sign is compatible with the problem geometry; the sign in the cosine captures the two possible values of ϕ due to the different possible values of Ω. Therefore, the information on the inclination of target and fragment orbits can be used to decide the sign for $\cos \phi$: positive, if they are both on direct or retrograde orbits (same direction of motion); negative otherwise. The condition on the sign of $\cos \phi$ allows the only four possible values for ϕ to be selected to estimate Δv, depending on the difference in inclination between the two orbits.

The formulation from Kessler (1981) is a useful starting point for the current application, but it requires some modifications to consider two aspects. Firstly, it introduces a dependence on the target latitude β, which is not followed in the propagation because of its fast evolution compared to the time scale of the problem. As already observed, in the current case, the value of the latitude β at a certain time instant is not representative of the entire time step as it is much longer than one orbit. Following the target trajectory with a very fine time step (i.e. shorter than one orbit) would result in a unnecessary large computational effort, so the formulation should be modified to consider an average value for β or to be independent of it. Secondly, the value of Δv is found by averaging the four possible solutions compatible with the problem geometry, whereas in our case it would be convenient to exploit the fact that there is a large number of fragments that occupy all the possible geometrical configuration, rather than performing the average operation for each fragment.

5.1.2 Relative velocity between the target and a cloud of fragments

Kessler (1981) applies the expressions to a small number of objects[1], so the value of the relative velocity is found as an average of all the possible values from Equation 5.2. In the case of space debris clouds there are thousands of objects with (Ω, ω) equally distributed among them. In this case, averaging among the extremes of the distribution leads to a systematic error because the relationship between the angle ϕ and the distributed angles (Ω, ω) is not linear. This was observed considering in particular the dependence of ϕ on the difference in the longitude of the ascending nodes $\Delta\Omega$ in the case of two circular orbits,[2] and it was used in Chapter 3 to express the relative velocity in the 1D case. There it was found that ϕ can be rewritten as

$$\cos\phi = \sin(i_T)\sin(i_F)\cos(\Delta\Omega) + \cos(i_T)\cos(i_F). \tag{5.7}$$

Given that Ω is uniformly distributed among the fragments, the average relative velocity $\Delta\bar{v}$, can be found computing the integral mean[3] of the function

$$\Delta v = \sqrt{v_T^2 + v_F^2 - 2v_T v_F \cos\gamma_F \left[\sin(i_T)\sin(i_F)\cos(\Delta\Omega) + \cos(i_T)\cos(i_F)\right]} \tag{5.8}$$

for $\Delta\Omega$ from 0 to 2π. Observe that in Equation 5.8 the term $\cos\gamma_F$ from Kessler (1981) was reintroduced to consider that in the studied collision scenarios the fragments are usually in non-circular orbits.[4] Similarly to what was done in Chapter 3, by setting

$$\chi = v_T^2 + v_F^2 - 2v_T v_F \cos\gamma_F \cos(i_T)\cos(i_F) \qquad \eta = 2v_T v_F \cos\gamma_F \sin(i_T)\sin(i_F)$$

the average value of the relative speed can be written as

$$\Delta\bar{v} = \frac{2}{\pi}\sqrt{\chi+\eta}\,\mathrm{E}\left[\frac{2\eta}{\chi+\eta}\right], \tag{5.9}$$

where $\mathrm{E}[x]$ is the complete elliptic integral of the second kind.

5.1.3 Orbital parameter distribution

The expression in Equation 5.9 was obtained assuming v_T and v_F as known. This is true for the target, whose trajectory is numerically propagated and whose parameters are all known. However, the velocity of the single fragments is not known because the analytical propagation provides the distribution of the fragments in the (a, e)-plane, so this is the only available information to estimate the fragment velocity. Given that the

[1] The eight outer moons of Jupiter.

[2] We are assuming that the inclination i and the longitude of the ascending node Ω are the parameters that drive the value of ϕ because they define the difference in the two orbital planes.

[3] Integral mean of a generic function f obtained from $\frac{1}{b-a}\int_a^b f(x)\,dx$

[4] while the target is still assumed to be in a circular orbit

information on the velocity of the fragments is required at the intersection of the target orbit, v_F can be estimated computing the orbital speed at the target latitude for an object with given semi-major axis

$$v_F = \sqrt{2\mu \left(\frac{1}{r_T} - \frac{1}{2a_F} \right)}. \tag{5.10}$$

Equation 5.10 is applied to all the points in the (a, e)-plane, so Equation 5.8 is actually a matrix expression

$$\boldsymbol{\Delta \mathbf{v}} = \sqrt{v_T^2 + \mathbf{v_F}^2 - 2 v_T v_F \cos \boldsymbol{\gamma_F} \left[\sin\left(i_T\right) \sin\left(i_F\right) \cos\left(\Delta\Omega\right) + \cos\left(i_T\right) \cos\left(i_F\right) \right]} \tag{5.11}$$

with $\mathbf{v_F}$ and $\boldsymbol{\gamma_F}$ varying across the domain.

The scalar single value of Δv, which will then be used in Equation 3.3 to estimate the collision probability, is finally obtained through a weighted average using the density as a weighting factor

$$\Delta \bar{v} = \frac{\iint n(a,e) \Delta v(a,e) \, \mathrm{d}a\mathrm{d}e}{\iint n(a,e) \, \mathrm{d}a\mathrm{d}e}. \tag{5.12}$$

The estimation is refined by considering which combinations of (a, e) actually correspond to orbits that intersect the target trajectory. A matrix $\mathbf{C}(a, e)$ can be defined in the following way

$$\mathbf{C}(a_j, e_k) = \begin{cases} 1, & \text{if } a_j(1 - e_k) \leq r_T \leq a_j(1 + e_k) \\ 0, & \text{otherwise} \end{cases}$$

and then Equation 5.12 becomes

$$\Delta \bar{v} = \frac{\iint \mathbf{C}(a,e) n(a,e) \Delta v(a,e) \, \mathrm{d}a\mathrm{d}e}{\iint \mathbf{C}(a,e) n(a,e) \, \mathrm{d}a\mathrm{d}e}. \tag{5.13}$$

5.2 Validation

Equation 5.13 provides a fast method to estimate the average relative velocity between the target and the fragments once the target trajectory and the cloud density are known. On the other hand, some hypotheses were introduced to deal with the lack of information about the parameters ω and Ω. For this reason, the approach was validated with the same numerical procedure used as a benchmark for the 1D case and detailed in Appendix A.3. The numerical estimation is based on the computation of the minimum distance along the nodal line between the orbit of the target and the one of each fragment (Figure 5.3). When the distance is below a certain threshold (e.g. $10\,\mathrm{km}$), the relative velocity between the target and the fragment is computed and stored to estimate the average value.

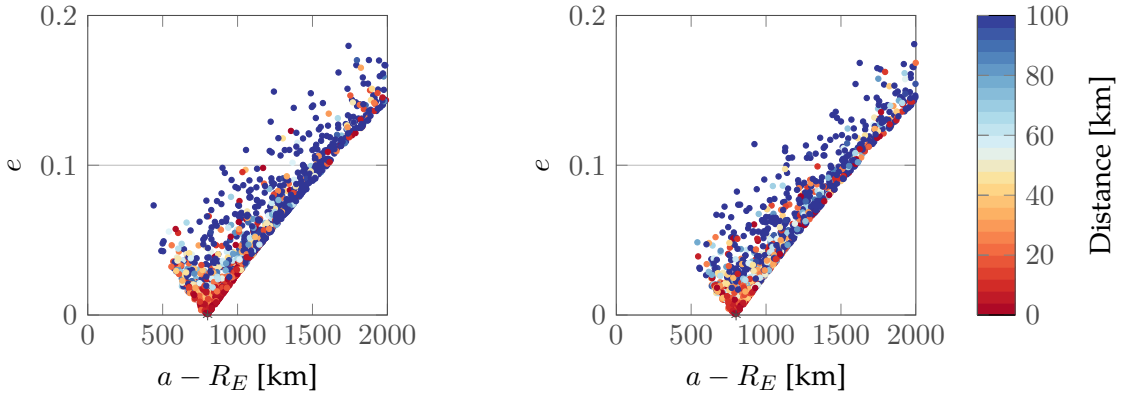

(a) F(30,800)T(60,800) **(b)** F(60,800)T(60,800)

Figure 5.3: Distribution of the distance from the target orbit among the fragments at the band formation for two simulated cases. The cases are indicated with the notation F(i_F,$a_F - R_E$)T(i_T,$a_T - R_E$).

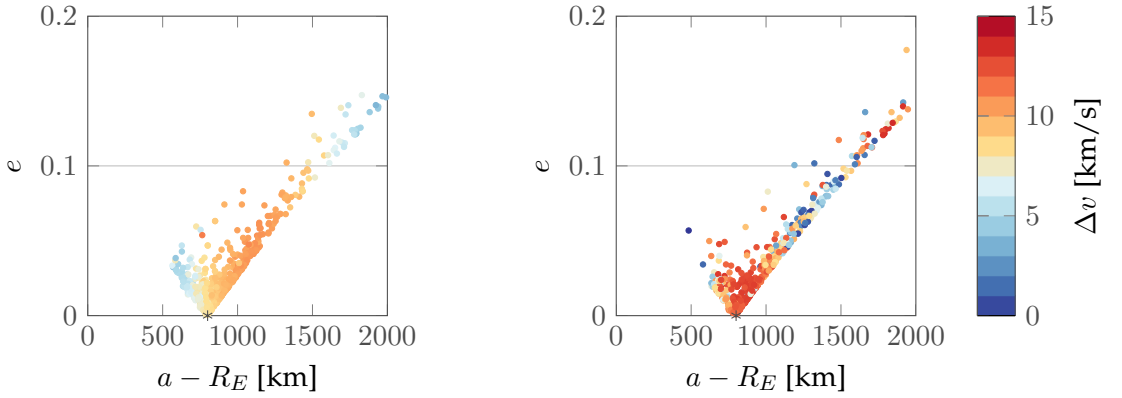

(a) F(30,800)T(60,800) **(b)** F(60,800)T(60,800)

Figure 5.4: Relative velocity Δv_N distribution among the fragments with distance lower than 50 km at the band formation for two simulated cases. The cases are indicated with the notation F(i_F,$a_F - R_E$)T(i_T,$a_T - R_E$).

The validation process was carried out for different combinations of target altitudes and inclinations with respect to the parent orbit from which the cloud is generated. The target mass and size were set considering the average values among possible targets (Rossi et al., 2013); in particular,

$$A_T = 11\,\mathrm{m}^2 \quad M_T = 2322\,\mathrm{kg}.$$

The propagation of the target starts from the moment when the fragment band is formed. Some examples of the results obtained during the validation process are presented in Figure 5.4, which shows the distribution of the relative velocity Δv among the fragments for different cases, indicated with the notation

$$\mathrm{F}(i_F,a_F - R_E)\mathrm{T}(i_T,a_T - R_E),$$

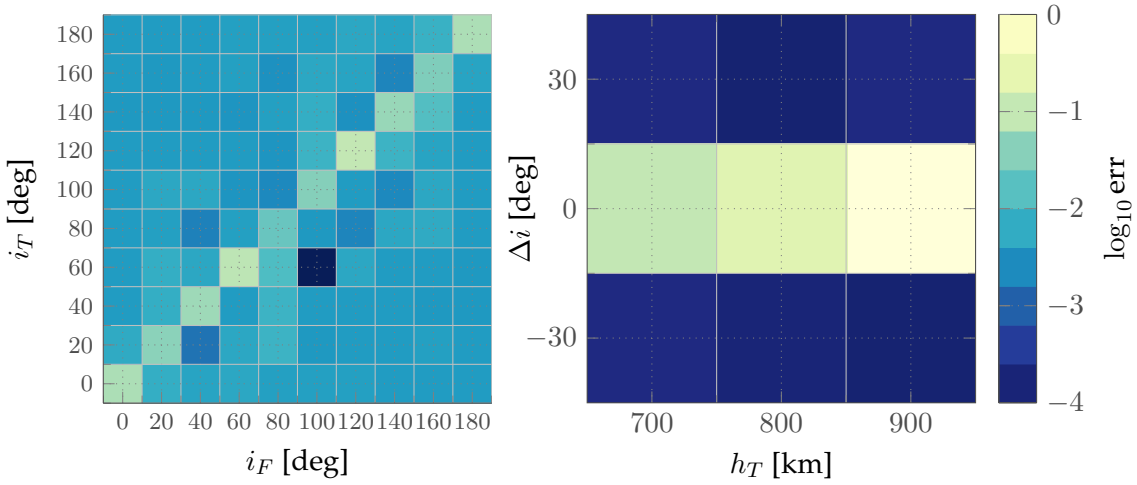

Figure 5.5: Relative error in the estimation of the relative velocity between target and fragments for several configurations with variation (a) in inclination and (b) in altitude. Propagation time equal to five years.

where F refers to the orbital parameters of the fragmentation parent orbit and T to the ones of the target spacecraft crossing the cloud. It is possible to observe how the value of Δv is affected by the inclination of the target orbit and by the one of the fragmentation orbit. Keeping in mind the velocity diagram in Figure 5.2b, in the case F(60,800)T(60,800) the maximum Δv (i.e. the one when fragments and target have opposite directions of motion) is much larger than in the case F(30,800)T(30,800) and this is reflected in the distribution of the velocity in Figure 5.4. While in Figure 5.4a a dependence on the semi-major axis is visible, in Figure 5.4b the value of Δv appears less correlated with the semi-major axis. This suggests that for increasing inclination values other parameters play a major role, As larger inclination means slower band formation and larger orbital plane differences, the distribution may be explained as a result of the non-uniform distribution of the longitude of the ascending nodes among the fragments that intersect the target orbit.

The results of the validation are shown in Figure 5.5 that presents the *average* relative error on a five-year simulation for different combinations of the target and the fragment inclination and altitude. As in Chapter 3, the accuracy of the approach is measured by computing

$$\overline{\text{err}}_{\text{rel}} = \frac{\int |\Delta v_A - \Delta v_N| \, \mathrm{d}t}{\int \Delta v_N \, \mathrm{d}t}, \tag{5.14}$$

where Δv_N is the estimation of the velocity obtained using the numerical procedure and Δv_A is the analytical estimation described in Section 5.1.

Focussing on the variation of inclination, it can be observed that the error is usually low, with an average value, among the 100 tested cases, equal to 0.0095. The error is

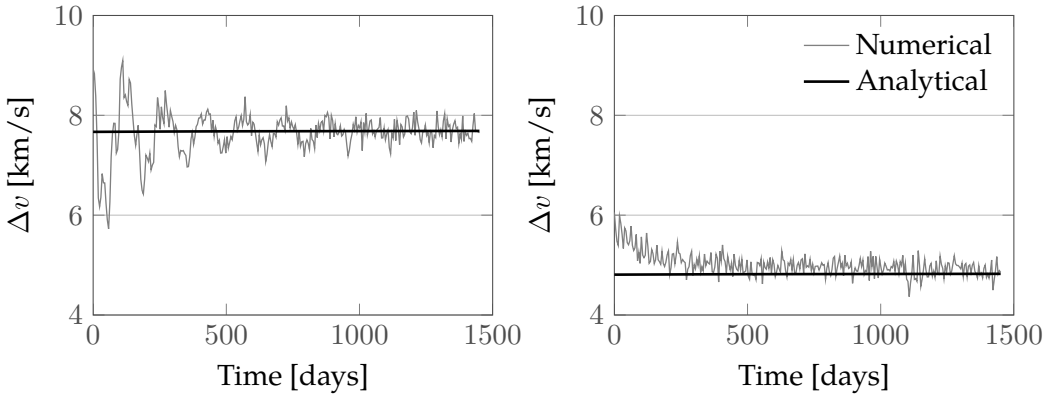

(a) F(30,800)T(60,800) ($\overline{\text{err}}_{\text{rel}} = 0.005$) **(b)** F(30,800)T(30,800) ($\overline{\text{err}}_{\text{rel}} = 0.039$)

Figure 5.6: Comparison between the reference relative velocity Δv_N in grey and the analytical estimation Δv_A in black. The time is measured from the band formation.

maximum for the cases with the same value of inclination for target and fragment cloud; the maximum error is equal to 0.0876.

Figure 5.6 is useful to better understand the numbers in Figure 5.5. Figure 5.6 represents the value of the reference relative velocity (in grey) and of the analytical estimation (in black) along the considered time window. In Figure 5.6a, the case F(30,800)T(60,800) with $\overline{\text{err}}_{\text{rel}} = 0.005$ is presented: the reference relative velocity oscillates with time because the target's and the fragments' orbits have different inclination, and, therefore, they are subject to different precession rates of their orbital planes. In addition, as Ω is not equally distributed among the fragments close to the target orbit, the average $\Delta\Omega$ between the target and the fragments changes with time. On the other hand, the analytical estimation changes much more slowly. In fact, considering the expressions in Equations 5.1 and 5.13, one can observe that having removed the dependence on the latitude, $\overline{\Delta v}$ varies only following the (slow) evolution of the target orbital parameters and of the cloud density. Figure 5.6b shows the case F(30,800)T(30,800) with $\overline{\text{err}}_{\text{rel}} = 0.039$: in this case target and fragments have the same inclination, so the oscillations are less defined than in the previous case.

Figure 5.7 shows the distribution of ϕ as a function of $\Delta\Omega$ for the case F(30,800)T(30,800) at $t = 500$ days after the band formation. Each grey dot represents a fragment and the light grey dashed line indicates the average ϕ among all fragments; the white dots represent the fragments with distance smaller than 50 km and the black dashed line indicates the average ϕ obtained from this set of fragments. Finally, Equation 5.7, the analytical expression for the dependence of ϕ on $\Delta\Omega$, is plotted in blue and the average value is indicated with the dashed blue line. As expected, the fragments are distributed along the theoretical line in black; the dispersion across the line is due to the effect of the fragment argument of perigee ω, which is not described in Equation 5.7.

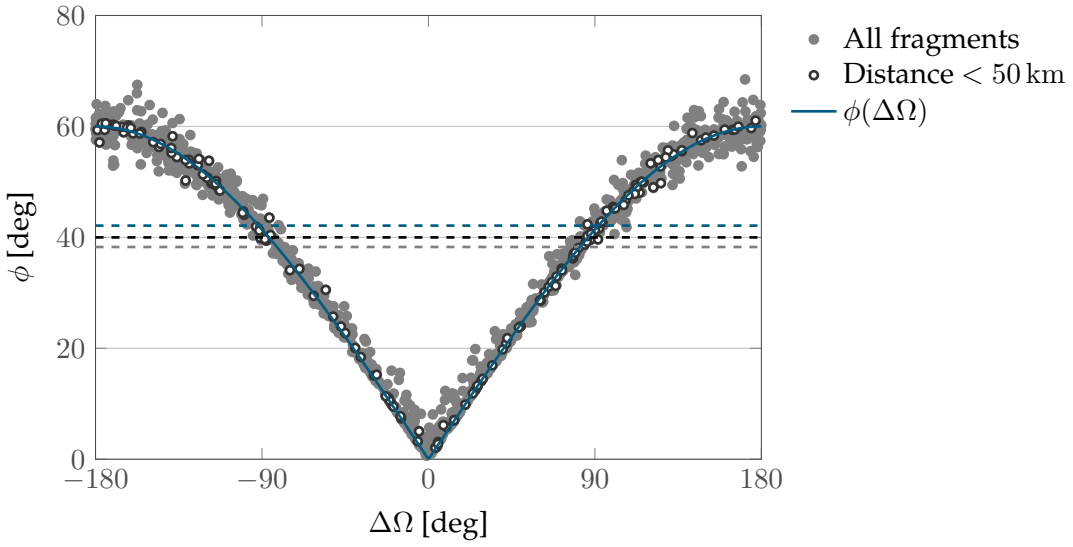

Figure 5.7: Distribution of ϕ as a function of $\Delta\Omega$ for the case F(30,800)T(30,800) at $t = 500$ days.

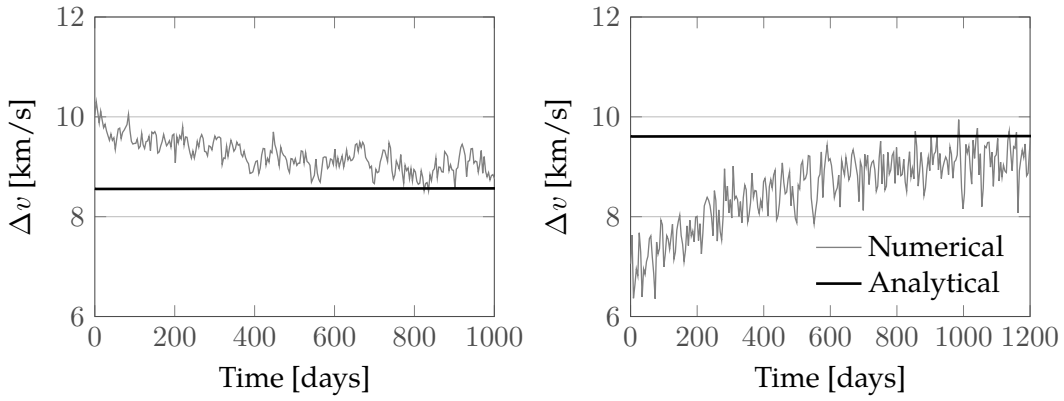

(a) F(63,800)T(63,800) ($\overline{\text{err}}_{\text{rel}} = 0.066$)

(b) F(90,800)T(90,800) ($\overline{\text{err}}_{\text{rel}} = 0.117$)

Figure 5.8: Comparison between the reference relative velocity Δv_N in grey and the analytical estimation Δv_A in black. The time is measured from the band formation. T_B = 203 days in a and T_B = 669 days in b.

It is also interesting to observe the two particular cases in Figure 5.8 that represents the estimated relative velocity for the case F(63,800)T(63,800) and F(90,800)T(90,800). These cases are interesting because for these values of inclination $\dot{\omega}$ and $\dot{\Omega}$ due to the Earth's oblateness are null. One could expect that the band would not form in these cases, but actually the breakup causes a dispersion of the initial inclination of the fragments, so that they spread and a band is formed also for fragmentation originating from these critical values of inclination, though in a longer time.

Still, the fragments with inclination very close to 63° or 90° will have a very slow variation of ω and Ω respectively and this can be observed in Figure 5.8 as the *delay* in approaching the asymptotic value given by the analytical method. This behaviour is more evident for the case at 90° ($\overline{\text{err}}_{\text{rel}} = 0.117$) than for the one at 63° ($\overline{\text{err}}_{\text{rel}} = 0.066$) because Ω defines

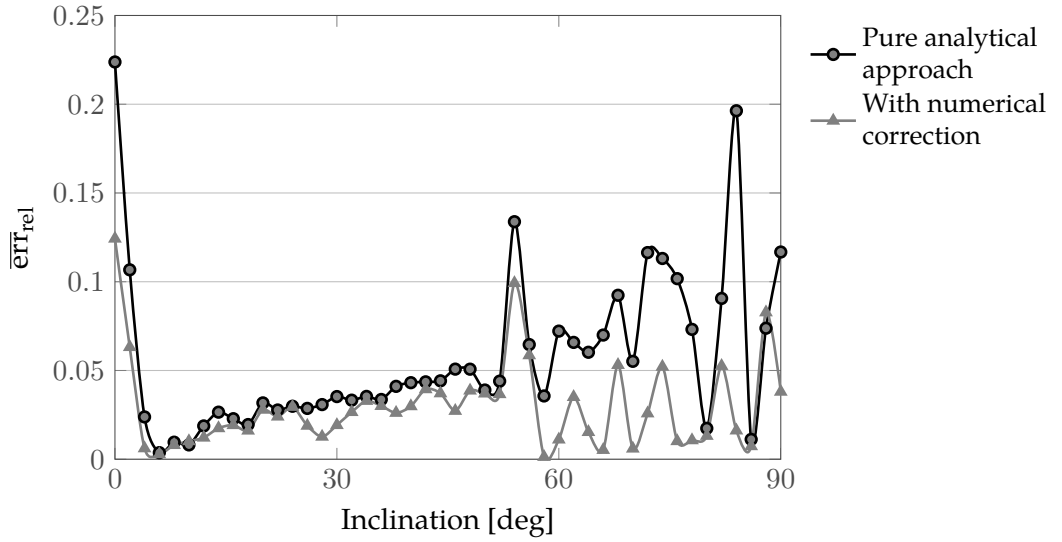

Figure 5.9: Relative error in the estimation of the relative velocity for the cases with $i_T = i_F$.

the orbital plane and has, therefore, a greater influence than ω on the value of the relative velocity.

5.2.1 Error for target and fragmentation with the same inclination

It was observed in Figure 5.5 that the error is maximum for the cases where $i_T = i_F$. The reason for this behaviour can be inferred by the comparison of Figure 5.6a and Figure 5.6b: as already discussed, when $i_T \neq i_F$, the evolution of Δv presents some oscillations around an average value that is well captured by the analytical approach; in the case $i_T = i_F$, instead, the value predicted by the analytical method acts as an *asymptotic* value, so the Δv is always underestimated (Figure 5.8a) or overestimated (Figure 5.8b). This explains why the error is larger for the cases with $i_T = i_F$. This behaviour is due to the fact that the initial $\Delta\Omega$ between the target and the fragments that cross its orbit is constant as for the orbit i is the same and so $\dot{\Omega}$. For the same fragmentation, the value of the relative velocity will be underestimated or overestimated depending on the initial value of Ω_T.

Figure 5.9 shows the value of the error on a fine grid with a simulation every two degrees of inclination; the plot shows only the values for $i \in [0, \pi/2]$ because the part for $i \in [\pi/2, \pi]$ is symmetrical. The curve clearly shows that for some inclinations the relative error reaches a very large value that can affect the reliability of the results. As already observed in Figure 5.8, excluding the equatorial case, the largest values of error are registered for those inclinations associated with a slow band formation.

For the equatorial case, the causes of the large error are still under investigation. The preliminary analysis seems to suggest that the probability of finding the fragments at

the target altitude should be included in Equation 5.13. This can be done by exploiting again Equation 2.24 that express the probability of finding an object at a certain altitude given its semi-major axis and eccentricity.

For the cases with slow band formation, it may be beneficial to *correct* the evolution of the Δv describing the approach towards the asymptotic value Δv_a with the classical expression of the transient for a first order system (Baruh, 1999)

$$\Delta v(t) = \Delta v_a + k \exp\left(-\frac{t}{\tau}\right). \tag{5.15}$$

The parameters k and τ need to be estimated from the initial (*real*) value of Δv and so they require to run once, at the band formation, the numerical method to estimate Δv. Indicating with Δv_0 the value of Δv at the initial time, k is simply

$$k = \Delta v_0 - \Delta v.$$

τ instead is the time constant of the problem and it can be estimated by looking at the evolution of the Δv from the breakup to the band formation. In detail, inverting Equation 5.15 to find τ, one gets

$$\tau = \frac{-t}{\log\left(\frac{\Delta v(t) - \Delta v_a}{k}\right)}$$

that can be evaluated at the breakup where both

$$t = -T_B \quad \text{and} \quad \Delta v(t) = \Delta v_B$$

are known. In fact, T_B is the time for the band formation and Δv_B is the relative velocity between the target and an object on the parent orbit of the fragmentation. An example of the results obtained with this approach is shown in Figure 5.10, which refers to the case with $i = 84°$.

Besides this numerical correction, also some analytical corrections were tested: they are based on the equation for $\dot{\Omega}$ and the fragment inclination distribution. They give good results for some values of inclinations, but they are not yet robust enough to be applied generally. In any case, this suggests the existence of a link between the evolution of Δv and the dispersion of Ω. Future work will further investigate this aspect with the aim of reaching a full analytical formulation.

5.2.2 The case at 84 degrees

Figure 5.9 shows the value of the relative error on the estimation of the velocity for the cases with $i_T = i_F$. In particular, it could be interesting to study why the maximum error is observed at 84 degrees. The process of formation of the band can be split into

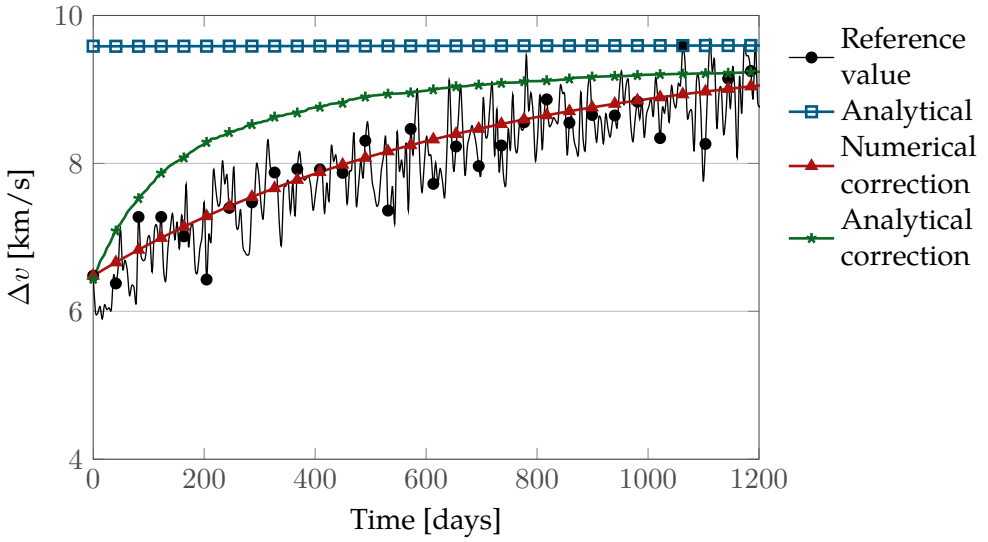

Figure 5.10: Δv evolution for the case $i = 84°$ and correction.

two steps: the fragment with the fastest nodal rate reaches the same Ω as the slowest one, then the fragments' Ω spreads within the band to reach a uniformly distributed configuration. The first phase can be described considering the difference between the minimum and the maximum rate of variation of ω and Ω within the cloud. As the focus is on the case at 84 degrees, only the effect of Ω will be considered. The variation of Ω is given by Equation 2.5

$$\dot{\Omega} = -\frac{3}{2} J_2 \frac{R_E^2}{p^2} \bar{n} \cos i$$

where J_2 is the second zonal harmonic coefficient for the Earth's gravitational potential, R_E is the Earth's radius, p is the orbit semilatus rectum, $\bar{n}$ the orbital mean motion and i the orbit inclination. Within a cloud, the element that affects $\dot{\Omega}$ the most is the semi-major axis a, present both in the $p = a(1 - e^2)$ and in $\bar{n} = \sqrt{\mu / a^3}$, as shown in Figure 5.11.

To highlight the effect of inclination, the hypothesis that all fragments have the same semi-major axis is introduced. After the breakup, the fragments will have a certain dispersion in inclination (as shown also in Figure 5.11). For a case with *low* inclination $\cos(i)$ will have the same sign for all the fragments. The process of the band formation will follow an evolution such as the one in Figure 5.12a, where each arc represents a different time instant. The innermost arc represents the dispersion of Ω in the cloud at the initial time, whereas arcs with larger radius indicate later time instants. In the case of 90° half of the fragments will have $\dot{\Omega} > 0$ and the other half $\dot{\Omega} < 0$, so the process of the band formation is such as in Figure 5.12b. Observe here that, even if the absolute value of $\dot{\Omega}$ is lower for the case with $i = \pi/2$, the band formation requires a similar amount of time because the band expands in two directions. The value of inclination where this behaviour starts to occur depends on the initial fragment spreading caused by the breakup. For the case studied in Figure 5.9, which represents a non-catastrophic collision with a projectile mass equal to $100\,\mathrm{g}$ and relative velocity equal to $1\,\mathrm{km/s}$, the

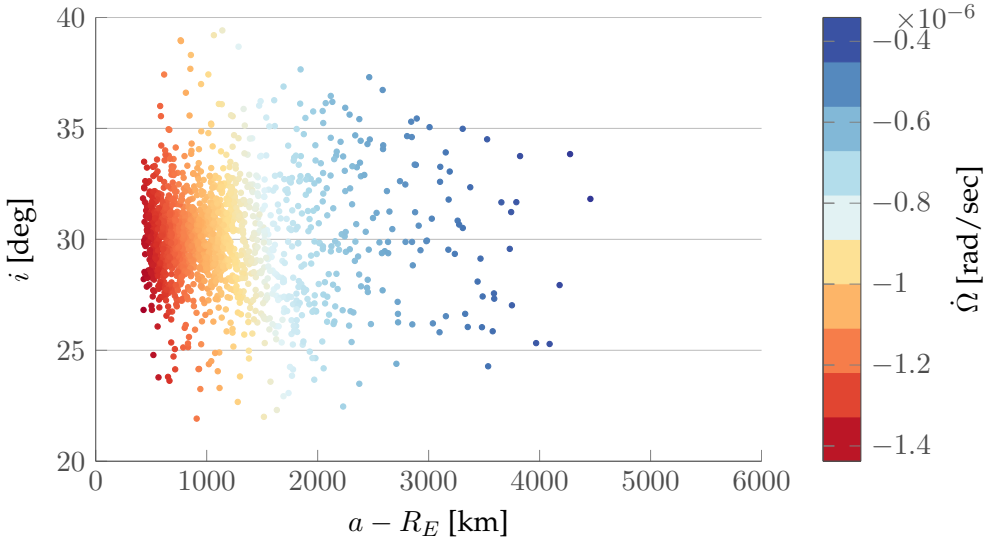

Figure 5.11: Distribution of $\dot{\Omega}$ across the cloud as a function of semi-major axis and inclination for a fragmentation on an orbit with 30 degrees of inclination.

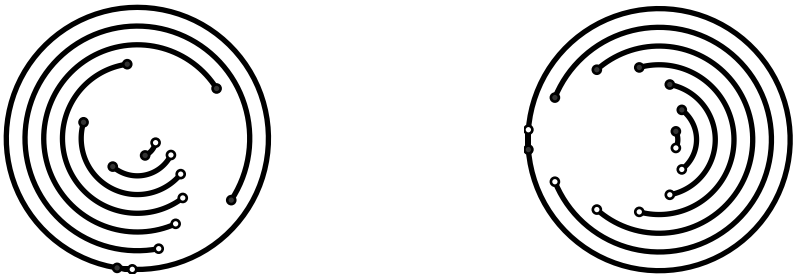

(a) 84°

(b) 90°

Figure 5.12: Representation of the band formation for two clouds at different inclinations.

maximum Δi is equal to 4.26° among the fragments with perigee altitude larger than $50\,\mathrm{km}$.

One could expect this value to have a strong dependence of the collision energy: this is true only if the absolute maximum inclination difference is registered; the dependence is less strong if only the fragments with perigee altitude h_p larger than $50\,\mathrm{km}$ and the value of 0.95 quantile are considered. This means that the transition in the behaviour of the time for the band formation is expected to occur always around the same values of inclinations.

For the case with projectile mass equal to $100\,\mathrm{g}$ and $v = 1\,\mathrm{km\,s^{-1}}$, the estimated time (at the breakup) for the band closure from the value of $\dot{\Omega}$ among the fragments with $h_p > 50\,\mathrm{km}$ and Δi within the 0.95 quantile is shown in Figure 5.14, where the maximum value is not at 90°, but, in this case, around 88°.

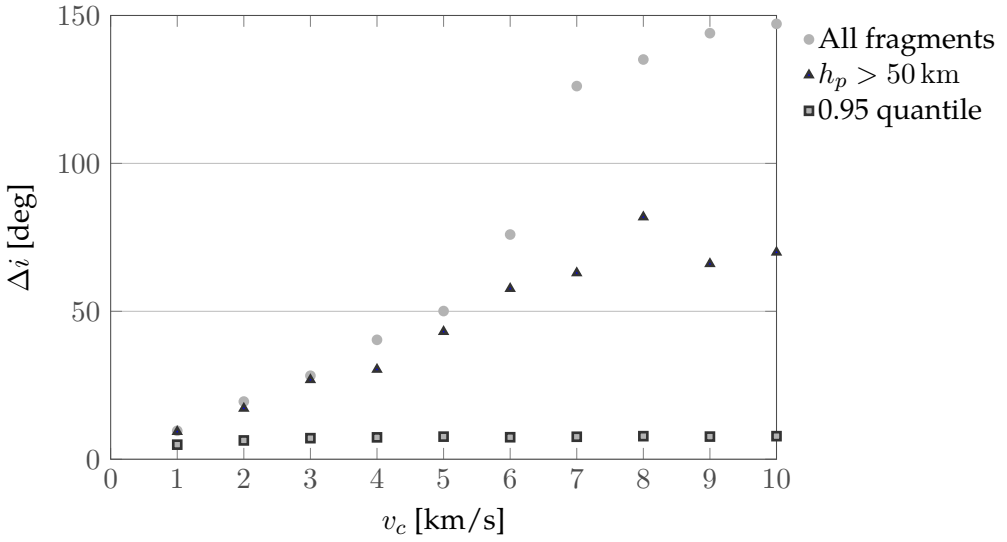

Figure 5.13: Maximum variation of inclination as a function of the collision velocity.

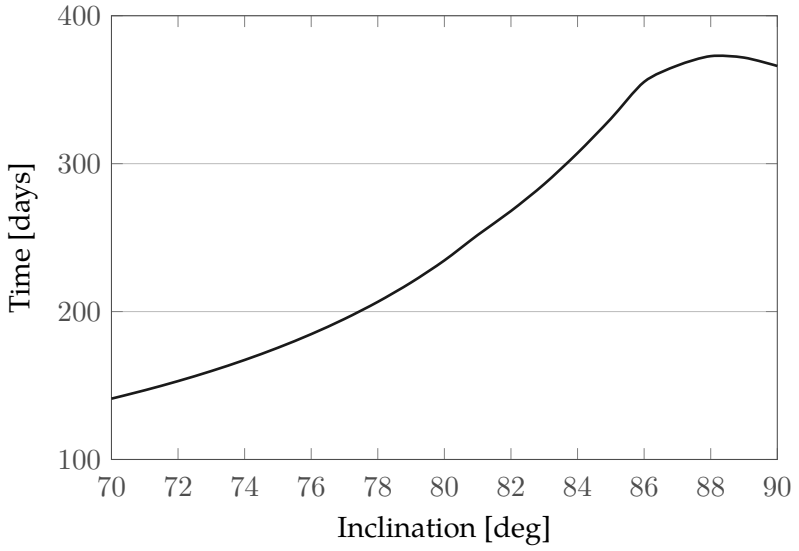

Figure 5.14: Time for band clousure.

5.3 Collision probability computation

As in Chapter 3, the analytical estimation of the relative velocity allows computing the average number of collisions N in a time interval Δt as in Equation 3.1

$$N = n\Delta v \sigma_c \Delta t$$

and the resulting collision probability Equation 3.3

$$p_c = 1 - \exp(-N).$$

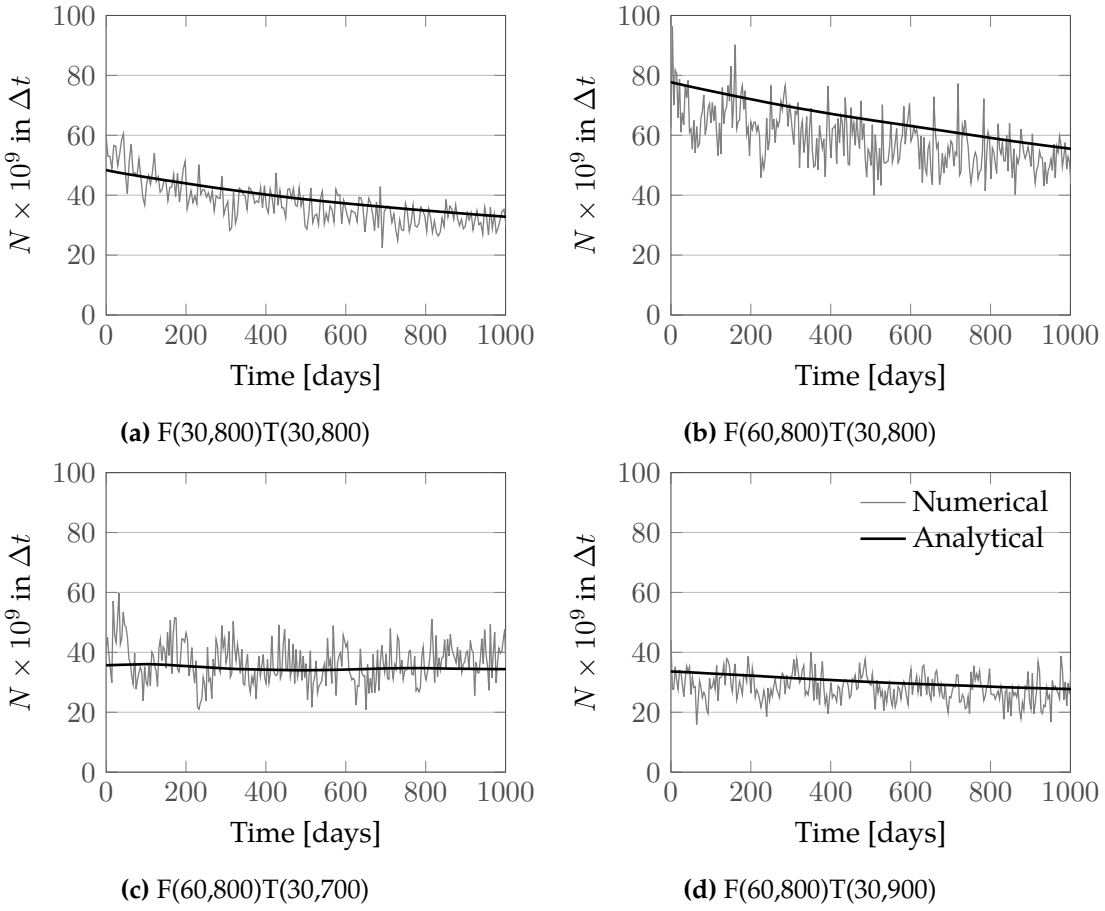

(a) F(30,800)T(30,800)

(b) F(60,800)T(30,800)

(c) F(60,800)T(30,700)

(d) F(60,800)T(30,900)

Figure 5.15: Comparison between the number of collision estimated with the numerical propagation (in grey) and with the analytical one (in black).

Figure 5.15 shows the number of collisions N predicted applying the analogy with the kinetic theory of gases using the value of density n and relative velocity Δv obtained form the numerical propagation (in grey) and the analytical one (in black). Four cases with different inclinations and altitudes are shown, finding similar results to the one obtained with the 1D approach in Figure 3.6. Also in this case one can observe the high frequency oscillations due to the fact that Ω is not uniformly distributed among the fragments that intersect the target orbit.

As an example, the results for the case F(60,800)T(60,700) are shown in detail. The considered debris cloud is formed by 2397 fragments, whose dynamics are studied for three years after the band formation T_B, which is equal to 286 days in this case.

Figure 5.16 shows the evolution of the cloud density in the (a, e)-plane; the white vertical line represents the target altitude and the two inclined lines define the limits of the region on the (a, e)-plane that contains the fragments that can affect the target. Figure 5.17 shows instead the temporal evolution of the target altitude h_T, the fragment spatial density at the target altitude n_T, the average relative velocity Δv and the collision probability p_c. It is possible to observe how n_T decreases in the first two years because

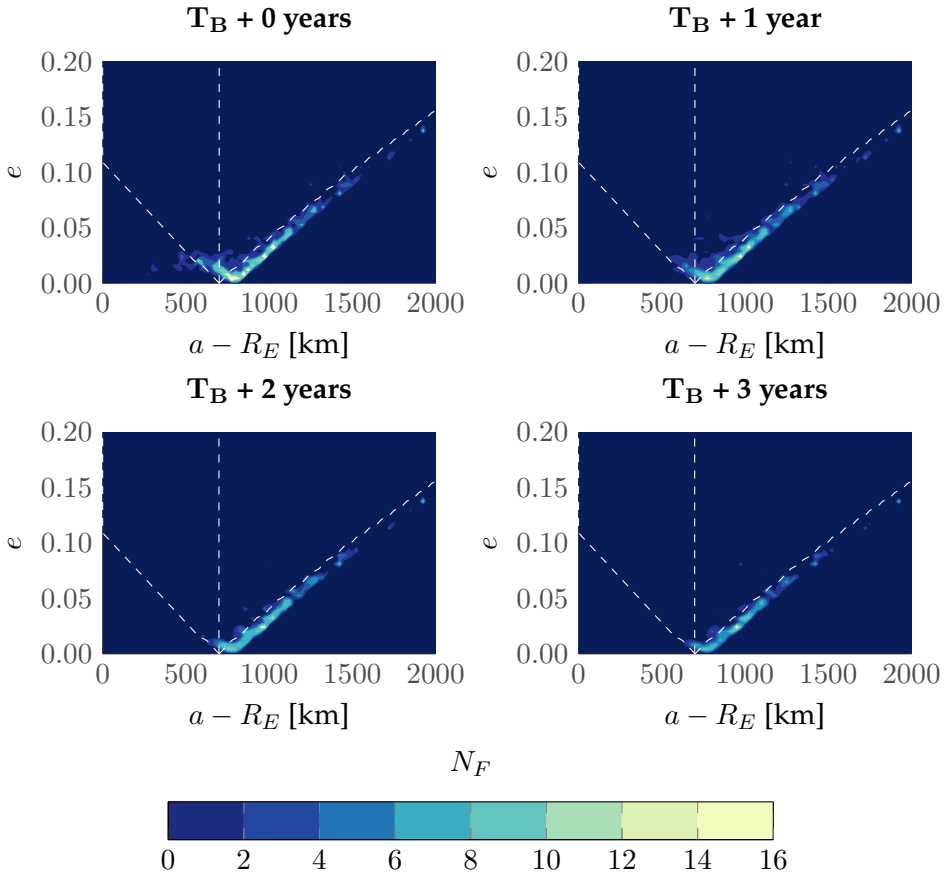

Figure 5.16: Evolution of the cloud density in the (a, e)-plane for the case F(60,800)T(60,700). Bin size equal to $25\,\mathrm{km}$ in a and 0.04 in e.

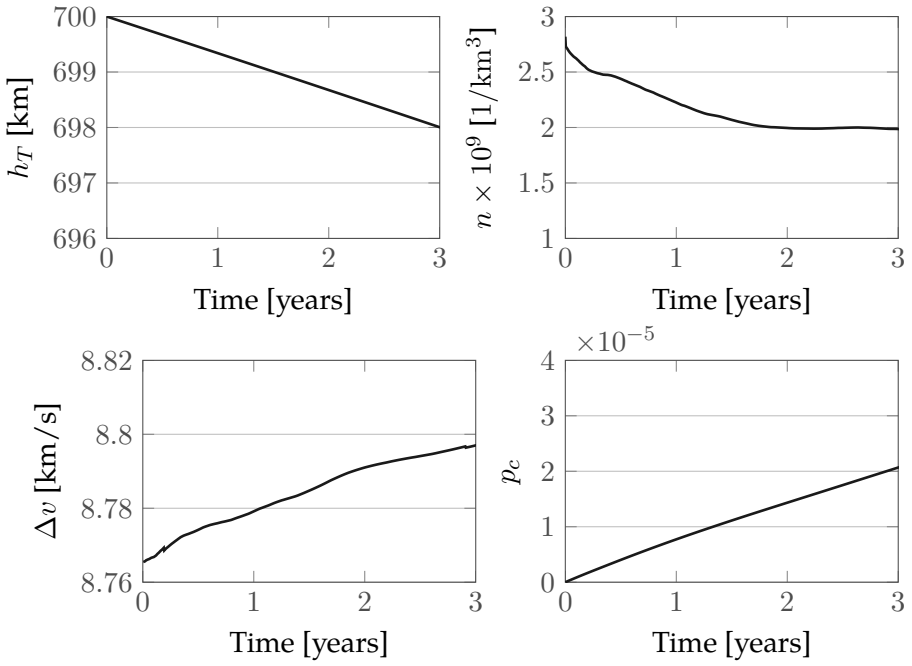

Figure 5.17: Temporal evolution of the target altitude h_T, the fragment density at the target altitude n_T, the average relative velocity Δv and the cumulative collision probability p_c.

during this period the fragments a low altitudes (left branch of the v-shaped distribution in Figure 5.16) are removed by the effect of drag. Afterwards, the density value is almost constant because the fragments that are still in orbit are less affected by drag. At the same time, the relative velocity increases as the target moves slowly to lower altitudes and the average semi-major axis increases. As a result, the collision probability grows with a slowly decreasing slope.

The result was obtained in 140.98 s on a PC with 4 CPUs at 3.40 GHz; most of the time was spent for the 2D analytical propagation (101.11 s): as mentioned in Chapter 4 this time could be reduced by changing how the initial condition is translated across the domain. The estimation of the relative velocity requires only 3.57 s.

5.4 Collision scenarios for the 2D approach

Similarly to what was done with 1D formulation of the method in Chapter 3.6, also with the 2D approach it is possible to study several fragmentation scenarios. In this case, using the 2D approach allows fragmentations at lower altitudes to be studied, covering the whole region of LEO where the debris density is the highest. Moreover, this extension in the method applicability can be exploited to study the impact of fragmentation also on active satellites, whose number is maximum at altitudes between 750 and $800\,\mathrm{km}$. In fact, also because of the presence of the Iridium constellation, this altitude band contains around 17% of all the active satellites in LEO (Union of Concerned Scientists, 2014). Therefore, whereas the percentage of satellites in LEO within the band of applicability of the 1D formulation (800-$1000\,\mathrm{km}$) is equal to 8.7%, for the 2D approach (700-$1000\,\mathrm{km}$) this percentage is equal to 30.23%. The percentage becomes much larger (63.89%) if only satellites heavier than $50\,\mathrm{kg}$ are considered. This Chapter will show how the method based on continuity equation can be used to study the impact of breakups not only on the debris population, but also on active satellites.

5.4.1 Single event simulations

As in the 1D case, the method is used to study the collision probability between fragments, resulting from some breakups, and a list of targets. The list used here is the same as in Section 3.6.1 (Table 3.1) and the parameters for the fragmentation are the one of the breakup of COSMOS 1867 (NASA Orbital Debris Program Office, 2014). The orbit of the satellite is between 775 and 800 km, so at the limit of the applicability of the 1D formulation; the inclination is equal to 65°.

Figure 5.18 shows the evolution of the cumulative collision probability for ten target spacecraft (Table 3.1), comparing the results obtained with the 2D (solid line) and the 1D formulation (dashed line). It is possible to observe how the ranking of the spacecraft

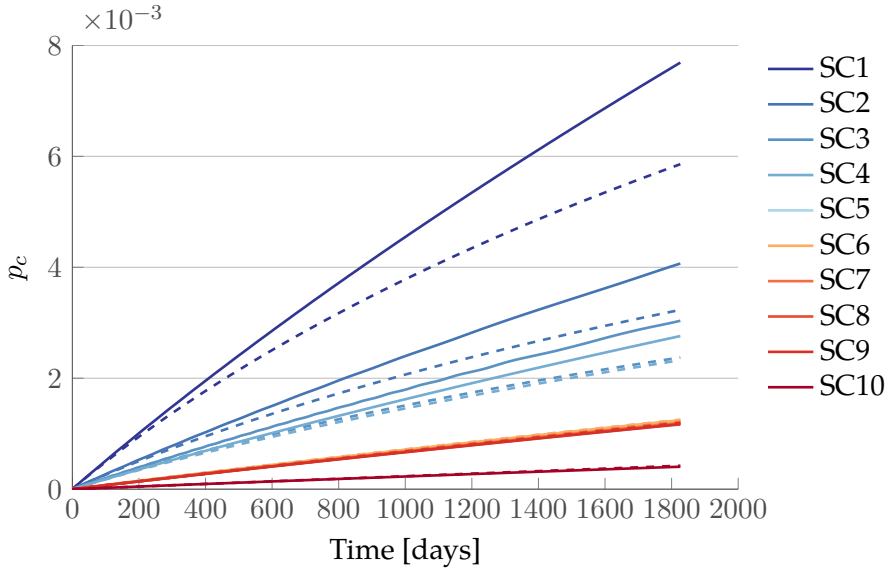

Figure 5.18: Cumulative collision probability resulting from the fragmentation of Cosmos 1867 for the ten target spacecraft in Table 3.1: the solid line represents the result obtained with the 2D formulation, the dashed line the one with the 1D formulation.

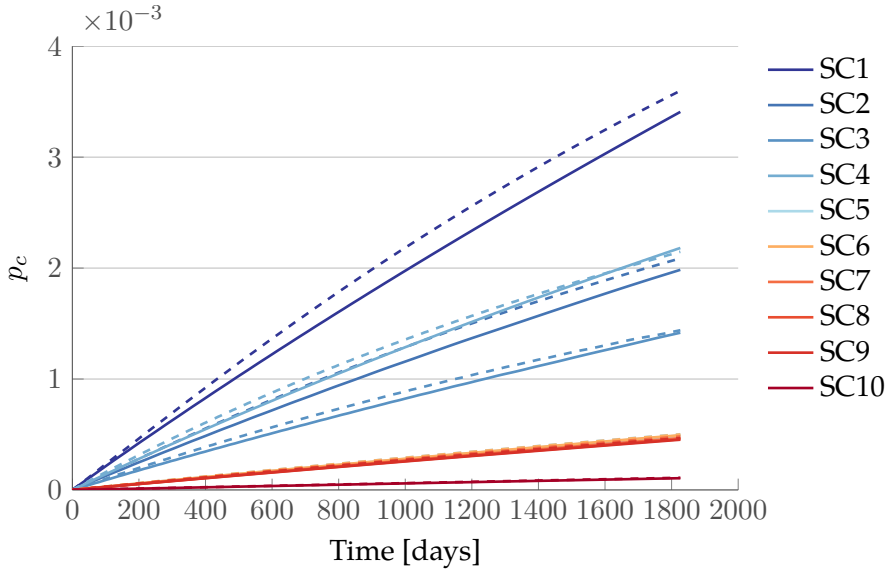

Figure 5.19: Cumulative collision probability resulting from the fragmentation of Cosmos 2428 for the ten target spacecraft in Table 3.1: the solid line represents the result obtained with the 2D formulation, the dashed line the one with the 1D formulation.

is the same (i.e. SC1 is the most affected spacecraft in both cases), but the 2D model computes higher collision probability values. This is related to the value of the cloud density encountered by a target along its orbit. This value is higher for the 2D than for the 1D method that, at this altitude, tends to overestimate the effect of drag, This was observed, for example, in Figure 4.12, where it was shown how the 1D approach predicts a steeper reduction of the cloud density around the peak. This behaviour results in an underestimation of the collision probability. When the fragmentation altitude is higher, as in the case of Cosmos 2428 (845-$860\,\mathrm{km}$) shown in Figure 5.19, the differences between the two models are reduced.

Another analysis that can be performed with the proposed method is to assess the effect of a fragmentation on the environment. The approach described in this Section can be used by spacecraft operators to have a quick estimation of the consequences of a newly discovered breakup.

The simulation of the fragmentation starts from the estimation of the input parameters required by the NASA breakup model, which are the kind of event (i.e. explosion, non-catastrophic collision, catastrophic collision), the class of object involved in the breakup, and the level of energy of the event. The first parameters are usually known as, when new objects are observed, their origin is often identified. The kind of fragmentation can be determined considering that explosions and collisions result in a different distribution of energy. Explosions tend to produce larger fragments with lower speed compared to collisions. Finally, the energy level of the event can be estimated knowing the number of objects added to the catalogue and assuming that they are larger than a threshold value (e.g. $5\,\mathrm{cm}$). In the case of an explosion no further information is required, whereas for collision also the impact velocity needs to be estimated or otherwise an average value is used. In the current implementation, an average collision velocity equal to 10 km/s is used. The event is simulated producing all the fragments down to $1\,\mathrm{mm}$. To identify which regions of space are the most affected by a given fragmentation, a grid in semi-major axis and inclination is defined. Each cell defines a fictitious spacecraft with given semi-major axis and inclination, for which the collision probability with the fragment cloud is computed. Average values for the spacecraft area and mass are used to describe its trajectory evolution. These values are the same as the ones mentioned at the beginning of this Chapter, namely $A_T = 11\,\mathrm{m}^2$ and $M_T = 2322\,\mathrm{kg}$.

The collision probability is computed starting from the moment when the fragment cloud is spread around the Earth forming a band. The resulting cumulative collision probability at the end of the time window is plotted as a function of the semi-major axis and the inclination to highlight which orbital regimes are the most affected. This graph is indicated as the *effect map*. The resulting *map* can be coupled with a database of spacecraft or space debris objects, such as the one in (Union of Concerned Scientists, 2014), to identify which are the most exposed targets. The idea here is not to propagate all the possible targets, but rather to use the information in the produced *effect map*. This

can be done by defining an index of *exposure* (η) and assigning it to all the spacecraft in the database. The index used here is composed of two elements: first, the value of the cumulative collision probability, obtained from the *effect map*, at the nominal orbit of the satellite; second, the mass of the satellite, taken as an indirect measure of the target cross-sectional area. The index is obviously an approximation because it does not consider the variation of the orbit during the years when the cumulative collision probability is computed; moreover, it implicitly assumes that all the spacecraft have the same area-to-mass ratio A/M. Nevertheless, it can give a first indication on which satellites are the most affected by a fragmentation event and then the result can be refined studying the collision probability for each target.

The index η for a spacecraft j for a given fragmentation is computed as

$$\eta_j = 1 - [1 - \mathbf{p_c}(a_j, i_j)]^{\frac{M_j}{M_T}} \tag{5.16}$$

where a_j, i_j are its semi-major axis and inclination; $\mathbf{p_c}$ is the map of collision probability in the *effect map*, so $\mathbf{p_c}(a_j, i_j)$ is the value for the spacecraft nominal orbit; M_j is the satellite mass and M_T is the reference value used to obtain $\mathbf{p_c}$. This expression for η was chosen because it can be related to the cumulative collision probability for the studied spacecraft. In fact,

$$1 - \eta = [1 - \mathbf{p_c}(a_j, i_j)]^{\frac{M_j}{M_T}} \tag{5.17}$$

$$\log(1 - \eta) = \frac{M_j}{M_T} \log[1 - \mathbf{p_c}(a_j, i_j)]; \tag{5.18}$$

for a Poisson process $1 - p_c = \exp(-N)$, so

$$1 - \eta = [1 - \mathbf{p_c}(a_j, i_j)] \exp\left(\frac{M_j}{M_T}\right) = \exp(-N) \exp\left(\frac{M_j}{M_T}\right) \tag{5.19}$$

and given the expression for N

$$1 - \eta = \exp\left(-n\Delta v \sigma_c \Delta t \frac{M_j}{M_T}\right). \tag{5.20}$$

Rewriting σ_c as

$$\sigma_c = \frac{A_T}{M_T} M_T$$

Equation 5.20 becomes

$$1 - \eta = \exp\left(-n\Delta v \Delta t \frac{A_T}{M_T} \frac{M_T}{M_T} M_j\right)$$

and using the assumption that A/M is the same for all the satellites

$$1 - \eta = \exp(-n\Delta v \sigma_{c,j} \Delta t) \quad \Rightarrow \quad \eta = 1 - \exp(-n\Delta v \sigma_{c,j} \Delta t) \approx p_{c,j}. \tag{5.21}$$

It is important to underline that Equation 5.21 is not the exact collision probability for the spacecraft j because the effect of the different values of the satellite area and mass on the trajectory evolution are not considered.

The method was applied to study the fragmentation of the satellite DMSP-F13 occurred in February 2015. As a result of the event, probably due to a malfunctioning of a battery, 160 new objects were added to the catalogue[5]. At the moment of fragmentation, the spacecraft was in an orbit with an altitude between 844 and 856 km, with inclination equal to 98.8 degrees.

Assuming the objects to be larger than $5\,\mathrm{cm}$ and applying the equations of the NASA breakup model for explosions, $83\,598$ fragments larger than $1\,\mathrm{mm}$ are expected. In fact, according to the NASA breakup model (Krisko, 2011), the distribution of fragments with size is given by

$$N_f = 6\,S\,L_c^{-1.6}, \tag{5.22}$$

where N_f indicates the number of fragments larger than the characteristic length L_c. S is a dimensionless parameter that depends on the exploding body. This parameter can be used to *tune* the explosion, so that setting L_c equal to $5\,\mathrm{cm}$, N_f is equal to the number of new observed objects (i.e. 160). In this way, $S = 0.221$ is obtained. Applying again Equation 5.22 with $S = 0.221$ and $L_c = 1\,\mathrm{mm}$, $N_f = 83598$ is obtained. The estimated total mas of the fragments is equal to $8.17\,\mathrm{kg}$, so compatible with the explosion of a battery.

The analysis of the effect of the breakup on the different orbital regimes is shown in Figure 5.20. It presents the *effect* map described in this Section considering 15 years of the cloud evolution. Figure 5.20 clearly shows that the most affected regions are the ones with altitude slightly lower than the one where the explosions occurred and with inclination i such that $\sin i \approx \sin i_F$, with $i_F = 98.8$ degrees inclination of DMSP-F13. With this orbital configuration, the target spacecraft crosses the cloud at the latitude extremes of the band, where the density is maximum. The orbits within $50\,\mathrm{km}$ below the fragmentation appear to be affected for any value of their inclination: as the fragmentation occurred at 98.8 degrees of inclination, the band extends up to 81.2 degrees in latitude. This means that all objects with i such that $\sin i \leq \sin i_F$ will spend their whole orbits within the fragment cloud. On the other hand, objects with $\sin i > \sin i_F$ will spend a portion of their orbits outside the fragment band. This explains why in Figure 5.20 the collision probability is lower for orbits with $i = 90$ degrees than for the adjacent values of inclination. The collision probability is still higher for $i = 90$ degrees than for $i = 70$ degrees because in the first case the target crosses the latitudes with the highest fragment density.

Figure 5.20 shows also the ten most affected spacecraft as extracted from the database in (Union of Concerned Scientists, 2014). The spacecraft are indicated in Figure 5.20 with

[5]Data retrieved from `https://www.space-track.org` on 14 September 2015

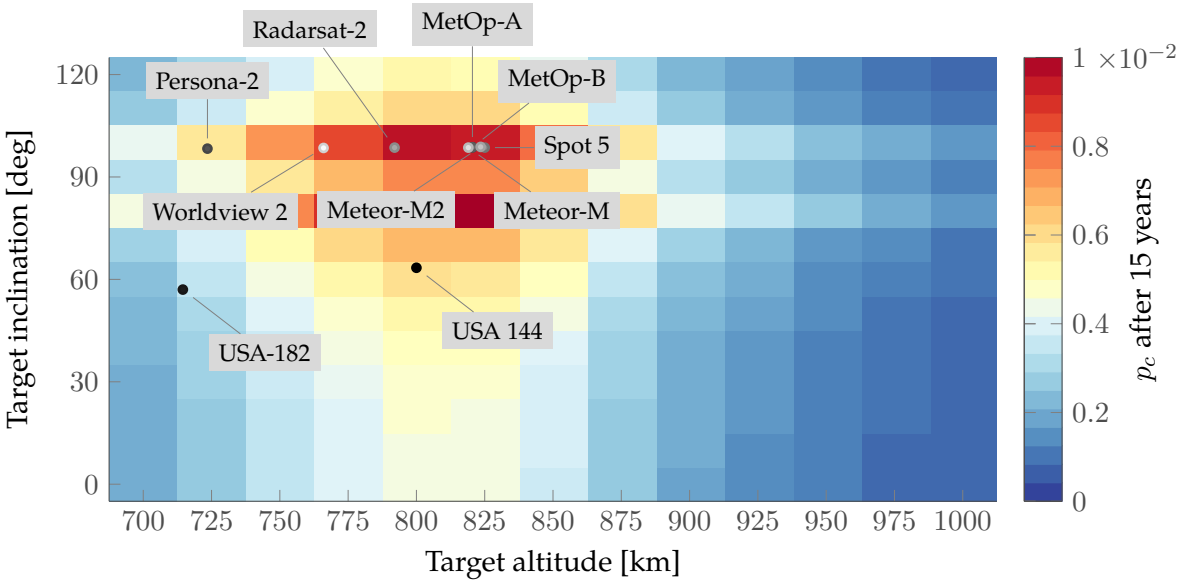

Figure 5.20: Effect map and top affected spacecraft for the explosion of DMSP-F13 from the database in (Union of Concerned Scientists, 2014).

Table 5.1: Top affected spacecraft for the explosion of DMSP-F13 from the database in (Union of Concerned Scientists, 2014).

Spacecraft	SATCAT	a [km]	i [deg]	m [kg]	η
USA-144	25744	800	63.4	18000	0.044150
USA-182	28646	714.5	57.01	14500	0.021326
MetOp-A	29499	820.5	98.7	4193	0.016808
Persona-2	39177	723.5	98.3	7000	0.016794
MetOp-B	38771	820.5	98.7	4085	0.016379
Spot 5	27421	825	98.6	3030	0.012175
Radarsat-2	32382	792	98.6	2924	0.011876
Meteor-M2	40069	823.5	98.81	2778	0.011168
Meteor-M	35865	819	98.6	2700	0.010856
Worldview 2	35946	766	98.5	2800	0.010201

a marker whose colour is related to the spacecraft exposure η, with the darkest markers associated with the highest values of η. The value of η for each spacecraft and their semi-major axis, inclination, and mass are reported in Table 5.1. For the top two spacecraft (USA-144 and USA-182), the dominant factor is the mass as these spacecraft have a mass at least double than any other object in the list. It is important to highlight that both satellites belong to classified projects by the United States National Reconnaissance Office[6], meaning that two-line elements are not available and their parameters (both orbital and physical) are deducted by the observations of amateur satellite observers. For this reason, the reliability of the data on these satellites is much lower than the other ones in the list. In any case, as in this work the main focus is on the description of the method to analyse a fragmentation, these spacecraft were kept in the database, using the values provided in (Union of Concerned Scientists, 2014). Within the hypotheses of the proposed approach, high mass translates into high cross-sectional area, so USA-144 and USA-182 dominates the η rank even if their orbits are not in the regions most affected by the fragmentation. For the other spacecraft in Table 5.1, the orbit parameters play a major role. For example, MetOp-A presents a higher value of η than Persona-2 even if its mass is much lower ($4193\,\mathrm{kg}$ versus $7000\,\mathrm{kg}$) because its orbits lies in one of the regions with the highest cumulative collision probability.

The approach was tested also with a different satellite database, DISCOS[7] (Flohrer et al., 2013), Database and Information System Characterising Objects in Space, maintained by ESA. Also in this case, the database[8] was pre-filtered to keep only spacecraft with perigee higher than $700\,\mathrm{km}$, apogee lower than $1000\,\mathrm{km}$, mass larger than $900\,\mathrm{kg}$. In addition, only spacecraft launched in the past ten years are considered, assuming that this threshold can be used to study only active satellites. Observe that this criterion removes Spot 5 from the database as it was launched in 2002, whereas includes Persona-1 that was launched in 2008, but failed some months after the launch. For the reasons already mentioned, USA-144 and USA-182 are not present in DISCOS. Besides these differences in the database, Figure 5.21 and Table 5.2 show coherent results with the previous database. Observe that the *effect* map in Figure 5.21 is not exactly the same as in Figure 5.20 as different runs of the breakup model were used. In addition, the numbers in Table 5.2 are different from the ones in Table 5.1 because the same spacecraft have different parameters (both for the orbit and for the mass) in the two databases. The results appear robust to this variation, with similar ranking in Table 5.1 and Table 5.2. In Table 5.2, as the spacecraft have more similar masses than the one in Table 5.1, the combined effect of mass, semi-major axis, and inclination can be better appreciated. Eight out of ten spacecraft have inclination very close to the one of DMSP-F13, so this parameter appears extremely relevant in identifying the most affected spacecraft. Observe also from Table 5.2 that analysing only the spacecraft features (i.e. mass, altitude, inclination) does not allow

[6] NASA National Space Science Data Center, `http://nssdc.gsfc.nasa.gov/`, last access 25 September 2015.

[7] `https://discosweb.esoc.esa.int`

[8] Data retrieved on 17 June 2015

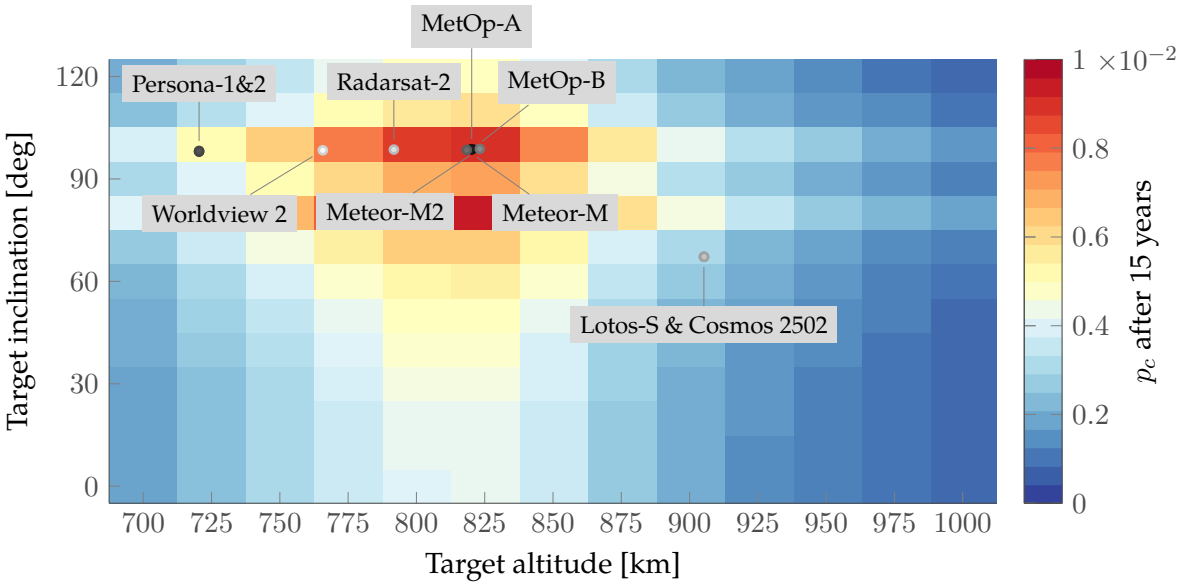

Figure 5.21: Effect map and top affected spacecraft for the explosion of DMSP-F13 from DISCOS database.

Table 5.2: Top affected spacecraft for the explosion of DMSP-F13 from DISCOS database.

Spacecraft	SATCAT	a [km]	i [deg]	m [kg]	η
MetOp-A	29499	820.24	98.7	4086	0.009357
MetOp-B	38771	820.34	98.7	4086	0.009357
Persona-1	33272	720.44	98	7000	0.009163
Persona-2	39177	720.44	98.2	7000	0.009163
Meteor-M	35865	818.44	98.5	2755	0.006319
Meteor-M2	40069	823.24	98.8	2755	0.006319
Lotos-S	36095	905.24	67.2	7000	0.005421
Cosmos 2502	40358	905.34	67.2	7000	0.005421
Radarsat 2	32382	791.74	98.6	2300	0.005199
Wordlview 2	35946	765.74	98.4	2615	0.005178

deriving directly how affected each spacecraft is or ranking them. The proposed method enables the translation of qualitative statements (e.g. spacecraft with altitude closer to the fragmentation one are highly affected) into a quantitative assessment of the risk for any object.

It is also important to highlight that DISCOS actually contains information on the objects' cross-sectional area: this value could be used to remove the hypothesis that all objects have the area-to-mass ratio and obtain more reliable results. Future work will investigate this option. For the moment, it was preferred to develop a tool that can be easily used by any operator exploiting the availability of a database such as the one in (Union of Concerned Scientists, 2014) which is publicly available online, whereas DISCOS requires a license.

For this reason, it is also important to briefly discuss the software structure and its computational requirements. All the code is currently written in MATLAB and it reads an input file with data on fragmentations (i.e. the orbital parameters of the fragmenting objects, the number of new detected objects, the class of breakup). The user then selects which case to simulate, the length of the simulated period (e.g. 15 years), the requested output and if the top affected spacecraft should be identified. In this case, also the name of the file containing the database with potential targets should be provided. A run starts with the simulation breakup and the propagation of the cloud density; the collision probability for each synthetic target is computed and, finally, if requested, the analysis of the target database is performed. Intermediate files are saved after the cloud propagation and after the computation of the collision probability, so that, respectively, analyses with different grids of the *effect* map and with different target database can be performed without re-running the whole simulation.

5.4.2 Maps of collision probability

As an opposite point of view with respect to the analysis in Figures 5.20 and 5.21, one can select a target and study under which conditions a fragmentation is more likely to affect it. The output of the analysis is similar to the maps in Figures 5.20 and 5.21, but in this case the target is *real* and several fictitious fragmentations are simulated. In the 1D case in Chapter 3.6 this approach was used to study the risk for objects in the debris population, whereas it is applied here on active satellites assuming that no manoeuvres are performed during the analysed time.

Figure 5.22 and Figure 5.23 show the cumulative collision probability after five year for, respectively, Landsat 8 and a satellite from the Iridium constellation; the parameters of the satellites are reported in Table 5.3. The simulated fragmentation is a non-catastrophic collision produced by a projectile of $100\,\mathrm{g}$ and collision velocity equal to $1\,\mathrm{km\,s^{-1}}$, so with collision energy equal to $50\,\mathrm{kJ}$. In both cases, the most critical fragmentations are the

Table 5.3: Parameters of the studied active satellites.

Satellite	a [km]	i [deg]	M [kg]
Landsat 8	702	98.2	18000
Iridium	777	86.4	14500

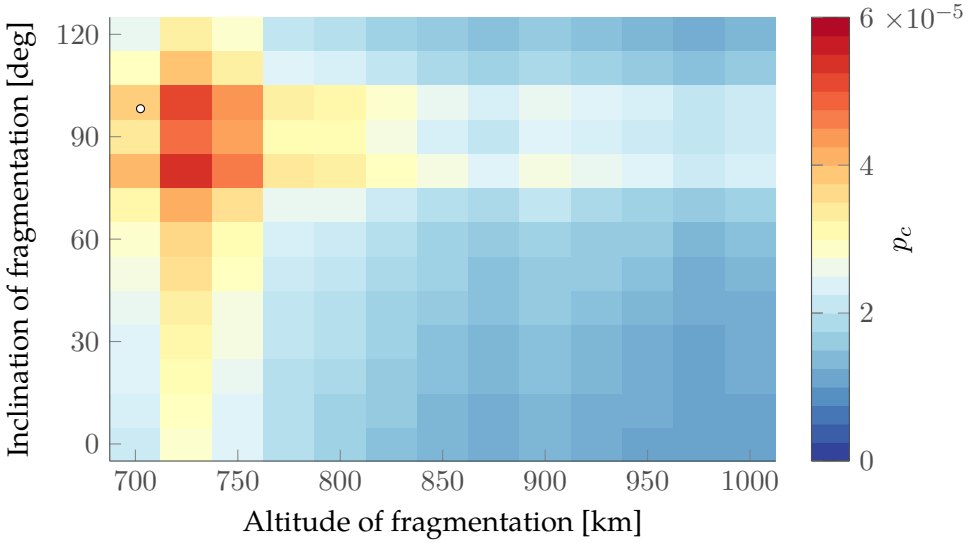

Figure 5.22: Cumulative collision probability after five years for Landsat 8. The simulated fragmentations are non-catastrophic collisions with collision energy equal to 50 kJ. The marker indicates the orbital parameters of Landsat 8.

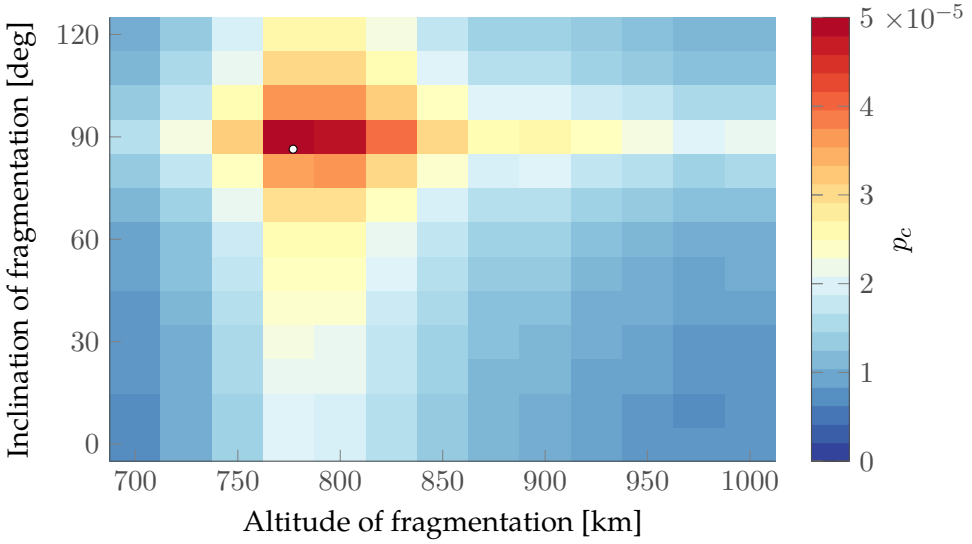

Figure 5.23: Cumulative collision probability after five years for a satellite in the Iridium constellation. The simulated fragmentations are non-catastrophic collisions with collision energy equal to 50 kJ. The marker indicates the orbital parameters of the studied satellite.

ones occurring just above the satellite initial altitude, with the highest values of collision probability within a band of $75\,\mathrm{km}$. As observed in Chapter 3, the collision probability is maximum for those inclination i_F close to $\sin i_F = \sin i_T$ because in these conditions the target crosses the fragment cloud at the latitudes where the fragment density is maximum. The values of collision probability are higher for Landsat because of its larger cross-sectional area. The analysis performed on Landsat 8 and an Iridium satellite can be easily extended to multiple targets to estimate the effect of a fragmentation on a set of satellites or objects in the debris population.

The output is obtained in two phases. First, all the fragmentations are simulated and the resulting fragment density with time is stored. When the 1D approach is used[9] the file size with the density history is 125 MB, whereas for the 2D case the file is 845 MB. This size is still manageable for modern machines but it obviously results in longer loading time ($54.81\,\mathrm{s}$ versus $4.35\,\mathrm{s}$ for the 1D case).The increase in the computational effort is justifiable if one wants to extend the scope of the analysis. In total, one map is obtained in $14\,\mathrm{s}$ for the 1D method and in $270\,\mathrm{s}$ for the 2D one, out of which more than $213\,\mathrm{s}$ are used for the computation of the relative velocity.

5.4.3 Performance at low altitudes

The approach of the collision maps was tested also on targets at lower altitudes than the ones of the fragmentations. In fact, whereas there is a limit on the fragmentation altitude due to the effect of the eccentricity on the accuracy of the analytical method, there should be no limits on the target orbit, whose evolution is obtained numerically. However, the collision map of the Hubble Space Telescope ($h = 557\,\mathrm{km}, i = 28.5°$) in Figure 5.24 shows a non-physical result as the collision probability is maximum at $900\,\mathrm{km}$ and it does not have a smooth variation with altitude. The reason for this unexpected result was investigated by checking the profile of the spatial density from fragmentations at different altitudes.

Figure 5.25 shows that according to both the analytical propagation and the numerical one, after 1000 days from the band formation the spatial density at $500\,\mathrm{km}$ is higher for higher values of the fragmentation altitude. This means that the error that causes the wrong results in Figure 5.24 is present in both the propagators. What is common between the two propagators and explains the error is that the exponential model of the atmosphere is used with constant reference values for H and ρ_{ref}.

Figure 5.26 shows the predicted value of the atmospheric density with different reference altitudes normalised with the value of density at that altitude: it is possible to observe that the predicted density tends to have an error larger than 20% for altitudes with more than $200\,\mathrm{km}$ of separation from the altitude where the parameters of the model (ρ_{ref}, H)

[9] To obtain a map of around 150 cells, with a time step of 1.5 days

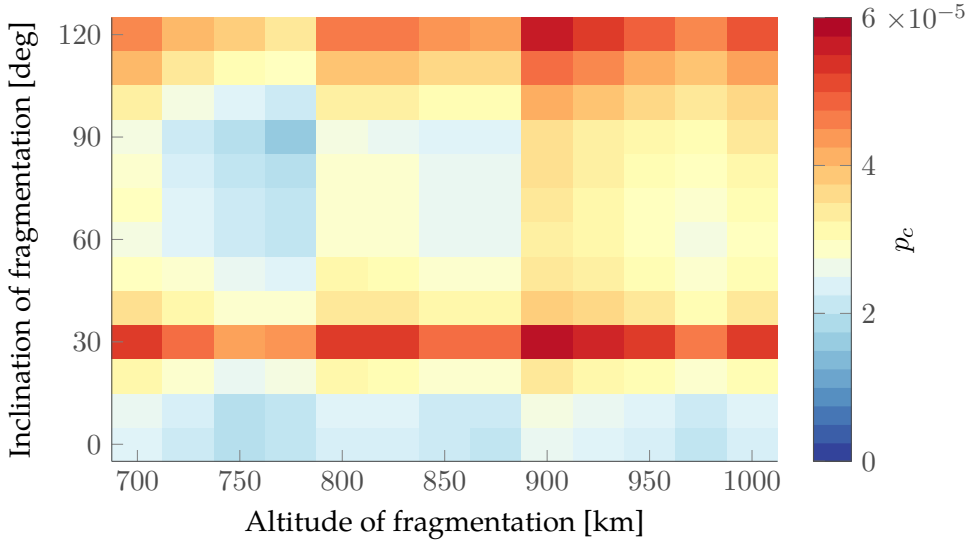

Figure 5.24: Cumulative collision probability after five years for Hubble Space Telescope. The simulated fragmentations are non-catastrophic collisions with collision energy equal to 50 kJ.

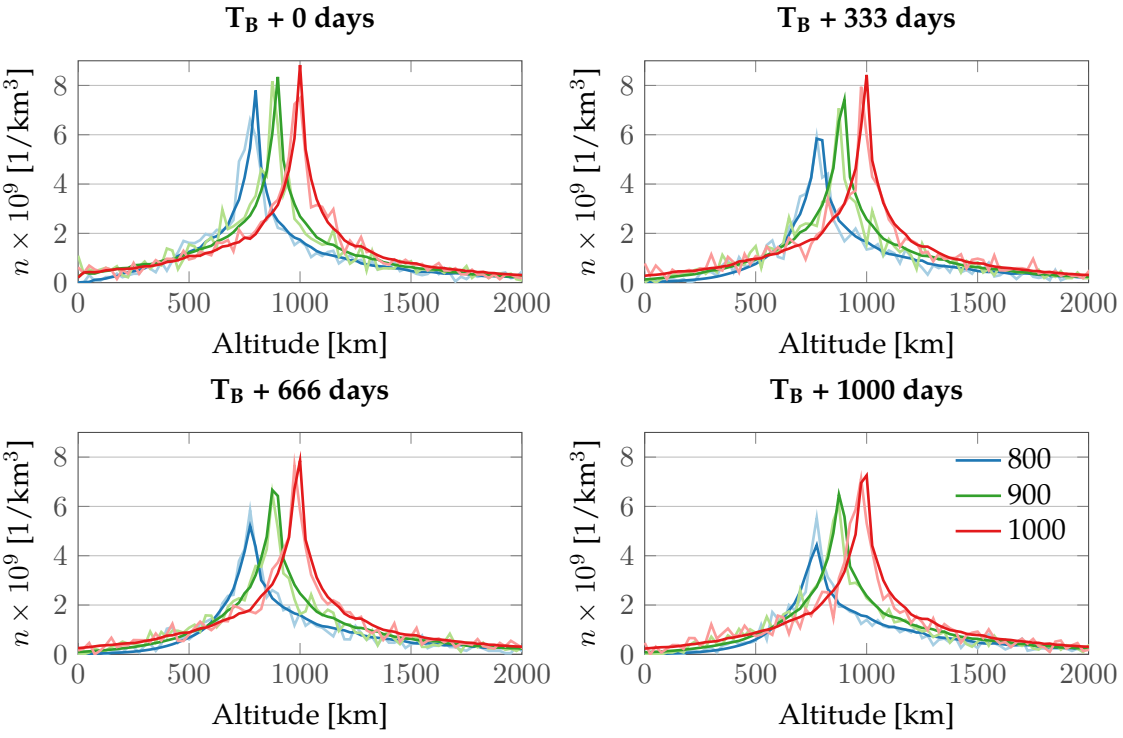

Figure 5.25: Evolution of the density profile for three fragmentations with different initial altitudes. The dark line represents the result from the analytical propagation, the light one from the numerical.

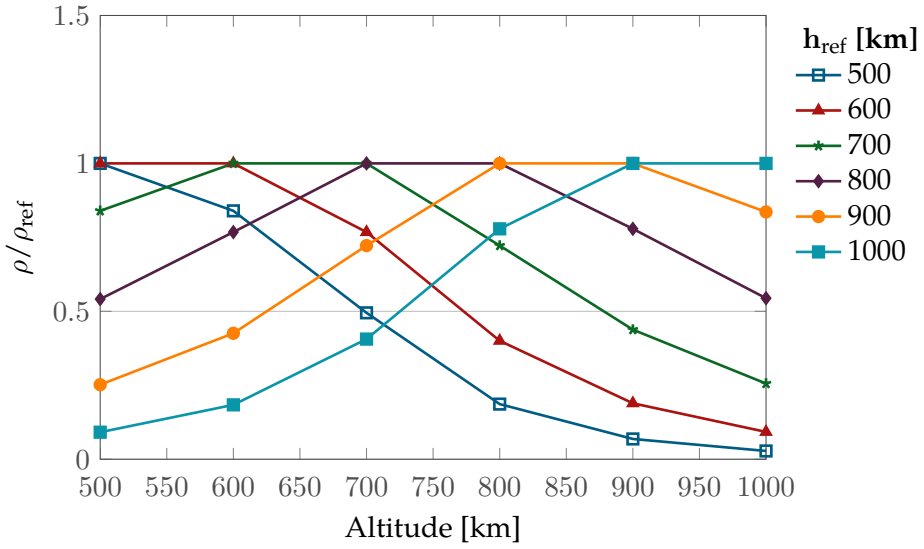

Figure 5.26: Predicted value of the atmospheric density with different reference altitudes normalised with the value of density at that altitude.

are defined. This has an impact on the propagation of the trajectories of fragments far from the fragmentation location and this error is present both in the analytical and in the numerical propagation. As the exponential model underestimates the value of density at distant altitudes, in the current analysis the effect of drag is underestimated, so the method is conservative with the current formulation. However, this error can lead to not physical behaviour in the cloud evolution as the observation that the density value at $500\,\mathrm{km}$ is higher for fragmentations originated at $1000\,\mathrm{km}$ than ones at 800 or $700\,\mathrm{km}$. In practice, this limits the applicability of the method to scenarios where the difference between the fragmentation altitude and the target latitude is smaller than $200\,\mathrm{km}$. In the collision maps, the domain is larger than $200\,\mathrm{km}$, but the results seem in any case coherent if the target is inside the studied domain, so this is set as constraint for the method applicability.

This limitation can be removed using different reference values of the atmospheric model for different altitudes. In particular, this requires changing the numerical propagation in such a way that the values of ρ_{ref}, H are updated as the propagated object moves across the bands where the parameters are defined. Also in this case, the values of $h_{\mathrm{ref}}, \rho_{\mathrm{ref}}, H$ are the ones in (Vallado, 2013). Also the analytical propagation should be changed defining ε not any more as a single scalar value that depends on the fragmentation altitude, but as a vector defined in each point of the integration domain. An example of the results that can be achieved with this modification is shown in Figure 5.27, which presents the density profile for a fragmentation at $800\,\mathrm{km}$ obtained using constant values for the atmospheric parameters or varying them with altitude, both for the analytical and the numerical propagation. When the parameters of the atmospheric model vary with altitude, as expected, the fragment density at low altitudes ($h < 500\,\mathrm{km}$) goes rapidly to zero. Moreover, it is possible to observe that also with this formulation the analytical

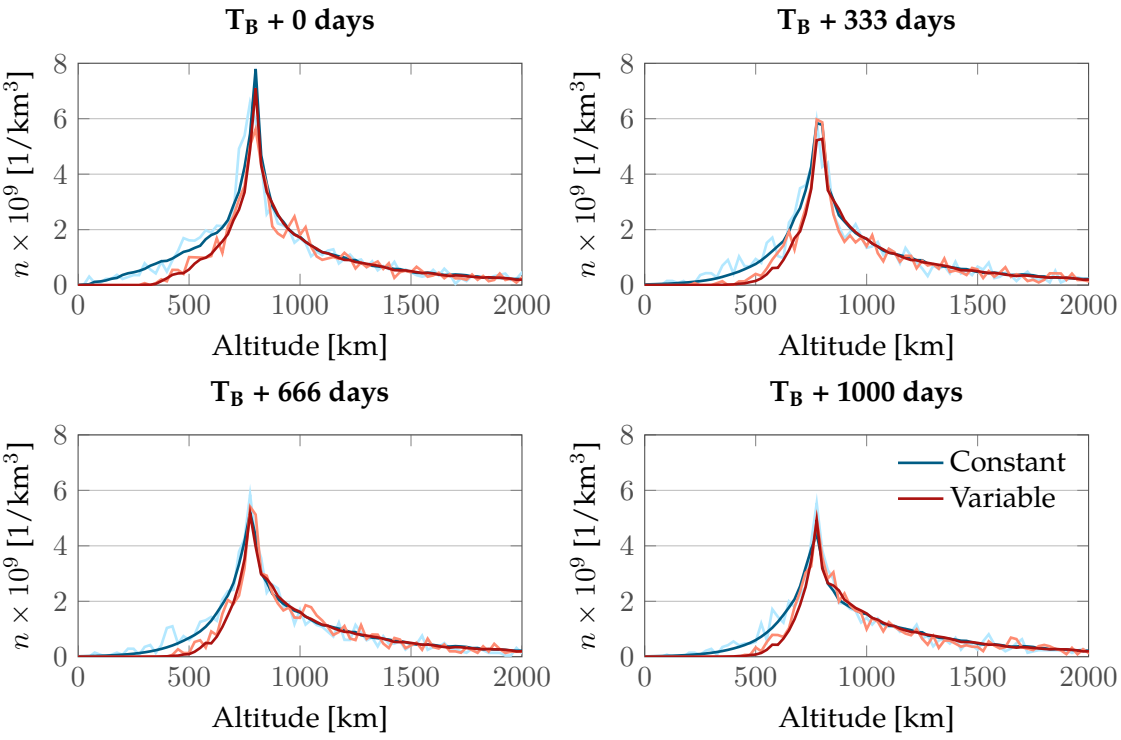

Figure 5.27: Density profiles for a fragmentation at 800 km using constant values for the atmospheric parameters or varying them with altitude. The dark line indicates the analytical propagation, the light line the numerical one.

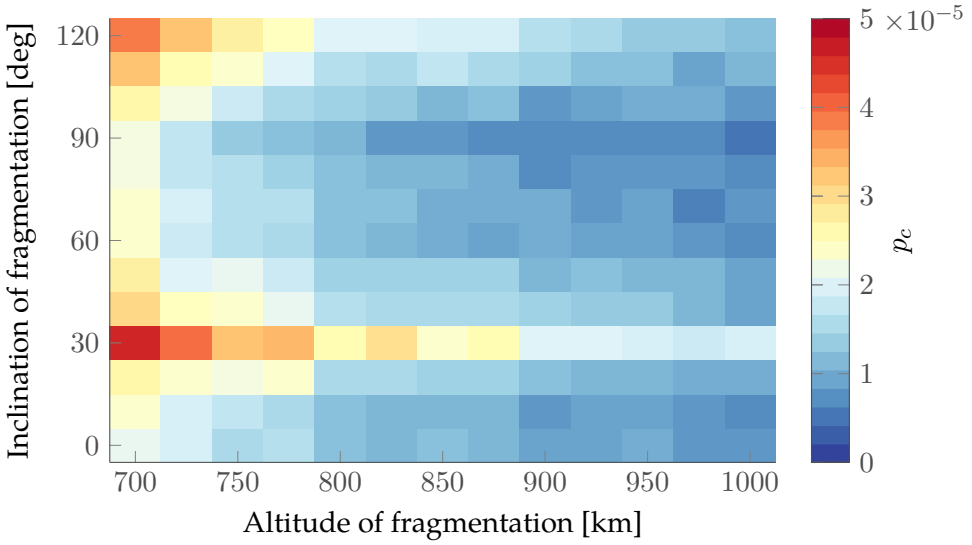

Figure 5.28: Cumulative collision probability after five years for Hubble Space Telescope. The simulated fragmentations are non-catastrophic collisions with collision energy equal to 50 kJ. The parameters of the atmospheric model change with altitude.

model follows very well the density profile obtained with the numerical propagation. With this implementation, the extraneous peak in the collision maps are removed as shown in Figure 5.28 that presents again the analysis on the Hubble Space Telescope, but with the modification to the atmospheric model. The new implementation is already used for the results in Chapter 6 and future work will investigate in detail the performance of the new formulation for different values of the fragmentation altitude and inclination.

5.4.4 Comments on the implementation

As already discussed in Section 3.3, using the analytical method allows an important reduction of the computational time. For example, the preparation of target maps with a fully numerical approach (both for propagation and computation of the velocity) requires a computational time larger than two hours on a cluster with 12 processors. Besides the saving in time (that could be irrelevant if high performance computing facilities are used or if the code is optimised), the real benefit from using the analytical method is that it allows many simulations to be *manageable* with a normal PC reducing the need of high performance computing facilities, and easily reproducible. In fact, the computation of the relative velocity with the numerical method can be quite intensive in terms of CPU; moreover if one wants to save all the data relative to the propagation of the cloud in terms of the fragment orbital parameters, the file can reach easily a size around 100 MB for small cases (3000 fragments) and up to some GB for fragmentation with hundred thousands of objects. This makes it more difficult to store the information and also to load it and reuse it. All these problems are not present with the analytical method as the information is always stored in terms of spatial density, so the size of the file depends on the grid used to describe the domain, but not on the number of fragments. For example, the case DMSP-F13 is stored in a file of 4 MB and it can be easily loaded to perform different analyses. Also for this reason the analytical method may be integrated in a global debris model without having a large impact on the computational effort of the simulation.

Summary

The 2D formulation of the continuity equation allows the information on the fragment distribution with eccentricity to be included in the propagation. This can be used not only to extend the applicability of the method to lower altitudes, but also to improve the estimation of the relative velocity between the target and the fragment cloud. In fact, it was possible to use the knowledge of the fragment distribution in semi-major axis and eccentricity, and the hypothesis that the fragments are uniformly distributed in Ω and ω to obtain an analytical expression for the relative velocity between the target and the

cloud. The validation of the 2D approach has shown that the average relative error is lower than 1% for the cases when target and fragmentation have different orbital inclinations; the average error is instead equal to 8.5% when the value of inclination is the same. This result was explained by observing that in the latter case the analytical approach estimates an asymptotic value for the relative velocity, which is reached with a certain delay depending on the rate of spreading of the fragments. For this reason, the worst cases can be found around 63° and 90° where, respectively, $\dot{\omega}$ and $\dot{\Omega}$ due to the Earth's oblateness are null. For these case it is suggested to numerically correct the relative velocity by modelling its evolution as the transient for a first order system. Further work is required to effectively connect the fragment spreading and the value of the relative velocity, and obtain a fully analytical formulation. The 2D formulation of the continuity equation approach was applied to study many collision scenarios as done with the 1D version. In addition, the recent explosion of DMSP-F13 was also studied evaluating the effect of the breakup on the collision probability in the near orbital regions. Using the 2D formulation enables linking the *collision map* with a database of active satellites, which are numerous in the altitude band 700-800 km of altitude, where the 1D method is not applicable. Using the 2D formulation, instead, it is possible to identify which spacecraft are the most affected by the explosion. Collision maps similar to the ones for the 1D case were obtained also with the 2D method, but in this case, they were prepared for active satellites instead of debris objects. This shows how the continuum approach is flexible and can give an insight on the collision risk for many different applications. Finally, some tests on spacecraft at low altitude (e.g. Hubble Space Telescope) were performed, finding some non-physical results. The reason for this was identified in the choice of the atmospheric model: not updating the coefficients in the model leads to an inaccurate description of the decay of the cloud at low altitudes. This behaviour can be fixed by introducing the dependence of the coefficients on the altitude. With this correction, the applicability of the method is extended and the accuracy of the prediction of the collision probability improved.

Part of the content of this Chapter is included in F. Letizia, C. Colombo, H. G. Lewis, and H. Krag. Assessment of breakup severity on operational satellites, 2015j. Manuscript submitted for publication.

6

Density-only formulation and its applications

In Chapter 4 it was explained how the formulation of the continuity equation into multiple dimensions can be used to model the first phase of the cloud evolution, under the dominant effect of the Earth's oblateness. It is a natural development then to combine the analytical description of the first phase of the cloud evolution with the one of the effect of drag after the band formation. In this way, a purely analytical description of the cloud evolution would be available, applicable both for short and long term analyses. This would make possible to simulate a fragmentation cloud drastically reducing the impact of the number of fragments on the simulation cost. In this Chapter, some ideas on how this objective can be reached are presented. The preliminary results show a good potential for this technique and confirm once more the convenience of the description of debris clouds in terms of spatial density. Further development and validation are suggested as future work.

6.1 Formulation

The purpose of this Chapter is to evaluate the feasibility of a propagation method for the long term evolution of debris clouds where the numerical propagation of single objects is completely removed. A way to achieve this goal is to combine the analytical model of the effect of the Earth's oblateness, described in Section 4.2, with the description of the effect of atmospheric drag presented in Section 2.4 and Section 4.4. It is convenient to represent

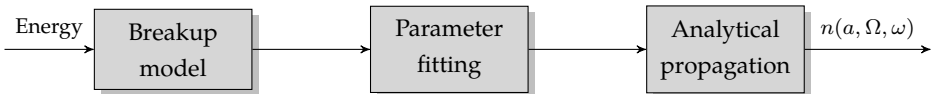

(a) Short term: Earth's oblateness effect.

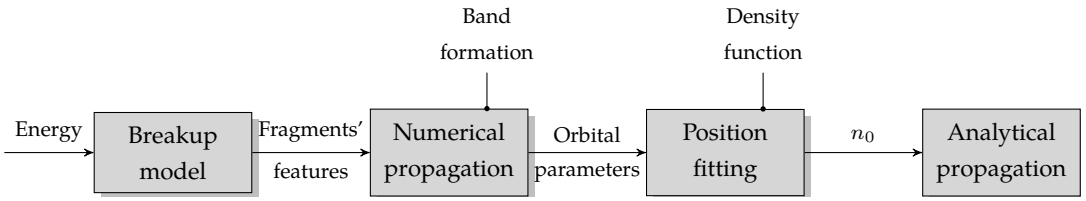

(b) Long term: atmospheric drag effect.

Figure 6.1: Building blocks for the two propagation methods.

once more the block diagrams of the two approaches to understand how to combine them (Figure 6.1). For the first phase, the transition from a dense configuration to the band, the model of the Earth's oblateness requires as input the energy of the breakup and gives as an output a distribution in a, Ω, ω; no numerical integration is performed. In the following phase, once the band is formed, the long term propagation under the effect of the atmospheric drag requires knowing the distribution in a, e and the division in area-to-mass A/M bins. As a first attempt to solve the problem, the eccentricity e and the area-to-mass ratio were included in the first phase of the propagation, together with a, ω, Ω. In this way, the initial condition for the long term propagation could be easily obtained by integrating $n(a, e, A/M, \Omega, \omega)$ on Ω and ω. However, this attempt was not successful as the computation becomes prohibitive because the data is represented with a variable with five dimensions. Using 100 grid points for the orbital parameters and 10 bins for the A/M, the simulation was not feasible on a PC with 16 GB of RAM. Future work may try to revise this approach and devise a better numerical implementation to cope with the increase in the number of dimensions. An alternative way could be also to test the application of the analytical propagation before the band formation as already suggested in Chapter 2.

A different approach was studied, focussing only on the long term propagation. The limit in the models discussed in Chapter 2 and in Section 4.4 is that the continuity equation is applied only once the band is formed, so the numerical propagation is used to describe the transition to the band. This introduces a dependence of the method performance on the number of fragments. To remove this dependence, alternative modelling techniques are required. Given this basis, the problem becomes how to describe the passage from the initial distribution of fragments in a and e at the breakup to the one when the band is formed (Figure 6.2) without integrating their trajectories. This can be done by applying a method similar to the one embedded in the continuity equation. When the continuity equation is solved with the method of characteristics, the value of the solution at a certain time is obtained by *reshaping* the initial condition according to the change prescribed by the conservation of the solution along the characteristics.

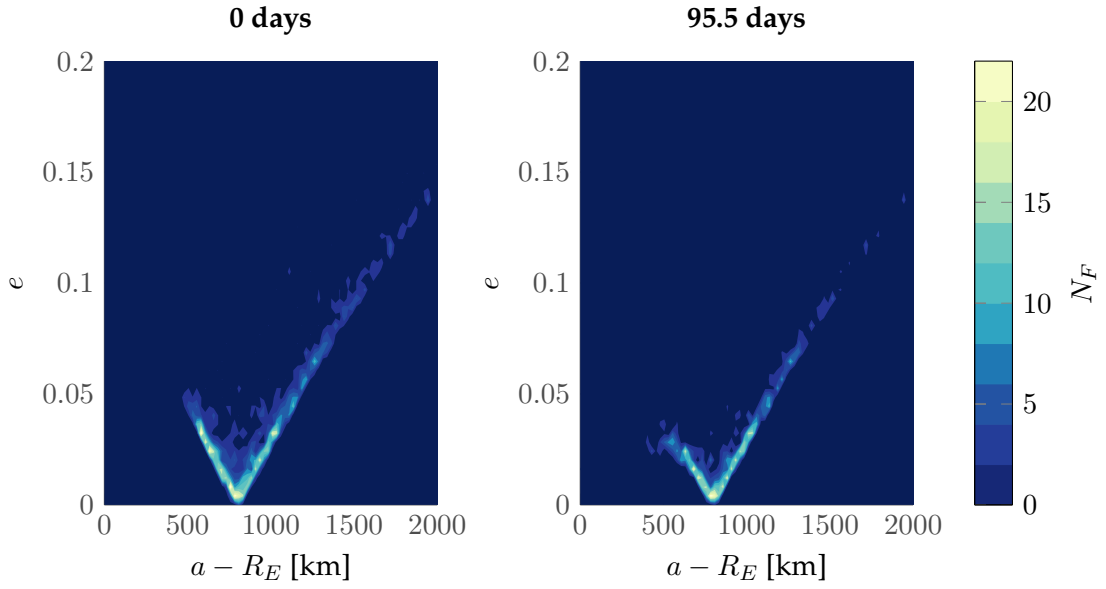

Figure 6.2: Visualisation of cloud density at the breakup and at the band formation T_B.

Similarly, in this case one may think about how the (a, e)-plane should change from the initial time of breakup to the time of band formation T_B to reproduce the evolution in Figure 6.2. The approach that is applied is similar to one developed by (Cordelli et al., 1995), where a cloud is divided in bins and a point of each bin is obtained by applying a semi-analytical propagator.

The change in $n(a, e)$ from the breakup to T_B is due to the effect of atmospheric drag only as the Earth's oblateness affects the distribution of ω and Ω, but not a and e. Therefore, only the effect of atmospheric drag is required for *reshaping* of the initial condition, whereas the model of the Earth's oblateness could be used to estimate the duration of the transition phase. To simplify the problem, in this work, the transformation of the initial condition is obtained neglecting the variation of eccentricity during T_B and considering only the change in semi-major axis due to drag. Note that in this work T_B is still defined starting from the expressions by Ashenberg (1994) in Equation 2.19. However, as anticipated, it should be possible to exploit the information available on the phase of the cloud spreading under the effect of the Earth's oblateness to assess directly when the band is formed. This point is left for future work.

For each point in the a-axis where n_0 is defined, the variation of a during the time span T_B is computed by applying the numerical propagation method described in Section 2.2. Observe that the variation in a depends on the area-to-mass ratio, so the computation should be repeated for each A/M bin. In this way, the distortion of the a-axis is obtained and the distribution n_0 is changed accordingly. In other words, the transformation of the initial condition is obtained by defining as many objects as the discretisation points of the semi-major axis times the number of A/M bins. Each object has initial semi-major axis equal to one point along the a-axis, eccentricity equal to zero, and area-to-mass ratio

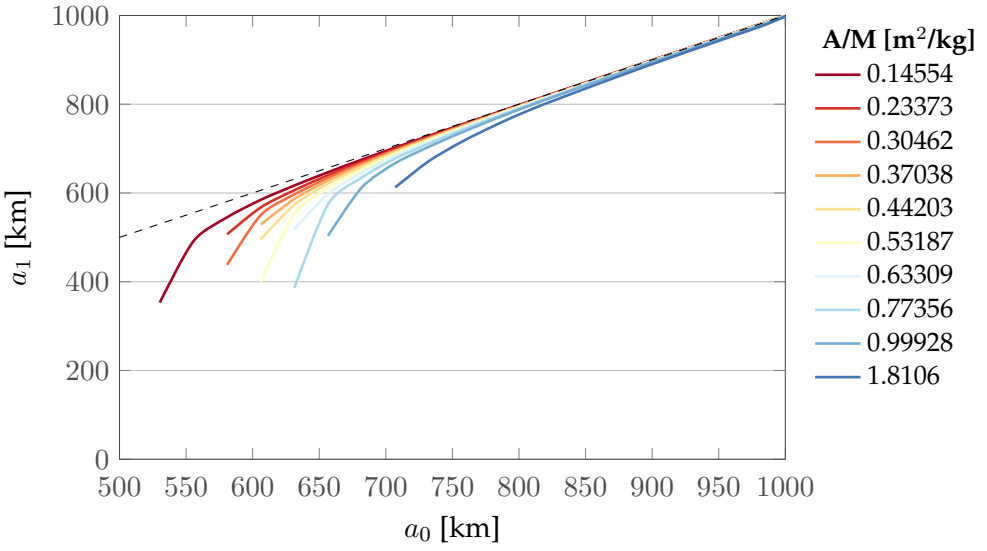

Figure 6.3: Resulting semi-major axis a_1 for the initial values of semi-major axis a_0 for all the A/M bins for a propagation time equal to T_B.

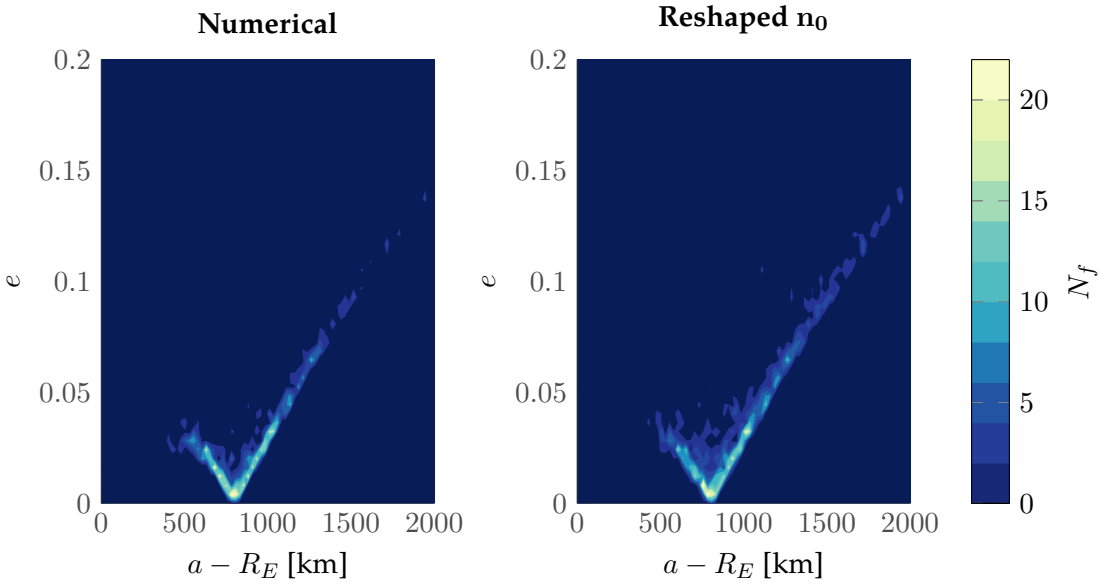

Figure 6.4: Distribution of the fragments in the (a, e)-plane at the band formation compared with the density reconstructed with the proposed procedure.

equal to one of the A/M bins. The evolution of the semi-major axis of the so-defined objects is studied over a time span equal to $\Delta t = T_B$ and the final value of the semi-major axis is used to *reshape* the initial condition. Figure 6.3 shows the resulting value of semi-major axis a_1 for the initial values of the semi-major axis a_0 along the grid where $n_0(a, e)$ is defined. The different colours refer to the different A/M bins in which the fragment cloud is divided.

Once each value of the initial grid is mapped onto its modified value, the distribution $n_B = n(a, e, T_B)$ is obtained from the initial one $n_0 = n(a, e, 0)$ with the following algorithm. Let a_j indicate the j-th point in the original grid and a_k its modified value

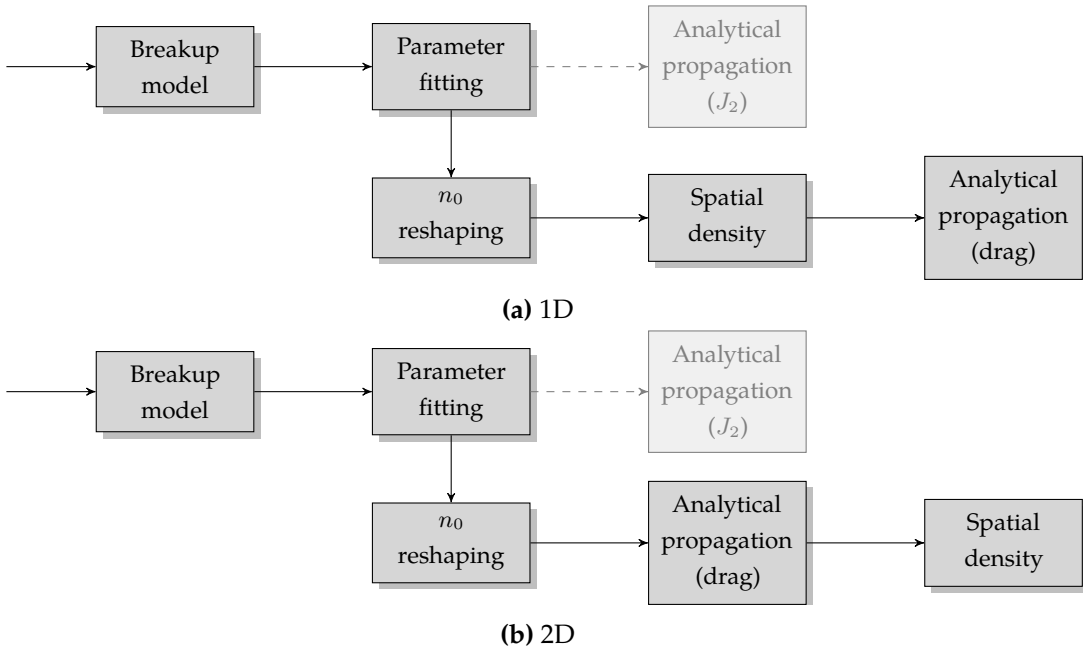

(a) 1D

(b) 2D

Figure 6.5: Building blocks for the two versions of the *density-only* method.

after T_B; if $a_k < 0$ the fragments originally at a_j have re-entered and so $n(a, e, T_B)$ is not updated; if $a_k > 0$, $n(a_k, e, T_B) = n(a_j, e, 0)$. By applying this procedure, the result in Figure 6.4 is obtained: the distribution obtained with the *reshaping* process appears similar to the numerical one as the reduction of the left branch is well captured. At this point, all the required information is available to proceed with the long term propagation both in 1D (Figure 6.5a) and in 2D (Figure 6.5b).

In both cases, the simulation starts with the breakup model and the definition of the initial condition in terms of the orbital parameters distribution (*Parameter fitting* in Figure 6.5). In this way n_0 is defined and the transformed value at the band formation n_B is obtained with the *reshaping* process described in this Section. In the case of the 1D propagation, $n_B(a, e)$ needs to be converted into a spatial density using Equation 2.24, similarly to what is discussed in Section 2.3. In the case of the 2D propagation, $n_B(a, e)$ is used directly as the initial condition of the long term analytical propagation based on the continuity equation. As with the version of the 2D propagation discussed in Section 4.4, the conversion into spatial density is performed *a posteriori*. The new formulation of the model is indicated in the following as *density-only* method because, differently from the previous cases, the problem is formulated in terms of density right after the breakup. With this modification, the computational effort of the model becomes independent on the number of fragments contained in the cloud.

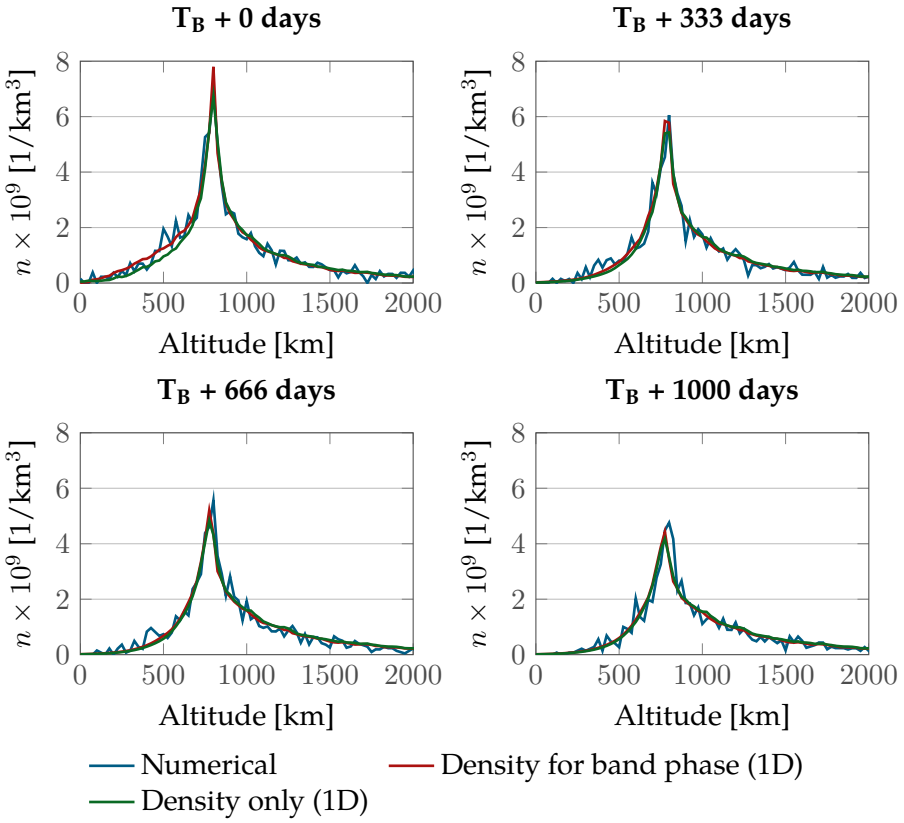

Figure 6.6: Fragment spatial density for a fragmentation at $800\,\mathrm{km}$.

6.2 Results

The *density-only* method, in its 1D version (Figure 6.5a), was tested with the same reference fragmentation used in Section 2.5, which is produced by a non-catastrophic collision with a projectile of mass equal to $100\,\mathrm{g}$ and relative velocity equal to $1\,\mathrm{km\,s^{-1}}$ and results in 2397 fragments at the breakup.

Figure 6.6 compares the density profile obtained from the all analytical approach with the one of the 1D method described in Chapter 2 (indicated as *density for band phase*) and with the distribution obtained from the numerical propagation with a single run of the breakup model. We can see how the behaviour of the *density-only* method is very similar to the one where the density is used only in the band phase. Same results were obtained for other values of inclinations (i.e. 30° and 60°) suggesting that, as observed with the *density for band phase* approach, the accuracy does not depend on the inclination. Further analysis, such as the one presented in Chapter 2.5, is required to assess more precisely the accuracy of the method and its dependence on inclination, altitude, and energy of the fragmentation. This analyses will be subject of future work.

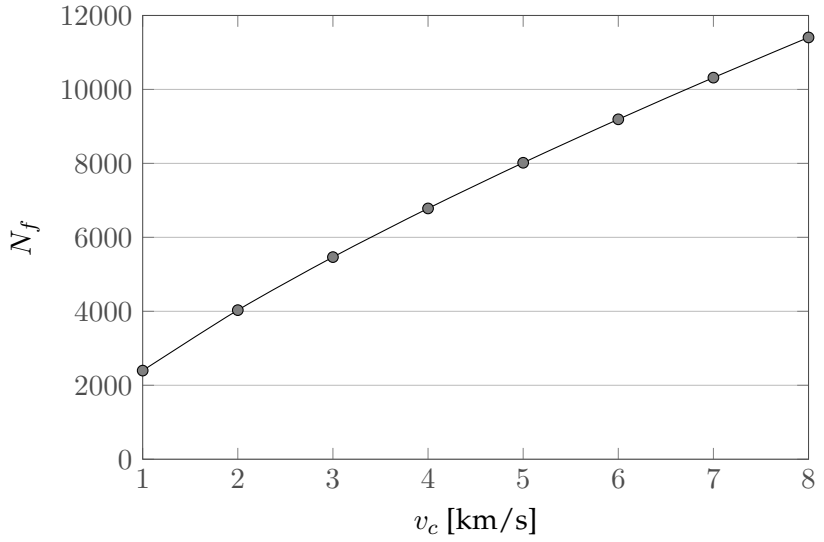

Figure 6.7: Number of fragments produced by a non-catastrophic collision with a projectile of $100\,\mathrm{g}$ as a function of the impact velocity v_c.

6.3 Applicability to large clouds

The debris cloud models described in Chapters 2 and 4 (*density for band phase*) rely on the numerical propagation of single objects to describe the evolution during the band formation. Even if this numerical propagation covers only a short fraction of the whole simulated time period, it limits the size of the clouds that can be analysed with a normal PC. The limitation is connected with the availability of RAM required to follow thousands of fragments.

In the case of non-catastrophic collisions, the number of fragments produced by a breakup depends on the collision velocity v_c. Figure 6.7 shows the dependence on the number of the produced fragments on the collision velocity for a non-catastrophic collision with a projectile of $100\,\mathrm{g}$. A way to test the *density-only* approach is to simulate breakups with increasing collision velocity to evaluate its computational time and assess whether, adopting this formulation, its dependence on the number of fragments is removed. Figure 6.8 shows the computational time for the simulation of breakup clouds resulting from non-catastrophic collisions with v_c between 1 and $8\,\mathrm{km/s}$ and total fragment number ranging between 2000 and $12\,000$. In all case, the computational time was always around $11\,\mathrm{s}$ on a machine with 4 CPUs and 16 GB of RAM. There is only a weak dependence of the computational time on the number of fragments and this is due to the process of grouping the fragments into the A/M bins; once this phase is complete, the problem is formulated purely in spatial density and its propagation is independent of the number of fragments. This aspect makes the proposed *density-only* method very promising for evaluating many collision and explosion scenarios with different energies.

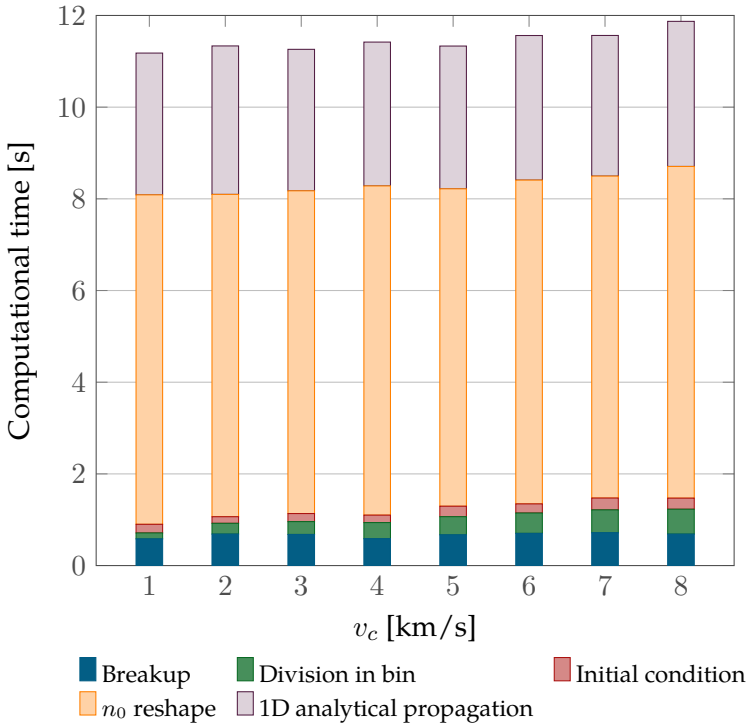

Figure 6.8: Computational time with the *density-only* method for non-catastrophic collisions with projectile mass equal to 100 g and different collision velocity v_c.

6.4 Example of application: environmental index

The ability of the *density-only* formulation to model large debris clouds with limited computational effort (both in terms of simulation time and RAM) makes it suitable to simulate a large number of breakup scenarios. This can be useful to rank different breakup conditions and build an *environmental index* able to quantify the influence of a specific satellite or of a piece of debris on the safety of the whole environment. This kind of indices may become particularly relevant once the technology would enable *active debris removal missions*: in that scenario, it would be essential to know which spacecraft should be removed first to have the largest global beneficial effect. Several authors have proposed different approaches to the problem and highlighted the relevance of having a quantitative measure of the environmental effect of an object in orbit (Bastida Virgili and Krag, 2013; Lang et al., 2013; Rossi et al., 2015b; Utzmann et al., 2012). Rossi et al. (2015a), for example, simulated 46 different fragmentations, considering location and targets representative of the distribution of intact objects in orbit. For each scenario 25 Monte Carlo runs were performed studying the number of objects present in orbit in the 200 years following the fragmentation. Similarly, Rossi et al. (2015b) introduced a *criticality* index, which depends on the background debris density, the object residual lifetime, the mass, and its orbital inclination. Similar parameters were identified also by Utzmann et al. (2012). A different approach was presented by Lewis (2014) where the proposed environmental index is computed considering the spacecraft orbital region,

the implementation of mitigation measures and the long term effect of the selected measure.

A different point of view is adopted in this work. The consequences of the breakup of specific spacecraft are evaluated in terms of the effect on an a set of *target* objects. The index presented in this Chapter, Environmental Consequences of Orbital Breakups (ECOB), was developed in collaboration with ESA Space Debris Office. The formulation of the index derives from the interest of ESA in evaluating the effect of fragmentations specifically on active satellites, so those will define the *target* set. This allows to assess how a breakup affects the operational aspects of space debris activities, namely if an increase in close conjunction alerts and collision avoidance manoeuvres should be expected. In addition, using active satellites as reference targets for the environmental index means that the consequences of a fragmentation are related to a potential loss for the spacecraft operators. From ESA perspective, an environmental index could also be applied, prior to launch, to support the licensing phase in the evaluation of the planned post-mission disposal strategies. For example, a licence system connected to an environmental index can distinguish between a CubeSat in orbit at $700\,\mathrm{km}$ at low inclination and a $4000\,\mathrm{kg}$ satellite in a polar orbit at $800\,\mathrm{km}$. As the environmental impact of a potential breakup involving the two spacecraft is different, a different level of reliability of the post-mission disposal may be requested.

The proposed method CiELO, in its *density-only* variation, allows the space of the most relevant spacecraft parameters (i.e. altitude, orbital inclination, and mass) to be *mapped* onto a value of environmental index, enabling to identify the most critical orbital configurations. This approach requires two steps. First, the potential sources of fragmentations and which kind of fragmentation to simulate should be defined. Second, the target set should be represented in such a way that the propagation of all the active satellites' trajectories is not required. The next Sections will explain in detail how these tasks are performed. Observe that the structure of the index can be applied also with different cloud propagation methods than CiELO, given that they are able to provide the cloud spatial density with time. As an example, it could be applied in GEO, where different analytical propagation methods are available, to study fragmentations within the GEO protected region and in the GEO graveyard orbit.

6.4.1 Sources of fragmentation

To keep the severity index as general as possible, a set of fictitious sources is defined to *map* the space of parameters for any possible space object; in other words, a large set of virtual fragmentations is created. In particular, a grid in semi-major axis, inclination, and spacecraft mass was used. The extremes of the grid in semi-major axis are limited by the applicability of the method: the highest limit is set equal to $1000\,\mathrm{km}$ as for higher

altitudes it will not be justifiable to model the atmospheric drag and not the solar radiation pressure. The lowest limit depends on the analytical formulation used for the propagation: as the 2D formulation of the method is used, the lower limit is set equal to $700\,\mathrm{km}$. The choice of using the 2D formulation is due to the fact that can accurately model the cloud evolution for a longer period than the 1D approach[1]. For the source spacecraft mass, a grid between $100\,\mathrm{kg}$ and $10\,000\,\mathrm{kg}$ was defined. Observe that the only way to consider the effect of the fragmenting mass within the NASA breakup model requires simulating catastrophic collisions and not explosions or non-catastrophic collisions. For all the simulated collisions the breakup of a spacecraft (rather than a rocket body) is assumed, even if in the size range of interest the impact of this hypothesis is minimal[2]. The collision velocity is set equal to $10\,\mathrm{km\,s^{-1}}$, which is an average value for LEO and which was used also by Rossi et al. (2015a). The mass of the colliding projectile is neglected. Using the NASA breakup model, the simulation of a catastrophic collision involving a mass equal to $1000\,\mathrm{kg}$ results in the generation of almost seven million fragments larger than $1\,\mathrm{mm}$. Even if the *density-only* formulation is only weakly dependent on the number of fragments, this large value results in a long computational time only for the initialisation of the cloud. For this reason, the lowest cut-off size of the fragments was set to $1\,\mathrm{cm}$ for the results discussed in this section.

6.4.2 Target set

The effect of the virtual fragmentations is assessed on a set of spacecraft targets. The selection of the possible targets follows an approach similar to the one proposed by Rossi et al. (2015a) to define representative fragmentations. The cross-sectional area A_c was identified as the most relevant parameter for a target. For this reason, the distribution of cross-sectional area across the LEO region was studied; also in this case, the semi major axis was limited to $700\,\mathrm{km} \leq a \leq 1000\,\mathrm{km}$ as in the definition of the potential fragmentation sources. DISCOS[3] database is used to extract the data of satellites orbiting in this region. As in Section 5.4.1, only satellites launched in the last ten years are included in the list, assuming that this criterion filters out inactive spacecraft. The studied LEO region is divided into cells in semi-major axis and inclination, applying the same grid used for the discretisation of possible fragmentation sources. For each cell, the cumulative cross-sectional area $\sum A_c$ is computed. The result of this analysis is shown in Figure 6.9, where the cells with the highest $\sum A_c$ are the most *vulnerable* in case of fragmentations.

Once the distribution of A_c is known, the target set can be defined by selecting for each cell in Figure 6.9 a *representative* spacecraft for which the collision probability is computed.

[1] In addition to using the 2D formulation of the method, all the results relative to the environmental index are obtained updating the parameters of the atmospheric model, as explained in Section 5.4.3.

[2] The kind of object involved in the fragmentation affects the definition of the parameters of fragments larger than $8\,\mathrm{cm}$ only.

[3] Stijn Lemmens, Space Debris Analyst, ESA, personal communication, 17/06/2015

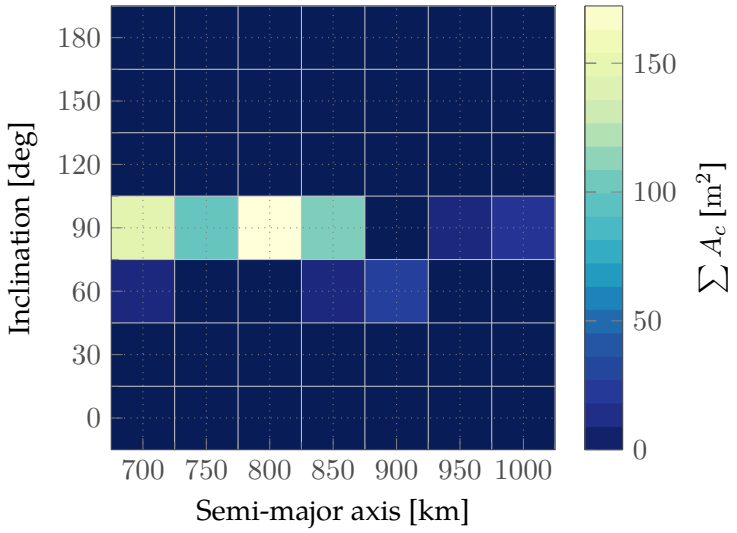

Figure 6.9: Distribution of cross-sectional area in the cells in semi-major axis and inclination. Data from DISCOS.

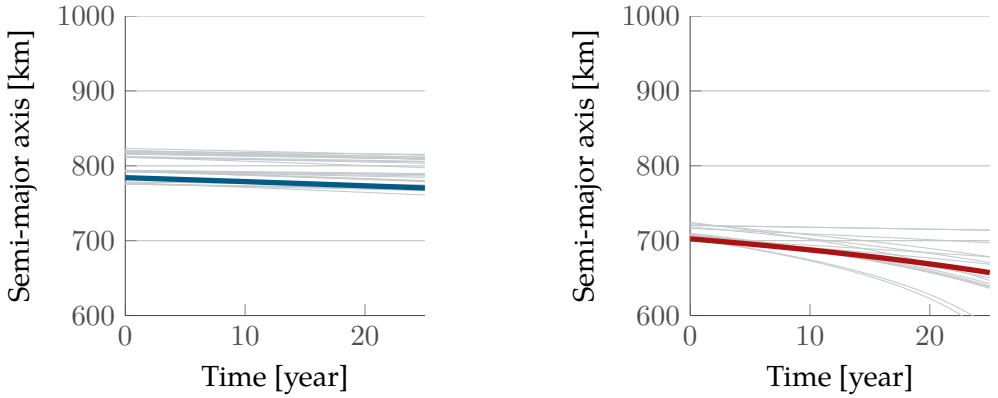

(a) Cell 1 (90°, 800 km)

(b) Cell 2 (90°, 700 km)

Figure 6.10: Evolution with time of the semi-major axis of the objects in a cell (in grey). The coloured line refer to the representative object (A_c closest to average value).

As it will be shown later, the environmental index is obtained combining the collision probability for each target, weighting their contribution depending on the share of A_c of the cell they represent. A fixed number of target can be used or the code can select the appropriate number of targets to represent a given percentage of the total A_c. In the results shown in Section 6.4.7 the second approach is used, setting the percentage equal to 90% of the total A_c.

Two main options for the selection of targets exist. The first one identifies a *real* object among the ones in the cell that is going to be used to represent the cell. The identification can be done, at the moment, choosing among the object with the maximum/minimum A_c within the cell or the one with A_c closest to the average value in the cell. The second option defines a *synthetic* object with A_c and mass equal to the average values in the cell, semi-major axis and inclination equal to the centre of the cell.

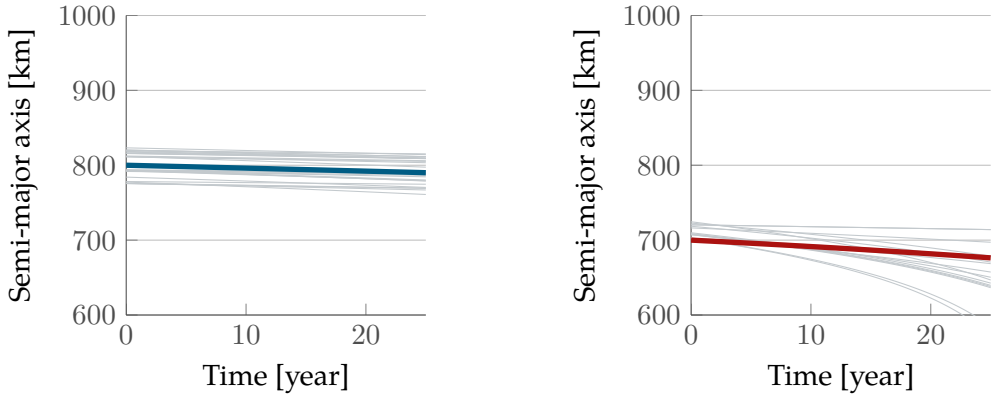

(a) Cell 1 (90°, 800 km)

(b) Cell 2 (90°, 700 km)

Figure 6.11: Evolution with time of the semi-major axis of the objects in a cell (in grey). The coloured line refer to the representative object (synthetic object).

Figure 6.10 and Figure 6.11 show the evolution of the semi-major axis of the representative object (coloured line) and of all the objects in the cell (in grey) for the two cells with the highest cumulative cross-sectional area. In Figure 6.10, the representative object is selected as the one with A_c closest to average value in the cell, whereas in the second case, Figure 6.11, a synthetic target is defined. As expected, a synthetic object has an evolution more representative of the whole cell. Moreover, choosing a synthetic object offers a more robust representation of the satellite population with time. In fact, the input population changes with time because of the launch of new satellites. This would require to re-run the algorithm for the selection of representative targets after each launch. However, one can assume that the development of space activities in LEO will be similar also in the future, with comparable missions to the current ones in each orbital regime. One could then expect a limited variation of the average cross-sectional area and mass. A tolerance on their value may be introduced to decide when the selection of the targets needs to be repeated. The other two options for the choice of the representative object, namely maximum and minimum A_c within a cell, could be used only to define the worst/best case, but one has to consider that A_c has a direct impact not only on the dynamics, through the effect of atmospheric drag, but also on the collision probability.

Figure 6.10 and Figure 6.11 were also used to assess if the propagation of the target trajectory is really required or if the orbit can be considered unperturbed. The object from cell 2 (90°, 700 km) is the one that experiences the maximum variation of the semi-major axis, equal to 40-$50\,\mathrm{km}$, depending on the object definition; for the other cells the variation is lower than $15\,\mathrm{km}$. Given these numbers and the fact that the propagation of the targets' trajectories is not expensive in terms of computational time, it was decided to keep the effect of atmospheric drag and Earth's oblateness in the description of the targets' trajectories. An alternative approach could be not to propagate the targets assuming that if

they are active satellites, their altitude may be controlled during mission lifetime. The evaluation of this option is left for future work.

6.4.3 Index definition

The purpose of the current analysis is to rank the *sources* of fragmentations evaluating their impact on a set of *targets* (i.e. the representative objects). As only the consequences of a breakup are evaluated, proposed environmental index ECOB is defined as a simple sum of the collision probability on each target multiplied by the weighting factor, if used. When synthetic objects are used, the index is simply

$$\text{ECOB} = \sum_{j=1}^{N_{\text{tar}}} w_j p_{c,j} \tag{6.1}$$

where

$$w_j = \frac{(A_c)_{\text{cell},j}}{(A_c)_{\text{tot}}} \tag{6.2}$$

is the ratio between the sum of A_c in the $j-$th cell and the total A_c on the whole target list; $p_{c,j}$ is the cumulative collision probability of the representative object of the $j-$th cell over the considered simulated time; N_{tar} is the total number of representative objects. When the representative object is chosen among one of the real satellites, Equation 6.1 may be modified in

$$\text{ECOB} = \sum_{j=1}^{N_{\text{tar}}} k_j w_j p_{c,j} \tag{6.3}$$

with

$$k_j = \frac{(\bar{A}_c)_{\text{cell},j}}{(A_c)_{\text{SC},j}}, \tag{6.4}$$

to take into account the used value of A_c is different from the average value in the cell.

Observe that the w_j are constant for the whole simulation, meaning that it is assumed that for the whole simulated time span the distribution of cross-sectional area will be constant. As mentioned before, this is equivalent to assume that, for the studied period, the space activities in the LEO region will be similar to the current ones.

6.4.4 Preliminary results

Some preliminary runs were performed using six reference targets and a coarse grid with a step equal to $50\,\text{km}$ for the semi-major axis and 30 degrees in inclination. The purpose of these runs is to analyse the general structure of the index.

6.4.5 Effect of selection criteria

In Section 6.4.2 different options for the selection of the targets were discussed. Figure 6.12 represents the value of ECOB computed on the coarse grid. It shows the comparison between the use of real spacecraft or synthetic objects to define the target set. When real spacecraft are used, the satellite with A_c closest to the cell average is selected. The targets are superimposed to Figure 6.12 and indicated with the markers. The colour indicates the value of the index for a fragmenting spacecraft with values of semi-major axis and inclination equal to the ones of the centre of the cell. The mass of the virtual fragmenting spacecraft is equal to $1000\,\mathrm{kg}$. One can observe how the distribution of the index is qualitatively similar because the value of A_c used in the two cases are close. This means that both the trajectory evolution and the computation of the collision probability will give similar results. This result can be interpreted also as a proof of the method robustness as the variation in semi-major axis and inclination within a single cell appear to have a limited impact on the final result.

Effect of propagation time As introduced in Section 6.4, ECOB is function of the propagation time as it is obtained as the sum of the cumulative (over time) collision probability of the reference targets. The variation of the index with time was studied by producing a heat map similar to the ones in Figure 6.12 after different propagation periods. Figure 6.13 shows the results obtained after 5, 15, and 25 years. In this case, no weighting factor is applied to compose the index, so that the dependence on the time is more evident. In this way, one can observe that with longer time of propagation the relative importance of fragmentations at higher altitudes increases. This is expected because if the time of propagation is longer, the fragments at lower altitudes may have the time to decay from the region where the targets are.

Effect of the mass As explained in Section 6.4, ECOB depends on the mass of the fragmentation that determines the number of fragments in the debris cloud and its spatial density. One simulation, with propagation time equal to 25 years, was run to evaluate the variation of the index with semi-major axis and breakup mass of the fragmenting object. This setup was chosen to allow the comparison with the Environmental Criticality (EC) by Kebschull et al. (2014b) where the variation of the index with inclination is not considered. For the mass a log-spaced grid was used. The results of the simulation are shown in Figure 6.14.

Similarly to Figures 6.12b and 6.13c, also in Figure 6.14 the dependence on the semi-major axis is dominated by the distribution of the targets. The dependence on the mass is also easy to explain as when a spacecraft with larger mass fragments, a larger number of objects is produced and a larger collision probability is registered. For comparison, the

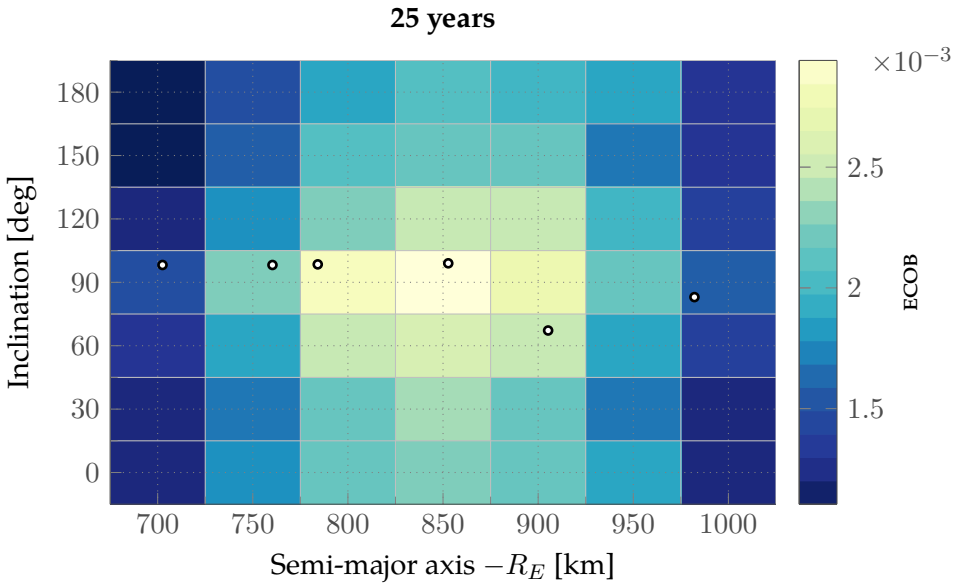

(a) Real targets

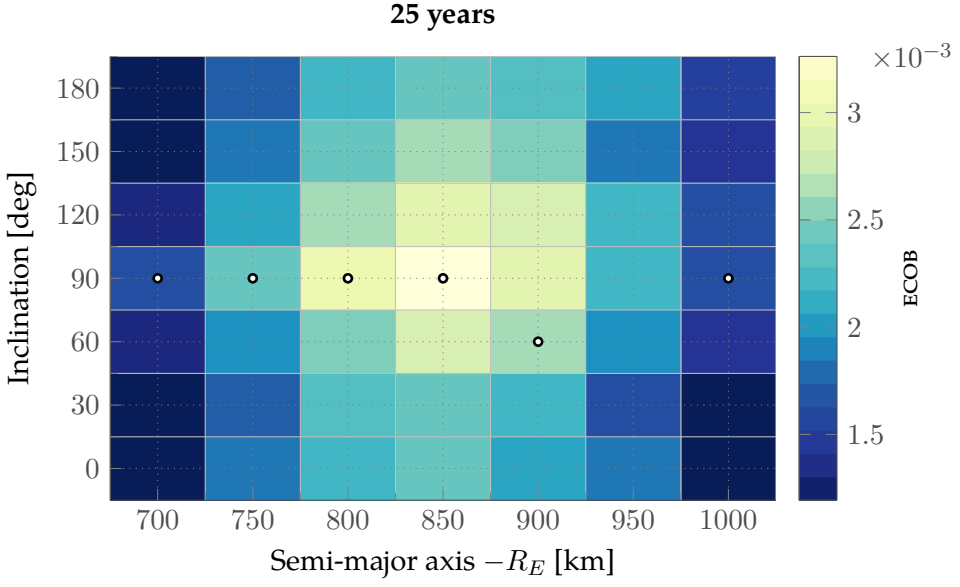

(b) Synthetic targets

Figure 6.12: Heat map for the criticality index for two different sets of targets. Fragmentation mass equal to 1000 kg. The markers indicate the reference targets.

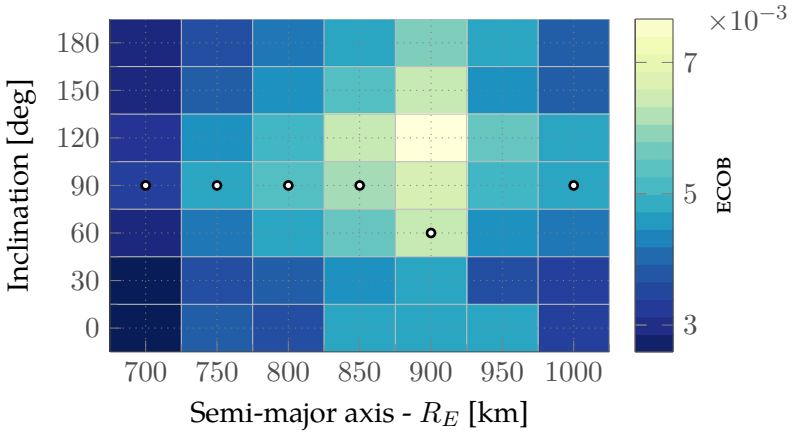

(a) 5 years

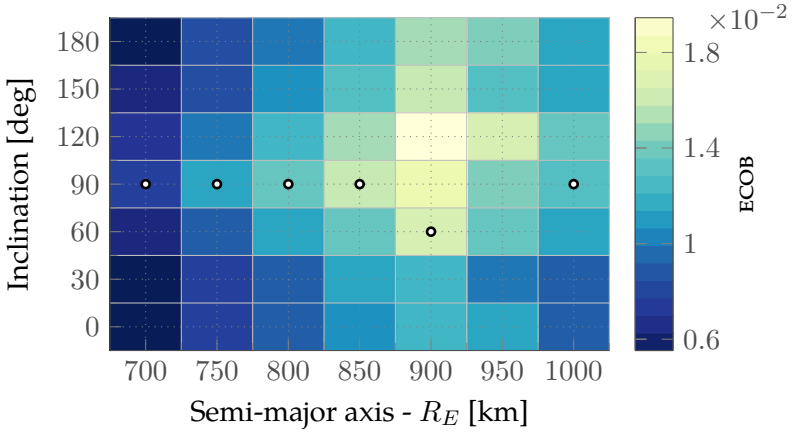

(b) 15 years

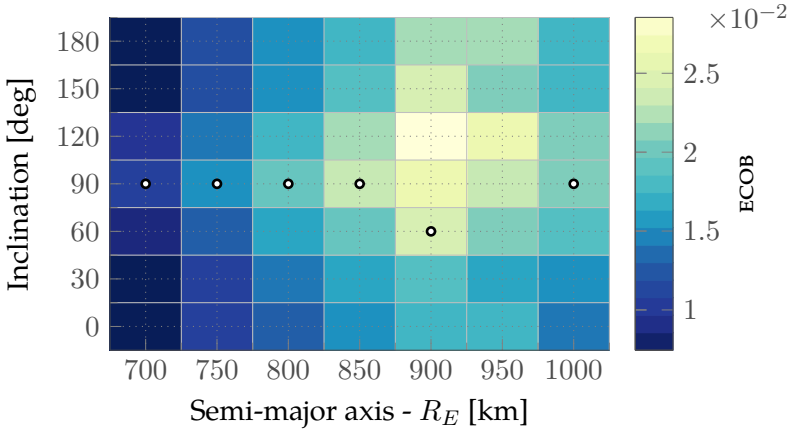

(c) 25 years

Figure 6.13: Heat map for the criticality index at three different time instants. Fragmentation mass equal to 1000 kg. The markers indicate the reference targets.

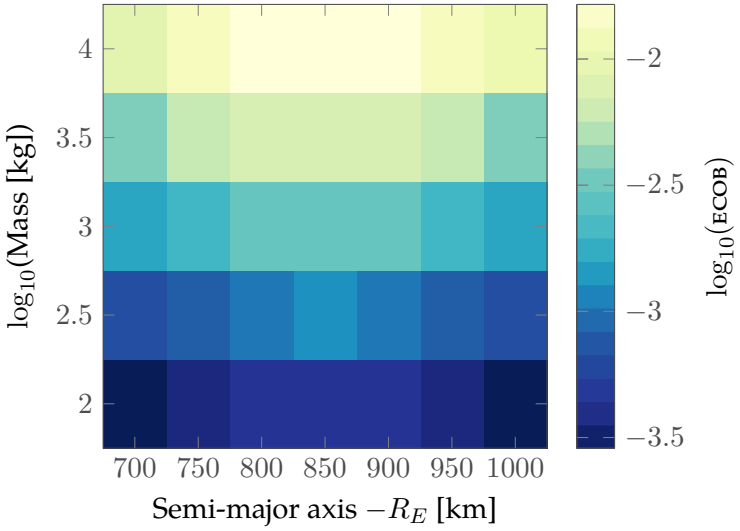

Figure 6.14: Heat map for ECOB as a function of the semi-major axis and the fragmenting mass.

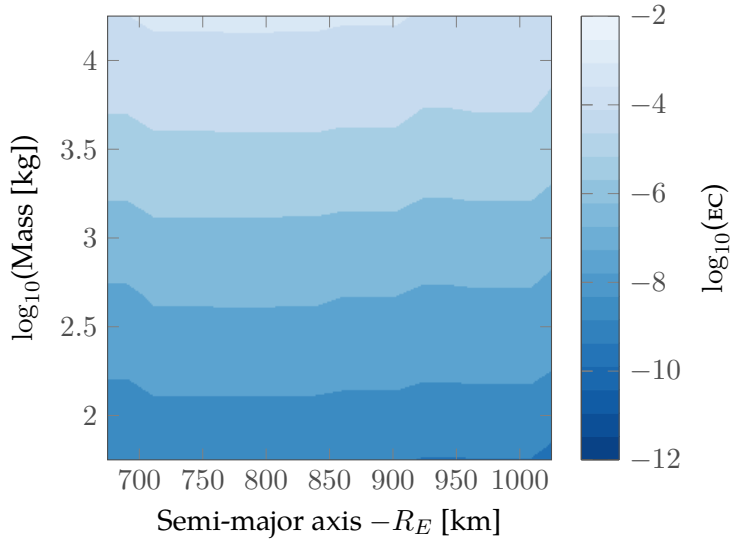

Figure 6.15: Heat map for EC as a function of the semi-major axis and the fragmenting mass. Figure by Jan Siminski.

results obtained with the EC defined by Kebschull et al. (2014b) are shown in Figure 6.15[4]. It is important to highlight that EC is based on very different principles from the ones used in ECOB, so the comparison can be only qualitative. In fact, the EC measures the change in the collision probability for the whole population (spacecraft, rocket bodies and debris) due to the fragmentation of a specific object, whereas ECOB considers only the collision probability for a selected set of objects representing the active satellites. In addition, in EC, several different fragmentation epochs are considered for a breakup, whereas in ECOB the effect of time is not present because the background debris population is not considered. Finally, EC takes into account the *feedback effect*, which is when a fragmentation triggers other new breakups, as the debris environment evolution is studied with the model SANE (Kebschull et al., 2014a), whereas ECOB describes the interaction of a single fragment cloud with the selected targets. Besides these differences, Figure 6.15 shows a similar dependence on the mass and on the semi-major axis. If the *feedback effect* were dominant in this time scale, then Figure 6.15 would show a stronger dependence on the mass and a dependence on the semi-major axis driven by the altitude and not by the target distribution. This suggests that the *feedback effect* is not particularly relevant for simulation of 25 years.

A closer look on the results in Figure 6.14 reveals that the dependence of the index ECOB on the mass M is predictable. Figure 6.16 shows the dependence of the index on the mass for different altitudes and one can observe how the curve is a straight line in the log-log representation. In particular, it can be found that

$$\text{ECOB}(M) = \left(\frac{M}{M_{\text{ref}}}\right)^{0.75} \cdot \text{ECOB}(M_{\text{ref}}), \tag{6.5}$$

where the exponent 0.75 is a direct results of the NASA breakup model. In fact, according to the model (Johnson and Krisko, 2001), the number of produced fragments larger than a given characteristic length is equal to

$$N_f(L_c) = 0.1(M)^{0.75} L_c^{-1.71}$$

with M equal to the sum of the target mass and the projectile mass in the case of catastrophic collisions.

6.4.6 Index computation

The observation in Equation 6.5 is important because it allows the required number of simulations to be reduced, simplifying the computation of the index for a generic object. In fact, the index can be computed through simulations using a single reference value for the mass (i.e. $10\,000\,\text{kg}$) and a grid in semi-major axis and inclination.

[4] Jan Siminski, Graduate Trainee, ESA, personal communication, 19/06/2015

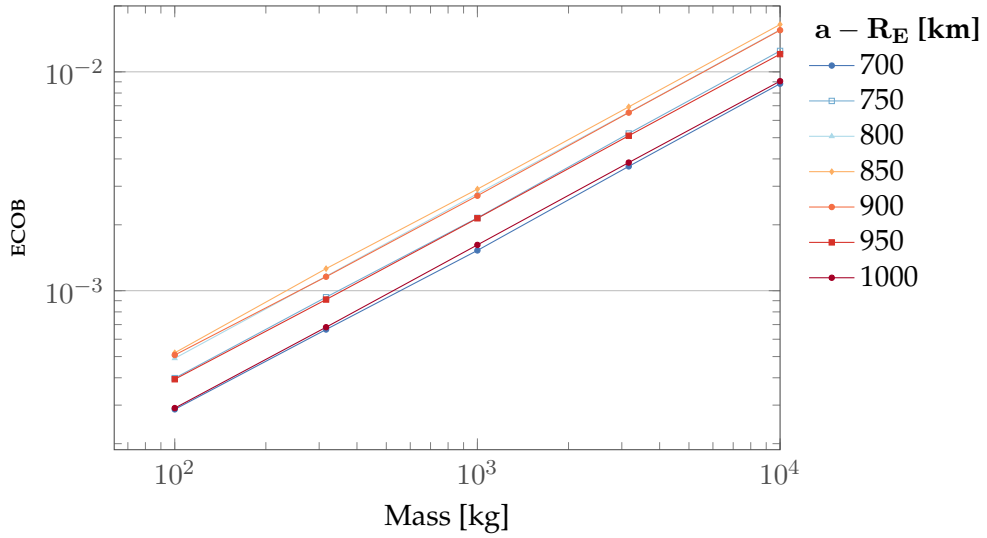

Figure 6.16: Index dependence on the mass for different altitudes.

Post-processing The value of the index on the plane of semi-major axis and inclination, with a fixed value of mass, can be stored and scaled to the value of the mass of the analysed fragmenting object. Then, finding the value of the index at the semi-major axis and inclination of the analysed object becomes a problem of fitting the surface defined by the value of ECOB in the grid of semi-major axis and inclination. The advantage of this approach is that the computational effort is required only to generate the surface (which as described in Section 6.4 is assumed to be *slowly*-changing if the development of space activities does not change abruptly). In this way, the reference surface is computed and stored, and severity index for all the objects in a database, such as DISCOS, can be quickly computed in post-processing, with a fitting procedure. Given the pairs $\{(\mathbf{x}_i^*, z_i^*)\}_i$, where $\mathbf{x}_i^*$ is a point of the grid in semi-major axis and inclination and z_i^* is the corresponding value of ECOB, the goal is to use these values to define a surface $Z = \{(\mathbf{x}_i, z_i)\}_i$ defined on the whole domain. Three options for the fitting were identified and tested with MATLAB.

- interpolation (Figure 6.17), which finds the value z_i at each point $\mathbf{x}_i$ of the domain using the values z_i^* at the nearest grid points; the number of the considered near grid points depends on the interpolation scheme (e.g. bilinear, bicubic, biharmonic) and in any case the value of the surface at the grid points is equal to the initial values, so that $Z(x_i^*) = z_i^*$;
- local regression smoothing methods (Figure 6.18), which uses least squares regression techniques in combination with a weighting function that gives larger importance to closer data points when computing the value z_i of a generic point $\mathbf{x}_i$ in the domain[5]; in this case is not assured that $Z(x_i^*) = z_i^*$;
- polynomial curve (Figure 6.19), which fits the data with a polynomial function in two dimensions, up to degree five.

[5]A description of the method can be found at `http://uk.mathworks.com/help/curvefit/smoothing-data.html`http://uk.mathworks.com/help/curvefit/smoothing-data.html, last access 5 January 2016.

Table 6.1: Methods for surface fit.

Method	Adj. R^2	Storable	Parametric
Interpolation	(1)	(Yes)	(Yes)
Local regression smoothing	0.9966	(Yes)	No
Polynomial	0.9687	Yes	Yes

In the three figures, the black dots represent the computed values of the index whereas the coloured surface is obtained by the different fitting methods. In all cases, representative targets are used, for a propagation time of 25 years and a fixed value of the fragmenting mass equal to $1000\,\mathrm{kg}$.

The main features of the comparison are summarised in Table 6.1. In the case of interpolation, MATLAB offers different options for the curve to use (e.g. linear, cubic, or bi-harmonic spline): in any case the adjusted R^2 is obviously equal to one as $Z(x_i^*) = z_i^*$, so this cannot be used as a measure of the quality of the fit. Figure 6.17 shows in any case how, even with a coarse grid, the interpolation provides a good representation of the surface. The interpolation does not give a strictly parametric expression of the surface Z, but analytical methods can be easily implemented to describe the surface. When MATLAB is used, the output of the fit can be stored in a special type of variable and reused to compute the index for different objects. When MATLAB is not used, it may be necessary to recompute the local interpolation for each object, but the operation is not expected to be computationally expensive.

When regression methods are applied, the whole shape of the surface is described. In this case MATLAB offers two options for the regression model: a linear or a quadratic one. The value of the adjusted R^2 is good, but this method is not parametric, has a more complex formulation and does not seem to offer any additional advantage compared to the interpolation. For this reason, the regression methods were discarded.

The third method, the polynomial curve, combines the positive features of the two previous approaches. Firstly, it describes the whole curve, so the coefficients needs to be computed only once and then the equation can be applied for the computation of the index for any object. Secondly, once the equation is obtained, it is completely independent from any programming language. However, the performance in terms of adjusted R^2 were not considered sufficient. Figure 6.19 shows the result for a polynomial curve of fifth order both in x and y: the polynomial representation appears to *smooth* the curve, especially at the peak. For these reasons, the local interpolation was preferred.

Tool structure The observations in the previous sections help defining the structure of the tool to compute the environmental index. This can be divided into two parts: first, the computation of index using a set of targets and a reference mass for the fragmentation

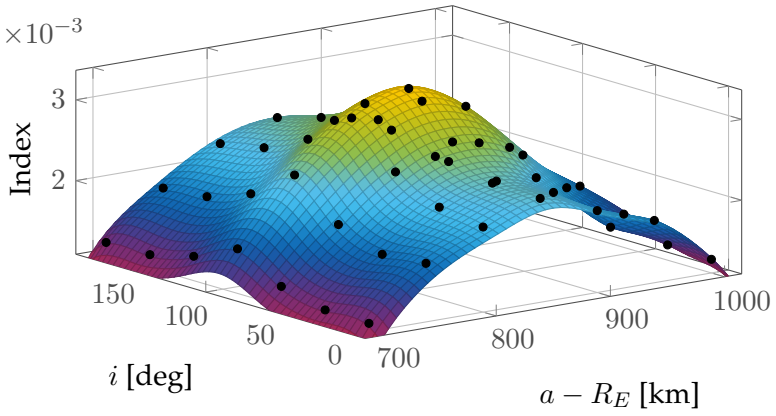

Figure 6.17: Index interpolation with biharmonic spline.

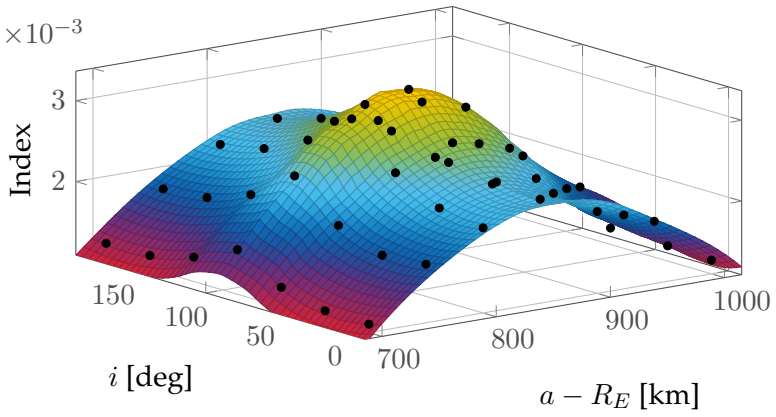

Figure 6.18: Index fit through a local regression smoothing method.

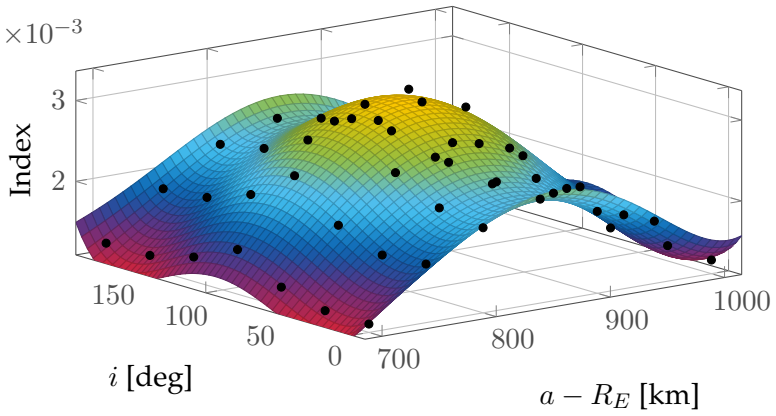

Figure 6.19: Index fit to a polynomial curve.

on a predefined grid in semi-major axis and inclination; second, the computation of the index for different fragmenting spacecraft and rocket bodies.

The first part of the tool uses the method based on the continuity equation and it is highly computationally expensive, so that the super-computer facilities of the University of Southampton, IRIDIS, are required. Once this phase is concluded, the output consists in the matrix plotted in Figure 6.12, which can be easily saved and exported in different formats (e.g. `ASCII` file), depending on the user platform. The matrix represents the input of the code that actually computes the environmental index for the objects of interest. The code performs the fitting of the surface using a local interpolation method and rescaling the index depending on the mass of the studied objects. The code can receive as an input a file containing the list of the objects to analyse. For example, the results in Section 6.4.7 are obtained using as a database the data extracted from DISCOS (Flohrer et al., 2013) considering objects in orbits between 700 and $1000\,\mathrm{km}$. For each object its kind (i.e. rocket body, spacecraft, other) and its year of launch are specified, so that the user can choose to study only a subset of the list. A maximum number of the objects to study can also be specified.

Computational time The tests with the coarse grid were used also to assess the computational time required by the simulations and identify the most effective parallelisation strategy to run cases with fine grids. Figure 6.20 shows the computational time for the cases as in Figures 6.12-6.13. The computational time refers to a machine with 4 CPUs; the whole code is written in MATLAB and exploits its built-in parallel statements (e.g. `parfor`). The histogram in Figure 6.20 shows the computational time for the three main functions in the code

- `propTarget` propagates the target trajectories for the desired time frame considering drag and J_2;
- `buildLayer` simulates a catastrophic collision for a given breakup mass in each cell and compute the cloud spatial density, including fragments down to 1 cm, for the whole desired time window
- `addCollProb` computes the collision probability for each target and the value of the index on the studied grid applying a weighting factor, if specified.

Applying the same settings to compute a case with a fine grid as the one used in Section 6.4.7 would require more than 22 hours of computation with 4 CPUs (that is 3.6 days in CPU time) assuming that the simulation is still manageable in terms of RAM[6].

For this reason, it was decided to use IRIDIS, the super-computer facilities at the University of Southampton, to run the simulations with fine grids. The computation of one *layer* was divided into columns (simulations with the same semi-major axis), which are launched as separate jobs, each one with 12 processors allocated (the maximum). In this

[6]This was not verified.

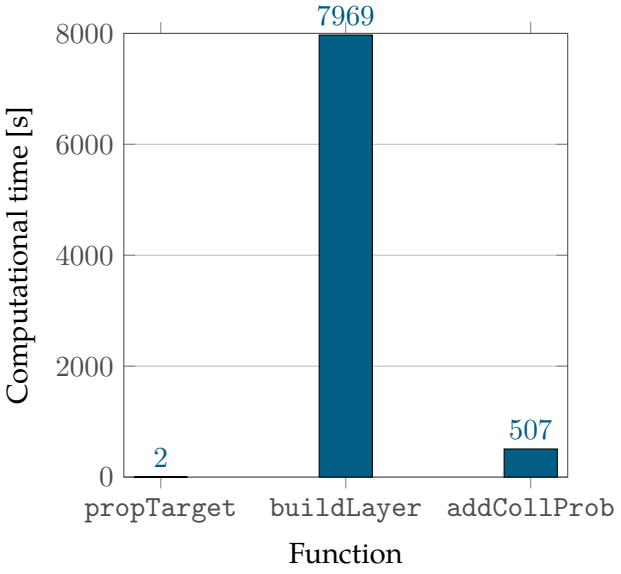

Figure 6.20: Computational time on a PC with 4 CPUs for a *layer* with coarse grid.

way one exploits not only the parallel features in MATLAB, but also the possibility of running multiple jobs at the same time. The submission of the jobs is fully automatised with a simple bash script. The whole setting allows obtaining a full layer in a period of time between one and three hours (depending on the availability of processors on the server). The *real* computational time (summing the running time of each job) would be around 19 hours (equal to almost six days of CPU time).

6.4.7 Results

Once the structure of the index was set, some simulations with a fine grid in semi-major axis and inclination were run. In this case, the grid is spaced of $10\,\mathrm{km}$ in semi-major axis and 10 degrees in inclination. The same grid is used both for the generation of the fragmentations and for the selection of the representative targets. Using, as before, the threshold of 90% for the represented A_c, 15 targets are identified, as shown in Figure 6.21. These targets are derived from the data from DISCOS considering only spacecraft (no rocket bodies) in orbit between 700 and $1000\,\mathrm{km}$, and launched in the last ten years. A reference breakup mass equal to $10\,000\,\mathrm{kg}$ was used.

As already presented in Figure 6.9, the cross-sectional area is not uniformly distributed across the whole LEO region: active satellites are mostly concentrated in polar orbits and this explains the distribution of the targets in Figure 6.21. The concentration of targets at latitudes around 80 degrees results in a much higher index in these regions. For fragmentations at these latitude, the targets can spend a large part of their orbits in the area (the extremes of the band) where the spatial density is maximum. The map appears quite symmetrical with respect to $i = 90$ degrees, so the possibility of reducing the grid in inclination to $[0, 90°]$ may be investigated in the future. For what concerns

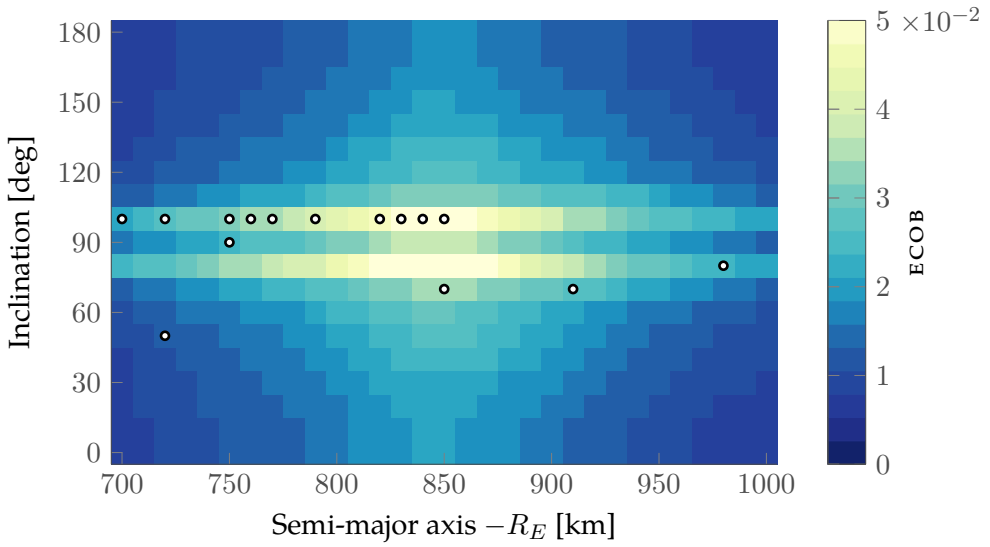

Figure 6.21: Resulting index for catastrophic collisions with breakup mass equal to $10\,000\,\mathrm{kg}$. Collision probability measured on the 15 targets indicated by a marker. Propagation time equal to 25 years.

the semi-major axis, a high density of targets around 800-$850\,\mathrm{km}$ makes this region the one with the highest environmental index.

The map in Figure 6.21 was combined with a database generated from DISCOS that contains all objects in orbits between 700 and $1000\,\mathrm{km}$[7] to evaluate the environmental index of objects already in orbit. Note that in this case, differently from the list used to define the target set, there is no filter on the launch date, and both rocket bodies (RB) and payloads (PL) are present. In this way, the index can be used to assess the environmental impact of both failed/not planned disposal strategies for payloads and of not sufficient passivation measures for rocket bodies[8].

As in Figure 6.21, Figure 6.22 represents the value of ECOB computed for a reference mass equal to $10\,000\,\mathrm{kg}$, and propagation time equal to 25 years, but in this case a contour plot is used to represent the surface obtained with the interpolation. The markers indicate the ten objects with the highest environmental index among the ones in the database. In particular, the location of the marker indicates the object orbital parameters and the size of the markers is proportional to the object mass. In this case, the markers have all similar size because all objects belong to the same family as shown in Table 6.2. The objects in Table 6.2 are sorted by the value of the environmental index ECOB, whereas the ID in the first column is related to the object mass, with ID $= 1$ for the most massive object in the database. All objects in Table 6.2 belong to the same family, SL-16 R/B: they combine high mass and orbits within the most critical regions.

[7] Stijn Lemmens, Space Debris Analyst, ESA, personal communication, 25/06/2015

[8] The failure of a rocket body due to insufficient passivation measures may be modelled more accurately by an explosion than by a collision. As discussed in Chapter 2, the two classes of fragmentation produce fragments with a different distribution in size and in energy. For this reason, future work may investigate the difference in ECOB if explosions are modelled instead of catastrophic collisions.

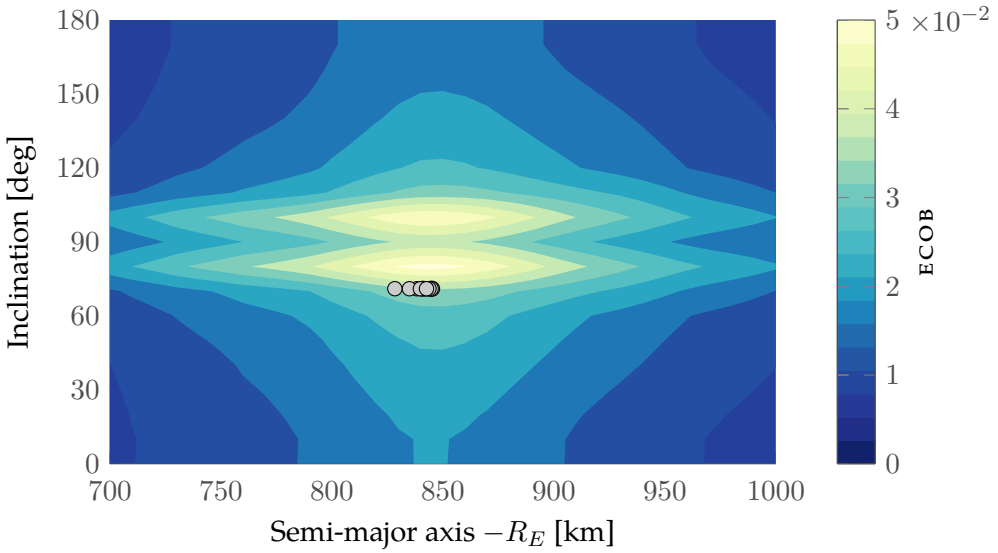

Figure 6.22: Contour plot of the environmental index for a breakup mass equal to $10\,000\,\mathrm{kg}$. The markers indicate the ten objects with the highest environmental index, from DISCOS data. The size of the marker is proportional to the mass of the object. Propagation time equal to 25 years.

Table 6.2: Top ten objects with the largest environmental index ECOB among DISCOS data considering all objects in orbits between 700 and $1000\,\mathrm{km}$. $\bar{h} = a - R_E$.

ID	COSPAR	Name	Type	$\bar{h}$ [km]	i [deg]	Mass [kg]	ECOB
2	2004-021B	SL-16 R/B	RB	845	70.9997	9000	0.032896
3	2007-029B	SL-16 R/B	RB	845	70.9753	9000	0.032837
1	2000-006B	SL-16 R/B	RB	841	71.0029	9000	0.032679
7	1990-046B	SL-16 R/B	RB	844	70.9989	8226	0.030711
5	1992-093B	SL-16 R/B	RB	842	71.0226	8226	0.030682
10	1993-016B	SL-16 R/B	RB	843	71.0068	8226	0.030667
9	1988-102B	SL-16 R/B	RB	840	71.0004	8226	0.030476
4	1985-097B	SL-16 R/B	RB	838	71.0039	8226	0.030420
6	1987-041B	SL-16 R/B	RB	835	71.0084	8226	0.030223
8	1988-039B	SL-16 R/B	RB	828	71.0160	8226	0.029394

The same analysis was performed also considering only spacecraft launched at least ten years ago. The results are shown in Table 6.3 and Figure 6.23. Also in this case, most objects belong to the same family (Cosmos satellites) with the exception of Envisat. It presents a much larger environmental index due to its large mass.

6.4.8 Comparison with other formulations

The proposed index ECOB was compared to the other environmental index formulations developed in the framework of the ESA study *Fragmentation Consequence Analysis for LEO and GEO Orbits*.

Comparison with EC and FOM As already mentioned, EC is the index developed by Kebschull et al. (2014b). EC is based on the computation of the change in the collision probability for the whole debris population due to the fragmentation of a selected object. A catastrophic collision is simulated at different time instants within the considered time window and its effect on the global debris population is obtained by applying an analytical model of the debris evolution, SANE. The proposed index of criticality takes into account both the consequences of the fragmentation c_{impact} and its probability of happening c_{risk}

$$\text{EC} = c_{\text{risk}} \cdot c_{\text{impact}} = \sum_{t=t_0}^{t_f} \left[(c_{\text{risk}})_t \cdot (c_{\text{impact}})_t \right], \tag{6.6}$$

where t_0 and t_f are the extremes of the considered time interval. The probability of a fragmentation happening is computed as

$$(c_{\text{risk}})_t = \Phi \, A_c \, (t - t_0), \tag{6.7}$$

with Φ flux of the background debris population on the object's orbit. The value of Φ is obtained with SANE as the product of the debris density at the object's orbit and the relative velocity between the objects and the debris population. The effect of the fragmentation is computed as

$$(c_{\text{impact}})_t = \sum_{t=t_{\text{frag}}}^{t_{\text{end}}} (\Delta p) \Delta\tau = \sum_{t=t_{\text{frag}}}^{t_{\text{end}}} (\Phi_{\text{frag}} - \Phi_{\text{no frag}}) \, A_c \, (t - t_{\text{frag}}), \tag{6.8}$$

where Φ_{frag} and $\Phi_{\text{no frag}}$ are respectively the flux in the scenario with the studied fragmentation and the flux without the fragmentation and $\Delta\tau = t_{\text{end}} - t_{\text{frag}}$.

Radtke et al. (2014) compares EC with an alternative index developed by AIRBUS (Utzmann et al., 2012). The index by AIRBUS, called Figure Of Merit (FOM), is computed as

$$\text{FOM} = \Phi A_c M^{0.75} \Delta t_{\text{orb}} \tag{6.9}$$

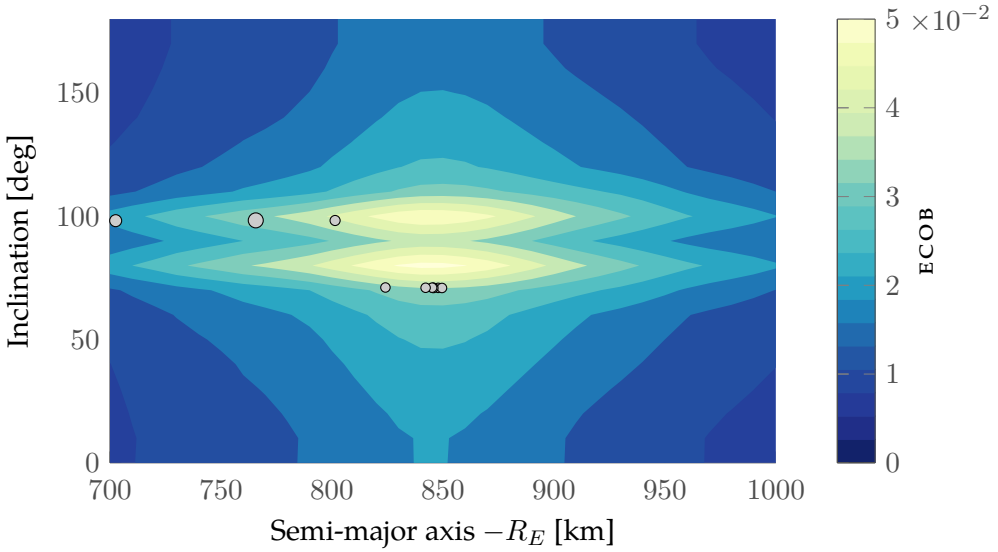

Figure 6.23: Contour plot of the environmental index for a breakup mass equal to $10\,000\,\mathrm{kg}$. The markers indicate the ten objects with the highest environmental index, considering only spacecraft launched more than ten years ago. The size of the marker is proportional to the mass of the object. Propagation time equal to 25 years.

Table 6.3: Top ten objects with the largest environmental index ECOB among DISCOS data considering only spacecraft launched more than ten years ago and in orbits between 700 and $1000\,\mathrm{km}$. $\bar{h} = a - R_E$.

ID	COSPAR	Name	Type	$\bar{h}$ [km]	i [deg]	Mass [kg]	ECOB
20	2002-009A	Envisat	PL	766	98.3338	8111	0.028247
32	2002-056A	Cosmos 1656	PL	801	98.2865	3680	0.018946
39	1990-046A	Cosmos 2082	PL	845	71.0418	3221	0.015260
36	1984-106A	Cosmos 1603	PL	846	71.0240	3221	0.015245
34	1985-097A	Cosmos 1697	PL	848	70.9634	3221	0.015166
40	1988-039A	Cosmos 1833	PL	842	71.0020	3221	0.015163
38	1987-041A	Cosmos 1844	PL	846	70.9001	3221	0.015133
37	1987-027A	Cosmos 1943	PL	850	70.9178	3221	0.015092
35	1985-042A	Terra	PL	824	71.1123	3221	0.014349
25	1999-068A	Adeos 2	PL	703	98.2107	5190	0.013461

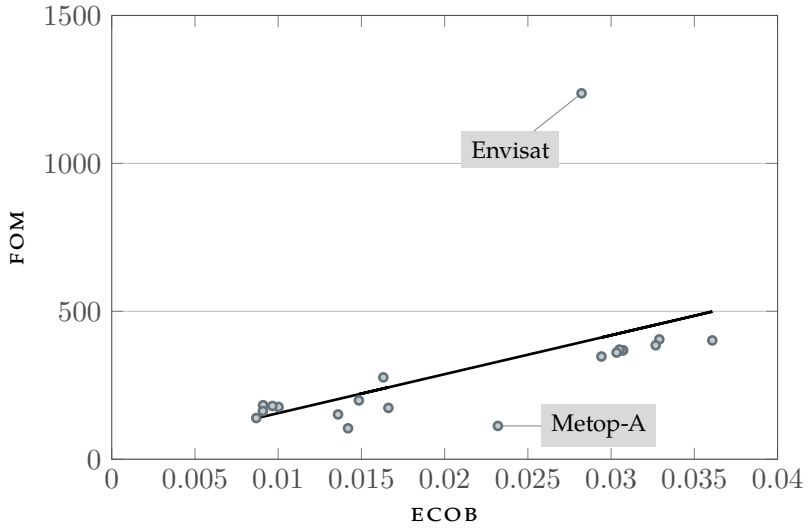

Figure 6.24: Correlation between the proposed index ECOB and FOM.

where Φ, in this case with units $[\mathrm{m}^{-2}\,\mathrm{yr}^{-1}]$, is the debris flux in the object's orbit, A_c and M are respectively the cross-sectional area and the mass of the object, Δt_{orb} $[\,\mathrm{yr}]$ is the remaining orbital lifetime.

The index ECOB proposed in this work was computed for the top 20 objects with the highest criticality according to EC (Radtke et al., 2014): the list of objects is reported in Table 6.4 and for each object the criticality estimated by the three methods is shown. Note that it is more interesting to study the ranking obtained with the different approaches more than the numerical value of the indices for the studied cases. For this reason, the results were analysed studying the correlation among the methods. Firstly, Figure 6.24 shows the correlation between the proposed index ECOB and FOM. The results show a good coherence between the two methods except for the case of Envisat and MetOp-A. For Envisat, the large difference may be explained by the fact that FOM takes into account the *exposure* of the object to the background population (ΦA_c). This term is particularly relevant for Envisat as its orbit is within the most affected region by the Iridium-Cosmos fragmentation. On the other hand, the value for MetOp-A may be explained by the fact that, as it is an operational spacecraft, in FOM its orbital lifetime is computed as

$$\Delta t_{\mathrm{orb}} = \Delta t_{\mathrm{act}} + 25$$

where Δt_{act} is the remaining mission duration. In this way, its orbital lifetime results much shorter than Envisat, f MetOp-A is on a orbit with higher altitude. The distinction between active and not-active satellites is not trivial; moreover, one can be interested in evaluating the environmental impact of a spacecraft without considering post-disposal manoeuvres exactly to assess how necessary those manoeuvres are. For this reason, active and inactive objects are treated in the same way in the computation of ECOB.

Table 6.4: Top 20 objects with the highest criticality according to EC (Radtke et al., 2014). $\bar{h} = a - R_E$.

ID	COSPAR	Name	Type	$\bar{h}$ [km]	i [deg]	Mass [kg]	ECOB	FOM	EC	Rank ECOB	Rank FOM	Rank EC
1	1998-043G	SL-16	RB	807.5	98.39	8226	0.036078	401.6	2.638	1	3	1
17	2004-021B	SL-16	RB	845	71	9000	0.032895	405.1	0.0463	2	2	17
18	2000-006B	SL-16	RB	841	71	9000	0.032676	385.2	0.0463	3	4	18
19	1990-046B	SL-16	RB	844	71	8226	0.030724	368.5	0.04173	4	6	19
20	1992-093B	SL-16	RB	842.5	71.02	8226	0.030685	367.9	0.04173	5	7	20
2	1998-045B	SL-16	RB	840	71.01	8226	0.030502	370.7	2.638	6	5	2
3	1987-027B	SL-16	RB	836.5	71	8226	0.03033	360.5	2.638	7	12	3
4	1988-039B	SL-16	RB	828.5	71.02	8226	0.029418	347.3	2.638	8	19	4
5	2002-009A	ENVISAT	PL	765.5	98.33	8111	0.028224	1236.9	0.867	9	1	5
6	2006-044A	METOP-A	PL	820.5	98.67	4086	0.023197	112.6	0.7502	10	66	6
10	1999-008A	ARGOS	PL	828	98.71	2490	0.016619	173.6	0.4283	11	44	10
9	1998-043A	RESURS O1-N4	PL	810.5	98.47	2775	0.016316	276.7	0.4834	12	25	8
7	1998-045A	COSMOS 2360	PL	850.5	70.85	3171	0.014848	198.9	0.7431	13	29	7
8	1989-089A	COBE	PL	877	98.98	2245	0.014195	104.6	0.5082	14	67	9
11	1993-061A	SPOT 3	PL	828.5	98.85	1891	0.013593	151.5	0.3161	15	56	11
15	1993-061H	ARIANE 40	RB	787	98.86	1764	0.010021	176.7	0.0929	16	41	15
13	1998-017B	ARIANE 40	RB	780.5	98.46	1764	0.00965	180	0.0929	17	35	13
12	1995-021B	ARIANE 40+	RB	766.5	98.73	1764	0.009093	182.6	0.0929	18	33	12
16	1990-005H	ARIANE 40	RB	766	98.79	1764	0.009081	162.8	0.0929	19	48	16
14	1991-050F	ARIANE 40	RB	756.5	98.7	1764	0.008683	139.3	0.0929	20	60	14

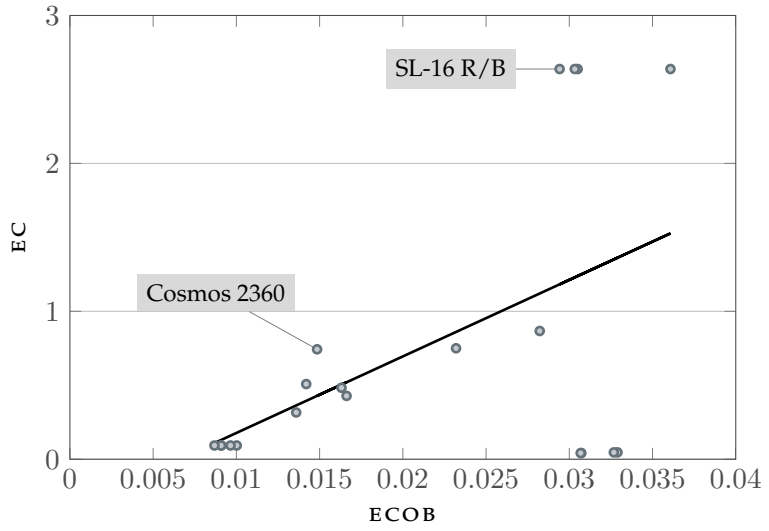

Figure 6.25: Correlation between the proposed index ECOB and EC.

Figure 6.25 shows the analysis on the correlation between EC and the proposed index ECOB. Also in this case it is important to remark that the two indices rely on very different models. In both cases it is true that not only the mass plays an important role in the value of the index, but also the orbital region. However, for ECOB this refers to the interaction with the reference targets, whereas for EC also the effect of the background population is considered. Observing the results in Figure 6.25 there is an evident difference in the evaluation of the objects with ECOB between 0.03 and 0.04. These objects are all SL-16 R/B with similar mass and similar orbits. For this reason, their ECOB (and also their FOM) is similar. However, the ranking with EC is very different, with four objects with the highest criticality and the other ones with the lowest criticality among all the 20 tested objects. This result is explained by the lack of interpolation between cells in the evaluation of the background population within SANE (Radtke et al., 2014). A small difference is present also in the evaluation of Cosmos 2360: with ECOB this object is less critical than objects with smaller mass (i.e. Argos and Resurs O1-N4) because its inclination is such that it is not in the most critical area. On the other hand, EC does not consider the dependence on the inclination, so the object is ranked 7th versus 13th with ECOB.

It can be concluded that ECOB gives consistent results as a small change in the orbit results in a small change in ECOB. This does not happen with EC, but the behaviour can be easily fixed by implementing the interpolation of the background population. The dependence on the inclination, not present in FOM and in SANE, appears relevant in ECOB. On the other hand, differently from ECOB, FOM allows for an immediate computation, whereas EC for a very long-term analysis of fragmentations (e.g. more than 100 years).

Comparison with CONCEPT The tool developed by the University of Southampton, independently from this work, CONCEPT, is based on the capabilities of the evolutionary

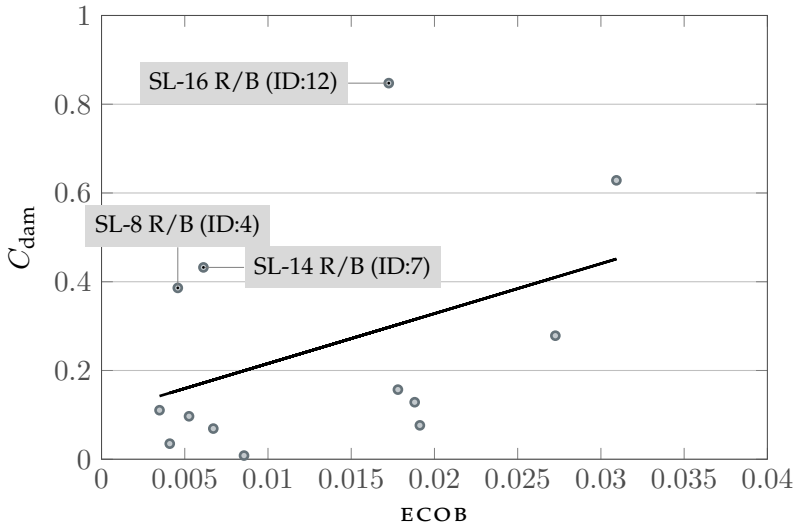

Figure 6.26: Correlation between the proposed index ECOB and the criticality index computed in DAMAGE.

model, DAMAGE, and a two-stage process to evaluate the criticality of a given object. Firstly, the evolution of the background population is simulated with DAMAGE and its state at different time steps is saved and stored. Secondly, the fragmentation of the object is superimposed to the scenario, by propagating all fragments produced by the breakup and larger than 10 cm. At each time step CONCEPT evaluates the probability of a collision for the fragments, so that consequent events can be modelled. The criticality index C_{dam} is based on the difference in the total number of objects between the case with fragmentation and the reference case with no breakup. A Monte Carlo approach is adopted to give statistical meaning to the results. An alternative criticality index P_{con} is defined; it indicates the probability that a run with the fragmentation has a larger number of objects than the reference scenario (Lewis, 2015).

Table 6.5 presents a subset of the objects analysed by Lewis (2015): only objects in LEO in orbits between 700 and 1000 km were analysed. Table 6.5 shows for each object its main features and the criticality as computed in DAMAGE, CONCEPT, and with the proposed index ECOB.

Analysing the results more in detail, Figure 6.26 shows the correlation between the criticality index computed by DAMAGE and ECOB. The two methods appear to give different results, especially for the three objects (ID 4, 7, 12) highlighted in the figure. These three objects have relative high altitude that results in a long orbital lifetime of their fragments. The simulation time frame is equal to 200 years versus only 25 years for ECOB, so this may explain the difference in the results as 25 years may not be enough to observe the large effect of the altitude. However, this does not explain why the index C for ID 1 and ID 8 is not as high as for ID 4.

Table 6.5: Objects in LEO with the highest criticality according to CONCEPT (Lewis, 2015). $\bar{h} = a - R_E$.

ID	Name	Type	$\bar{h}$ [km]	i [deg]	Mass [kg]	ECOB	C_{dam}	P_{con}	Rank ECOB	Rank C_{dam}	Rank P_{con}
2	SL-16 R/B	RB	844	71	8300	0.030931	0.6285	0.6632	1	2	2
13	Envisat	PL	759	98.2	8050	0.027263	0.2784	0.6102	2	5	8
6	Vostok R/B	RB	853	81.2	2750	0.019124	0.0764	0.5807	3	10	10
5	Meteor-2	PL	859	81.2	2750	0.018812	0.1285	0.6133	4	7	7
12	SL-16 R/B	RB	997	99	8000	0.017804	0.8475	0.8744	5	1	1
10	SSO S/C R/B	PL	780	98.5	4000	0.017254	0.1569	0.5961	6	6	9
11	NOAA-19	PL	855	99	1000	0.008560	0.0083	0.5744	7	13	11
3	SL-8 R/B	RB	771	74	1400	0.006715	0.0691	0.5617	8	11	12
7	Sl-14 R/B	RB	948	82.5	1410	0.006122	0.4323	0.6503	9	3	3
8	SL-8 R/B	RB	969	83	1400	0.005256	0.0968	0.6298	10	9	6
4	SL-8 R/B	RB	985	74	1400	0.004582	0.3861	0.6362	11	4	5
1	SL-8 R/B	RB	976	65.8	1400	0.004098	0.1105	0.6425	12	8	4
9	Iridium	PL	778	86.4	700	0.003484	0.0351	0.5521	13	12	13

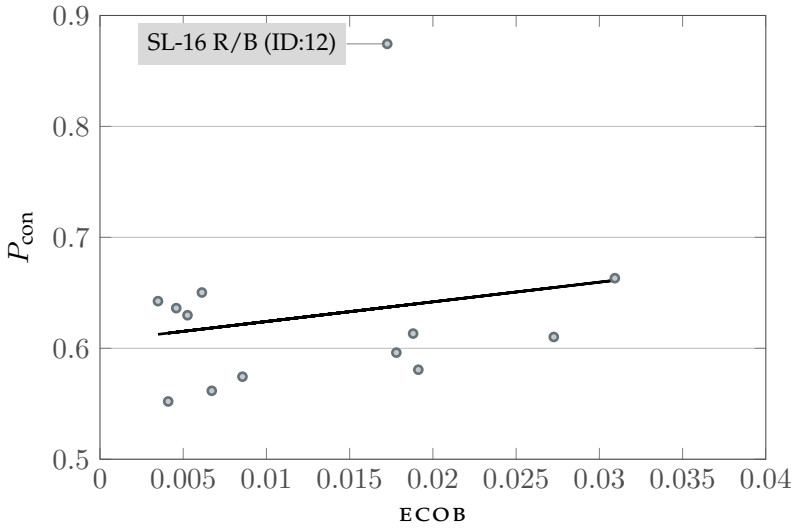

Figure 6.27: Correlation between the proposed index ECOB and the criticality index computed in CONCEPT.

Figure 6.27 shows the comparison with the criticality index computed in CONCEPT. Also in this case there is not a strong correlation between the indices. The large difference in the evaluation of the object with ID 12 is due to the fact that this object generates a large *feedback* effect when CONCEPT is used.[9] This object has a large mass, so it produces a large cloud with fragments with long orbital lifetime due to the high initial altitude. For this reason, the fragments can collide with other objects and generate new fragmentations. This behaviour was partially present also in the simulation with DAMAGE and it is the reason why this object has a such a large criticality index according to the analysis by Lewis (2015). In the proposed index ECOB the *feedback* effect cannot be modelled, so this can explain the difference in the results.

Comparison with CSI Rossi et al. (2015b) define a criticality index that takes into account four key-elements: environmental dependence, lifetime dependence, mass, and inclination. All these factors are combined in one index, Ξ, that is called the *Criticality of Spacecraft Index*. The expression of Ξ is

$$\Xi = \frac{M}{M_0} \frac{D(h)}{D_0} \frac{\text{life}(h)}{\text{life}(h_{1000})} \frac{1 + k\Gamma(i)}{1 + k},$$

where

- $\frac{M}{M_0}$ factors in the mass of the analysed spacecraft M, divided by a reference mass $M_0 = 10\,000\,\text{kg}$
- $\frac{D(h)}{D_0}$ considers the effect of the environment through $D(h)$, which is the spatial density of objects at the orbital altitude h, normalised by D_0, the spatial density of objects at $770\,\text{km}$

[9] Hugh G. Lewis, University of Southampton, personal communication, 09/07/2015.

Table 6.6: Comparison with the Criticality of Spacecraft Index as defined by Rossi et al. (2015b). $\bar{h} = a - R_E$.

ID	Type	$\bar{h}$ [km]	i [deg]	Mass [kg]	Ξ	ECOB	Rank Ξ	Rank ECOB
10	RB	843.84	71	9000	0.139	0.032861	10	1
11	RB	843.44	70.98	9000	0.139	0.032803	11	2
13	RB	849.14	70.88	8226	0.135	0.030435	13	3
1	RB	994.04	99.25	9000	0.313	0.019288	1	4
9	PL	953.94	64.98	4955	0.143	0.010199	9	5
4	PL	963.94	65.04	4955	0.16	0.009499	4	6
15	PL	955.14	65.08	4500	0.131	0.009426	15	7
3	PL	964.94	64.99	4955	0.161	0.009424	3	8
14	PL	957.34	64.86	4500	0.134	0.009223	14	9
12	PL	958.44	64.7	4500	0.135	0.009114	12	10
7	PL	964.74	64.95	4500	0.146	0.008771	7	11
6	PL	968.34	65.28	4500	0.151	0.008637	6	12
8	PL	971.14	64.81	4500	0.145	0.008399	8	13
5	PL	977.04	64.49	4500	0.154	0.008065	5	14
2	PL	987.54	64.98	4500	0.163	0.007637	2	15

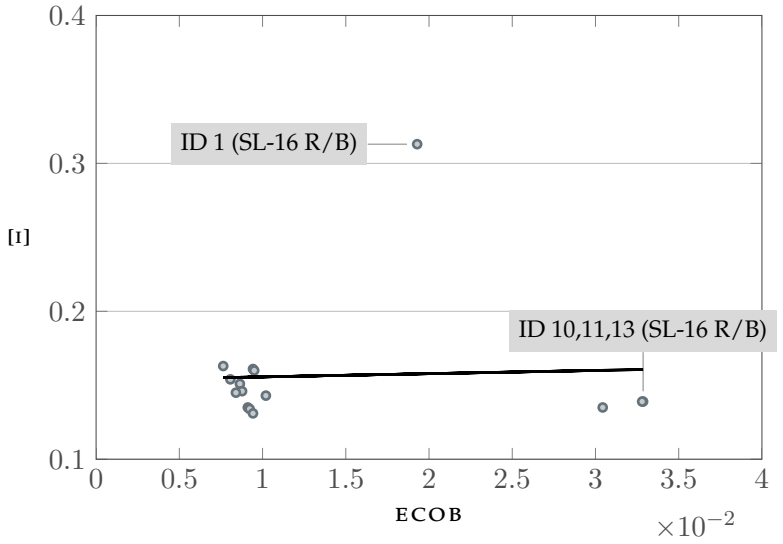

Figure 6.28: Correlation between the proposed index ECOB and Ξ as defined by Rossi et al. (2015b).

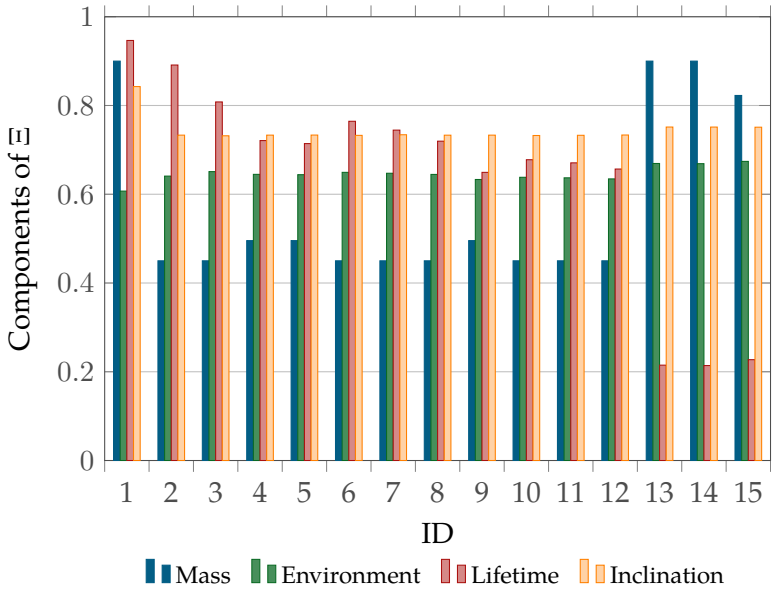

Figure 6.29: Analysis of the components of Ξ for the objects in Table 6.6.

- $\frac{\text{life}(h)}{\text{life}(h_{1000})}$ compares the expected orbital lifetime of the object given its orbital altitude h to the orbital lifetime of an object with $h_{1000} = 1000\,\text{km}$
- $\frac{1+k\Gamma(i)}{1+k}$, with $k = 0.6$ and $\Gamma(i) = (1 - \cos i)/2$, considers the effect of inclination.

The objects evaluated by Rossi et al. (2015b) and their value of Ξ are listed in Table 6.6, where also the value of ECOB is reported. Figure 6.28 shows clearly that the two indices predict very different criticality for the objects in Table 6.6. As in the case of CONCEPT, the same kind of object (a SL-16 R/B at high altitude) presents a much higher criticality index than the others.

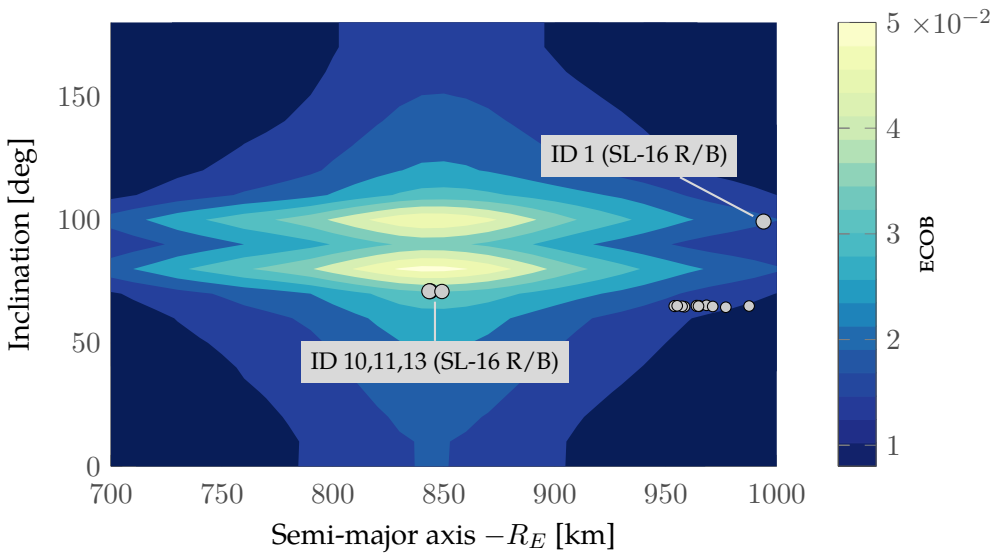

Figure 6.30: Contour plot of the environmental index ECOB for a breakup mass equal to 10 000 kg and objects from Table 6.6. The size of the marker is proportional to the mass of the object.

The simple expression of Ξ allows to analyse in detail the reason of this result. Figure 6.29 compares the four components of Ξ for all the tested objects. The spacecraft with ID1 presents the largest mass, the longest lifetime, and the most critical inclination among all 15 objects. When ECOB is computed the mass and the inclination contribute to a large value of the criticality index, but the altitude actually reduces the criticality of the object. In fact, its orbit appears to be *far* from the ones with the largest effect on the selected targets (Figure 6.30). The opposite happens for the objects with ID 10, 11, 13, which have a large ECOB because they are in an orbital region with a large influence on the reference targets, but a small Ξ because of their orbital lifetime. The same observation explains the negative correlation in the cluster of objects[10] in the bottom left of Figure 6.28: for these objects, ECOB increases when their altitude decreases because their distance from the targets' orbits decreases, whereas Ξ increases if the altitude increases. This observation reflects the fact that two indices are measuring the environmental impact on two distinct set of objects: ECOB only active satellites in a *medium* term timespan, whereas Ξ on the whole LEO region with an indefinite timespan. Both descriptions are possible, but it should be clarified which is more relevant to rank the criticality of space objects.

Summary

The extension of the continuity equation to multiple dimensions made it possible to describe also the first phase of the cloud evolution in an analytical way. This could

[10] These objects have orbital parameters similar to Cosmos satellites launched in 1976, 1986, 1988; however, the mass in Table 6.6 does not match the data in DISCOS database, so it was not possible to identify the objects.

could be used to build a fully analytical method, totally independent of the number of fragments. A first attempt to include all the parameters of the problem (a, e, Ω, ω) in a single propagation did not give the expected results because of RAM issues. Therefore, an alternative approach was designed based on mapping the initial distribution in (a, e) of the fragments into the distribution at the band formation. The method shows very similar accuracy to the previous formulation of the continuity equation method in Chapters 2 and 4, so it seems valuable to perform an extensive validation also for this formulation. Moreover, it was shown that applying the *density-only* method it is possible to simulate also clouds with a large number of fragments with no RAM issues and with almost constant computational time. This capability makes the *density-only* formulation very interesting as one could simulate also large breakups, such as the recent observed breakups, on a normal PC with no need of supercomputing facilities. Another proposed application is the computation of an environmental index. A grid of possible breakups is defined by considering different values of mass, semi-major axis, and inclination. For each breakup, the *density-only* propagation is applied to describe the evolution of the fragment cloud and estimate the increase in the collision probability for active satellite. The value of the index on the grid points is then interpolated and adjusted for the spacecraft mass, so that the index can be computed for any spacecraft. The results obtained with the proposed approach were compared with other environmental indices defined in the literature and the differences among the approaches were highlighted.

7

Conclusions

This Chapter provides a short summary of the main findings of the thesis together with a discussion on its limitations and on possible development of the method in the future.

7.1 Summary of the thesis

The current work has investigated the formulation of an analytical model for the dynamics of space debris clouds. The purpose of an analytical formulation is to include all the relevant fragments produced by a breakup, considering for example also small objects, the ones smaller than $10\,\mathrm{cm}$, that are usually neglected in space debris modelling. In fact, their number is so large that following each object individually with a purely numerical method would result in a prohibitive computational time. For this reason, some techniques such as the introduction of representative objects, which collect a set of small fragments, were proposed in the past. In this work, the point of view of the analysis has been changed from the description of the trajectories of individual objects to the evolution of the whole space debris cloud. This was done by using the cloud spatial density as the parameter of study, including all the fragments larger than $1\,\mathrm{mm}$. In this way, the spatial density accounts for all the objects that can interfere with a mission by creating anomalies; other thresholds (e.g. $1\,\mathrm{cm}$) can be used to consider only the fragments that have the potential of destroying a satellite in case of collision. The advantage of this approach is that it has a more direct connection with the statistical nature of the problem, in particular for what concerns the computation of the collision probability for a spacecraft crossing the cloud.

Model formulation The proposed method is based on four main parts

- a breakup model, which defines the characteristics of the fragments depending on the energy and the typology of the breakup event;
- a numerical propagator, which describes the trajectories of the fragments in the first phase of the cloud evolution, dominated by the Earth's oblateness, until they spread around the Earth;
- a *fitting* function, which converts the information on the positions of the single fragments into a continuous function;
- a purely analytical propagator, which follows the cloud in its long term evolution.

The analytical propagator is based on the continuity equation, following and expanding the method proposed by McInnes (1993) to describe the effect of atmospheric drag on a set of objects.

Model validation The proposed method has been extensively validated through the comparison with the results obtained by applying a numerical propagator to follow also the long term evolution of the cloud. The results have been compared in terms of the resulting spatial density as this value is then used to compute the collision probability within the cloud. The proposed method has been tested under different conditions by changing the kind of breakup event, the breakup energy, the inclination and the altitude of the event. The accuracy of the method has been measured by the relative error on the total integral of the spatial density and on the peak of the density distribution. In the case of the numerical method, ten runs of the breakup models were used to obtain statistical relevant data, whereas this is not required by the analytical model. The proposed method shows a good level of accuracy for most of different tested conditions, but fails at altitudes lower than $800\,\mathrm{km}$. For low altitudes, in fact, one of the assumptions introduced to obtain an analytical expression for the density, namely that the fragments are on circular orbits, introduces a large error on the prediction of the effect of the atmospheric drag. On the other hand, in the region above $800\,\mathrm{km}$ the method shows a combination of good level of accuracy and reduced computational time with respect to the numerical propagation. This is particularly interesting as the region above $800\,\mathrm{km}$ is where the debris density is the highest and where many important missions for Earth observation can be found. Having a method to estimate the collision probability in this orbital regimes considering also the contribution of small objects could be, therefore, particularly interesting for operators of such important missions.

Method applications Given the positive outcome of the validation process, the method has been applied to compute the collision probability for a spacecraft crossing a debris cloud in many different scenarios. This requires, first of all, a way to compute the collision probability given the density of objects in a region of space. Poisson's distribution

and the analogy with the kinetic theory of gases was used for this purpose. To avoid assuming a fixed impact angle, an analytical approximation of the average relative velocity between the fragments in the cloud and a spacecraft passing through it has been developed.

Three possible applications of the method were identified:

- the study of real breakups in terms of the increase in the collision probability for a set of objects in the debris and satellite population;
- the study of *collision maps*, for the same set of objects, evaluating their exposure to fragmentations with different values of inclination and altitude;
- the study of the *influence* among these targets, assessing how a fragmentation starting from one object is able to affect the collision probability of another one.

In all three cases the analytical method offers an important reduction in the computational time and gives an interesting insight on the contribution of small fragments to the collision risk. For example, the *collision maps* help identifying under which conditions a fragmentation is more likely to have a large impact on a set of targets and highlighting which regions of space should be kept as *clean* as possible. On the other hand, the study of the influence among the target can be useful to identify good candidates for active debris removal missions.

Extension to multiple dimensions The limitation in applicability to altitudes lower than $800\,\mathrm{km}$ has been tackled by expressing the evolution of the cloud density as a function not only of the altitude, but of two parameters (the semi-major axis and the eccentricity). In fact, following the method by Gor'kavyi (1997), the continuity equation admits a natural extension to multiple dimensions. The dimensions do not have to be physical ones, so that the problem can be written in the most convenient set of coordinates and then translated into a physical spatial density *a posteriori*. This approach has been applied to describe the cloud evolution considering the effect of the Earth's oblateness (using the semi-major axis, the argument of perigee, and the longitude of ascending node as variables), the distribution of area-to-mass ratio and eccentricity within the cloud. This last case, in particular, allows the applicability of the method to be extended to orbits between 700 and $800\,\mathrm{km}$. As a result, the method can be applied to study the whole region of high debris density and the one with the largest number of active satellites. Some applications of the method exploiting the new scope were presented: also in this case, the analytical method offers a relevant reduction in the computational time, enabling new analyses on the consequences of a fragmentation event.

***Density-only* formulation** The potential of the method is fully exploited if the numerical propagation of single objects is completely removed. An attempt in this direction

was done describing the transition to the band as a *distortion* of the initial fragment distribution. The preliminary results obtained with this approach are extremely interesting because they present a level of accuracy equal to the formulation with the numerical propagation and a computational time only very weakly dependent on the number of fragments. This allows simulating clouds with a very large number of fragments. It also enable to perform a large number of simulations to compute an environmental index to quantify the effect of specific fragmentations on a set of relevant targets (e.g. active satellites).

Main findings The main results of the work can be summarised in the following list:

- an analytical method for the description of the evolution of space debris clouds generated by breakups has been developed; the method is based on the representation of the problem in terms of spatial density and it uses the continuity equation to obtain an analytical solution to the problem of the cloud long term evolution under the effect of atmospheric drag;
- three versions of the method have been devised: in the first one, the fragment density is function of the altitude only and the long term effect of atmospheric drag is studied; in the second one, the density can be expressed as a function of the most suitable parameters, depending on the modelled perturbation (e.g. semi-major axis and eccentricity for the case of atmospheric drag); in the third version, the cloud is modelled through its density right after the breakup, with two different propagation techniques for short term and long term evolution, without computing the trajectory of single fragments;
- the performance of the method has been evaluated finding a good level of accuracy for altitudes larger than $700\,\mathrm{km}$ and the ability of simulating different breakups not only in terms of fragmentation location, but also of breakup type and energy;
- the method has been extended to assess also the collision probability for a spacecraft crossing the fragment cloud, developing an analytical estimation of the relative velocity between the spacecraft and the cloud;
- the method has been applied to model many different scenarios of collisions proving the flexibility of the new approach and its ability of enabling new analyses on the collision risk due to small fragments;
- an environmental index to assess the consequences, on active satellites, of a fragmentation in LEO has been developed and applied to different databases of spacecraft.

7.2 Limitations of the work

The research here presented has clearly shown the two main advantages of the proposed method. Firstly, switching to a representation in terms of spatial density appears a natural formulation of the problem as it offers not only a reduction in the computational time, but especially a strong connection with the phisics of the problem and the analysis of the resulting collision probability. Secondly, applying the continuity equation provides an analytical solution to the problem while still keeping a certain degree of flexibility on the modelling. Nevertheless, also some limitations of the method have been identified.

Most critical phase in the cloud evolution The proposed method is mostly applied only once the cloud is spread to form a band. However, other authors (Hoots and Hansen, 2014; Theil and Sdunnus, 2003) focus on the earlier phases of the cloud evolution, when the cloud is less diluted and the spatial density is higher. In that case, the cloud is localised, so the conditions for crossing are much stricter, but, when they are respected, the resulting collision probability is much higher. Therefore, modelling also this part of the cloud evolution would be particularly relevant when studying the collision probability for a target in an orbit very close to the one of the fragmentation. In this case, which could be represented, for example, by a breakup within a constellation, neglecting the phase before the band formation may result in missing the most important part of the cloud evolution.

Band formation Another problem related with applying the method only once the band is formed is the estimation of the time for the band formation. As discussed in Chapter 2, the expressions available in literature describe the process of the cloud enveloping the Earth, but not the actual spreading of the fragments to reach a uniform distribution. For this reason, a safety factor was introduced; however, using this factor hides a gap in the modelling of the initial evolution of the cloud. Ideally, a better estimation of the time for band formation should be sought starting either from the equation for $\dot{\omega}$ and $\dot{\Omega}$ applied to the fragments generated by the breakup or from the application of the analytical model to the cloud spreading. In any case, Chapter 2 showed a weak dependence of the density profile on the time for band formation, so this suggests that additional work is required to understand from which point of the cloud evolution the method starts to be applicable.

Perturbation modelling The current version of the method is able to model the effect of the Earth's oblateness, relevant in the short time, and the one of atmospheric drag, relevant in the long time. However, at the altitudes where the method is used ($h > 700\,\mathrm{km}$) and especially for $h > 800\,\mathrm{km}$ also the effect of solar radiation pressure should be considered. Moreover, the effect of drag is described through a very simplified model

that has shown already some of its limits. In Section 5.4, a solution to the problem of the atmospheric model has been presented, which could lead to the inclusion of atmospheric models different from the exponential. In any case, the largest advantage of the application of the continuity equation is obtained when an analytical solution of the problem is obtained. This limits the number of the perturbations that it is possible to include and also the level of complexity of their models. This may also limit the practical application of the method if other perturbations, besides the atmospheric drag, are found to noticeable affect the cloud density profile. This limitation may be partially overcome by keeping only the description in terms of spatial density, but using other methods rather than the continuity equation to propagate the spatial density with time.

Single events versus background population The study of the collision probability was developed considering only the effect of the *new* fragments produced by a specific fragmentation event without considering the background population. However, if one focusses on the phase after the band formation, the *new* fragments occupy roughly the same volume (except for the effect of the maximum latitude) of the background population that outnumbers the fragments in the *new* cloud. This means that all the results involving the collision probability should be read in a *relative* way with respect to a baseline scenario without the studied breakup. This also suggests that the most natural context of application of the analytical model is within a global model of the space debris environment. In this framework, the analytical formulation can be used to the describe the production, the evolution and the accumulation of small fragments in the debris population.

7.3 Future works

The analysis of the limitations of the work has already suggested some possible elements for the development of the work and they are here discussed starting from the closest one to the formulation proposed in this work.

Updated parameters for the exponential atmospheric model The analysis at the end of Chapter 5.4 has shown that the present implementation of the exponential atmospheric model may lead to wrong results for what concerns the predicted density at low altitudes. It was also shown that this behaviour can be easily corrected both in the numerical and in the analytical propagator by using at each altitude band the corresponding values of the parameters in the atmospheric mode. Therefore, a new campaign of validation is required to the estimate the method accuracy. If the validation has a positive outcome, the method will have an extended scope as it could be applied to study the collision probability for spacecraft a low altitude (e.g. Hubble Space Telescope). In addition, changing the atmosphere parameters across different altitude bands may enable

to include more realistic atmospheric models, with the condition what locally (within each altitude band) they can be approximated by exponential functions.

***Density-only* formulation** Similarly to the case just discussed, also the results in Chapter 6 on the *density-only* formulation suggest to perform a detailed validation of this approach, studying the dependence of the accuracy on parameters such as the breakup altitude, and the energy and kind of fragmentation. The *density-only* approach appears very promising, so it is worth investigating if its result may be improved, for example, considering the distribution of eccentricity when the initial condition is *reshaped* into the distribution at the band formation.

Band formation The description of the first phase of the cloud evolution, under the effect of the Earth's oblateness, should be improved. This task is twofold: firstly, it should be possible to estimate more accurately the process of the band formation; secondly, a formulation to assess the collision probability also in this phase should be obtained.

Eccentricity, perturbations and alternative propagation methods Chapter 4 presented some possible ways to account for the distribution of eccentricity within the cloud, but the hypotheses introduced to obtain an analytical solution are still quite strong and the evolution of the eccentricity is not modelled. A new analytical formulation may be obtained with further work on the expressions in Appendix B.5; otherwise, other propagation methods, such as differential algebra, may be applied. A preliminary study in this direction is under development (Colombo et al., 2015).

The modelling of the cloud with Finite Element Methods (FEM) could be another interesting option as it would keep the advantageous point of view of describing the problem in terms of spatial density, but it would also allow more complex expressions for the perturbations to be considered and it could leverage the existing numerical methods to obtain an efficient implementation.

Besides this radical change, a careful evaluation of the possibility of including additional perturbations (especially solar radiation pressure) already in the continuity equation should be undertaken. A campaign of validation with a more refined modelling of perturbations than the one used in this work can help identifying which elements (e.g. a more realistic atmospheric model) can provide the largest improvement to the accuracy.

Environmental index The environmental index proposed in Chapter 6 has given insight into the effect of different breakups on active satellites. A further formalisation of the index may include levels such as the severity number defined in (European Cooperation for Space Standardisation, 2009) to evaluate different failure modes. In that

case, four levels of severity are defined (i.e. catastrophic, critical, major, negligible) that could be related to the value of the environmental index. Observe that the connection between the environmental index and the severity levels cannot be done by setting a simple numerical threshold for the index. In fact, the absolute value of the index will change every time that the target set is redefined. The connection to the severity levels may be done by identifying for each level a reference fragmentation (e.g. the breakup of Envisat to represent a *catastrophic* level of severity). When another spacecraft is evaluated, its index is compared to the ones of the reference fragmentations to assess its level of severity. This would also give an immediate meaning to the value of the index.

Inclusion in evolutionary models The aim of evolutionary models is to define possible scenarios of the debris population depending on parameters such as the frequency of launches, the compliance with debris mitigation rules, the solar activity. They are able to simulate breakup events, identifying the most likely values for their energy and their location, but they cannot follow all the objects in a fragment cloud. The analytical approach can give these methods this ability, so that the description of space debris population can be more accurate by including also small fragments. A reference in this attempt could be the work by Wiedemann et al. (2011) where it is described how in MASTER fragmentation clouds can be plugged in by the user to study the resulting increase in spatial density. Similarly, the analytical model could be integrated with an evolutionary method in the following way. The evolutionary model determines the conditions for a breakup to happen, defining the values of the breakup energy, altitude and inclination. The breakup model is used to generate all the fragments down to a minimum size (e.g. $1\,\mathrm{mm}$). The fragments larger than $10\,\mathrm{cm}$ are followed individually, whereas the smaller ones are treated in terms of spatial density. The propagation of the spatial density is obtained analytically by using the continuity equation. In this case, going back to the original formulation by McInnes (1993), the continuity equation may be applied on the whole population of small fragments. With this setting, it may be relevant to model also the interaction among the small fragments and to treat differently the collision risk coming from large ($\leq 10\,\mathrm{cm}$), medium ($1\,\mathrm{cm} - 10\,\mathrm{cm}$), and small fragments.

Software implementation Throughout the thesis, the emphasis was put on the reduction in the computational time that can be achieved by adopting the proposed propagation method. However, the whole code is currently implemented in an interpreted language as MATLAB, which presents much longer running times than compiled languages. The choice of using an interpreted language in this work was motivated by the fact that this kind of programming languages offers a short development time. Once that the full approach has been developed and the obtained results prove valuable, it could be worth implementing the model with a compiled language to further reduce the computational time. Moreover, such an implementation would facilitate the distribution of the software in the form of tools (e.g. one for the assessment of the consequences of a

fragmentation, one for the computation of the environmental index) that could be tested and used by operators and space agencies.

A

Validations & Implementation

A.1 Breakup model

The NASA breakup model was introduced in 1998 and, in comparison with the previous NASA models, presents a better estimation of the generation of small fragments ($< 10\,\mathrm{cm}$) and the adoption of area-to-mass ratio A/M distribution; the latter parameter is of particular relevance, as the A/M value is related with the time each object will spend in orbit before being removed by atmospheric drag (Johnson and Krisko, 2001).

A.1.1 Implementation

The model uses the characteristic length L_c of the fragment as the independent variable to set most of the cloud characteristics (i.e., number of fragments, A/M, mass), except the velocity, which depends on the A/M. The definition of L_c is clearly explained by Krisko et al. (2008): it is based on radar measuring techniques and it was chosen as the independent parameter as it can be easily related to hypervelocity tests and on-orbit observations. The applicability of the NASA breakup model, in terms of characteristic length of fragment generated, is set between $1\,\mathrm{mm}$ and $1\,\mathrm{m}$ (Krisko, 2011). In the following, the equations applied in CiELO are given.

Collisions can be classified in two categories: catastrophic and non-catastrophic. A collision is called *catastrophic* if it causes the complete fragmentation of both the impactor and the target; experiments show that this occurs when the impact energy per target

mass exceeds $40\,\mathrm{J\,g^{-1}}$ (Krisko, 2007). The number of produced fragments N_f of a given size and larger depend on the reference mass M_e of the collision,

$$N_f(L_c[\mathrm{m}]) = 0.1(M_e)^{0.75} L_c^{-1.71}. \tag{A.1}$$

In the above equation, L_c is in metres and the value of M_e is defined as follows

$$\begin{aligned} \text{Catastrophic collision:} \quad & M_e[\mathrm{kg}] = M_t[\mathrm{kg}] + M_p[\mathrm{kg}] \\ \text{Non catastrophic collision:} \quad & M_e[\mathrm{kg}] = M_p[\mathrm{kg}](v_c[\mathrm{km/s}]/1[\mathrm{km/s}])^2 \end{aligned}$$

where M_t is the target mass, M_p is the projectile mass, v_c the relative impact velocity between the projectile and the target[1]

For what concerns the implementation in CiELO, the characteristic length is divided into 100 bins equally spaced on a logarithmic scale between $1\,\mathrm{mm}$ and $10\,\mathrm{cm}$: the number of fragments for each bin is computed and once each fragment is assigned to one bin, its characteristic length is defined using the built-in MATLAB function `rand` to extract a random value for L_c within the bin.

For each L_c it is possible to define the distribution of A/M. Here the model distinguishes between objects larger than $11\,\mathrm{cm}$ and smaller than $8\,\mathrm{cm}$, as different data have been used to build the model in the two ranges. For larger objects, the decay rates of catalogued objects was studied to express the dependence of A/M on L_c; different expressions are provided for upper stages and for spacecraft. For smaller objects, the results of hypervelocity impact tests have been implemented into the NASA model. In the original paper (Johnson and Krisko, 2001), a *bridge* function is said to be used to connect these two ranges, but no details on its formulation are given.

Figure A.1 shows the prescribed value of the mean μ and of the variance σ of the A/M distribution as a function of L_c. The dashed vertical lines limit the two regions that needs to be linked by the bridge function and it is possible to observe that the distributions for Rocket Bodies (RB) and Spacecraft (SC) are very different for any value of L_c. In absence of a precise definition of the bridge function, it was decided to extend the validity of the expressions for large fragments down to $8\,\mathrm{cm}$, observing that at least in two cases (μ for SC and σ for RB) the functions tend to be continuous for $L_c = 8\,\mathrm{cm}$. It will be shown in Section A.1.2 that this choice gives results coherent with other implementations of the model.

[1]For non-catastrophic collision, Johnson and Krisko (2001) report $M_e[\mathrm{kg}] = M_p[\mathrm{kg}]v_c[\mathrm{km/s}]$ while Krisko (2011) $M_e[\mathrm{kg}] = M_p[\mathrm{kg}](v_c[\mathrm{km/s}])^2$. A discussion with the authors (Paula Krisko, Senior Scientist at Jabobs Technology, personal communication (email), June 2013) allowed verifying that the second equation is the correct one, even if many current debris models were using the expression in (Johnson and Krisko, 2001).

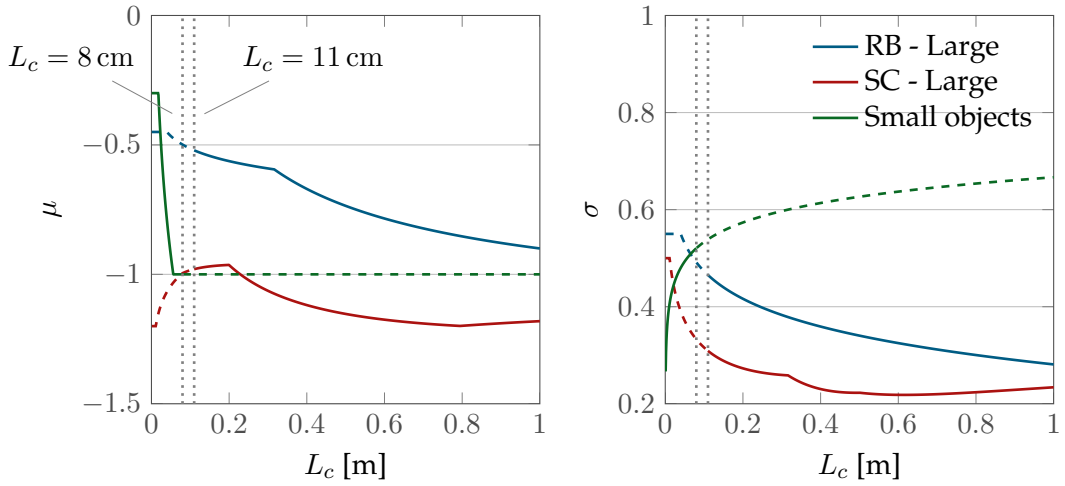

(a) μ **(b)** σ

Figure A.1: Value of the mean μ and of the variance σ of the A/M distribution as a function of L_c. The dashed vertical lines limit the two regions that needs to be linked by the bridge function. The three lines refer to large objects, $L_c > 11\,\text{cm}$, distinguishing between rocket bodies and spacecraft, and small objects, $L_c < 8\,\text{cm}$.

As here the focus is mainly on small objects, only the expressions for objects smaller than $8\,\text{cm}$ are shown. The distribution of A/M is written as

$$D_{A/M}(\lambda_c, \chi) = \mathcal{N}(\mu_{A/M}(\lambda_c), \sigma_{A/M}(\lambda_c), \chi); \tag{A.2}$$

$D_{A/M}$ represent the distribution of χ as a function of λ_c, where

$$\lambda_c = \log_{10}(L_c)$$
$$\chi = \log_{10}(A/M)$$

and $\mathcal{N}$ represents the normal distribution function

$$\mathcal{N}(\mu_{A/M}, \sigma_{A/M}, \chi) = \frac{1}{\sqrt{2\pi}\sigma_{A/M}} \exp\left(-\frac{(\chi - \mu_{A/M})^2}{2\sigma_{A/M}^2}\right),$$

whose parameters (i.e. $\mu_{A/M}$ mean value and $\sigma_{A/M}$ standard deviation) depend on the characteristic length

$$\mu_{A/M} = \begin{cases} -0.3, & \lambda_c \leq -1.75 \\ -0.3 - 1.4(\lambda_c + 1.75), & -1.75 < \lambda_c < -1.25 \\ -1.0, & \lambda_c \geq -1.25 \end{cases} \tag{A.3}$$

$$\sigma_{A/M} = \begin{cases} 0.2, & \lambda_c \leq -3.5 \\ 0.2 + 0.1333(\lambda_c + 3.5), & \lambda_c > -3.5. \end{cases} \tag{A.4}$$

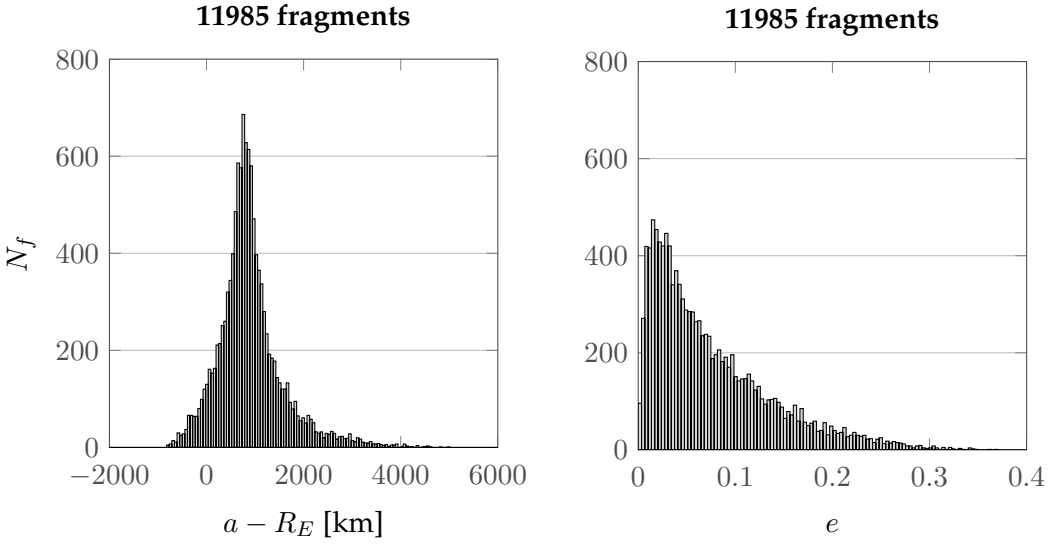

(a) Semi-major axis

(b) Eccentricity

Figure A.2: Distribution of fragments in orbital parameters for a non catastrophic collision with energy equal to $50\,\mathrm{kJ}$.

The built-in MATLAB function `randn` is used to generate (pseudo)random numbers drawn from a normal distribution.

The average cross-sectional area A is modelled as

$$A = \begin{cases} 0.540424\, L_c^2, & L_c < 0.001\,67\,\mathrm{m} \\ 0.556945\, L_c^{2.0047077}, & L_c \geq 0.001\,67\,\mathrm{m} \end{cases} \tag{A.5}$$

and so the mass is simply $M = A/(A/M)$.

Then, the Δv distribution is obtained as a function of the A/M and, also in this case, the distribution is modelled as a lognormal distribution

$$D_{\Delta V}(\chi, \xi) = \mathcal{N}(\mu_v(\chi), \sigma_v(\chi), \xi) \tag{A.6}$$

where $\xi = \log_{10}(\Delta v)$ and

$$\mu_v = 0.2\chi + 1.85$$
$$\sigma_v = 0.4.$$

A check is implemented to verify that the velocity variation is lower than $1.3\, v_c$: this is done because without any limit the method generates a small number of fragments with very high ejection velocity (in the order $60\,\mathrm{km\,s^{-1}}$). The function `randn` is called until the resulting velocity is lower than the threshold value. The velocity direction is randomly chosen using the function `rand`, which picks (pseudo)random numbers from a uniform distribution, to generate the velocity unit-vector.

An example of the resulting distributions in terms of semi-major axis a and eccentricity e is shown in Figure A.2 that refers to the mean over five multiple runs of the NASA breakup model considering an energy of $50\,\mathrm{kJ}$.

A.1.2 Validation

The implementation of the NASA breakup model in CiELO was compared with the available data on other implementations by space agencies. In particular, the document prepared by Rossi et al. (2006) for an Inter-Agency Space Debris Coordination Committee (IADC) meeting in 2006 was used as a reference as it contains the results of the implementations from five space agencies: ASI, CNSA, DLR, ESA, NASA. The document defines two scenarios, one explosion and one catastrophic collision, for which the implementation of the breakup model are compared in terms of the resulting distribution in fragment size, mass, area, and velocity variation.

Explosion case The fragmented object is a $1000\,\mathrm{kg}$ rocket body and the results include any object equal or larger than $1\,\mathrm{mm}$. Table A.1 summarises the number of objects larger than a given size according to the different agencies.

It is evident that there is a difference between the implementation in CiELO and the others for what concerns the generation of fragments equal or larger than $1\,\mathrm{m}$. Firstly, following what stated by Krisko (2011), in the implementation in CiELO $1\,\mathrm{m}$ is the largest possible size for objects generated by a fragmentation, whereas from the document by Rossi et al. (2006) appears that ESA arrives to generate objects larger than $10\,\mathrm{m}$ and NASA larger than $3\,\mathrm{m}$. One can conclude that they apply some modifications to the original equations of the breakup model (Johnson and Krisko, 2001; Krisko, 2011), whose expressions are not available in literature. It is likely that these modifications are connected to the procedure, introduced in (Krisko, 2011), to assure that the mass is conserved through the fragmentation. The mass conservation affects the generation of large fragments ($> 10\,\mathrm{cm}$), so it is not implemented in CiELO. Besides this difference, the implementation of the NASA breakup model in CiELO appears from the values in Table A.1 for $L_c < 1\,\mathrm{m}$ and from the distributions shown in Figure A.3.

Collision case This scenario describes a catastrophic collision involving a rocket body with target mass equal to $1000\,\mathrm{kg}$, projectile mass equal to $10\,\mathrm{kg}$ and impact velocity of $10\,\mathrm{km/s}$. The resulting distribution in fragment size, area, mass, and velocity variation are shown in Table A.2 and Figure A.4. Also in this case it is possible to observe a good agreement between the results obtained with CiELO and the ones from other implementations[2].

[2] ESA implementation of the NASA breakup model was updated after 2006, when the results by (Rossi et al., 2006) were obtained.

Table A.1: Size distribution for the different implementation of the NASA breakup model for an explosion involving a rocket body with mass equal to 1000 kg (Rossi et al., 2006).

	ASI	CNSA	DLR	ESA	NASA	CiELO
$L_c > 1\,\text{mm}$	378581	37865	1217054	324886	434928	378568
$L_c > 1\,\text{cm}$	9403	960	11724	8159	10731	10312
$L_c > 10\,\text{cm}$	234	32	230	206	248	253
$L_c > 1\,\text{m}$	7	9	0	6	8	1

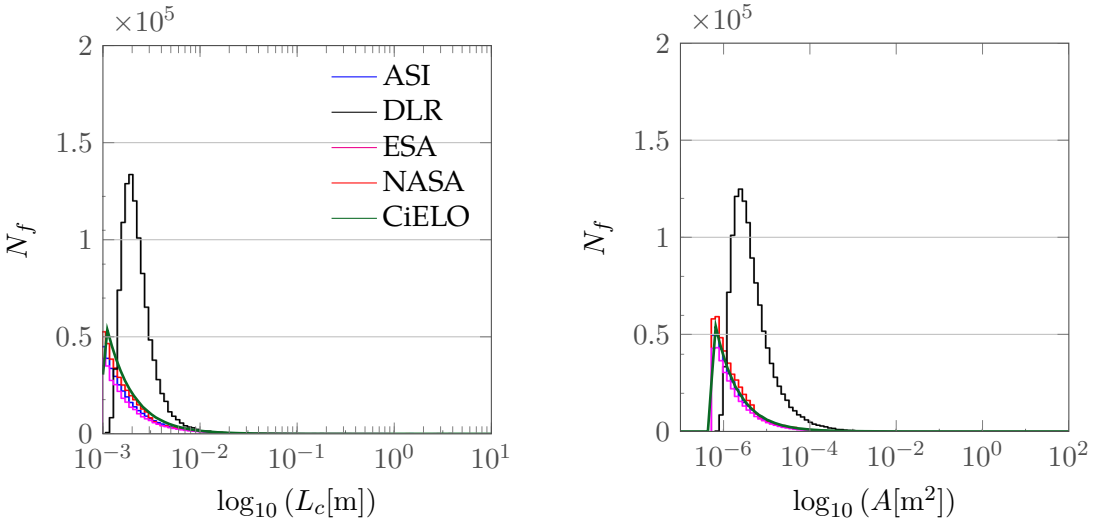

(a) Characteristic length

(b) Area

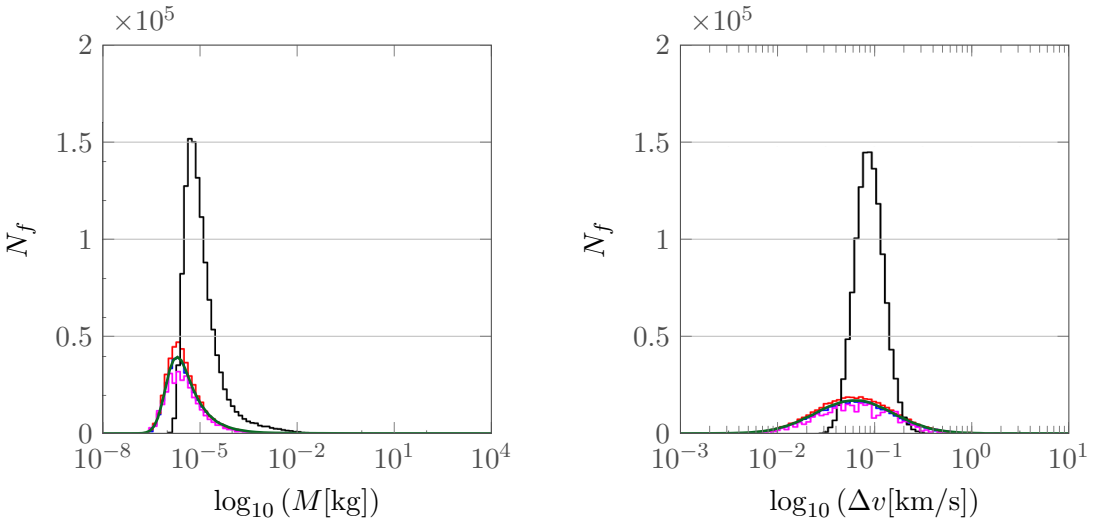

(c) Mass

(d) Velocity variation

Figure A.3: Distribution of fragments in size, area, mass, and velocity variation for an explosion involving a rocket body with mass equal to 1000 kg. Data for ASI, DLR, ESA and NASA from Rossi et al. (2006).

Table A.2: Size distribution for the different implementation of the NASA breakup model for a catastrophic collision involving a rocket body with target mass equal to 1000 kg, projectile mass equal to 10 kg and impact velocity to 10 km/s (Rossi et al., 2006).

	ASI	CNSA	ESA	NASA	CiELO
$L_c > 1\,\mathrm{mm}$	2416795	2416790	4723391	2957159	2416783
$L_c > 10\,\mathrm{cm}$	850	935	1539	862	1017

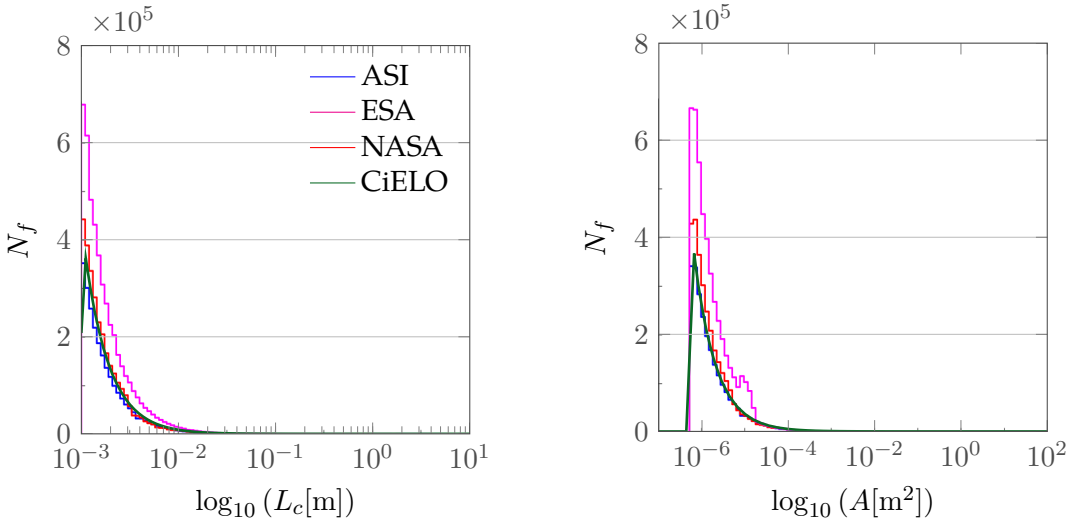

(a) Characteristic length

(b) Area

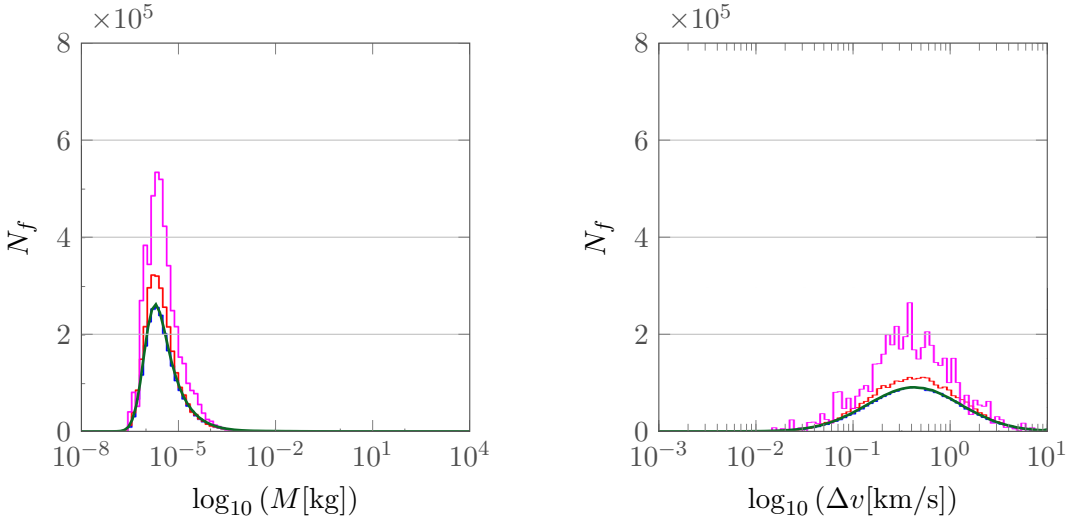

(c) Mass

(d) Velocity variation

Figure A.4: Distribution of fragments in size, area, mass, and velocity variation for a catastrophic collision involving a rocket body with target mass equal to 1000 kg, projectile mass equal to 10 kg and impact velocity to 10 km/s. Data for ASI, ESA and NASA from Rossi et al. (2006).

A.2 Propagation of drag effect

The effect of drag is modelled using King-Hele (1987)'s expressions for the secular variation of the orbital elements in one orbit. In particular, considering only the expression for eccentricity $e \leq 0.2$, these are the expressions for the average variation of the semi-major axis a and the eccentricity e

- $0.01 \leq e \leq 0.2$

$$\frac{da}{dt} = -\frac{c_d A}{M}\sqrt{\mu_E a}\rho_{\text{ref}} \exp\Big(-\frac{a-R_h}{H}\Big)\Big[I_0 + 2eI_1 + \frac{3}{4}e^2(I_0+I_2) + \frac{e^3}{4}(3I_1+I_3)\Big]$$
$$\frac{de}{dt} = -\frac{c_d A}{M}\sqrt{\frac{\mu_E}{a}}\rho_{\text{ref}} \exp\Big(-\frac{a-R_h}{H}\Big)$$

- $0.001 \leq e < 0.01$

$$\frac{da}{dt} = -\frac{c_d A}{M}\sqrt{\mu_E a}\rho_{\text{ref}} \exp\Big(-\frac{a-R_h}{H}\Big)\Big[I_0 + 2eI_1\Big]$$
$$\frac{de}{dt} = -\frac{c_d A}{M}\sqrt{\frac{\mu_E}{a}}\rho_{\text{ref}} \exp\Big(-\frac{a-R_h}{H}\Big)\Big[I_1 + \frac{e}{2}(I_0+I_2)\Big] \tag{A.7}$$

- $e < 0.001$

$$\frac{da}{dt} = -\frac{c_d A}{M}\sqrt{\mu_E a}\rho_{\text{ref}} \exp\Big(-\frac{a-R_h}{H}\Big)$$
$$\frac{de}{dt} = 0$$

where c_d is the drag coefficient, A is the cross-sectional area; M is the mass and, indicating the Earth's radius with R_E, $R_h = R_E + h_{\text{ref}}$; I_k indicates the modified Bessel function of the first kind and order k with argument $z = ae/H$.

With the hypothesis of a non-rotating atmosphere, the inclination of the orbit does not change; similarly, the argument of the perigee and the longitude of the ascending node do not change. It was already shown by Jehn (1996) that the spreading of the fragments in inclination is limited compared to the distribution in semi-major axis and eccentricity. In addition, the variation of inclination of the fragments' orbits was estimated. This was done using once more the analytical expressions by King-Hele (1987). Only the case of west-to-east winds was considered and the equations for objects with $e \leq 0.2$ were applied. The aerodynamic force due to the atmosphere rotation is normal to the orbital plane and it is written as

$$f_n = \frac{\rho v c_d A}{2M} r w \sin i \cos u \tag{A.8}$$

where w is the wind speed. The resulting rate of variation of the inclination is

$$\frac{di}{dt} = -\frac{\rho v r^2 w c_d A}{2M\sqrt{\mu p}} \sin i \cos^2 u. \tag{A.9}$$

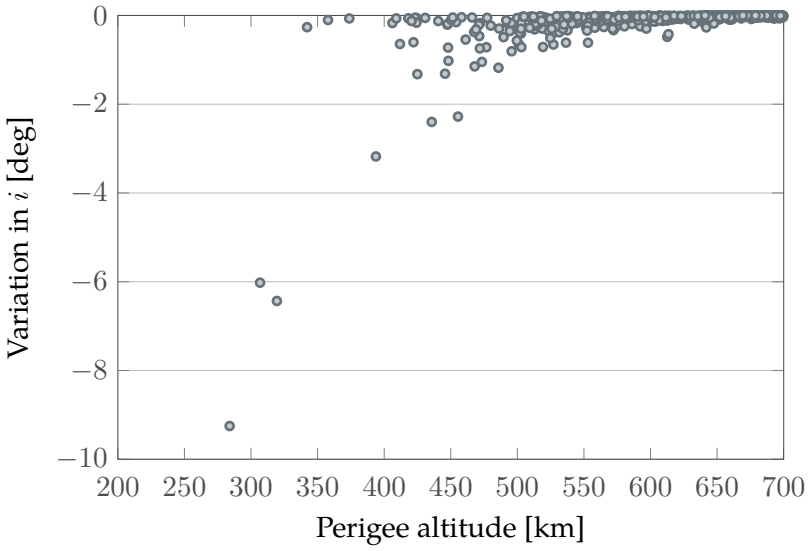

Figure A.5: Variation of the fragment inclination after 1000 days from the breakup for a fragmentation at 700 km on a polar orbit.

Equation A.9 expresses that the inclination continuously decreases over time. For quasi-circular orbits, the average $\frac{di}{dt}$ over a revolution is equal to

$$\frac{di}{dt} \approx -\frac{1}{4}\rho r w c_d \frac{A}{M} \sin i. \tag{A.10}$$

This expression was applied to evaluate the variation in inclination, using as value of the wind speed the fitting function by Vilhena de Moraes (1994). It expresses the variation of the atmosphere rotation with altitude as

$$w = w_E \left[B h_p + C - 2.5 \exp 1.47 + 1.610^{-4} h_p \right] \tag{A.11}$$

where w_E is the Earth's angular rate, h_p is the perigee height in [km] and B, C are constants. Their values can be found putting the atmosphere rotation equal to 0.7 rev/day at $500\,\mathrm{km}$ and equal to 0 at $900\,\mathrm{km}$. In this way, Equation A.11 is applicable for h_p going from 200 to $900\,\mathrm{km}$. The values of the constants are

$$B = 0.000196202 \quad C = 12.38057431.$$

Figure A.5 shows the variation in the fragments' inclination after 1000 days for a fragmentation at 700 km and on a orbit with inclination equal to 90 degrees; the average variation is equal to -0.0906 degrees. For this reason, the variation of inclination is not considered.

A.2.1 Implementation

The rate of variation of the parameters is obtained by dividing the average variation in one orbit by the orbital period

$$\frac{d\alpha}{dt} = \frac{\Delta\alpha}{T} \quad \alpha = a, e.$$

Finally, the obtained equations of the dynamics are integrated in MATLAB using the `ode45` function, which is a variable step integrator based on an explicit Runge-Kutta(4,5) method (also known as Dormand-Prince pair).

The propagation is stopped when the perigee altitude h_p gets below $50\,\mathrm{km}$ as, in this case, the fragment is considered to be re-entering through the atmosphere. This is implemented in MATLAB by setting an *event* function that checks the value of the perigee during the integration. The *event* functions are used also to manage the switch among different regions of eccentricity as in Equation A.2. It is interesting to observe that the implementation with event functions, indicated with KHS, reduces the computational time by 50% compared to the implementation where the value of the eccentricity is checked directly within the function with the dynamics. On the other hand, KHS is slower than implementing only one branch of the dynamics, but it allows an improvement of the method accuracy as it will be shown later.

A.2.2 Validation

The accuracy of the integration based on King-Hele (1987)'s formulation was evaluated by comparing its results with a full implementation of Gauss' equation (Vallado, 2013) and with the integration in Cartesian coordinates. The results of this comparison are summarised in Table A.3, which shows the computational time and relative error with respect to the Cartesian result for the different formulations of the dynamics. The results are obtained by computing the evaluating the evolution of the orbit of an object with mass equal to $1\,\mathrm{kg}$ and cross-sectional area equal to $10\,\mathrm{cm}^2$ for one month; only the effect of drag is considered here. The results refer to the simulation of trajectories with fixed perigee altitude, set equal to $500\,\mathrm{km}$, and different values of eccentricity, chosen to cover all the different ranges defined by King-Hele (1987)'s formulation (Equation A.2). The computational time is measured using a PC with 4 CPUs; the relative error is measured on the final value of the semi-major axis.

It is possible to observe how King-Hele (1987)'s formulation presents a very good level of accuracy together with a remarkable reduction in the computational time, both compared to the integration in Cartesian coordinates and to Gauss' equations. On average Gauss' equations allow a reduction of the computational time around two orders of

Table A.3: Computational time and relative error with respect to the Cartesian result for the different formulation of the dynamics.

		Computational time [s]				Relative error		
h_p	e	Cartesian	Gauss	KH	KHS	Gauss	KH	KHS
500	0.0005	73.1190	5.7314	0.0094	0.0772	2.90E-08	2.42E-08	1.96E-08
500	0.01	72.4265	4.9480	0.0098	0.0967	2.83E-08	7.61E-08	6.47E-08
500	0.021	70.5236	4.2254	0.0094	0.0451	2.80E-08	9.15E-09	9.15E-09
500	0.25	47.6288	0.2948	0.0092	0.0663	2.65E-08	3.84E-08	3.84E-08

magnitude compared to the Cartesian coordinates, whereas KHS and KH present respectively a reduction of three and four orders of magnitude. The relative error on the semi-major axis is of the same order of magnitude for Gauss, KHS, KH. As expected, the relative error is lower for KHS than KH for $e < 0.02$.

A.3 Geometric procedure for velocity estimation

In Chapters 3 and 5 two analytical approximations of the relative velocity between the fragments and a spacecraft (target), crossing the fragment cloud, were introduced. Equations 3.25 and 3.25 provide a fast method to estimate the average relative velocity, but some hypotheses were introduced to deal with the lack of information about the parameters ω and Ω. For this reason, the approach was validated adopting an independent, numerical procedure based on knowledge of all the orbital parameters both for the target and for the fragments.

The reference average velocity at any time of the analysis is computed with the following work-flow (Figure A.6):

1. the orbital plane of the target is intersected by the orbital plane of each fragment
2. the line obtained from the intersection of the planes is used to find the intersections between the line itself and the orbits
3. the two pairs of points obtained are checked measuring their distance
4. if the distance is lower than a given threshold value ($10\,\mathrm{km}$ in this case) the relative velocity between the target and the fragment at the intersection point is computed and stored
5. the average value among all the stored velocities is computed and used as reference value.

The approach is similar to computation of the Minimum Orbital Intersection Distance (MOID), defined as "a measure for the distance between the orbits of an asteroid and of the Earth, not considering the positions that the bodies occupy in them" (Bonanno, 2000). In fact, also with the method used in this work to estimate the relative velocity, the check is

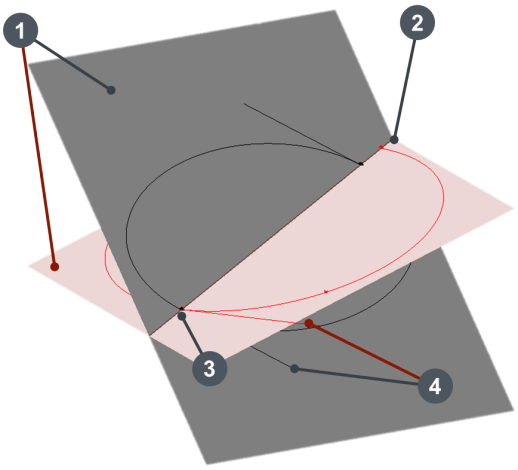

Figure A.6: Sketch of the validation procedure.

not made on the current positions of target and fragments because, as discussed already for the latitude, comparing the target and the fragment positions at only one instant is not representative of the whole time step. In other words, this approach computes the relative velocity considering that if the orbits of two objects intersect, then the two objects will both be at the intersection point at a certain time as the information of the distribution of the objects along the orbit is already contained in the expression of the spatial density.

The distance between the orbit of the target and the one of a fragment is computed starting from the output of the numerical propagation performed with a semi-analytical method, Planetary Orbital Dynamics (PlanODyn) (Colombo, 2015), based on averaged Gauss' equations for the evolution of the orbital parameters.

A.3.1 Equations

At a certain time t, the vectors of the orbital parameters of both the objects are known. From the orbital parameters, position and velocity can easily expressed in the perifocal system, which is the reference system centred in the Earth, with (x, y)-plane coincident with the orbital plane and the x-axis directed towards the pericentre (Bate et al., 1971).

The following symbols

$$(\mathbf{r})_{\text{PF,T}} \quad (\mathbf{v})_{\text{PF,T}} \quad (\mathbf{r})_{\text{PF,F}} \quad (\mathbf{v})_{\text{PF,F}}$$

are introduced to indicate the distance and the velocity of the target (T) and the fragment (F) in their respective perifocal systems. Then, a rotation matrix $\mathbf{R}$, with

$$\mathbf{R}_T = R(i_T, \omega_T, \Omega_T) \quad \mathbf{R}_F = R(i_F, \omega_F, \Omega_F),$$

can be used to transform the components of these vector in a Geocentric Equatorial Intertial (GEI) (Bate et al., 1971)

$$\mathbf{r}_T = \mathbf{R}_T(\mathbf{r})_{\text{PF,T}} \quad \mathbf{v}_T = \mathbf{R}_T(\mathbf{v})_{\text{PF,T}} \quad \mathbf{r}_F = \mathbf{R}_F(\mathbf{r})_{\text{PF,F}} \quad \mathbf{v}_F = \mathbf{R}_F(\mathbf{v})_{\text{PF,F}}.$$

From these vectors it is possible to compute the angular momentum vectors ($\mathbf{h}$)

$$\mathbf{h}_T = \mathbf{r}_T \times \mathbf{v}_T \quad \mathbf{h}_F = \mathbf{r}_F \times \mathbf{v}_F$$

that are perpendicular to their respective orbital planes. The line of intersection between the two planes is found by identifying the direction perpendicular to both the normals to the plane, so in this case

$$\mathbf{n} = \mathbf{h}_T \times \mathbf{h}_F.$$

The line of intersection, or *nodal* line, $\mathbf{n}$ can be projected back to the two perifocal systems

$$(\mathbf{n})_{\text{PF,T}} = \mathbf{R}_T^{-1}\mathbf{n} \quad (\mathbf{n})_{\text{PF,F}} = \mathbf{R}_F^{-1}\mathbf{n},$$

so that the problem becomes finding, on each perifocal plane, the intersection between a line and the ellipse representing the orbit. The problem is solved considering that the points of intersection will have true anomaly equal to

$$\nu_i = \arctan\left[\frac{(n_y)_{\text{PF}}}{(n_x)_{\text{PF}}}\right] + k\pi \quad k = 0, 1$$

where $(n_x)_{\text{PF}}$ and $(n_y)_{\text{PF}}$ indicate respectively the first and the second component of the vector $(\mathbf{n})_{\text{PF,}}$. Once the true anomaly is known, the position and the velocity in the points are known too, and they can be projected onto the GEI to measure the distance between the distance between the two couples of points.

A.3.2 Validation

The geometrical procedure for the computation of the relative velocity here described basically assumes that the point of minimum distance between two orbits lays on the nodal line. This may not be true for orbits with very similar inclination and different eccentricity, so the method needs to be validated through the comparison with a numerical method based on MOID computation. With the MOID approach, an optimisation problem needs to be solved for any pair target-fragment and once the point of minimum

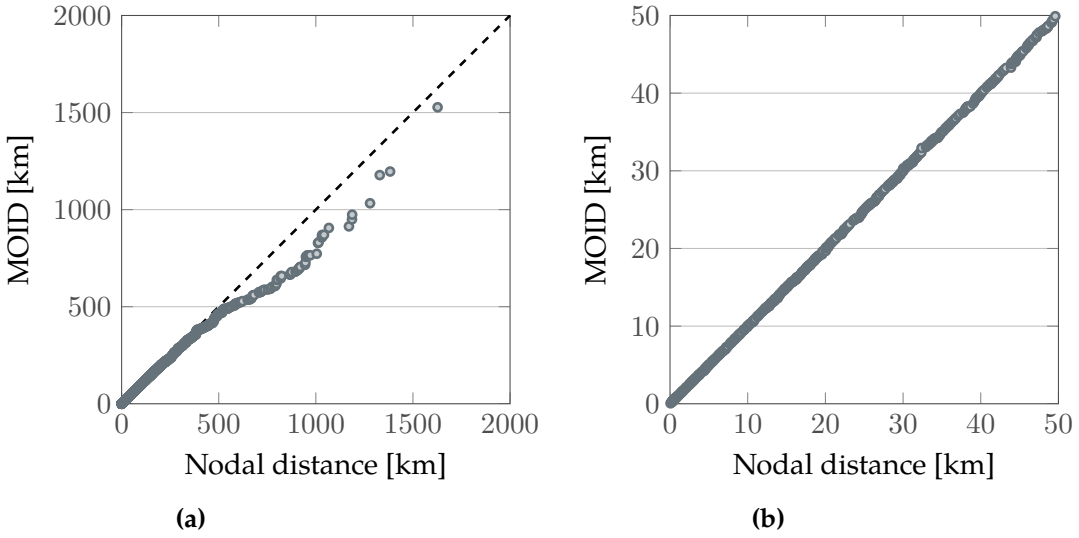

Figure A.7: Validation of the geometrical procedure for the computation of the relative velocity through the comparison with a numerical method based on MOID computation. (a) Whole cloud; (b) fragments with distance from the target lower than $50\,\mathrm{km}$.

distance is identified, the velocity of both object in that point is computed. The resulting relative velocity is then computed and compared with the one obtained with the geometrical method. The results for this comparison in the case where both the target and the fragments are on orbits inclined of 30 degrees is shown in Figure A.7; similar results were obtained for different orbital configurations.

One can observe from Figure A.7a that for high distance the two methods predict different values and, as expected, the MOID is always lower than (or equal to) the distance measured along the nodal line. On the other hand, zooming the graph to lower values of distance as in Figure A.7b shows a very good agreement between the two method. The advantage of the geometrical approach is that it is much faster than the MOID computation: the average running time for the MOID computation between a target and a cloud of 2397 fragments (such as the one used in Figure A.7) is equal to $78.57\,\mathrm{s}$ on a PC with 4 CPUs at 3.40 GHz; the time for the geometrical approach is, instead, $12.9\,\mathrm{s}$. Considering that the reference relative velocity needs to be computed at each time step during the validation process, using the geometrical approach results in a substantial saving in time.

A.4 Implementation of J_2 effect

In Chapter 4 three different approaches to model the effect of the Earth's oblateness were presented. When the effect of drag is neglected (Section 4.2.1), the formulation is particularly simple as it was found

$$n(a, \Omega, \omega, t) = n_0(a, \Omega_i, \omega_i),$$

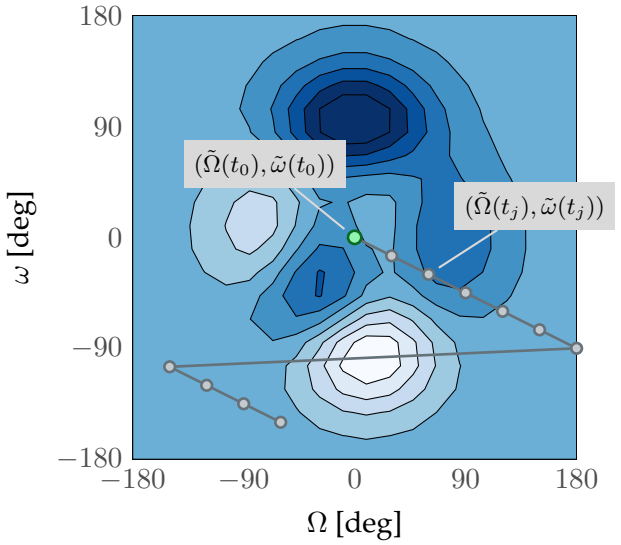

Figure A.8: Representation of the motion of the point where the density is measured at different time instants.

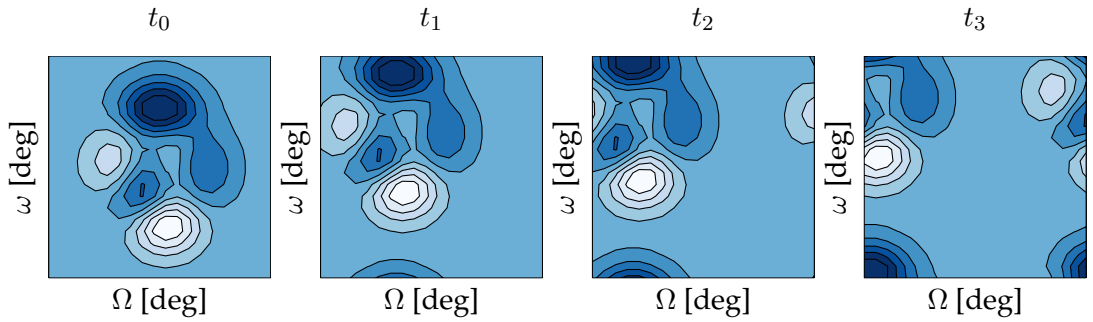

Figure A.9: Representation of the domain translation.

which means that the spatial density in the point (a, Ω, ω) at the time t is the same as the one at the initial time in the point (a, Ω_i, ω_i), where

$$\tilde{\Omega} = \Omega + f(a, t) \tag{A.12}$$

$$\tilde{\omega} = \omega + g(a, t), \tag{A.13}$$

where f and g are the functions that express the rate of variation of the parameters, respectively Equation 4.23 and Equation 4.24, derived in Section 4.2.

Figure A.8 represents this process: the contour plot shoes the initial condition n_0 and the green marker indicates the point $(0, 0)$. The value of density at $(0, 0)$ at a time instant t_j is obtained using Equations A.12 and A.13 to find $\tilde{\Omega}_j$ and $\tilde{\omega}_j$, so that $n(a, 0, 0, t_j = n_0(a, \tilde{\Omega}_j, \tilde{\omega}_j)$. This is equivalent to a translation of the domain along the characteristic lines as shown in Figure A.9.

When drag is neglected, the initial distribution n_0 at a certain semi-major axis is constant. For this reason, the cloud is divided into as many *slices* in (Ω, ω) as many point in the

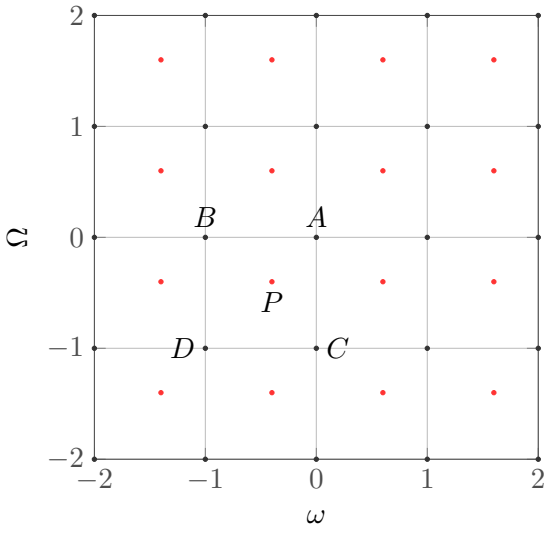

Figure A.10: Representation of the simplified local linear fit.

discretisation of the semi-major axis. As the semi-major axis is constant, each *slice* evolves independently from the others. In MATLAB this is translated into the following simple code, where, in this case, `a1v=a0v` because drag is neglected.

```
1  for jnd = 1:ngrid

   % find the closest value in semi-major axis
       [~,iav] = min(abs(a1v(jnd)-a0v));

6  % compute the shift for the angles
       O1new = O0v(1)+rateOmega(a1v(jnd),a0v(jnd));
       o1new = o0v(1)+rateomega(a1v(jnd),a0v(jnd));

   % find the closest points in angle grid
11     [~,iO] = min(abs(O1new-O0v));
       [~,io] = min(abs(o1new-o0v));
       vettO = [iO:nel,1:iO-1];
       vetto = [io:nel,1:io-1];

16 % find the new value of density
       n2d(jnd,:,:) = n02d(iav,vettO,vetto);

   end
```

The method outlined above corresponds to an order-zero fit to the nearest neighbour because in line 17 the initial value n_0 is used directly to assign the value n at a different time. This formulation appears prone to numerical instability. The performance of the method, in terms of numerical dissipation, can be improved by using more than one vertex to compute the value of the density, but still without performing a full 2D fit of the surface. The way to perform this task, indicated in the following as *local fit*, is represented in Figure A.10, where the black grid represent the initial reference and the red one the resulting after a certain time of propagation. Considering the point P, with the previous method it would get the value in A, which is the nearest point. The contribution of all

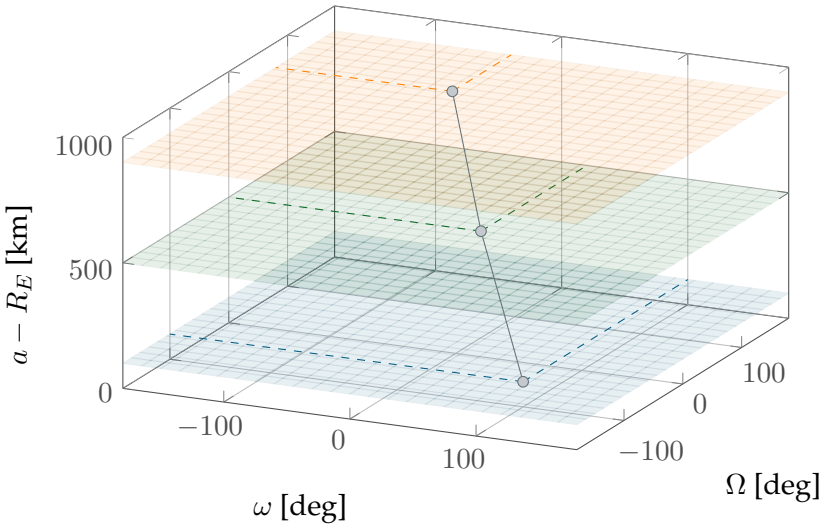

Figure A.11: Representation of the motion of the point where the density is measured at different time instants.

the neighbouring (B, C, D) can be easily added. The distance between P and the four points is used to perform a weighted average. As the translation of the domain is rigid, the value found for one point is valid for all the points in the grid.

In the case where the atmospheric drag is considered, the cloud is still divided in (Ω, ω) *slices*. At each time step, the value at a semi-major axis is obtained using the initial distribution in (Ω, ω) from a different *slice* Figure A.11. The approach of the *local fit*, explained in Figure A.10, can be extended to multiple dimensions to consider the change in a due to the effect of drag. Observe that in these cases the distances to be compared need to be normalised as they present very different absolute values. The computational time for all the cases are reported in Table A.4; the measured computational times refer to a PC with 4 CPUs at 3.40 GHz.

Table A.4: Computational time in seconds for J_2 implementation methods.

Method	Fit	No fit	Local fit
Only J_2	-	0.09	0.15
Drag $+J_2$ (3D)	19.64	0.51	0.33
Drag $+J_2$ (2D)	1.14	0.08	-

B

Demonstrations

B.1 Equivalence of Sykes' and Kessler's formulations

The spatial density as a function of the distance r and the latitude β is written by Kessler (1981) as

$$S(r, \beta) = s(r) f(\beta)$$

with

$$s(r) = \frac{1}{4\pi^2 r a \sqrt{(r - r_p)(r_a - r)}} \tag{B.1}$$

where r_p and r_a are respectively the pericentre and the apocentre

$$r_p = a(1 - e) \quad r_a = a(1 + e); \tag{B.2}$$

the dependence on the latitude is expressed by

$$f(\beta) = \frac{2}{\pi \sin \alpha \cos \beta} \tag{B.3}$$

where

$$\cos \alpha = \frac{\cos i}{\cos \beta}. \tag{B.4}$$

In Sykes (1990) the expressions for s and f are instead

$$s(r) = \frac{k}{a^2 r} \frac{1}{\sqrt{e^2 - \left(\frac{r}{a} - 1\right)^2}} \tag{B.5}$$

$$f(\beta) = \frac{1}{2\pi^2} \frac{1}{\sqrt{\cos^2 \beta - \cos^2 i}}, \tag{B.6}$$

where k is defined as a constant of normalisation.

The two formulations are actually identical as it can be seen by transforming the expressions by Kessler (1981) into the same notation as in Sykes (1990). Starting from the expression for the distance, the expressions for the pericentre and the apocentre in Equation B.2 can be inserted into Equation B.1 obtaining

$$s(r) = \frac{1}{4\pi^2 r a \sqrt{(r - r_p)(r_a - r)}} = s(r) = \frac{1}{4\pi^2 r a \sqrt{[r - a(1-e)][a(1+e) - r]}};$$

the argument of the square root can be manipulated in the following way

$$\begin{aligned}[r - a(1-e)][a(1+e) - r] = [r - a + ae][a + ae - r] = [ae - (a - r)][ae + (a - r)] = \\ = a^2 e^2 - (a - r)^2 = a^2 \left[e^2 - \frac{(r-a)^2}{a^2}\right] = a^2 \left[e^2 - \left(\frac{r}{a} - 1\right)^2\right],\end{aligned} \tag{B.7}$$

so that

$$s(r) = \frac{1}{4\pi^2} \frac{1}{r a^2} \frac{1}{\sqrt{e^2 - \left(\frac{r}{a} - 1\right)^2}},$$

which is the same as Equation B.5 besides the normalisation.

For what concerns $f(\beta)$, the expression for α in Equation B.4 can be used to rewrite the term $\sin\alpha \cos\beta$ in Equation B.3 obtaining

$$\sin\alpha \cos\beta = \sqrt{1 - \cos^2 \alpha} \cos\beta = \sqrt{1 - \frac{\cos^2 i}{\cos^2 \beta}} \cos\beta = \sqrt{\cos^2 \beta - \cos^2 i},$$

so Equation B.3 becomes

$$f(\beta) = \frac{2}{\pi} \frac{1}{\sqrt{\cos^2 \beta - \cos^2 i}},$$

that, besides a constant, is equal to the equation in Sykes (1990).

B.2 Derivation of the expression of the spatial density

The expression of the spatial density can be obtained starting from the hypothesis of the mean anomaly M equally distributed as done by McInnes and Colombo (2013). In this

case the density $n_M(M)$ will be constant with M and the follow condition holds

$$\int_0^{2\pi} k\, dM = 1. \tag{B.8}$$

The first step is to obtain the distribution with the true anomaly ν. Starting from the definition of M

$$M = E - e \sin E, \tag{B.9}$$

with E eccentric anomaly, dM can be written as

$$dM = \left(\frac{dE}{d\nu} - e \cos E \frac{dE}{d\nu} \right) d\nu \tag{B.10}$$

$$= \left[\frac{\sqrt{1-e^2}}{1+e\cos\nu} - e \frac{e+\cos\nu}{1+e\cos\nu} \frac{\sqrt{1-e^2}}{1+e\cos\nu} \right] d\nu \tag{B.11}$$

$$= \frac{(1-e^2)^{\frac{3}{2}}}{(1+e\cos\nu)^2} d\nu. \tag{B.12}$$

Therefore,

$$n_\nu(\nu) = \frac{(1-e^2)^{\frac{3}{2}}}{(1+e\cos\nu)^2} \tag{B.13}$$

which is identical to the expression by McInnes and Colombo (2013), beside a constant term due to the different choice in the normalisation.

The following step is the translation into a distribution in r. Starting from the definition of r the expression for $d\nu$ is found.

$$r = \frac{a(1-e^2)}{1+e\cos\nu} \quad \Rightarrow \quad dr = \frac{a(1-e^2)}{(1+e\cos\nu)^2} e \sin\nu\, d\nu \tag{B.14}$$

It is convenient to express $\sin\nu$ as

$$\sin\nu = \sqrt{1-\cos^2\nu} = \sqrt{1 - \frac{1}{e^2}\left[\frac{a}{r}(1-e^2) - 1\right]^2} \tag{B.15}$$

$$= \sqrt{1-e^2}\frac{a}{er}\sqrt{e^2 - \left(\frac{r}{a} - 1\right)^2} \tag{B.16}$$

so that

$$d\nu = \frac{(1+e\cos\nu)^2}{(1-e^2)^{\frac{3}{2}}} \frac{r}{a^2} \frac{1}{\sqrt{e^2 - \left(\frac{r}{a}-1\right)^2}}\, dr. \tag{B.17}$$

Substituting the expression of $d\nu$ in Equation B.17 in Equation B.13

$$\int_0^{2\pi} k \frac{(1-e^2)^{\frac{3}{2}}}{(1+e\cos\nu)^2}\, d\nu = 1 \tag{B.18}$$

one obtains

$$\int_0^{2\pi} k\frac{r}{a^2}\frac{1}{\sqrt{e^2-\left(\frac{r}{a}-1\right)^2}}\,dr = 1 \tag{B.19}$$

so the distribution $n_r(r)$ in r is

$$n_r(r) = k\frac{r}{a^2}\frac{1}{\sqrt{e^2-\left(\frac{r}{a}-1\right)^2}}. \tag{B.20}$$

Equation B.20 has as dimensions [1/km]; to obtain a real spatial density other two steps are required. Firstly, the number of objects in a bin are counted and secondly, the number is divided by the volume of the shell defined by the altitude bin.

For the first step, a rigorous approach will require

$$N(r;\Delta h) = \int_r^{r+\Delta h} k\frac{r}{a^2}\frac{1}{\sqrt{e^2-\left(\frac{r}{a}-1\right)^2}}\,dr; \tag{B.21}$$

if we consider $\Delta h \to 0$,

$$N(r;\Delta h) = \int_{-\infty}^{r} k\frac{r}{a^2}\frac{1}{\sqrt{e^2-\left(\frac{r}{a}-1\right)^2}}\,dr - \int_{-\infty}^{r+\Delta h} k\frac{r}{a^2}\frac{1}{\sqrt{e^2-\left(\frac{r}{a}-1\right)^2}}\,dr \tag{B.22}$$

$$\approx k\frac{r}{a^2}\frac{1}{\sqrt{e^2-\left(\frac{r}{a}-1\right)^2}}\Delta h. \tag{B.23}$$

Similarly the volume of the spherical shell of radius r and height Δh can be written as

$$V = \frac{4}{3}\pi[(r+\Delta h)^3 - r^3] = \frac{4}{3}\pi[3\Delta h r^2 + O(\Delta h^2)] \approx 4\pi r^2\Delta h. \tag{B.24}$$

The spatial density s is finally obtained as

$$s(r) \approx \frac{n_r(r)\Delta h}{4\pi r^2\Delta h} = \frac{k}{4\pi a^2 r}\frac{1}{\sqrt{e^2-\left(\frac{r}{a}-1\right)^2}}, \tag{B.25}$$

which is identical to the expressions by Kessler (1981) and Sykes (1990) apart from a constant ($k = 1$ in his expression).

B.3 Method of characteristics

The method of characteristics is a common approach to the solution of Partial Differential Equation (PDE). For the reader's convenience, the main points of the method are recalled

here, following the clear explanation prepared by Levandosky[1]. The general formulation of the method of characteristics will be then applied to the case of space debris cloud propagation.

B.3.1 General formulation

Let's consider the following equation where the solution u is a function of two variables

$$a(x,y)u_x + b(x,y)u_y = c(x,y) \tag{B.26}$$

The graph of the solution $u(x,y)$ is given by

$$S \equiv \{(x,y,u(x,y))\}$$

and at each point (x,y)

$$(a(x,y), b(x,y), c(x,y)) \bullet (u_x(x,y), u_y(x,y), -1) = 0$$

where $\bullet$ indicates the dot product; the vector $(a(x,y), b(x,y), c(x,y))$ lies in the tangent plane to S. Consequently, to find a solution to Equation B.26, one can look for a surface S such that at each point (x,y,z) on S, the vector $(a(x,y), b(x,y), c(x,y))$ lies in the tangent plane. To obtain such a surface, one can start by constructing a curve $\mathcal{C}$ parametrized by s such that at each point on the curve $\mathcal{C}$, the vector

$$(a(x(s), y(s)), b(x(s), y(s)), c(x(s), y(s)))$$

is tangent to the curve. In particular, the curve $\mathcal{C} = \{(x(s), y(s), z(s))\}$ will satisfy the following system of Ordinary Differential Equation (ODE)s:

$$\frac{dx}{ds} = a(x(s), y(s)) \tag{B.27}$$

$$\frac{dy}{ds} = b(x(s), y(s)) \tag{B.28}$$

$$\frac{dz}{ds} = c(x(s), y(s)). \tag{B.29}$$

Such a curve $\mathcal{C}$ is known as an integral curve for the vector field $(a(x,y), b(x,y), c(x,y))$. For a PDE of the form of Equation B.26, one looks for integral curves for the vector field $V = (a(x,y), b(x,y), c(x,y))$ associated with the PDE. These integral curves are known as the characteristic curves for Equation B.26. These characteristic curves are found by solving the system of ODE in B.27-B.29. This set of equations is known as the set of characteristic equations for Equation B.26. Introducing these characteristic equations, it

[1] Julia Levandosky, First-Order Equations: Method of Characteristics, Lecture notes from the course *Partial Differential Equations of Applied Mathematics*, Stanford University, 2002.

is possible to reduce the partial differential equation to a system of ordinary differential equations.

B.3.2 Application

Equation 2.28 is equivalent to Equation B.26, so the corresponding ODE system is the following

$$\frac{dt}{ds} = 1 \tag{B.30}$$

$$\frac{dr}{ds} = v_r \tag{B.31}$$

$$\frac{dn}{ds} = -\Big[\frac{2}{r}v_r + v_r'\Big]n(r,t). \tag{B.32}$$

From Equation B.30 it is possible to conclude that the parameter s is the time t. Therefore, Equation B.31 can be rewritten as

$$\frac{dr}{dt} = v_r = -\varepsilon\sqrt{r}\exp\Big(-\frac{r-R_h}{H}\Big); \tag{B.33}$$

that is integrable by separating the variables. As a result, as McInnes (1993),

$$t = -\frac{1}{\varepsilon}\sqrt{\pi H}\text{Erfi}\left[\frac{\sqrt{r}}{\sqrt{H}}\right] + C,$$

which is an implicit solution for the orbital radius, where the imaginary error functions $\text{Erfi}(z)$ is defined as

$$\text{Erfi}(z) = \frac{2}{\sqrt{\pi}}\int_0^z \exp\left(u^2\right)du$$

and it holds

$$\text{Erfi}(z) = -j\text{Erf}(jz).$$

To obtain an explicit solution, it is possible to introduce the approximation $\sqrt{r} \approx \sqrt{R_h}$, approximating the actual distance with the reference altitude for the atmospheric model. Equation B.33 becomes

$$\frac{dr}{dt} \approx -\varepsilon\sqrt{R_h}\exp\Big(-\frac{r-R_h}{H}\Big),$$

whose solution is

$$\exp\Big(\frac{r-R_h}{H}\Big) + \varepsilon\frac{\sqrt{R_h}}{H}t = \tilde{C}. \tag{B.34}$$

This approximation is accurate to order 10^{-2} for altitude below $1000\,\text{km}$ (McInnes, 2000).

From Equations B.31 and B.32 it is possible to write

$$\left[\frac{2}{r}v_r + v_r'\right]\frac{dr}{v_r} = -\frac{dn}{n}$$

and the left-hand side of the equation can be integrated as

$$\int \frac{1}{v_r}\left[\frac{2}{r}v_r + v_r'\right] dr = \log\left(\frac{1}{r^2 v_r}\right) + c.$$

So the evolution of the density is described by

$$n(r,t) = \frac{\Psi[G(r,t)]}{r^2 v_r(r)}$$

where $\Psi[G(r,t)]$ is an arbitrary function of the characteristic functions.

The function Ψ can be obtained from the initial distribution $n(r,0)$ at $t = 0$

$$\Psi(z) = n(r,0)[r^2 v_r(r)] = n(H\log z + R_h, 0)[-\varepsilon z^{-1}(H\log z + R_h)^{5/2}]$$

with the independent variable $z = G(r,0) = \exp\left[(r - R_h)/H\right]$.

The solution of the evolution equation becomes

$$n(r,t) = \frac{\Psi\{\exp\left[(r - R_h)/H\right] + (\varepsilon\sqrt{R_h}/H)t\}}{-\varepsilon r^{5/2}\exp\left[-(r - R_h)/H\right]} \tag{B.35}$$

B.4 Modification of the shape of the initial distribution

The analytical method obtained from the continuity equation is able to modify the function shape to follow the cloud evolution. This point can be demonstrated considering a case where the initial condition is defined by a normal distribution

$$n(r,0) = n_m \exp\left[-\lambda(r - R_h)^2\right] \tag{B.36}$$

where n_m is a scale factor and R_h is the fragmentation distance as in Chapter 2. The expression for n in Equation 2.43 can be rewritten as

$$\begin{aligned} n(r,t) =& n_m \exp\left\{ -\lambda\left[H\log\left(\exp\left[\frac{r - R_h}{H}\right] + \varepsilon\frac{\sqrt{R_h}}{H}t\right)\right]^2\right\}\cdot \\ &\cdot\left[H\log\left(\exp\left[\frac{r - R_h}{H}\right] + \varepsilon\frac{\sqrt{R_h}}{H}t\right) + R_h\right]^{5/2}\cdot \\ &\cdot\frac{1}{\exp\left[\frac{r-R_h}{H}\right] + \varepsilon\frac{\sqrt{R_h}}{H}t}\frac{1}{r^{5/2}\exp\left[-\frac{r-R_h}{H}\right]}. \end{aligned} \tag{B.37}$$

Introducing

$$\tilde{z} = H \log\Big(\exp\Big[\frac{r - R_h}{H}\Big] + \varepsilon\frac{\sqrt{R_h}}{H}t\Big) + R_h \tag{B.38}$$

Equation B.37 becomes

$$\begin{aligned} n(\tilde{z}) =& n_m \exp\left[-\lambda(\tilde{z} - R_h)^2\right] \frac{\tilde{z}^{5/2}}{\exp\left[z - \tilde{R}_h/H\right]} \cdot \Big(\exp\Big[\frac{\tilde{z} - R_h}{H}\Big] + \varepsilon\frac{\sqrt{R_h}}{H}t\Big) \cdot \\ & \cdot \Big[H \log\Big(\exp\Big[\frac{\tilde{z} - R_h}{H}\Big] - \varepsilon\frac{\sqrt{R_h}}{H}t\Big) + R_h\Big]^{5/2}. \end{aligned} \tag{B.39}$$

Equation B.39 demonstrates that the shape of the initial condition ($n_m \exp\left[-\lambda(\tilde{z} - R_h)^2\right]$) is modified by a factor that depends on the dynamics of the problem.

B.5 2D formulation of drag effect

The continuity equation can be written as

$$\frac{\partial n}{\partial t} + \nabla \bullet \mathbf{f} = \dot{n}^+ - \dot{n}^-;$$

in the 2D case, the equation is written in the phase space of semi-major axis a and eccentricity e, so the vector field $\mathbf{f}$ has two components

$$f_a = v_a n(a, e, t) \quad f_e = v_e n(a, e, t),$$

where v_a and v_e come respectively from Equation 4.44 and Equation 4.45, so

$$\begin{aligned} v_a &= -\sqrt{\mu a}\frac{c_d A}{M}\rho_0 \exp\Big(-\frac{a - R_h}{H}\Big) f(a, e, H) \\ v_e &= -\sqrt{\frac{\mu}{a}}\frac{c_d A}{M}\rho_0 \exp\Big(-\frac{a - R_h}{H}\Big) g(a, e, H) \end{aligned} \tag{B.40}$$

where

$$\begin{aligned} f(a, e, H) &= I_0 + 2eI_1 + \frac{3}{4}e^2(I_0 + I_2) + \frac{e^3}{4}(3I_1 + I_3) + O(e^4) \\ g(a, e, H) &= I_1 + \frac{e}{2}(I_0 + I_2) - \frac{e^2}{8}(5I_1 - I_3) - \frac{e^3}{16}(5I_0 + 4I_2 - I_4) + O(e^4). \end{aligned} \tag{B.41}$$

Following the approach of Gor'kavyi et al. (1997), the divergence in the phase space is simply written in Cartesian coordinates, so that the continuity equation becomes

$$\frac{\partial n}{\partial t} + \frac{\partial n}{\partial a}v_a + \frac{\partial n}{\partial e}v_e + \Big[\frac{\partial v_a}{\partial a} + \frac{\partial v_e}{\partial e}\Big] n = \dot{n}^+ - \dot{n}^-. \tag{B.42}$$

The terms of sink and source are neglected also in this case, so applying the method of characteristics the following system of ODEs is obtained

$$\frac{dt}{ds} = 1 \tag{B.43}$$
$$\frac{da}{ds} = v_a(a, e) \tag{B.44}$$
$$\frac{de}{ds} = v_e(a, e) \tag{B.45}$$
$$\frac{dn}{ds} = -\Big[\frac{\partial v_a}{\partial a} + \frac{\partial v_e}{\partial e}\Big] n(a, e, t). \tag{B.46}$$

B.5.1 First characteristic

As both v_a and v_e depend on both a and e, the first characteristic to solve is the one which relates a and e:

$$\frac{da}{de} = \frac{v_a}{v_e} = a\frac{f(a, e, H)}{g(a, e, H)}. \tag{B.47}$$

As in the previous case in 1D, here is necessary to introduce the approximation $f(a, e, H) \approx f(R_h, e, H)$ and $g(a, e, H) \approx g(R_h, e, H)$, so that the separation of variables can be applied to Equation B.47 obtaining

$$\frac{da}{a} = \frac{f(R_h, e, H)}{g(R_h, e, H)} de. \tag{B.48}$$

The term $\frac{f(R_h,e,H)}{g(R_h,e,H)}$ cannot be integrated analytically in e, so it is expressed with a Maclaurin series expansion centred at $e = 0$

$$\frac{f(R_h, e, H)}{g(R_h, e, H)} \approx \frac{2H}{H + R_h}\frac{1}{e} + \frac{11H^3 + 19H^2R_H + 7HR_H^2 + R_h^3}{4H(H + R_h)^2} e + O(e^2); \tag{B.49}$$

that holds for low eccentricity. Equation B.49 can be integrated in e obtaining

$$\int \frac{f(R_h, e, H)}{g(R_h, e, H)}\, de \approx \frac{2H}{H + R_h} \log e + \frac{11H^3 + 19H^2R_H + 7HR_H^2 + R_h^3}{4H(H + R_h)^2} e^2 + O(e^4); \tag{B.50}$$

The first characteristic can then be written as

$$K_1 + A \log e + Be^2 = \log a \tag{B.51}$$

with

$$\begin{aligned} A &= \frac{2H}{H + R_h} \\ B &= \frac{11H^3 + 19H^2R_H + 7HR_H^2 + R_h^3}{4H(H + R_h)^2} \\ K_1 &= \frac{a_0}{e_0^A \exp Be_0^2} \end{aligned} \tag{B.52}$$

where $a_0 = a(t=0), e_0 = e(t=0)$.

Equation B.51 fulfils the first requirement for the characteristics as it provides an explicit expression to compute the value of the characteristic at different stages of the problem evolution. To fulfil also the second requirement, it should be possible to obtain from Equation B.51 an explicit expression for a and e. The case for a is straightforward as from Equation B.51

$$a = K_1 e^A \exp Be^2; \tag{B.53}$$

the expression for e can be obtained introducing the Lambert W-function

$$e = \sqrt{\frac{A}{2B} W\Big[\big(2^{A/2}\frac{a}{K_1}\big)^{2/A}\frac{B}{A}\Big]}. \tag{B.54}$$

The Lambert W-function is the inverse function of

$$f(W) = W \exp W \tag{B.55}$$

or, in another terms,

$$\alpha = W(\beta) \tag{B.56}$$

is the solution to

$$\beta = \alpha \exp(\alpha). \tag{B.57}$$

The Lambert W-function requires to be evaluated numerically, but it is usually implemented in computing software such as in MATHEMATICA (where it is called `ProductLog`) or in MATLAB (where it is called `lambertw`). This means that in theory the solution can be easily implemented exploiting the built-in Lambert W-function; however, the computational time is affected by this evaluation, so an alternative expression for the characteristic may be considered.

Neglecting the term in e^2 in Equation B.50 the first characteristic becomes

$$K_1 + A \log e = \log a \tag{B.58}$$

where A is the same as before and K_1 becomes

$$K_1 = \frac{a_0}{e_0^A}$$

as e_0^2 is neglected. In this case, the expressions for a and e are simply

$$a = K_1 e^A \tag{B.59}$$

$$e = \big(\frac{a}{K_1}\big)^{1/A}. \tag{B.60}$$

The accuracy of these two expressions for the first characteristic can be appreciated from Figure B.1: the Equations B.40 are solved numerically to find the evolution of a and e with time. Then, starting from the knowledge of a, Equation B.54 and Equation B.60 are used to obtain the corresponding approximated evolution of e. In Figure B.1 *II order approximation* refers to Equation B.54 and *I order approximation* refers to Equation B.60.

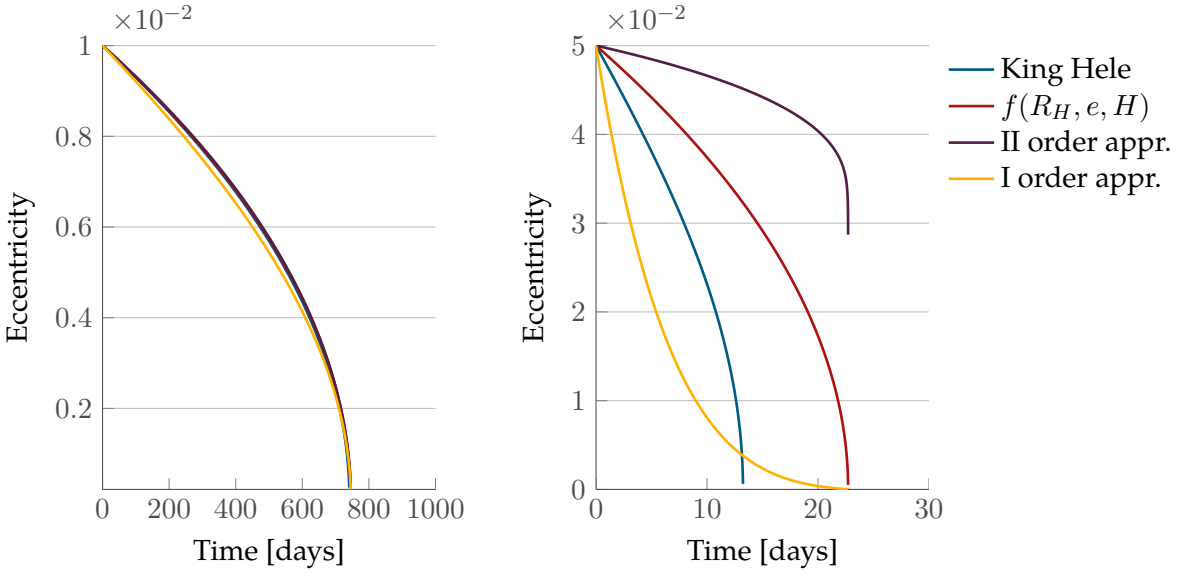

(a) $e_0 = 0.01$ **(b)** $e_0 = 0.05$

Figure B.1: Variation of the eccentricity with time with different approximations of Equations B.40 for two different values of the initial eccentricity and fixed semi-major axis of $500\,\mathrm{km}$. *II order approximation* refers to Equation B.54 and *I order approximation* refers to Equation B.60.

In the case of $e_0 = 0.01$, the approximation with the Lambert W-function (Equation B.54) follows very well the numerical solution; the expression from Equation B.60 instead introduces a relative error of 8% compared to the numerical propagation[2]. As expected, the results become worse if the eccentricity is increased up to 0.05 as in Figure B.1b. It was already observed in Figure 2.39 that in a fragment cloud the 75% of the fragments have an eccentricity value between 0 and a maximum value that depends on the altitude, ranging from 0.14 at $500\,\mathrm{km}$ to 0.08 at $1000\,\mathrm{km}$. This means that the approximation in Equation B.54 and Equation B.60 maybe not accurate for all the fragments, but they represent in any case an improvement compared to the assumption of circular orbits in Chapter 2.

[2]The numerical propagation used as a reference for these cases includes the approximations $f(a, e, H) \approx f(R_h, e, H)$ and $g(a, e, H) \approx g(R_h, e, H)$.

B.5.2 Second characteristic

Once the first characteristic is solved, it is necessary to solve the combination of other two equations from the system of Equations B.43-B.45. The solution of the equation

$$\frac{de}{dt} = v_e(a, e)$$

requires a chain of approximations that leads to an expression not able to capture that the decay depends on the exponential profile of the atmosphere. To keep a correct representation of this phenomenon, it is necessary to solve the equation

$$\frac{da}{dt} = v_a(a, e).$$

In detail,

$$\begin{aligned} \frac{da}{dt} &= -\sqrt{\mu a}\frac{c_d A}{M}\rho_0 \exp\Big(-\frac{a-R_h}{H}\Big) f(a, e(a), H) \\ &\approx -\sqrt{\mu R_h}\frac{c_d A}{M}\rho_0 \exp\Big(-\frac{a-R_h}{H}\Big) f(R_h, e(a), H); \end{aligned} \tag{B.61}$$

where $e(a)$ come from Equation B.54 or Equation B.60. For the sake of simplicity, from this point onwards only the first term of f is considered, so the previous expression becomes

$$\frac{da}{dt} \approx -\sqrt{\mu R_h}\frac{c_d A}{M}\rho_0 \exp\Big(-\frac{a-R_h}{H}\Big) I_0(R_h, e(a), H) \tag{B.62}$$

and separating the variables the following expression is obtained

$$\frac{\exp\left(\frac{a-R_h}{H}\right)}{I_0(R_h, e(a), H)}\, da = -\sqrt{\mu R_h}\frac{c_d A}{M}\rho_0\, dt. \tag{B.63}$$

Unfortunately, Equation B.63 does not admit an explicit integral (neither an explicit expression of an accurate approximation), so with this expression is not possible to fulfil the requirements for the characteristics as it is not possible to write an explicit integral, and, as a obvious consequence, it is not possible to invert its expression. For this reason, the simplified approach described in Section 4.4 was developed. However, the results in this Section may be used to identify a way to represent the connection between the semi-major axis and the eccentricity. Alternatively, these expressions may be integrated and inverted with appropriate numerical methods to obtain the advantage of working directly on the debris density. This will be subject of future work to extend the applicability of the method to elliptical orbits.

C

Research data

Part of the work in this thesis was funded by EPSRC (Engineering and Physical Science Research Council) EP/K503150/1. In line with EPSRC policy on research data management, The data generated for the validation of the propagation method and the estimation of the relative velocity has been archived and made publicly available. This chapter describes the structure of the database, the type of data and the relationship with the results in the thesis. When using any of this data or publishing results derived from analysis of this database, please cite this thesis or the corresponding published papers as indicated in the following. Please contact the author for updated references to the work.

C.1 Access to the data

Access to the database is open to the public but needs to be requested to the University of Southampton. Please contact Dr. Camilla Colombo (C.Colombo@soton.ac.uk) to request access.

C.2 Structure of the database

The database is organised in three main directories, respectively named

- `A-Propagation`, with results from Chapters 2 and 4
- `B-VelocityEstimation`, with results from Chapters 3 and 5

🗀 C-Applications, with results from Chapters 3, 5 and 6.

All data is saved as MATLAB .mat and .fig files.

C.2.1 Propagation

The folder 🗀 A-Propagation contains the result of the numerical propagation of breakup clouds, considering each fragment individually and describing their trajectories in terms of the orbital parameters. The folder has three subfolders:

🗀 Averaged, with the results from different collision altitudes as summarised in Figure 2.27 and Figure 4.14,
🗀 Energy, with the results from different collision energies as in Figures 2.32-2.34,
🗀 Inclination, with results from different inclinations of the parent orbit where the collision occurs as in Figure 2.25.

In the folder 🗀 Averaged there are ten files of with name cj.mat, with j going from 1 to 10 indicating the run of the breakup model. Each file loads in MATLAB a structure, named cloud, with the following fields

- lc, characteristic length in $[\mathrm{m}]$,
- am, area-to-mass ratio in $[\mathrm{m^2\,kg^{-1}}]$,
- mf, fragment mass in $[\mathrm{kg}]$,
- vv, velocity variation, Δv, in $[\mathrm{km\,s^{-1}}]$.

The result of the propagation of these clouds applied to different parent orbits are saved in subfolders with name hxxxiyy, where xxx should be substituted with the altitude in $[\mathrm{km}]$ and yy with the inclination in degrees. In each folder, the file po.mat is saved: it is a structure containing the orbital parameters of the fragments in the cloud. Each orbital parameter represents a field of the structure (e.g. av refers to semi-major axis) and it is stored as a matrix having as number of columns the number of fragments and as number of row the number of used instants of time. The value of the time used in the evaluation of the trajectories are stored as well in the variable po, in the field tv.

In the folder 🗀 Energy four subfolders can be found, which correspond to the four cases in Figure 2.32. Also in this case, the subfolders contain a file with the parameters of the cloud (cloud.mat) and a file with the resulting orbital parameters (po.mat).

Similarly, in the folder 🗀 Inclination, ten subfolders can be found corresponding to the simulation of a collision on a equatorial orbit in 🗀 inc1 and then with inclination increasing of ten degrees for each case, up to 90 degrees for the case in 🗀 inc10. Also in this case, the file with the parameters of the cloud (cloud.mat) and the one with the resulting orbital parameters (po.mat) are stored.

All the data in the folder 🗀 A-Propagation was used as a reference for the article

F. Letizia, C. Colombo, and H. G. Lewis. Analytical model for the propagation of small debris objects clouds after fragmentations. *Journal of Guidance, Control, and Dynamics*, 38(8):1478–1491, 2015c

and

F. Letizia, C. Colombo, and H. G. Lewis. Multidimensional extension of the continuity equation method for debris clouds evolution. *Advances in Space Research*, 2015a. doi:10.1016/j.asr.2015.11.035. Accessed 8 December 2015.

C.2.2 Velocity estimation

The folder `B-VelocityEstimation` contains 100 subfolders corresponding to the cells in Figure 3.5a and Figure 5.5a. The case `VVT0F0` corresponds to the bottom-left corner of the figure, `VVT10F10` to the top-right corner. In this case the relevant data for the validation in stored in the file `pvt.mat`, which contains the variable `vresults`, where the eighth column is the result of the numerical procedure in Section A.3 and the eleventh column is the result from Equation 5.9.

All the data in the folder `B-VelocityEstimation` was used as a reference for the article

F. Letizia, C. Colombo, and H. G. Lewis. Collision probability due to space debris clouds through a continuum approach. *Journal of Guidance, Control, and Dynamics*, 2015i. doi: 10.2514/1.G001382. Accessed 10 September 2015

and

F. Letizia, C. Colombo, and H. G. Lewis. Improved continuity equation method for space debris cloud collision analysis, 2015e. Manuscript in preparation.

C.2.3 Applications

The folder `C-Applications` is organised considering the different types of applications identified:

- `CollisionMaps`, with results as in Figure 3.12 and Figure 5.22;
- `EffectMaps`, with results as in Figure 5.20;
- `EnvironmentalIndex`, with results as in Chapter 6;
- `InfluenceMatrix`, with results as in Figure 3.14;

SingleBreakup, with results as in Figure 5.18.

The directory CollisionMaps is organised in two subfolders, referring respectively to ActiveObjects and InactiveObjects. The files saved in the folders are .mat file and a .fig file as the one in Figure 3.12. For what concerns the inactive objects, the ID of the simulations are coherent with Table 3.1. Each .mat file contains

- the evolution on the clouds generated by each cell (nconK),
- the evolution of the altitude of the studied object (hsv),
- the used time steps (tf),
- the spatial density at the target altitude for each simulated fragmentation (SPDfK),
- the resulting cumulative collision probability (in time) for each simulated fragmentation (collprobK).

These results are part of

> F. Letizia, C. Colombo, and H. G. Lewis. Collision probability due to space debris clouds through a continuum approach. *Journal of Guidance, Control, and Dynamics*, 2015i. doi: 10.2514/1.G001382. Accessed 10 September 2015

and

> F. Letizia, C. Colombo, and H. G. Lewis. Improved continuity equation method for space debris cloud collision analysis, 2015e. Manuscript in preparation.

The directory EffectMaps contains the data used for the generation of Figure 5.20 (in the subfolder UCS) and Figure 5.21 (in the subfolder Discos). In the main folder the file event3.mat contains the MATLAB variable scenario with the resulting evolution of the cloud in terms of density (n), on a grid in semi-major axis (a0v) and eccentricity (e0v), at each time instant (tvet). In each subfolder, the file immap.mat contains the resulting cumulative collision probability over time. The .fig files of Figure 5.20 and Figure 5.21 are also provided, together with a visualisation of the persistence of the fragments in orbit, similarly to Figure 2.16. The resulting top ten affected spacecraft, their orbital parameters and their mass are listed in the file targetlist.txt. These results are part of

> F. Letizia, C. Colombo, and H. G. Lewis. Improved continuity equation method for space debris cloud collision analysis, 2015e. Manuscript in preparation.

The directory EnvironmentalIndex contains the .fig files of the visualisations of the environmental index for the objects in the four considered databases:

- cnp... refers to the objects in Table 6.5,

- `csi...` refers to the objects in Table 6.6,
- `dis...` refers to the objects in Table 6.2 and Table 6.3,
- `tubs...` refers to the objects in Table 6.4.

The data on the correlation between different couples of indices is also provided. All the results are part of

> F. Letizia, C. Colombo, H. G. Lewis, and H. Krag. Assessment of breakup severity on operational satellites, 2015j. Manuscript submitted for publication.

The directory 🗀 `InfluenceMatrix` contains the data of Figure 3.14 and Figure 3.16, both for the 1D and for 2D analytical propagation. The `.mat` files contain the description of the targets (`target`), the spatial density at the target altitude for each simulated fragmentation (`SPDfK`), and the resulting cumulative collision probability (in time) for each simulated fragmentation (`collprobK`). These results are part of

> F. Letizia, C. Colombo, and H. G. Lewis. Collision probability due to space debris clouds through a continuum approach. *Journal of Guidance, Control, and Dynamics*, 2015i. doi: 10.2514/1.G001382. Accessed 10 September 2015.

The directory 🗀 `SingleBreakup` contains the data of Figures 3.11, 5.18, and 5.19. The results of the two studied events are saved in two separated subfolders, 🗀 `RBE1` and 🗀 `RBE2`. For each event, the file `pototal.mat` contains the orbital parameters of all the objects produced by the fragmentation. The remaining `.mat` file contain the analysis for each object in Table 3.1, with similar structure to the file saved in the folder 🗀 `CollisionMaps`.

Bibliography

P. V. Anderson and H. Schaub. Longitude-dependent effects of fragmentation events in the geosynchronous orbit regime. *Acta Astronautica*, 105(1):285–297, December 2014.

L. Anselmo, A. Rossi, and C. Pardini. Updated results on the long-term evolution of the space debris environment. *Advances in Space Research*, 23(1):201–211, January 1999.

J. Ashenberg. On the short-term spread of space debris. In *AIAA/AAS Astrodynamics Conference*, pages 157–163, Hilton Head, August 1992.

J. Ashenberg. Formulas for the phase characteristics in the problem of low-Earth-orbital debris. *Journal of Spacecraft and Rockets*, 31(6):1044–1049, November 1994.

J. Ashenberg and R. Broucke. The effect of the Earth's oblateness on the long-term dispersion of debris. *Advances in Space Research*, 13(8):171–174, 1993.

S. Barrows. *Evolution of artificial space debris clouds*. PhD thesis, University of Southampton, 1996.

S. Barrows, G. Swinerd, and R. Growther. Review of debris-cloud modeling techniques. *Journal of Spacecraft and Rockets*, 33, 1996.

H. Baruh. *Analytical Dynamics*. Engineering Mechanics Series. WCB/McGraw-Hill, 1999. ISBN 9780073659770. Chapter 1, Basic Principles.

B. Bastida Virgili and H. Krag. Active Debris Removal for Leo Missions. In L. Ouwehand, editor, *Sixth European Conference on Space Debris*, pages 22–25. ESA Communications, August 2013. ISBN 978-92-9221-287-2.

R. R. Bate, D. D. Mueller, and J. E. White. *Fundamentals of astrodynamics*. Dover, 1th edition, 1971. Pages 53–57, 74–82. ISBN-13: 978-0486600611.

B. Berger. Weather Satellite Breakup No Big Risk to Nearby ESA Missions. SpaceNews.com, March 2015. [Online] Retrieved on 12/03/2015.

B. Berger and M. Gruss. 20-year-old Military Weather Satellite Apparently Exploded in Orbit. SpaceNews.com, February 2015. [Online] Retrieved on 04/03/2015.

T. D. Bess. Mass distribution of orbiting man-made space debris. Recon Technical Report, NASA, 1975.

C. Bonanno. An analytical approximation for the MOID and its consequences. *Astronomy and Astrophysics*, 416:411–416, 2000.

F. K. Chan. *Spacecraft collision probability*. Aerospace Press El Segundo, CA, 2008. ISBN 9781884989186. Chapter 12, Close Encounters with Multiple Satellites.

V. Chobotov. Dynamics of orbiting debris clouds and the resulting collision hazard to spacecraft. *Journal of the British Interplanetary Society*, 43:187–195, 1990.

V. Chobotov. *Orbital mechanics*. AIAA, Reston, 3rd edition, 2002. ISBN 1563475375.

V. A. Chobotov, D. B. Spencer, D. L. Schmitt, R. P. Gupta, R. G. Hopkins, and G. Hopkins. Dynamics of Debris Motion and the Collision Hazard to Spacecraft Resulting from an Orbital Breakup. Technical report, Space Division Air Force Systems Command, 1988.

C. Colombo and C. R. McInnes. Orbital Dynamics of "Smart-Dust" Devices with Solar Radiation Pressure and Drag. *Journal of Guidance, Control, and Dynamics*, 34(6): 1613–1631, May 2011a.

C. Colombo. Long-term evolution of highly-elliptical orbits: luni-solar perturbation effects for stability and re-entry. In *25th AAS/AIAA Space Flight Mechanics Meeting*. AAS/AIAA, January 2015. AAS 15-395.

C. Colombo and C. R. McInnes. Evolution of swarms of smart dust spacecraft. In *New Trends in Astrodynamics and Applications VI*, New York, June 2011b. Courant Institute of Mathematical Sciences.

C. Colombo, A. Wittig, F. Letizia, and R. Armellin. Density of debris fragments through differential algebra and averaged dynamics. In *25th AAS/AIAA Space Flight Mechanics Meeting*. AAS/AIAA, January 2015. AAS 15-391.

A. Cordelli, P. Farinella, and A. Rossi. Study on long term evolution of earth orbiting debris. Study note of work package 3200, ESA/ESOC Contract No. 10034/92/D/IM(SC), 1995.

R. Crowther. Space debris: mitigation and remediation. In *Clean Space Workshop*, Harwell-Oxford Campus, October 2013.

J. C. Dolado-Perez, B. Revelin, and R. Di-Costanzo. Sensitivity analysis of the long-term evolution of the space debris population in LEO. In *65th International Astronautical Congress*. International Astronautical Federation, September 2014. IAC-14-A.6.2.3.

J. C. Dolado-Perez, C. Pardini, and L. Anselmo. Review of the uncertainty sources affecting the long-term predictions of space debris evolutionary models. *Acta Astronautica*, 113(August-September):51–65, 2015.

European Cooperation for Space Standardisation. Space product assurance: Failure modes, effects (and criticality) analysis (FMEA/FMECA). Technical Report ECSS-Q-ST-30-02C, ESA Requirements and Standards Division, March 2009.

D. Finkleman. The Dilemma of Space Debris. *American Scientist*, 102(1):26–33, 2014.

T. Flohrer, S. Lemmens, B. Bastida Virgili, H. Krag, H. Klinkrad, E. Parrilla, N. Sanchez, J. Oliveira, and F. Pina. DISCOS - Current status and future developments. In L. Ouwehand, editor, *Sixth European Conference on Space Debris*. ESA Communications, August 2013. ISBN 978-92-9221-287-2.

J. L. Foster. The analytic basis for debris avoidance operations for the International Space Station. In *Third European Conference on Space Debris*, pages 441–445, Darmstadt, April 2001.

W. Fucke and H. Sdunnus. Population model of small size space debris. ESOC Contract NO. 9266/90/D/MD, Battelle Europe, May 1993.

J. E. Gentle. Estimation of functions. In *Elements of computational statistics*, pages 146–161. Springer, 2002. ISBN: 0-387-95489-9.

C. Giacomuzzo, A. Francesconi, and L. Anselmo. Impact risk analysis for a spacecraft in Cosmo-Skymed orbit. *Advances in Space Research*, 46(7):846–858, 2010.

N. Gor'kavyi. A new approach to dynamical evolution of interplanetary dust. *The Astrophysical Journal*, 474(1):496–502, 1997.

N. Gor'kavyi, L. Ozernoy, J. Mather, and T. Taidakova. Quasi-stationary states of dust flows under Poynting-Robertson drag: New analytical and numerical solutions. *The Astrophysical Journal*, 488(1):268–276, 1997.

T. Hanada, J.-C. Liou, T. Nakajima, and E. Stansbery. Outcome of recent satellite impact experiments. *Advances in Space Research*, 44(5):558–567, September 2009.

W. Heard. Dispersion of ensembles of non-interacting particles. *Astrophysics and Space Science*, 43:63–82, 1976.

F. R. Hoots and B. W. Hansen. Satellite breakup debris cloud characterization. In *24th AAS/AIAA Space Flight Mechanics Meeting*. AAS/AIAA, January 2014. AAS 14-329.

R. S. Hujsak. Predicting spatial density characteristics from breakup models. *Advances in Space Research*, 13(8):157–160, August 1993.

IADC. Space debris: IADC assessment report for 2011. Iadc-12-06, Inter-Agency Space Debris Coordination Committee, April 2013. [Online] Retrieved on 18/03/2015.

D. Izzo. Statistical Distribution of Keplerian Velocities. *Journal of Guidance, Control, and Dynamics*, 29(1), 2006.

D. Izzo and C. Valente. A mathematical model representing the statistical properties of sets of orbits. *Acta Astronautica*, 54(8):541–546, April 2004.

R. Jehn. Dispersion of debris clouds from In-orbit fragmentation events. *ESA Journal*, 15 (1):63–77, 1991.

R. Jehn. *Modelling debris clouds*. PhD thesis, Technischen Hochschule Darmstadt, 1996.

A. Jenkin. Probability of collision during the early evolution of debris clouds. *Acta Astronautica*, 38(96):525–538, 1996.

A. Jenkin and R. Gick. Dilution of disposal orbit collision risk for the medium Earth orbit constellations. Technical Report 8506, The Aerospace Corporation, Los Angeles, 2005.

N. L. Johnson and P. H. Krisko. NASA's new breakup model of EVOLVE 4.0. *Advances in Space Research*, 28(9):1377–1384, 2001.

C. Kebschull, V. Braun, S. K. Flegel, J. Gelhaus, M. Möckel, J. Radtke, C. Wiedemann, H. Krag, I. Carnelli, and P. Voersmann. A simplified approach to analyze the space debris evolution in the Low Earth Orbit. In *64th International Astronautical Congress*. International Astronautical Federation, September 2013. IAC-13.A6.2.3.

C. Kebschull, H. Krag, V. Braun, S. Hesselbach, J. Radtke, and P. Scheidemann. Simulation of the space debris environment in leo using an analytical approach. In *40th COSPAR Scientific Assembly*, August 2014a.

C. Kebschull, J. Radtke, and H. Krag. Deriving a priority list based on the environmental criticality. In *65th International Astronautical Congress*. International Astronautical Federation, September 2014b. IAC-14.A6.P48.

D. J. Kessler. Collision probability at low altitudes resulting from elliptical orbits. *Advances in Space Research*, 10(3):393–396, 1990.

D. J. Kessler. Derivation of the collision probability between orbiting objects: the lifetimes of Jupiter's outer moons. *Icarus*, 48(1):39–48, October 1981.

D. J. Kessler and B. G. Cour-Palais. Collision frequency of artificial satellites: The creation of a debris belt. *Journal of Geophysical Research: Space Physics*, 83(A6):2637–2646, 1978.

D. King-Hele. *Satellite orbits in an atmosphere: theory and application*. Blackie, Glasgow and London, 1987. ISBN 0216922526.

H. Klinkrad, H. Sdunnus, and J. Bendisch. Development status of the ESA space debris reference model. *Advances in Space Research*, 16(11):93–102, 1995.

P. H. Krisko. The predicted growth of the low-Earth orbit space debris environment an assessment of future risk for spacecraft. *Proceedings of the Institution of Mechanical Engineers, Part G: Journal of Aerospace Engineering*, 221(6):975–985, January 2007.

P. H. Krisko. Proper Implementation of the 1998 NASA Breakup Model. *Orbital Debris Quarterly News*, 15(4):1–10, 2011.

P. H. Krisko, M. Horstman, and M. L. Fudge. SOCIT4 collisional-breakup test data analysis: With shape and materials characterization. *Advances in Space Research*, 41(7): 1138–1146, January 2008.

P. H. Krisko, S. Flegel, M. J. Matney, D. R. Jarkey, and V. Braun. ORDEM 3.0 and master-2009 modeled debris population comparison. *Acta Astronautica*, 113 (August-September):204–211, 2015.

T. Lang, R. Destefanis, L. Evans, L. Grassi, S. Kempf, F. Schaefer, and T. Donath. Assessing Debris Mitigation Efficiency Using Risk- Oriented Criteria : Application To Leo European Mission. In L. Ouwehand, editor, *Sixth European Conference on Space Debris*, pages 22–25. ESA Communications, August 2013. ISBN 978-92-9221-287-2.

F. Letizia, C. Colombo, H. G. Lewis, and C. R. McInnes. Debris cloud evolution in Low Earth Orbit. In *64th International Astronautical Congress*, Paris, France, September 2013. International Astronautical Federation. IAC-13.A6.P.12.

F. Letizia, C. Colombo, and H. G. Lewis. Analytical model for the propagation of small debris objects after a fragmentation event. In *24th AAS/AIAA Space Flight Mechanics Meeting*. AAS/AIAA, January 2014a. AAS 14-324.

F. Letizia, C. Colombo, and H. G. Lewis. Continuity equation approach for the analysis of the collision risk due to space debris clouds generated by a fragmentation event. In *65th International Astronautical Congress*, Paris, France, September 2014b. International Astronautical Federation. IAC-14.A6.P.31.

F. Letizia, C. Colombo, and H. G. Lewis. Continuity equation method for debris cloud evolution. In *Key Topics in Orbit Propagation Applied to SSA*, April 2014c.

F. Letizia, C. Colombo, and H. G. Lewis. Multidimensional extension of the continuity equation method for debris clouds evolution. *Advances in Space Research*, 2015a. doi:10.1016/j.asr.2015.11.035. Accessed 8 December 2015.

F. Letizia, C. Colombo, and H. G. Lewis. Multidimensional extension of the continuity equation method for debris clouds evolution. *Advances in Space Research*, 2015b. doi:10.1016/j.asr.2015.11.035. Accessed 8 December 2015.

F. Letizia, C. Colombo, and H. G. Lewis. Analytical model for the propagation of small debris objects clouds after fragmentations. *Journal of Guidance, Control, and Dynamics*, 38(8):1478–1491, 2015c.

F. Letizia, C. Colombo, and H. G. Lewis. Small debris fragments contribution to collision probability for spacecraft in Low Earth Orbit. In *Space Safety is No Accident, 7th IAASS Conference*, pages 379 – 387. Springer International Publishing, May 2015d. ISBN 978-3-319-15981-2.

F. Letizia, C. Colombo, and H. G. Lewis. Improved continuity equation method for space debris cloud collision analysis, 2015e. Manuscript in preparation.

F. Letizia, C. Colombo, and H. G. Lewis. Density approach to debris propagation. In *Key Topics in Orbit Propagation Applied to SSA*, October 2015f.

F. Letizia, C. Colombo, and H. G. Lewis. 2D continuity equation method for space debris cloud collision analysis. In *25th AAS/AIAA Space Flight Mechanics Meeting*. AAS/AIAA, January 2015g. AAS 15-293.

F. Letizia, C. Colombo, and H. G. Lewis. Density based approach for collision risk computation. In *25th International Symposium on Space Flight Dynamics*, October 2015h.

F. Letizia, C. Colombo, and H. G. Lewis. Collision probability due to space debris clouds through a continuum approach. *Journal of Guidance, Control, and Dynamics*, 2015i. doi: 10.2514/1.G001382. Accessed 10 September 2015.

F. Letizia, C. Colombo, H. G. Lewis, and H. Krag. Assessment of breakup severity on operational satellites, 2015j. Manuscript submitted for publication.

H. G. Lewis, G. G. Swinerd, R. J. Newland, and A. Saunders. The fast debris evolution model. *Advances in Space Research*, 44(5):568–578, September 2009.

H. G. Lewis, A. E. White, R. Crowther, and H. Stokes. Synergy of debris mitigation and removal. *Acta Astronautica*, 81(1):62–68, 2012.

H. G. Lewis. Fragmentation Consequence Analysis for LEO and GEO Orbits. Technical note: Analytical Model. Technical Report ESA Contract No. 4000106543, University of Southampton, May 2015.

H. G. Lewis. ACCORD: Alignment of Capability and Capacity for the Objective of Reducing Debris. FP7 Final Report, University of Southampton, 2014.

J.-C. Liou. An active debris removal parametric study for LEO environment remediation. *Advances in Space Research*, 47(11):1865 – 1876, 2011.

J. C. Liou, N. Fitz-Coy, S. Clark, M. Werremeyer, T. Huynh, M. Sorge, M. Voelker, and O. J. Debrisat - a planned laboratory based satellite impact experiment for breakup fragment characterization. In L. Ouwehand, editor, *Sixth European Conference on Space Debris*. ESA Communications, August 2013a. ISBN 978-92-9221-287-2.

J. Liou, A. Rossi, H. Krag, M. Xavier James Raj, A. K. Anilkumar, T. Hanada, and H. G. Lewis. Stability of the future leo environment. Working Group 2, Action Item 27.1, IADC, January 2013b.

C. Martin, R. Walker, and H. Klinkrad. The sensitivity of the ESA DELTA model. *Advances in Space Research*, 34(5):969–974, January 2004.

C. R. McInnes. An analytical model for the catastrophic production of orbital debris. *ESA Journal*, 17(4):293–305, 1993.

C. R. McInnes. Compact analytic solutions for a decaying, precessing circular orbit. *The Aeronautical Journal*, 98(979):357–360, 1994.

C. R. McInnes. Simple analytic model of the long term evolution of nanosatellite constellations. *Journal of Guidance Control and Dynamics*, 23(2):332–338, 2000.

C. R. McInnes and C. Colombo. Wave-like patterns in an elliptical satellite ring. *Journal of Guidance, Control, and Dynamics*, 36(6):1767–1771, 2013.

D. McKnight and G. Lorenzen. Collision matrix for low earth orbit satellites. *Journal of Spacecraft and Rockets*, 26(2):90–94, 1989.

D. S. McKnight. A phased approach to collision hazard analysis. *Advances in Space Research*, 10(3-4):385–388, January 1990.

D. S. McKnight. Determination of breakup initial conditions. *Journal of Spacecraft and Rockets*, 28(4):470–477, July 1991.

D. S. McKnight and F. R. Di Pentino. Semi-empirical satellite anomalies analysis highlighting contributions from the Fengyun-1C event. In *64th International Astronautical Congress*. International Astronautical Federation, September 2013. IAC-13.A6.2.1.

D. S. McKnight, F. R. Di Pentino, and S. Knowles. Massive collisions in LEO – A catalyst to initiate ADR. In *65th International Astronautical Congress*. International Astronautical Federation, September 2014. IAC-14-A.6.2.1.

NASA Orbital Debris Program Office. Iridium Anomalous Debris Events. *Orbital Debris Quaterly News*, 16(1):1–2, 2012a.

NASA Orbital Debris Program Office. A New Collision in Space? *Orbital Debris Quaterly News*, 19(1):2, 2015.

NASA Orbital Debris Program Office. Two Derelict NOAA Satellites Experience Anomalous Events. *Orbital Debris Quaterly News*, 16(1):1–2, 2012b.

NASA Orbital Debris Program Office. Flurry of Small Breakups in First Half of 2014. *Orbital Debris Quaterly News*, 18(3):1–2, 2014.

NASA Orbital Debris Program Office. Small Satellite Possibly Hit by Even Smaller Object. *Orbital Debris Quaterly News*, 17(2):1, 2013.

A. Nazarenko. The development of the statistical theory of a satellite ensemble motion and its application to space debris modeling. *Second European Conference on Space Debris*, 1997.

A. Nazarenko. Modeling Technogenous Contamination of the Near-Earth Space. *Solar System Research*, 36(6):513–521, 2002.

A. Nazarenko and I. Menshikov. Engineering model of space debris environment. In *Proceedings of the Third European Conference on Space Debris*, pages 293 – 298, Darmstadt, 2001.

Orbital Debris Program Office. History of on-orbits satellite fragmentations, May 2014. [Online] Retrieved on 26/08/2015.

C. Pardini and L. Anselmo. Dynamical evolution of debris clouds in geosynchronous orbit. *Advances in Space Research*, 35(7):1303–1312, January 2005.

C. Pardini and L. Anselmo. Evolution of the debris cloud generated by the Fengyun-1C fragmentation event. *NASA Space Flight Dynamics Symposium*, pages 1–13, 2007.

C. Pardini and L. Anselmo. Physical properties and long-term evolution of the debris clouds produced by two catastrophic collisions in Earth orbit. *Advances in Space Research*, 48(3):557–569, August 2011.

C. Pardini and L. Anselmo. Review of past on-orbit collisions among cataloged objects and examination of the catastrophic fragmentation concept. *Acta Astronautica*, 100: 30–39, August 2014.

D. S. F. Portree and J. P. Loftus, Jr. Orbital debris: A chronology. Technical Report NASA/TP-1999-208856, NASA, January 1999.

J. Radtke, S. K. Flegel, V. Braun, C. Kebschull, C. Wiedemann, F. Schäfer, M. Rudolph, U. Johann, J. Utzmann, and M. Höss. Fragmentation consequence analysis for LEO and GEO orbits. In *GreenOps Workshop*, Noordwijk, November 2013. ESA AO 1/7121/12/F/MOS.

J. Radtke, C. Kebschull, S. Flegel, V. Braun, F. Schäfer, M. Rudolph, and J. Utzmann. Fragmentation Consequence Analysis for LEO and GEO Orbits. Technical Report ESA Contract No. 4000106517/12/F/MOS, Technische Universität Braunschweig, September 2014.

S. Ross. *A first course in probability*. Pearson, 9th edition, 2013. ISBN 1292024925.

A. Rossi, G. Koppenwallner, P. H. Krisko, M. Oswald, , and M. Xu. Nasa breakup model implementation: Comparison of results. In *24th IADC Meeting*, Tsukuba, April 2006. Inter-Agency Space Debris Coordination Committee.

A. Rossi, A. Cordelli, C. Pardini, and L. Anselmo. Long term evolution of Earth orbiting objects. In *46th IAF International Astronautical Congress*, Oslo, 1995a.

A. Rossi, A. Cordelli, C. Pardini, L. Anselmo, and P. Farinella. Modelling the space debris evolution: Two new computer codes. In *Advances in the Astronautical Sciences - Space Flight Mechanics*, pages 1217–1231, San Diego, April 1995b. Univelt.

A. Rossi, L. Anselmo, A. Cordelli, P. Farinella, and C. Pardini. Modelling the evolution of the space debris population. *Planetary and Space Science*, 46(11-12):1583–1596, November 1998a.

A. Rossi, L. Anselmo, A. Cordelli, P. Farinella, and C. Pardini. Modelling the evolution of the space debris population. *Planetary and Space Science*, 46(11-12):1583–1596, nov 1998b.

A. Rossi, G. B. Valsecchi, L. Anselmo, C. Pardini, H. G. Lewis, and C. Colombo. Fragmentation consequence analysis for LEO and GEO orbits. In *GreenOps Workshop*, Noordwijk, November 2013. ESA AO 1/7121/12/F/MOS.

A. Rossi, H. G. Lewis, A. E. White, L. Anselmo, C. Pardini, H. Krag, and B. Bastida Virigili. Analysis of the consequences of fragmentations in Low and Geostationary orbits. *Advances in Space Research*, 2015a.

A. Rossi, G. B. Valsecchi, and E. M. Alessi. The Criticality of Spacecraft Index. *Advances in Space Research*, 56(3), 2015b. Special Issue: Advances in Asteroid and Space Debris Science and Technology - Part 1.

F. Schäfer, M. Quarti, M. Roll, P. Matura, M. Rudolph, R. Putzar, M. Reichel, J. Hupfer, and K. Buehler. Fragmentation studies of simple cubic structures at fraunhofer emi. In L. Ouwehand, editor, *Sixth European Conference on Space Debris*. ESA Communications, August 2013a. ISBN 978-92-9221-287-2.

F. Schäfer, M. Rudolph, and U. Johann. Fragmentation consequence analysis for LEO and GEO orbits. In *GreenOps Progress Meeting*, Noordwijk, November 2013b. ESA AO 1/7121/12/F/MOS.

H. Sdunnus, P. Beltrami, H. Klinkrad, M. Matney, A. Nazarenko, and P. Wegener. Comparison of debris flux models. *Advances in Space Research*, 34(5):1000–1005, January 2004.

N. Smirnov, A. Nazarenko, and A. Kiselev. Modelling of the space debris evolution based on continua mechanics. *Space Debris*, 2001.

M. E. Sorge. Satellite Fragmentation Modeling with IMPACT. In *AIAA/AAS Astrodynamics Specialist Conference*, pages 1–11, Honolulu, August 2008. AIAA 2008-6265.

S.-Y. Su and D. J. Kessler. Contribution of explosion and future collision fragments to the orbital debris environment. *Advances in Space Research*, 5(2):25–34, January 1985a.

S.-Y. Su and D. J. Kessler. Contribution of explosion and future collision fragments to the orbital debris environment. *Advances in Space Research*, 5(2):25–34, January 1985b.

M. Sykes. Zodiacal dust bands: Their relation to asteroid families. *Icarus*, 9, 1990.

D. L. Talent. Analytic model for orbital debris environmental management. *Journal of Spacecraft and Rockets*, 29(4):508–513, 1992.

S. Theil and H. Sdunnus. Assessing the short- and long-term collision risk due to fragmentation clouds. *Acta Astronautica*, 53(3):191–201, August 2003.

Union of Concerned Scientists. Satellite database, July 2014. [Online] Retrieved on 04/03/2015.

J. Utzmann, M. Oswald, S. Stabroth, P. Voigt, and I. Retat. Ranking and characterization of heavy debris for active removal. In *63rd International Astronautical Congress*. International Astronautical Federation, September 2012. IAC-12-A6.2.8.

S. Valk, N. Delsate, A. Lemaître, and T. Carletti. Global dynamics of high area-to-mass ratios GEO space debris by means of the MEGNO indicator. *Advances in Space Research*, 43(10):1509–1526, May 2009a.

S. Valk, A. Lemaître, and F. Deleflie. Semi-analytical theory of mean orbital motion for geosynchronous space debris under gravitational influence. *Advances in Space Research*, 43(7):1070–1082, April 2009b.

D. A. Vallado. *Fundamentals of astrodynamics and applications*. Springer, 4th edition, 2013. Pages 551–573, 619–688. ISBN: 978-1881883180.

R. V. d. Moraes. Non-gravitational disturbing forces. *Advances in Space Research*, 14(5): 45 – 68, 1994.

R. Walker, P. H. Stokes, J. E. Wilkinson, and G. G. Swinerd. Long-term collision risk prediction for low earth orbit satellite constellations. *Acta Astronautica*, 47:707–717, 2000.

R. Walker, C. Martin, P. Stokes, and H. Klinkrad. Sensitivity of long-term orbital debris environment evolution to the deployment of nano-satellite swarms. *Acta Astronautica*, 5(1):439–449, 2002.

A. E. White and H. G. Lewis. The many futures of active debris removal. *Acta Astronautica*, 95:189–197, February 2014.

C. Wiedemann, S. K. Flegel, J. Gelhaus, M. Möckel, V. Braun, and H. Krag. Flux calculation using population event clouds. In *62nd International Astronautical Congress*. International Astronautical Federation, October 2011. IAC-11.A6.2.16.

C. Wiedemann, C. Kebschull, S. K. Flegel, J. Gelhaus, M. Möckel, V. Braun, J. Radtke, I. Retat, B. Bischof, and P. Voersmann. On-orbit fragmentation of Briz-M. In *64th International Astronautical Congress*. International Astronautical Federation, September 2013. IAC-13.A6.2.2.

A. Wittig, C. Colombo, and R. Armellin. Density of high area-to-mass objects in geostationary and medium earth orbits through semi-analytical equations and differential algebra. In *65th International Astronautical Congress*. International Astronautical Federation, September 2014. IAC-14-C.1.2.2.

Y.-L. Xu, M. Horstman, P. H. Krisko, J.-C. Liou, M. J. Matney, E. G. Stansbery, C. L. Stokely, and D. Whitlock. Modeling of LEO orbital debris populations for ORDEM2008. *Advances in Space Research*, 43(5):769 – 782, 2009.